Universität
Augsburg
University

Perpendicular magnetic anisotropy for magnetoresistive sensor technologies

Dissertation

zur Erlangung des
Doktorgrades der Naturwissenschaften
(Dr. rer. nat.)

eingereicht an der
Mathematisch-Naturwissenschaftlich-Technischen
Fakultät der Universität Augsburg

vorgelegt von
Matthias Clemens Mühlenhoff
geb. 30. August 1990
in Düsseldorf

Juni 2021

1. Gutachter: Prof. Dr. Manfred Albrecht
2. Gutachter: Prof. Dr. Dieter Suess

Tag der mündlichen Prüfung: 15.10.2021

Abstract

Magnetoresistive (xMR) sensors find extensive application in science and industry, replacing Hall sensors in various low magnetic field environments. While there have been some efforts in increasing the dynamic magnetic field range of xMR sensors, Hall sensors remain to dominate high field applications. In this thesis, the implementation of perpendicular magnetic anisotropy (PMA) in xMR sensors is proposed, in order to increase the magnetic field range of xMR technology from a few hundred Oe to several kOe. The here developed devices cover the gap between established xMR and Hall effect based sensors in terms of their tradeoff in sensitivity and magnetic field range.
Through a dominant PMA in either the xMR reference layer (RL) or free layer (FL), the respective layer's magnetic easy axis is oriented out-of-plane (OOP), while that of the other layer is in-plane (IP). Thereby, high magnetic anisotropy fields and magnetic field ranges are realized.

First, the PMA RL concept is investigated, where the PMA is generated at the interfaces of Co/Pt multilayers. The multilayers are optimized for high PMA, which includes several fabrication parameters, such as seed layer structure and layer thicknesses. To serve as a magnetically stable reference system, the multilayers are coupled via interlayer exchange coupling, forming perpendicular synthetic antiferromagnets (p-SAFs). These are improved for high field stability and the concept of a double p-SAF is explored, which yields higher exchange fields of up to 10 kOe at room temperature. The magnetization reversal behavior of p-SAFs is investigated and modeled using micromagnetic simulations. Strong spin-canting effects are found to dominate at high magnetic fields. Furthermore, giant magnetoresistance (GMR) and anisotropic magnetoresistance (AMR) effects are studied in stacked p-SAF structures. A simple model is proposed that accurately reproduces the measured transfer curves. It is found that the GMR increases linearly with the number of Ru spacer layers, whereas the AMR has layer thickness dependent and independent contributions.
The p-SAF structures are then used for the development of GMR sensors with OOP field sensitivity and high dynamic field ranges. While the optimized p-SAFs enable GMR sensor field ranges up to 9 kOe, an introduced magnetic anisotropy control of different FL systems allows sensor customization for magnetic field range and sensor sensitivity. Tunnel magnetoresistance (TMR) sensors on wafer level are fabricated and characterized in terms of sensitivity, hysteresis, and non-linearity. The influence of various fabrication parameters, such as post annealing temperature and magnetic layer thicknesses, is studied.

Thereafter, TMR sensors with an IP reference system and OOP FL concept are designed and investigated, where the PMA stems from spin-orbit hybridization at the interface of CoFeB/MgO bilayers. Sensors with PMA FLs in superparmagnetic and ferromagnetic states are fabricated and put in comparison. The influence of post annealing temperature, capping layer, free layer thickness, CoFeB composition and measurement temperature is studied. While ferromagnetic FLs yield greater sensitivities, their effective magnetic anisotropy is also found to be highly tem-

perature dependent.

Finally, the developed PMA sensors are compared to established technologies, i.e. Hall effect based sensors, as well as magnetic shape anisotropy and vortex anisotropy xMR sensors. The conclusions drawn from the previous chapters are taken into account to map PMA sensors in the sensitivity/magnetic range spectrum, and to identify their advantages and disadvantages for application purposes. The PMA application in a magnetic angle sensor is presented, which yields smaller angle errors at low magnetic fields than a conventional TMR angle sensor.

Zusammenfassung

Magnetoresistive (xMR) Sensoren finden umfangreiche Anwendung in Wissenschaft und Industrie und ersetzen Hall-Sensoren in verschiedenen Umgebungen niedriger Magnetfelder. Obwohl einige Anstrengungen unternommen wurden, um den dynamischen Magnetfeldbereich von xMR-Sensoren zu erhöhen, dominieren Hall-Sensoren weiterhin in Hochfeldanwendungen. In dieser Arbeit wird die Implementierung von senkrechter magnetischer Anisotropie (*perpendicular magnetic anisotropy*, PMA) in xMR-Sensoren für die Erhöhung des Magnetfeldbereichs der xMR-Technologie von einigen hundert Oe auf mehrere kOe vorgestellt. Die hier entwickelten Bauteile schließen die Lücke zwischen etablierten xMR und Hall-Effekt basierten Sensoren hinsichtlich ihres Kompromisses zwischen Empfindlichkeit und Magnetfeldbereich.
Durch eine dominante PMA in der xMR Referenzschicht (RL) oder der freien Schicht (FL) ist die magnetische Vorzugsachse der jeweiligen Schicht außerhalb der Ebene (*out-of-plane*, OOP) ausgerichtet, während die der anderen Schicht in der Ebene (*in-plane*, IP) liegt. Dadurch werden hohe magnetische Anisotropiefelder und magnetische Feldbereiche realisiert.

Zunächst wird das Konzept des PMA RL untersucht, bei welchem die PMA an den Grenzflächen von Co/Pt-Multilagen erzeugt wird. Die Multilagen sind für eine hohe PMA optimiert. Diese Optimierung umfasst mehrere Herstellungsparameter, wie z.B. Saatschichtstruktur und Schichtdicken. Um als magnetisch stabiles Referenzsystem zu dienen, werden die Multilagen über eine Zwischenschichtaustauschwechselwirkung gekoppelt und zu senkrechten synthetischen Antiferromagneten (*perpendicular synthetic antiferromagnets*, p-SAFs) gebildet. Diese werden für eine hohe Feldstabilität verbessert und das Konzept eines doppelten p-SAF wird untersucht, welcher höhere Austauschfelder von bis zu 10 kOe bei Raumtemperatur erreicht. Das Magnetisierungsumkehrverhalten von p-SAFs wird mit mikromagnetischen Simulationen untersucht und modelliert. Es zeigt sich, dass starke Spinverkantungseffekte bei hohen Magnetfeldern dominieren. Darüber hinaus werden die Effekte des Riesenmagnetowiderstands (*giant magnetoresistance*, GMR) und des anisotropen Magnetowiderstands (*anisotropic magnetoresistance*, AMR) in gestapelten p-SAF-Strukturen untersucht. Es wird ein einfaches Modell vorgestellt, das die gemessenen Widerstandskurven akkurat reproduziert. Es zeigt sich, dass der GMR linear mit der Anzahl der Ru Zwischenschichten zunimmt, während der AMR schichtdickenabhängige und unabhängige Beiträge enthält.
Die p-SAF-Strukturen werden dann für die Entwicklung von GMR-Sensoren mit OOP Feldempfindlichkeit und hohen dynamischen Feldbereichen verwendet. Während die optimierten p-SAFs bis zu 9 kOe in den GMR-Sensorfeldbereichen ermöglichen, erlaubt eine eingeführte magnetische Anisotropiesteuerung verschiedener FL-Systeme die Anpassung des Sensors an den Magnetfeldbereich und die Sensorempfindlichkeit. Magnetische Tunnelwiderstand-Sensoren (*tunnel magnetoresistance*, TMR) auf Wafer-Ebene werden hergestellt und hinsichtlich Empfindlichkeit, Hysterese und Nichtlinearität charakterisiert. Der Einfluss verschiedener Fertigungsparameter, wie z.B. Wärmebehandlungstemperatur und magnetische Schichtdicken, wird untersucht.

Danach werden TMR-Sensoren mit einem IP Referenzsystem und OOP FL-Konzept entworfen und untersucht, bei denen die PMA aus einer Spin-Bahn-Hybridisierung an der Grenzfläche von CoFeB/MgO-Doppelschichten stammt. Sensoren mit PMA FLs in superparmagnetischen und ferromagnetischen Zuständen werden hergestellt und verglichen. Der Einfluss von Wärmebehandlungstemperatur, Deckschicht, freier Schichtdicke, CoFeB-Zusammensetzung und Messtemperatur wird untersucht. Ferromagnetische FLs ergeben höhere Empfindlichkeiten, weisen aber auch starke Temperaturabhängig ihrer effektiven magnetischen Anisotropie auf.

Abschließend werden die entwickelten PMA-Sensoren mit etablierten Technologien verglichen, d.h. Hall-Effekt basierten Sensoren sowie magnetischen Formanisotropie- und Vortex-Anisotropie-xMR-Sensoren. Die Schlussfolgerungen aus den vorangegangenen Kapiteln werden berücksichtigt, um PMA-Sensoren im Empfindlichkeits-/Magnetfeldbereichsspektrum abzubilden und deren Vor- und Nachteile für Anwendungszwecke aufzuzeigen. Es wird die PMA-Anwendung in einem magnetischen Winkelsensor vorgestellt, die bei geringen Magnetfeldern zu kleineren Winkelfehlern führt als ein konventioneller TMR-Winkelsensor.

Contents

List of Figures

List of acronyms and symbols

$A_{\|\|}$	AMR between polar and parallel alignment
$A_{\perp}$	AMR between polar and IP orthogonal alignment
AFM	Antiferromagnet(ic)
AMR	Anisotropic magnetoresistance
CIP	Current in-plane
CIPT	Current in-plane tunneling
FC	Field cooled
FCW	Field cooled warming
FL	Free layer
FM	Ferromagnet(ic)
FS	Full scale
G	Conductance
$\hat{G}$	$= GMR(M_S)$, for $GMR(0\,\mathrm{kOe}) := 0\,\%$ in chapter 4.4
GMC	Giant magnetoconductance
GMR	Giant magnetoresistance
$\boldsymbol{GMR}^{\ddagger}$	Simulated giant magnetoresistance
H	Magnetic field
$H_{\mathbf{c}}$	Coercivity field
$H_{\mathbf{k}}$	Magnetic anisotropy field
$H_{\mathbf{ex}}$	Exchange field in SAF structures
$H_{\mathbf{SF}}$	Magnetization reversal (state-flip) field
$H_{\mathbf{in}}$	p-SAF transition field from FM to AFM
$H_{\mathbf{in}}{}^{*}$	completed p-SAF transition field from FM to AFM
$H_{\mathbf{out}}$	p-SAF transition field from AFM to FM
I	Current
IEC	Interlayer exchange coupling
IP	In-plane
$K_{\mathbf{eff}}$	Effective magnetic anisotropy
$K_{\mathbf{S}}$	Interface contribution of the magnetic anisotropy
$K_{\mathbf{V}}$	Volume contribution of the magnetic anisotropy
$L_{\mathbf{bot}}$	Bottom p-SAF layer
$L_{\mathbf{mid}}$	Middle p-SAF layer
LR	Linear magnetic field range
$L_{\mathbf{top}}$	Top p-SAF layer
M	Magnetization
ML	Multilayer
MOKE	Magneto-optic Kerr effect
$M_{\mathbf{res}}$	Residual (or remanence) magnetization

$M_{\mathbf{S}}$	Saturation magnetization
$M_{\mathbf{z}}$	Magnetization in z-direction (out-of-plane)
N	Number of Co/Pt bilayers in the ML structure
$N_{\mathbf{Ru}}$	Number of Ru spacer layers in stacked p-SAFs
NL	Non-linearity
OOP	Out-of-plane
PA	Post annealing
PCB	Printed circuit board
PMA	Perpendicular magnetic anisotropy
p-SAF	Perpendicular synthetic antiferromagnet
RKKY	Ruderman–Kittel–Kasuya–Yosida
S	Sensitivity
$\mathbf{S_a}$	FL System a: Single layer
$\mathbf{S_b}$	FL System b: Multilayer
$\mathbf{S_c}$	FL System c: Single layer + Multilayer
$\mathbf{S_d}$	FL System d: Bilayer Co + CoFe
SAF	Synthetic antiferromagnet
SP	Superparamagnetic
S_V	Noise power
SQUID	Superconducting quantum interference device
-VSM	- vibrating sample magnetometer
R	Resistance
RL	Reference layer
RT	Room temperature
T	Temperature
t	Thickness
$T_{\mathbf{k}}$	Temperature coefficient (relative change in $S(T)$)
$T_{\mathbf{b}}$	Blocking temperature for superparamagnetic states
TB	Tunnel barrier
TMR	Tunnel magnetoresistance
TRM	Thermoremanent magnetization
U	Voltage
V	Volume
xMR	(Giant, Tunnel and Anisotropic) Magnetoresistance
ZFCW	Zero field cooled warming
β	Angle between applied field and magnetic easy axis
β_θ	Fit parameter for θ
β_ψ	Fit parameter for ψ
θ	Angle between OOP axis and FM magnetization
ρ	Resistivity
$\rho_{\mathbf{l}}$	Longitudinal resistivity ($\mathbf{M} \parallel \mathbf{I}$)
$\rho_{\mathbf{p}}$	Polar resistivity ($\mathbf{M}$ OOP, $\mathbf{M} \perp \mathbf{I}$)
$\rho_{\mathbf{t}}$	Transverse resistivity ($\mathbf{M}$ IP, $\mathbf{M} \perp \mathbf{I}$)
σ	Conductivity
φ	Angle between $\mathbf{M}_{\mathrm{IP}}$ and $\mathbf{I}$
ψ	Angle between magnetizations of two FM layers

Chapter 1

Introduction

Spintronics, i.e. the study of electrical devices that use the spin degree of freedom of charge carriers [1], is an essential part of modern day technology. One of the best known applications is the magnetic read head in hard disk drives, where a magnetoresistance (xMR) sensor is used to measure the information stored ("0" or "1") in form of the magnetization direction of each bit. For many years, the use of spintronics has expanded. Magnetic sensor devices in particular are used in a wide spectrum of applications, as technologies become aware of their internal processes and their environment: Mobile phones and home appliances such as blenders, green energy generators like wind turbines, or industrial devices such as motor control sensors. A major market is the automotive industry, as shown in Fig. 1.0.1 where the estimated market for automotive magnetic sensors from 2016–2030 is presented [2]. While a steady increase is expected for Hall effect based sensors, the growth of xMR sensors (AMR, TMR and GMR) is even more significant.

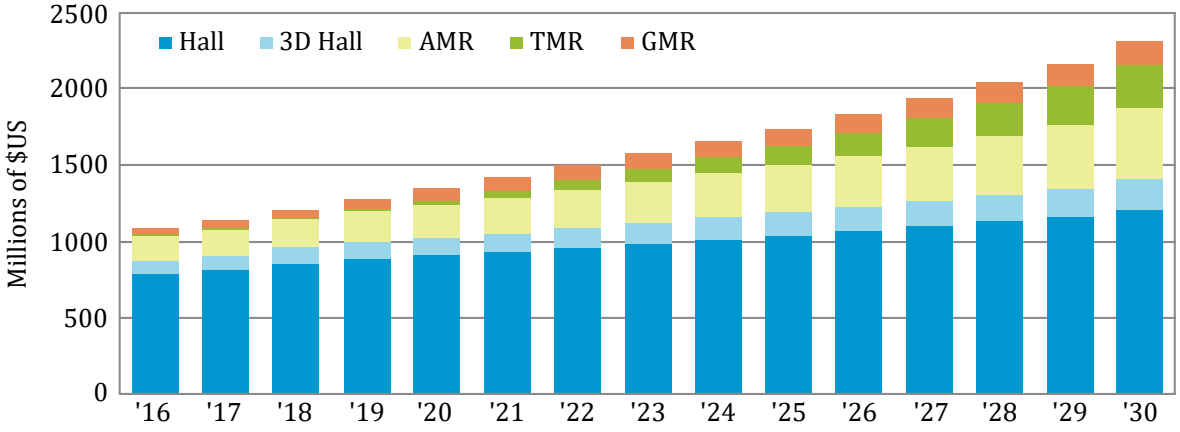

Fig. 1.0.1: Estimated market for automotive magnetic sensors by technology for the years 2016–2030. Adapted from [2].

Sensitivity vs. magnetic field range. Depending on the purpose, different requirements to the magnetic sensor performance apply. For some applications, such as magnetic wheel speed sensors [3], high magnetic field sensitivities are needed, whereas others require the ability to sense high magnetic field ranges. An example for the latter is a magnetic current sensor. Here, a magnetic

sensor is used to measure the magnetic field that is generated by the current in a wire (often in combination with a magnetic core to amplify the field). Currently, magnetic current sensors with xMR technology are available in closed-loop concepts only, which means that a feedback loop is used with an internally installed electromagnet that counteracts the external field, so that the magnetic sensor only detects field changes around zero field. This requires a sensor with only a small magnetic field range. However, the currents for the internal electromagnet are limited due to their heat generation. Furthermore, the closed-loop requires more power and additional electrical elements compared to open-loop concepts. In the open-loop concept, the magnetic field is measured directly, which simplifies the sensing device. However, to measure high electrical currents as they appear in electromobility applications, high sensing ranges of several kOe are necessary [4].

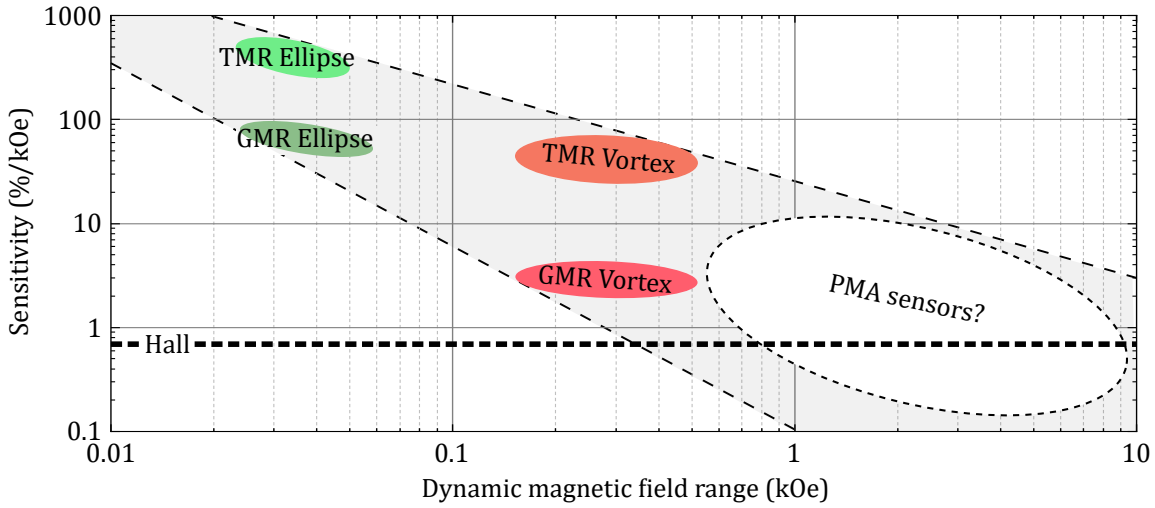

Fig. 1.0.2: Illustration of sensitivity and dynamic field range regime for different magnetic sensor technologies. The illustrated areas represent estimates based on references [5–8].

In order to fulfill these various requirements, several technologies with in parts fundamentally different magnetic sensing principles are found in industry applications. As shown in Fig. 1.0.1, the most used linear magnetic sensors include Hall, Giant Magnetoresistance (GMR), and Tunnel Magnetoresistance (TMR) sensors. While the Hall effect has no field range limit, its sensitivity towards field changes is orders of magnitude smaller than those of TMR and GMR sensors, which in turn have magnetic range constraints due to the magnetization saturation fields of their respective magnetic layers. Depending on their design, the field range of xMR sensors can be customized to some extend [9]. Magnetic vortex sensors in particular have been developed in recent years to reach field ranges of several hundred Oe [8,10]. However, increased magnetic field range comes at the cost of a lower sensor sensitivity.

The correlation is summarized in Fig. 1.0.2, with dashed lines indicating the estimated region limits for the sensitivity/magnetic field range tradeoff. The illustration also discloses an area of several kOe magnetic field range, which goes beyond the range of vortex xMR sensors and has the potential to yield higher sensitivities than Hall effect based sensors. This gap in available performance parameters has yet to be filled with alternative xMR sensor designs. Besides a

superior sensitivity, further advantages of the xMR sensor technology, such as low power consumption and high frequency bandwidths, make this region interesting for applications. In this thesis, suitable magnetic thin film systems with crossed magnetic anisotropies are proposed to unlock these high magnetic field ranges for xMR sensor technology.

PMA sensor concepts. The idea of the perpendicular magnetic anisotropy (PMA) sensor concept is to utilize a cross-geometric anisotropy of free layer (FL) and reference layer (RL), i.e. using PMA to create an out-of-plane easy axis, either in FL or RL. Thus, an applied field along the sensing axis (i.e. the magnetic easy axis of the RL) acts along the magnetic hard axis of the FL, which requires high magnetic fields to reach magnetization saturation. The working principles of PMA sensors are illustrated in Fig. 1.0.3, showing the sensor resistance R as a function of applied field H. Figure 1.0.3(a) depicts a system with PMA FL and in-plane RL, thus having a linear response in an in-plane field H_{in}, whereas Fig. 1.0.3(b) features a perpendicular synthetic antiferromagnet (p-SAF) in the reference system and an in-plane FL, thereby forming an xMR sensor that is sensitive to out-of-plane fields H_{OOP}.

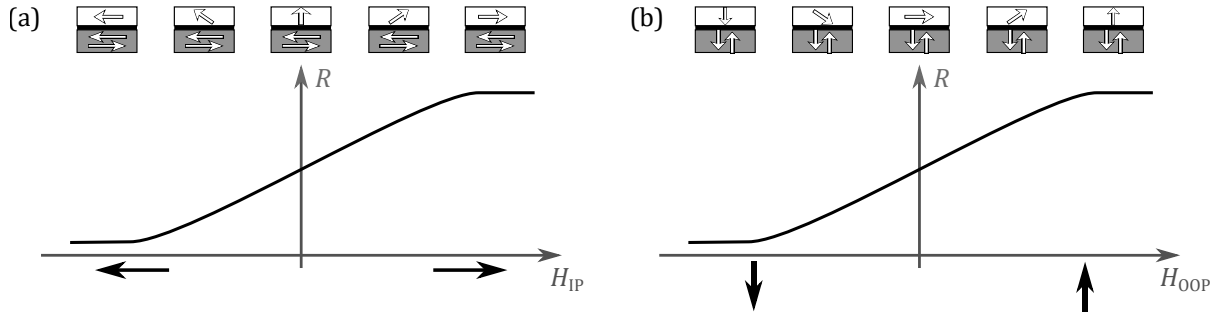

Fig. 1.0.3: Working principle of GMR and TMR sensors with a cross-geometric anisotropy. In (a), the reference layer has an in-plane magnetic anisotropy, while PMA dominates in the free layer. In (b), a perpendicular SAF is used as reference system, while the free layer has an in-plane magnetic anisotropy. By operating the sensor along the magnetic hard axis of the free layer, the sensor features a wide magnetic field range.

State of the art. PMA in magnetic thin films has been researched for many decades [11] but has received a lot of interest particularly since 2002 [12] because of its potential use in magnetoresistive random-access memory (MRAM) devices built from magnetic tunnel junctions (MTJ) [13, 14]. Here, bilayer structures are utilized to establish PMA at the interface of a metal oxide (e.g. MgO) and a $3d$ transition metal. The metal oxide simultaneously acts as the tunnel barrier of the MTJ.

Using these bilayers for PMA FLs, P. Wisniowski et al. [15, 16] have fabricated in-plane TMR sensors with wide dynamic field ranges, as shown in Fig. 1.0.4(a). Since the PMA stems from the interface of the bilayer, a smaller thickness of the transition metal alloy (here CoFeB) yields an increased out-of-plane anisotropy. However, the tendency of these thin FLs to develop nanocrystals and superparamagnetic states [17] can make the TMR sensor development challenging.

While different approaches for a PMA RL can be found in the literature [18, 19], the overwhelmingly dominant technique is to use metal multilayers (e.g. Co/Pt) [20] as elements for the fabrication of p-SAF in the reference system [21]. Both, GMR sensors [22–27] and TMR

sensors [28] with cross-geometric magnetic anisotropy can be constructed this way. However, in most cases, these p-SAFs withstand externally applied fields of only a few hundred Oe before they experience significant destabilization. Therefore, the research results of T. Nakano, T. Ogasawara et al. (group of Y. Ando, Tohoku University) are particularly noteworthy [4–6, 29–33], who adopted the optimized p-SAF structures from Yakushiji et al. [34–36] to develop TMR sensors with magnetic field ranges up to 3.5 kOe (see Fig. 1.0.4(b)).

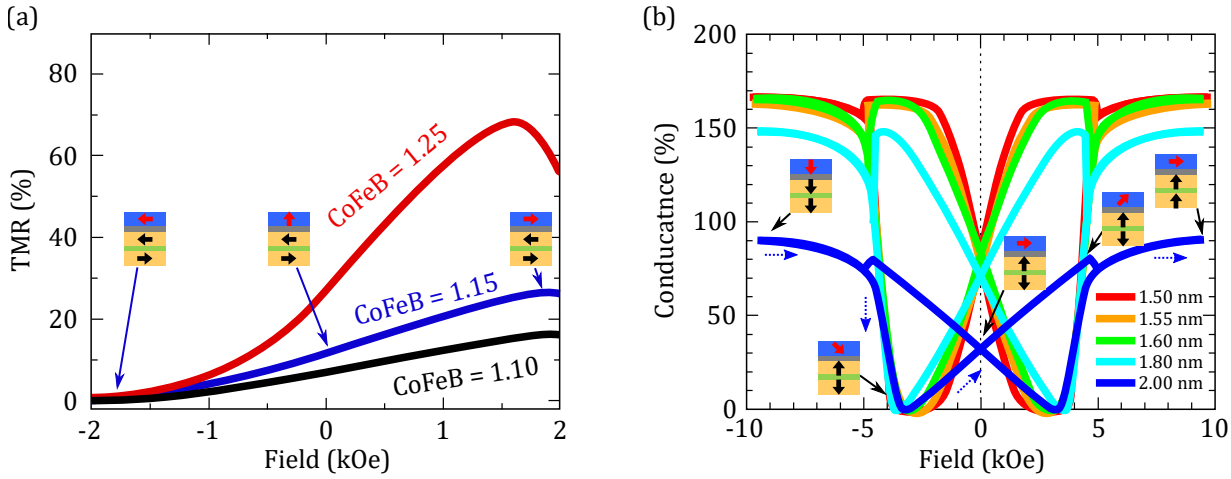

Fig. 1.0.4: Results reported on TMR sensors with cross-geometric magnetic anisotropy. (a) TMR with PMA free layer with up to 2 kOe dynamic field range, adapted from [15] (seed/$Pt_{40}Mn_{60}$(16)/$Co_{30}Fe_{70}$(2.3)/Ru(0.85)/$Co_{40}Fe_{40}B_{20}$(t_{CoFeB})/MgO(2.4)/$Co_{40}Fe_{40}B_{20}$(t_{CoFeB})/cap). (b) TMR sensor with a p-SAF in the reference system, yielding H_{ex} around 4 kOe, adapted from [32] (seed/[Co(0.28)/Pt(0.16)]$_9$/Co(0.28)/Ru(0.4)/Co(0.28)/[Pt(0.16)/Co(0.28)]$_5$/Ta(0.2)/$Co_{40}Fe_{40}B_{20}$(1)/MgO(2)/$Co_{20}Fe_{60}B_{20}$(t_{CoFeB})/cap). All thicknesses in nm.

Scope. In this thesis, both PMA concepts shown in Fig. 1.0.3 are pursued. The goal is to design and fabricate GMR as well as TMR sensors with magnetic field ranges of several kOe (>3.5 kOe). This work aims for a better understanding of the PMA sensor performance with respect to underlying magnetization processes, sensor sensitivity, linear magnetic field range, magnetic hysteresis, and temperature sensitivity.

Thesis structure.

In this thesis, magnetoresistive sensors with cross-geometric anisotropy are developed and investigated, which includes the study of PMA in magnetic thin films, and coupling mechanisms for p-SAF construction. Therefore, the fundamentals of magnetic anisotropy, interlayer exchange coupling, and magnetoresistance effects are covered in **chapter 2**.

In **chapter 3**, the experimental methods are presented, which are used for the fabrication of the magnetic structures, as well as measurements of their magnetization behavior and magnetotransport characteristics.

Measurement results are presented and discussed in **chapters 4** and **5**. In **chapter 4**, xMR sensors with PMA RL and in-plane FL are developed (see Fig. 1.0.3(b)). For that purpose, Co/Pt multilayers and thereafter p-SAF structures are studied and optimized for high magnetic field stability. Different p-SAF designs are investigated and studied in regards to their magnetic reversal process, spin-canting, and magnetoresistance effects. Subsequently, p-SAFs are used

to build full GMR and TMR stacks, with a particular focus on free layer magnetic anisotropy control.
The concept of in-plane RL and PMA FL (see Fig. 1.0.3(a)) is covered in **chapter 5**. In addition, a comparison is given for TMR sensors with ferromagnetic and superparamagnetic free layers regarding their sensitivity, FL dynamic magnetic field range and temperature sensitivity.
In **chapter 6**, the results of the previous chapters are summarized, focusing on the advantages and disadvantages of PMA based sensors for applications. For that purpose, established technologies and designs are introduced (Hall sensors, shape anisotropy xMR sensors and vortex anisotropy xMR sensors) and compared to the PMA based designs. Finally, a magnetic angle sensor with PMA FL is presented.

Chapter 2

Fundamentals

In this chapter, the most relevant fundamentals for the development of magnetoresistive sensors with perpendicular magnetic anisotropy are presented. First, the concept of magnetic anisotropy as well as the different contributions to the effective magnetic anisotropy are discussed. Perpendicular magnetic anisotropy is discussed in more detail for material systems most relevant in this thesis. Subsequently, interlayer exchange coupling (IEC) is presented, which occurs when two ferromagnetic layers are separated by a non-magnetic metallic spacer layer of suitable thickness. Finally, the origins of the giant (GMR), tunnel (TMR) and anisotropic (AMR) magnetoresistance effects are examined. For the AMR, different resistivity contributions in a Pt/Co/Pt system are considered in more detail.

2.1 Magnetic anisotropy

Magnetic anisotropy (from ancient Greek, meaning *unequal direction/rotation*) is the characteristic of a magnetic body to have a preferential magnetization direction. The change of magnetization in a ferromagnetic material, inflicted by an externally applied magnetic field, depends on the spatial axis of that field with regard to the ferromagnetic body. For a simple illustration, one can consider a Stoner-Wohlfarth particle [37], i.e. a single domain particle, with uniaxial magnetic anisotropy, as shown in Fig. 2.1.1(a). When a field H is applied at an angle β to the *easy axis* (here shown as dashed line), the magnetization $\mathbf{M}$ with value M_S (saturation magnetization) is rotated by an angle γ. The easy axis is characterized by the magnetization direction at zero field. An applied field parallel to the easy axis ($\beta = 0°$) doesn't rotate $\mathbf{M}$ until H exceeds the coercive field H_c, meaning the magnetic moments are still directed along the easy axis but have reversed in opposite direction. Fields along the *hard axis* ($\beta = 90°$) result in a continuous, hysteresis-free rotation of the magnetization until fully aligned with the direction of H. The corresponding hysteresis curves are shown in Fig. 2.1.1(b).

The total energy E is a sum of the anisotropy energy E_ani and the energy associated with

the field (*Zeeman energy*) E_{H}, which can be expressed with

$$E = \underbrace{K_1 \sin^2(\gamma - \beta)}_{E_{\mathrm{ani}}} \underbrace{-\mu_0 M_{\mathrm{S}} H \cos(\gamma)}_{E_{\mathrm{H}}}, \tag{2.1}$$

where K_1 is the uniaxial anisotropy constant and μ_0 denotes the vacuum permeability.

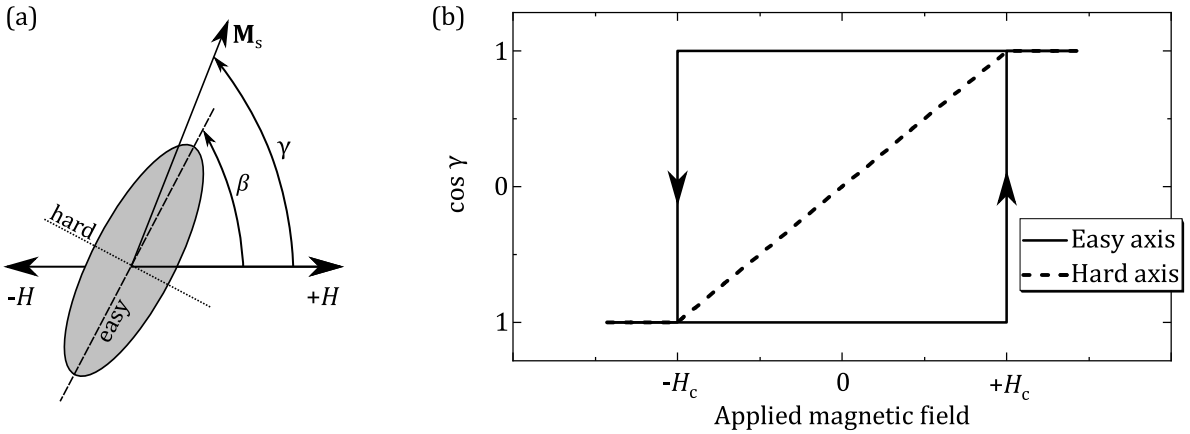

Fig. 2.1.1: Illustration of the Stoner-Wohlfarth model. (a) A Stoner-Wohlfarth particle in an external magnetic field H, directed at an angle β to the particle's easy axis (dashed line). The hard axis is represented as dotted line. The rotation of the magnetization of an angle γ to H depends on β and the strength of H. (b) Magnetization angle γ as a function of H for an applied field along the easy axis ($\beta = 0°$) and along the hard axis ($\beta = 90°$). Figures are adapted from the original publication of Stoner and Wohlfarth [37].

In macroscopic magnetic systems, the *effective* magnetic anisotropy, denoted as K_{eff}, is composed of several contributions [20], which are discussed in the next chapter. Generally, K_{eff} represents the energy that is required to align the magnetization along its hard axis, and can be calculated using the enclosed area between M-H hysteresis loops along the easy and the hard axis with

$$K_{\mathrm{eff}} = \int_{OOP} \mu_0 M \, dH - \int_{IP} \mu_0 M \, dH. \tag{2.2}$$

K_{eff} is illustrated in Fig. 2.1.2 by the hatched area. Hysteresis loop branches are averaged [20]. In case of $K_{\mathrm{eff}} > 0$, i.e. the area underneath the hysteresis curve in an out-of-plane (OOP) measurement is bigger than the area in an in-plane (IP) measurement, one considers the sample to have an OOP effective magnetic anisotropy. Accordingly, an IP effective magnetic anisotropy is present when $K_{\mathrm{eff}} < 0$. In the literature, an approximation is often found for K_{eff} [20,38], being

$$K_{\mathrm{eff}} = \pm \mu_0 H_{\mathrm{k}} M_{\mathrm{S}} / 2, \tag{2.3}$$

with magnetic anisotropy field H_{k}, determined from an M-H hysteresis loop along the magnetic hard axis, as shown in Fig. 2.1.2. Depending on whether the easy axis is OOP (+) or IP (−), the correct sign must be selected for Eq. 2.3. However, in case of a perpendicular easy axis ($K_{\mathrm{eff}} > 0$), this approximation may not always be applicable. When very small magnetic domains form, the magnetostatic interaction between the domains introduces an additional energy term, which causes the average (i.e. hysteresis adjusted) OOP magnetic saturation to be reached at non-zero

saturation fields (Fig. 2.1.2(b)). This leads to K_{eff} having no relation to the saturation fields. Therefore, Eq. 2.3 may not be used in such cases, whereas the enclosed area between OOP and IP M-H hysteresis loops still yield the correct K_{eff} [20].

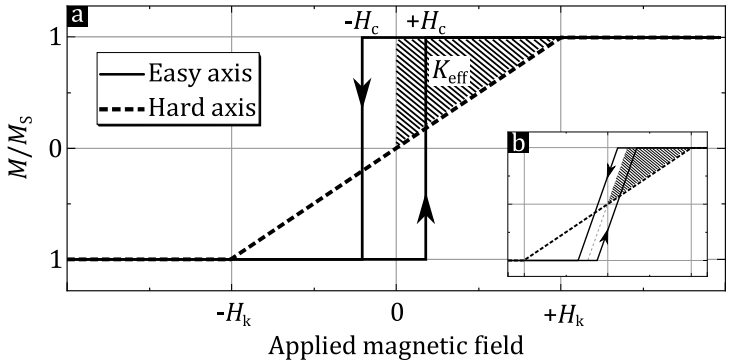

Fig. 2.1.2: (a) Graphical determination of the effective magnetic anisotropy K_{eff}, here shown as the hatched area, enclosed by the M-H hysteresis loops along the magnetic easy and magnetic hard axes. (b) Hysteresis loop for a sample with small domains.

2.1.1 Anisotropy contributions

Since the magnetic anisotropy is determined by several different magnetic interactions, it accounts for a broad subject, of which only a brief introduction can be given here. The focus lies on magnetic anisotropy in thin film structures. A more detailed discussion on that topic is given by J. Bland and B. Heinrich [39] and in a review article by M. Johnson et al. on metallic multilayers [20].

2.1.1.1 Magnetic dipolar anisotropy

Due to the large difference in spatial dimensions, the magnetic dipolar anisotropy, also often referred to as magnetic *shape anisotropy*, plays an important role in magnetic thin film structures. Furthermore, in contrast to spin-orbit derived anisotropies, the magnetic dipolar anisotropy stems from the comparatively long ranged magnetic dipole-dipole interaction. The energy term from this interaction is expressed as the demagnetization energy E_{d} [40], with

$$E_{\text{d}} = -\frac{\mu_0}{2V}\int \mathrm{d}V \mathbf{M}\cdot\mathbf{H}_{\text{d}}. \tag{2.4}$$

μ_0 represents the magnetic permeability in vacuum and $\mathbf{H}_{\text{d}}$ the demagnetization field, with

$$\mathbf{H}_{\text{d}} = -\mathcal{N}\mathbf{M}. \tag{2.5}$$

Here, $\mathcal{N}$ is the shape-dependent demagnetization tensor. An analytical calculation of $\mathcal{N}$ is only possible for simple geometries, such as ellipsoids, infinite rods, and infinite planes. The latter is used as an approximation for thin film geometries, which simplifies $\mathcal{N}$ to be zeros for all directions with the exception of the direction perpendicular to the film plane, i.e. $\mathcal{N}^{\perp} = 1$.

Therefore, inserting Eq. 2.5 in 2.4 yields

$$E_\mathrm{d} = \frac{\mu_0}{2} M_\mathrm{S}^2 \cos^2\theta, \tag{2.6}$$

where θ is the angle between film normal and $\mathbf{M}$. From Eq. 2.6 it is easy to see that E_d is minimized for $\theta = \pm 90°$, i.e. with the magnetization $\mathbf{M}$ lying in-plane. Thus, the magnetic dipolar anisotropy in magnetic thin films adds an in-plane contribution to the effective magnetic anisotropy. It should be noted that in the case of the thin film limit used here, the resulting Eq. 2.6 is independent of the film thickness.

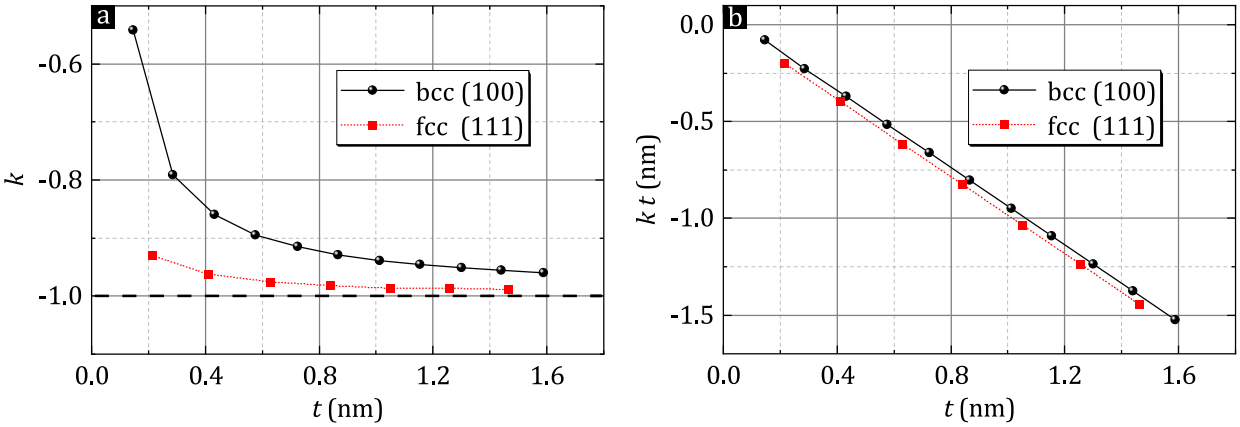

Fig. 2.1.3: Calculation results for magnetic dipole anisotropy using a discrete approach, adapted from Draaisma and de Jonge [40]. Results are given for a bcc (100) and an fcc (111) Co thin film. (a) k as a function of t, showing the convergence of k towards -1 at high thicknesses. (b) $k\,t$ as a function of t, displaying a linear relation with slope k_V.

The calculation above is based on a continuum approach, which disregards the discrete atomic layers of a thin film. To take this into account, one can treat the magnetic system as a collection of discrete magnetic dipoles [40], where the magnetic anisotropy of dipoles at the surface is different to that of dipoles in the center of the film. Specifically, the center dipoles show nearly the exact same anisotropy values as is found through a continuum approach, whereas surface dipoles deviate from the continuum results and can even contribute an out-of-plane magnetic anisotropy. The calculation results of this approach are shown in Fig. 2.1.3 for the Co textures bcc (100) and fcc (111), derived by H. Draaisma and W. de Jonge [40]. The plotted magnetic dipole anisotropy k is the averaged magnetic dipole anisotropy for all atomic layers, with

$$k(n) = E_\mathrm{a}(n) / \frac{\mu_0 M_\mathrm{S}^2}{2}. \tag{2.7}$$

$E_\mathrm{a}(n)$ is the anisotropy energy contributed by dipoles in atomic layer n. An anisotropy $k < 0$ is considered in-plane, whereas $k > 0$ denotes an out-of-plane magnetic anisotropy. As this effect scales with the thickness of the sample t, it is particularly relevant for film thicknesses below approximately 2 nm. At high thicknesses, k converges to the same anisotropy from the continuum approach, namely $k \to -1$. Furthermore, it shows that magnetic dipole anisotropy

can be separated into an interface (or *surface*) anisotropy k_S and a volume anisotropy k_V with

$$k = 2k_S \frac{d}{t} + k_V. \tag{2.8}$$

The factor d represents the distance between two atomic layers. The volume anisotropy produces the slope for a plot of $k\,t$ as a function of t, as shown in Fig. 2.1.3(b).

2.1.1.2 Magnetocrystalline anisotropy

The anisotropy that stems from the crystal structure of the magnet is called magnetocrystalline anisotropy. Its cause is spin-orbit interaction (SOI), because of which the electron spin is coupled to the orbit angular momentum, while the orbit is also influenced by the crystal structure. An illustration of one of the origins of magnetocrystalline anisotropy is given by C. Kittel [41], here adapted in Fig. 2.1.4.

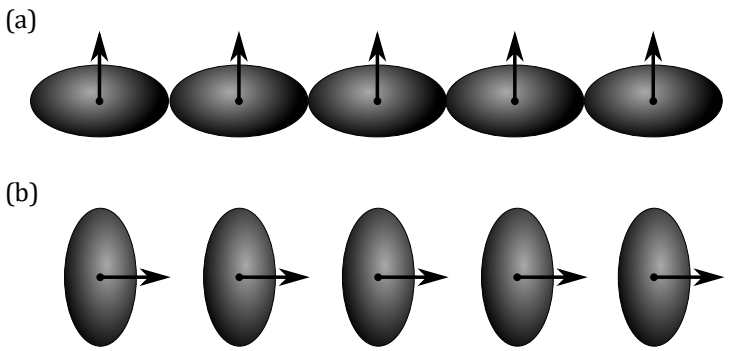

Fig. 2.1.4: Illustration of atomic charge distributions in a crystal lattice. The distribution is not spherical due to spin-orbit interaction. A rotation of the spin direction from (a) to (b) changes both exchange energy and electrostatic interaction energy of the charge distributions. The difference in energy from (a) to (b) is the magnetoctrystalline anisotropy energy. Figure is adapted from [41].

Due to SOI, the charge distribution of the atom in a crystal is not spherical but spheroidal, and depends on the crystal structure and the spin direction. Therefore, the overlap of electron distributions in the crystal is asymmetric. A rotation of the spin through an applied magnetic field changes both the exchange energy as well as the electrostatic interaction energy of the charge distributions. Accordingly, the magnetocrystalline anisotropy energy E_{crystal} is a function of the angle between applied field and crystal axis. For example, in case of cobalt in hexagonal crystal structure with said angle to the hexagonal crystal axis here defined as ξ, E_{crystal} is given by

$$E_{\text{crystal}} = K_1 \sin^2 \xi + K_2 \sin^4 \xi + ... \tag{2.9}$$

Higher orders of K_i become negligible.

2.1.1.3 Magneto-elastic anisotropy

It was shown that the magnetocrystalline anisotropy can be derived from *ab initio* calculations [42, 43], which match well with certain material structures. Nevertheless, influences which affect the magnet's microstructure, such as roughness [44], strain, interdiffusion, and incoherent growth, are challenging to fully account for in these calculations. Instead, strain related anisotropy contributions are often dealt with separately from the magnetocrystalline anisotropy, under the name of magneto-elastic anisotropy, even though the origin is also SOI. For some material structures the magneto-elastic anisotropy is even considered to be the dominating contribution [45]. There are several possible causes for strain, such as thermal strain from different thermal expansion coefficients, strain coming from crystal growth defects, or various external influences like surface acoustic waves [46]. Of particular interest in magnetic thin films is the strain caused by lattice mismatch at the interface of two different materials. The resulting anisotropy contribution is therefore an interface anisotropy. This spin-orbit coupling derived interface anisotropy can be significantly stronger than the previously introduced magnetic dipole interface anisotropy k_S [20].

2.1.1.4 Phenomenological approach

Experimentally, it is convenient for magnetic thin films to not separate the magnetic anisotropy contributions into their physical causes, but differentiate magnetic anisotropy contributions that scale with film thickness t from those that are thickness independent [47, 48]. The first set of contributions is summarized as volume contribution K_V, the latter as interface (or *surface*) contribution K_S. In fact, this perspective inspired the same separation for the magnetic dipolar anisotropy by Draaisma and de Jonge [40], shown earlier in this chapter. Accordingly, the expression for the effective magnetic anisotropy K_eff is similar to Eq. 2.8, with

$$K_\mathrm{eff} = K_\mathrm{V} + 2K_\mathrm{S}/t. \tag{2.10}$$

The factor 2 stems from the assumption of two identical interfaces of the layer. For a more general expression, $2K_\mathrm{S}$ is separated into two independent contributions K_S1 and K_S2 [49].

2.1.2 Perpendicular magnetic anisotropy in metal multilayer

As already discussed, there are several causes for magnetic anisotropies involved in a magnetic system, of which the magnetic dipolar anisotropy in thin films contributes to an in-plane anisotropy. Therefore, an effective out-of-plane anisotropy must stem from a dominating contribution of spin-orbit interaction. For bulk Co, however, the magnetocrystalline anisotropy is negligible in fcc Co and with $5.3\,\mathrm{Merg/cm^3}$ in hcp Co still smaller than the magnetic dipolar anisotropy in thin films. In total, the volume contributions are $K_\mathrm{V} = -12.7\,\mathrm{Merg/cm^3}$ for bulk fcc Co, and $K_\mathrm{V} = -7.4\,\mathrm{Merg/cm^3}$ for bulk hcp Co [20]. Thus, perpendicular magnetic anisotropy in Co-based multilayers must arise from magneto-elastic contributions or other elements leading to a dominating interface anisotropy K_S.
In 1985, PMA was achieved the first time in Co/Pd multilayers by P. Carcia, A. Meinhaldt, and

A. Suna [48]. The effective magnetic anisotropy is strongly Co thickness t_{Co} dependent with PMA emerging for $t_{Co} < 0.8\,nm$, and, in a subsequent study by P. Carcia [50], for approximately $t_{Co} < 1.4\,nm$ in Co/Pt multilayer systems. While assuming an hcp Co texture in their Co/Pd multilayers, the interface anisotropy was measured to be $K_S = 0.16\,erg/cm^2$, but was found to be generally higher ($0.25–0.92\,erg/cm^2$) in later studies, depending on deposition technique and substrate [20]. Similarly distributed are the results for K_S in Co/Pt multilayer systems, varying from $0.2\,erg/cm^2$ [51] to $0.97\,erg/cm^2$ [52], and K_V values found between $-7\,Merg/cm^3$ [51] and $-60\,Merg/cm^3$ [52]. Most K_V values, however, are reported to be around $-10\,Merg/cm^3$ [20]. Figure 2.1.5(a) shows the measurement results by M. Bersweiler et al. for K_{eff} of Co/Pt multilayers on a Si/Si oxide substrate with Ta/Pt seed layer [53]. The extrapolation of $K_{eff}t_{Co}$ values from high t_{Co} towards $t_{Co} = 0\,nm$ discloses the interface anisotropy contribution $2K_S$ ($K_S = 0.72\,erg/cm^2$, $K_V = -13\,Merg/cm^3$).

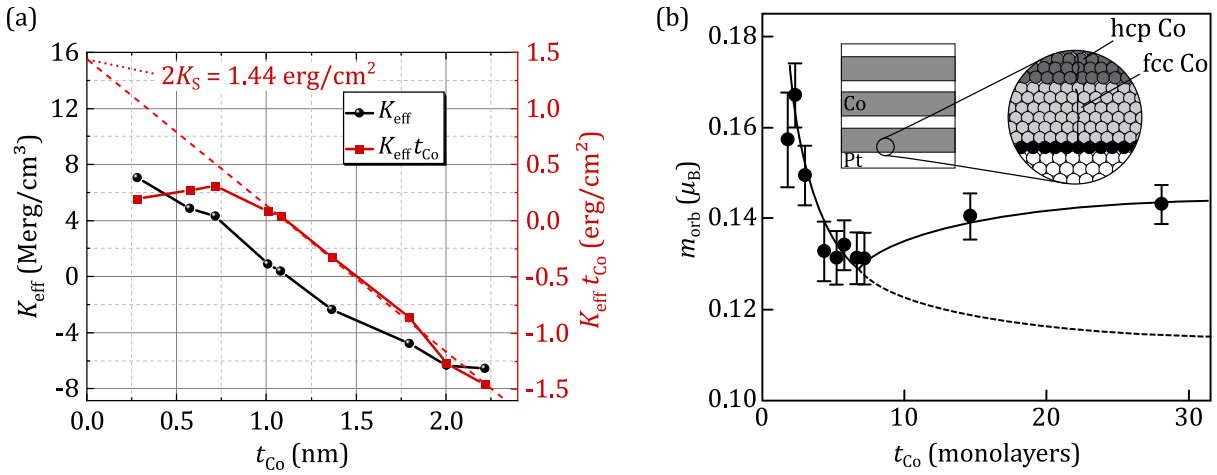

Fig. 2.1.5: PMA in Co/Pt multilayers. (a) K_{eff} and $K_{eff}t_{Co}$ as functions of t_{Co} show PMA emerging for $t_{Co} < 1.2\,nm$. $2K_S$ is found through a linear extrapolation of $K_{eff}t_{Co}$ values from higher t_{Co} towards $t_{Co} = 0\,nm$. (a) is adapted from [53]. (b) Orbital magnetic moment of Co perpendicular to the film plane for a Co/Pt multilayer system with varying t_{Co}. Data was obtained from XMCD and XAS measurements. A measurement fit is shown as a solid line, with consideration of a transition from Co fcc to hcp structure, as illustrated in the inset. The extrapolation (the dashed line) represents m_{orb} without this transition. (b) is reproduced from [54].

The origin of PMA in Co/Pt multilayers was experimentally identified by Nakajima et al. [54] using X-ray magnetic circular dichroism measurements (XMCD) and X-ray absorption spectroscopy (XAS). A strong hybridization of Pt 5*d* orbitals with Co 3*d* orbitals, localized at the Co/Pt interface, causes an enhancement of the orbital magnetic moment m_{orb}, which drives the PMA. A Pt spin moment parallel to that of Co is produced. Therefore, m_{orb} decreases with increasing t_{Co} as a smaller portion of Co atoms is involved in the orbital hybridization. Furthermore, it was shown that a structural transition from fcc to hcp Co occurs with increasing t_{Co}, as illustrated in Fig. 2.1.5(b). Since hcp Co has a higher magnetic moment than fcc Co, the initial decrease of m_{orb} is followed by a small increase as the Co structure changes from fcc to hcp. With the orbital hybridization being the stronger contribution, Co/Pt interface properties, such as roughness and lattice quality, are critical for high PMA [34].

2.1.3 Perpendicular magnetic anisotropy in transition metal/oxide interfaces

Another interface at which a significant PMA is generated is that between a $3d$ transition metal and a metal oxide. Most notable examples are the material systems CoFe/AlO_x and CoFeB/MgO. The first time PMA was observed at such an interface was by Monso et al. [12] in 2002 using a stack of Pt/CoFe/AlO_x. Since then the topic attracted considerable interest, mostly driven by its potential use for spin-transfer-torque magnetoresistive random-access memory (STT-MRAM). Already in the study by Monso et al., the interface PMA was found to be a function of oxidation level in the metal oxide. A significant development came in 2010 by Ikeda et al. [55], where a Ta layer was placed adjacent to a CoFeB/MgO bilayer. CoFeB is an amorphous material, while MgO crystallizes into a bcc lattice structure upon annealing. Since Ta is able to remove boron from CoFeB during annealing [56], the then left CoFe is able to adopt the MgO's bcc structure [57–60] (see Fig. 2.1.6), which yields astonishingly high interface anisotropies at around $K_{\mathrm{Ta/CoFe}} + K_{\mathrm{CoFe/MgO}} = 1.8\,\mathrm{erg/cm^2}$ [61], with theoretical values up to $3\,\mathrm{erg/cm^2}$ [62]. The origin of the high PMA lies in the orbital hybridization of the Co and Fe $3d$ orbitals with the p orbitals of oxygen. Specifically, the hybridization of the respective out-of-plane orbitals $3d_{z^2}$, $3d_{xz}$ and $3d_{yz}$, with $2p_z$. This introduces a charge transfer to the oxygen orbitals, leaving a lack of electrons in the out-of-plane $3d$ orbitals compared to the in-plane orbitals $3d_{x^2-y^2}$ and $3d_{xy}$. The result is an enhanced out-of-plane orbital moment, generated by the uncompensated in-plane orbitals [63]. For a more detailed overview on the theoretical mechanism and *ab initio* calculations of PMA, the reader may be referred to the review article by B. Dieny and M. Chshiev [14].

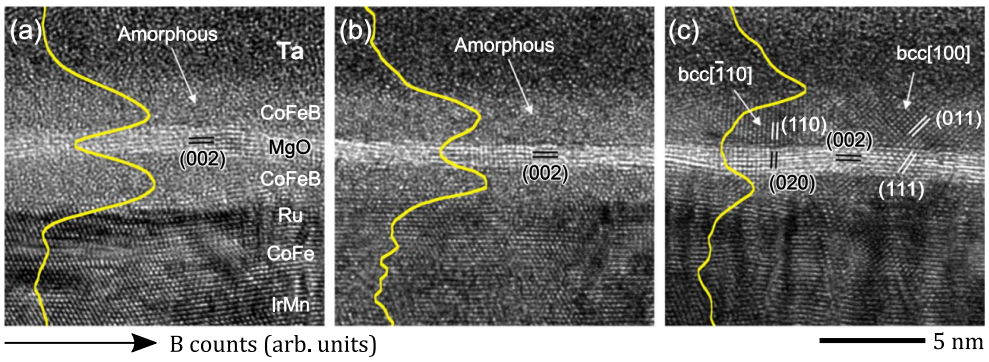

Fig. 2.1.6: High resolution transmission electron microscope (HRTEM) images of a magnetic tunnel junction (MTJ) with MgO/$Co_{60}Fe_{20}B_{20}$/Ta stack. Solid lines indicate the count of boron atoms, determined from electron energy-loss spectroscopy (EELS). (a) As-deposited, (b) after annealing at 270 °C for 4 h, (c) after annealing at 320 °C for 4 h. With higher annealing, boron diffuses into Ta and the CoFe(B) adopts a bcc crystallography. Figure reproduced from Miyajima et al. [59].

As PMA is generated at the interface, whereas the bulk anisotropy of CoFe(B) is in-plane, the effective magnetic anisotropy K_{eff} depends on the CoFeB layer thickness t_{CoFeB}. The values for t_{CoFeB} at which $K_{\mathrm{eff}} < 0$ vary depending on multiple factors such as CoFeB composition, post annealing temperature, and seed layer. Typically, PMA is observed for t_{CoFeB} around 1.2 nm [61], but has also been reported for thicknesses as high as $t_{\mathrm{CoFeB}} = 1.6\,\mathrm{nm}$ [64].

2.1.3.1 Superparamagnetism

Before perpendicularly magnetized CoFeB/MgO structures became the preferred choice for perpendicular magnetic tunnel junctions (MTJ) and MRAM devices, Fe/MgO stacks [65, 66] and Ta/CoFeB/MgO stacks [67] were found to show superparamagnetic behavior with an out-of-plane easy axis at small thicknesses. Superparamagnetism [68] is a form of magnetism in which the magnetization direction of a magnetic particle is overcome just by thermal energy. When no external field is applied, the magnetization direction of a magnetic particle of volume V fluctuates between the two antiparallel directions along its magnetic easy axis, energetically separated by an energy barrier $E_\mathrm{b} = K_\mathrm{eff}V$, illustrated in Fig. 2.1.7(a). Described by the Néel-Brown model [69, 70], the average relaxation time τ until a superparamagnetic particle flips its magnetization is

$$\tau = \tau_0 e^{E_\mathrm{b}/k_BT} = \tau_0 e^{K_\mathrm{eff}V/k_BT}, \tag{2.11}$$

with material specific constant τ_0, Boltzmann constant k_B, and temperature T. Above a temperature T_b, the measurement time is larger than τ, therefore a measurement averages over the magnetization fluctuations and detects zero magnetic moment. Only when an external magnetic field is applied, a magnetic moment parallel to the external field is detected hysteresis-free (similar to paramagnetism, thus the name *superparamagnetism*; *super*, as their susceptibility is much larger than that of paramagnets.). T_b is called the *blocking temperature*[1)] as a magnetization flip is blocked for temperatures below T_b. In a measurement setup with measurement time t_m [71], T_b is given by

$$T_\mathrm{b} = \frac{K_\mathrm{eff}V}{k_B \ln\left(t_\mathrm{m}/\tau_0\right)}. \tag{2.12}$$

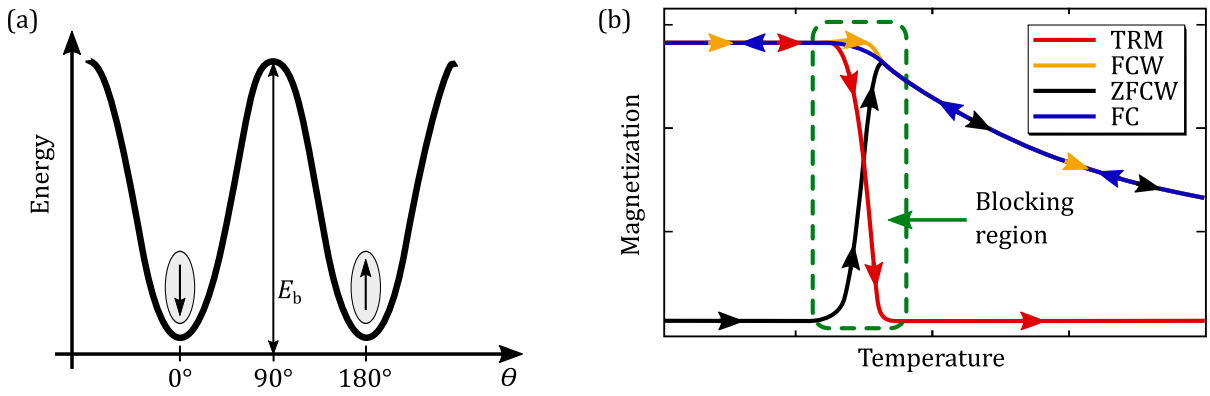

Fig. 2.1.7: (a) Illustration of the potential of a magnetic nanoparticle against θ, where θ denotes the angle between magnetic easy axis and magnetization. Two magnetization minima are located along the easy axis, separated by energy barrier E_b. (b) M-T measurements for an ensemble of magnetic nanoparticles. FCW, ZFCW, and FC measurements are conducted with a small applied magnetic field. TRM measurements are performed at zero field. For a ZFCW measurement, the ensemble starts at low T with randomized magnetizations. (b) is reproduced from [72].

To detect superparamagnetism and find T_b experimentally, a series of four M-T measurements can be conducted, as illustrated in Fig. 2.1.7(b). Thermoremanent magnetization (TRM) is

[1)] Note that the temperature at which antiferomagnets lose the ability to pin the magnetization of adjacent ferromagnetic layers is also called blocking temperature. Despite having the same name, there is no correlation.

detected with magnetized nanoparticles being heated up at zero field. Above T_b, the measured magnetization rapidly drops as particle magnetization flips too quickly for the measurement setup and thereby randomize. If a small field is applied during warming (field cooled warming – FCW), the magnetization declines with increasing T more slowly. If the particles were cooled at zero field (random magnetization) and heated up with a small applied field (ZFCW), the magnetization starts at zero and shoots up at T_b, as the magnetizations are no longer blocked. Finally, if the particles are cooled with an applied field (FC), their magnetization increases with decreasing T until their magnetization is blocked.

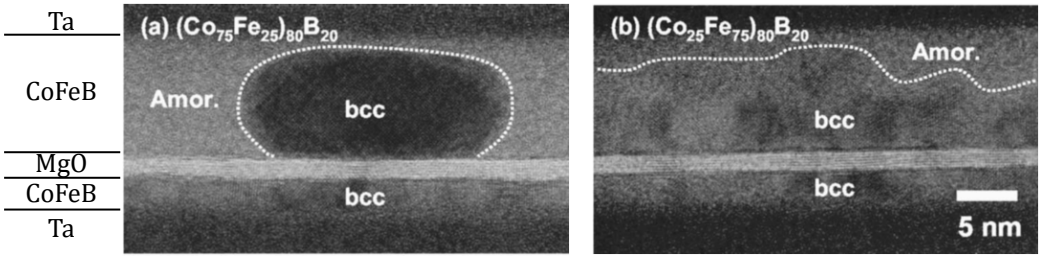

Fig. 2.1.8: HRTEM images of a MTJ with (a) $(Co_{75}Fe_{25})_{80}B_{20}$ and (b) $(Co_{25}Fe_{75})_{80}B_{20}$ composition, post-annealed at 450 °C for 1 h. Crystallization of the top magnetic layer (10 nm) is clustered for the $(Co_{75}Fe_{25})_{80}B_{20}$ composition, whereas it is laterally continuous for $(Co_{25}Fe_{75})_{80}B_{20}$. Figure reproduced from [78].

Interestingly, the thicknesses at which superparamagnetism is observed for CoFeB/MgO stacks [67,73–76] are the same at which other groups manage to obtain ferromagnetic layers with strong perpendicular magnetic anisotropy [35,55,77] (see Yang et al. for further discussions [17]). Since the superparamagnetic behavior depends on the particle volume (compare Eqs. 2.11 and 2.12), the difference between ferromagnetism and superparamagnetism in CoFeB/MgO stacks is that of continuous CoFeB films and CoFeB nanoparticles. While various fabrication parameters may influence the growth conditions of ultrathin films, a likely candidate responsible for superparamagnetism is a high concentration of Co in the CoFeB composition. Fe growth on oxides tends to show the preferred layer-by-layer growth, whereas Co tends to island growth [14]. Furthermore, higher Co concentrations increase the lattice mismatch between bcc MgO and bcc CoFe [58]. Generally, high Co concentrations impede the CoFeB bcc crystallization. As a results, inhomogeneous crystallization has been observed for $MgO/(Co_{75}Fe_{25})_{80}B_{20}$ stacks, while $MgO/(Co_{25}Fe_{75})_{80}B_{20}$ stacks formed continuous, homogeneous bcc lattices [78], as shown in Fig. 2.1.8.

2.2 Interlayer exchange coupling

For an ensemble of multiple magnetic layers, the phenomenon of interlayer exchange coupling (IEC) has become an important tool for magnetic devices. Different to the very short ranged exchange interaction [79, 80] and later found exchange bias effect [81], IEC is an indirect coupling mechanism of two ferromagnetic layers, separated by a metallic interlayer [82–86]. Itinerant electrons of the interlayer are the mediators of the coupling, which gives IEC a range of several nanometers. Nonetheless, the interlayer thickness plays an important role in IEC, as the interaction oscillates between ferromagnetic and antiferromagnetic coupling of the two ferromagnetic layers with interlayer thickness. IEC was observed in 1986 in Fe/Cr/Fe and Fe/Au/Fe layer structures, where the frequency shift of scattered light (Brillouin light scattering) from spin waves was investigated [87]. In 1990, S. S. P. Parkin et al. observed the damped oscillatory behavior in the magneoresistance effect of GMR spin valves consisting of Co/Ru and Fe/Cr multilayer structures [82]. Their results are presented in Fig. 2.2.1(a).

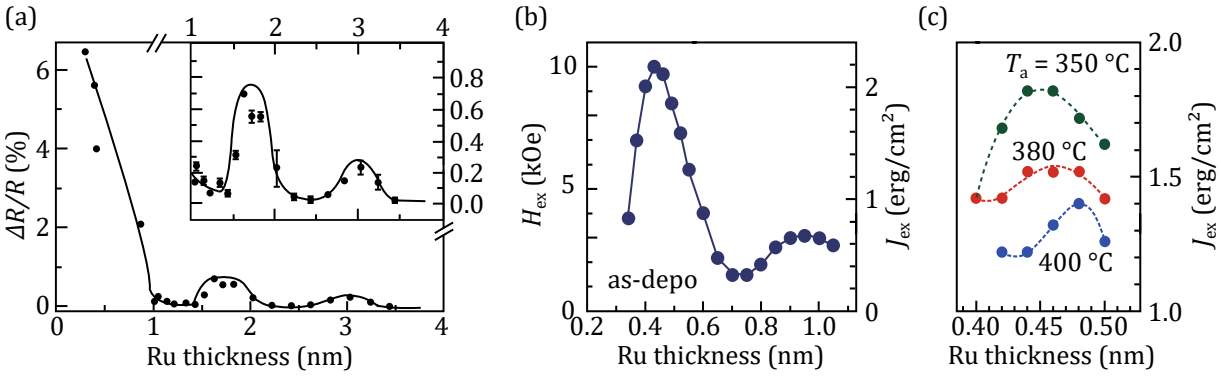

Fig. 2.2.1: Measurements on IEC with respect to Ru thickness. (a) Magnetoresistance effect in $[\mathrm{Co}(2\,\mathrm{nm})/\mathrm{Ru}(t_{\mathrm{Ru}})]_{20}$ multilayer systems [82]. (b) Exchange field H_{ex} and spacer layer energy density J_{ex} for $[\mathrm{Pt}(0.16\,\mathrm{nm})/\mathrm{Co}(0.24\,\mathrm{nm})]_5/\mathrm{Ru}(t_{\mathrm{Ru}})/[\mathrm{Co}(0.24\,\mathrm{nm})/\mathrm{Pt}(0.16\,\mathrm{nm})]_5$ p-SAFs as-deposited and (c) after annealing for 1 h at temperature T_{a} [35].

Besides spin valves, IEC is often used for the construction of synthetic antiferromagnets (SAF). Here, two or more ferromagnetic layers are coupled antiferromagnetically via IEC, ideally with zero magnetic net moment. In an externally applied magnetic field H with its direction parallel to the magnetization direction of the magnetic layers, the SAF remains in an antiferromagnetic alignment as long as no critical field $|H_{\mathrm{out}}|$ is reached, at which the magnetizations jump out of the SAF configuration. If the field is lowered to a critical field $|H_{\mathrm{in}}| < |H_{\mathrm{out}}|$ again, the IEC forces a jump back into the SAF configuration. Two characteristic parameters of SAFs with magnetic layer thickness t are the exchange field

$$H_{\mathrm{ex}} = \mathrm{mean}\left[|H_{\mathrm{in}}|\,;|H_{\mathrm{out}}|\right] \tag{2.13}$$

and the coupling energy

$$J_{\mathrm{ex}} = M_{\mathrm{S}}\, t\, H_{\mathrm{ex}}. \tag{2.14}$$

Figure 2.2.1(b) shows the oscillatory behavior of H_{ex} and J_{ex} as a function of Ru thickness t_{Ru} for

a perpendicular SAF (p-SAF) consisting of a Ru interlayer between two Co/Pt multilayers with out-of-plane effective magnetic anisotropy. Oscillation peaks appear at approximately $t_{\mathrm{Ru}} = 0.4$ and 0.9 nm. In both Fig. 2.2.1(a) and (b) it is visible that the IEC coupling strength experiences an overlaying decrease with increasing interlayer thickness. Figure 2.2.1(c) shows J_{ex} of the first oscillation peak after annealing at different temperatures, indicating changes in the coupling due to diffusion at the material interfaces. The results shown in Fig. 2.2.1(b) and (c) are taken from Yakushiji et al. [35].

Phenomenologically, J_{ex} can be expressed with the bilinear and biquadratic terms [88]

$$J_{\mathrm{ex}} = -J_1 \cos\phi - J_2 \cos^2\phi, \tag{2.15}$$

with ϕ being the angle between the magnetizations of the films on both sides of the interlayer. Minimization of Eq. 2.15 then discloses the coupling configuration. For dominating J_1, the coupling is ferromagnetic for $J_1 > 0$ and antiferromagnetic for $J_1 < 0$. For dominating $J_2 < 0$, a 90° coupling configuration occurs.
In regard to the theory of IEC, several different calculation approaches have been made shortly after the first experimental observations were published. Two classes of approaches were suggested: total energy calculations and model calculations. The difficulty with the former is that the energy difference of the ferromagnetic and antiferromagnetic state is extremely small in comparison to the total energy, which leads to problems in the numerical convergence of the calculation. Despite this and other difficulties with the total energy approach, calculated IEC oscillation periods yield good result. However, the results for coupling strength amplitudes do not match experimental observation by an order of magnitude [83]. The approach of calculations via models splits once more into several approaches for different models. Among the most popular approaches is that of extending the general theory of Ruderman-Kittel-Kasuya-Yosida (RKKY) interaction [89–91] to the problem of interlayer coupling [83, 92]. Here, the conduction electrons in the interlayer are spin polarized, which leads to an indirect exchange interaction between particle (*magnetic impurity*) i and j with spins $\mathbf{S}$ at position $\mathbf{R}$ being

$$H_{ij} = J(\mathbf{R}_{ij})\ \mathbf{S}_i \cdot \mathbf{S}_j, \tag{2.16}$$

where $J(\mathbf{R}_{ij})$ is the position dependent exchange integral. The exchange coupling in RKKY shows an oscillatory behavior as a function of the product of Fermi wavevector k_{F} and distance between lattice atoms R, with $J_{\mathrm{RKKY}} \propto \cos(2k_{\mathrm{F}}R) / (2k_{\mathrm{F}}R)^3$ [93]. The key difference of the IEC extension to the conventional theory of RKKY interaction lies in the discreteness of the spacer layer, which leads to Bragg scattering of electrons [83]. While the periodicity of the coupling is the same, the IEC interaction decays with D^2 at a slower rate than RKKY, where D is the thickness of the spacer between the ferromagnetic layers: $J_{\mathrm{IEC}} \propto -\sin(2k_{\mathrm{F}}D) / D^2$.

In 1993, P. Bruno proposed a general formulation for the problem of IEC, which allows first-principles calculations of the coupling [86, 94, 96]. It unifies the previous approaches, since it

reduces to the various models in limit cases. In the formulation, the mechanism of IEC is described by quantum interference due to spin-dependent reflections of the Bloch waves at the paramagnetic-ferromagnetic interfaces, resulting in electron confinement in the spacer layer.

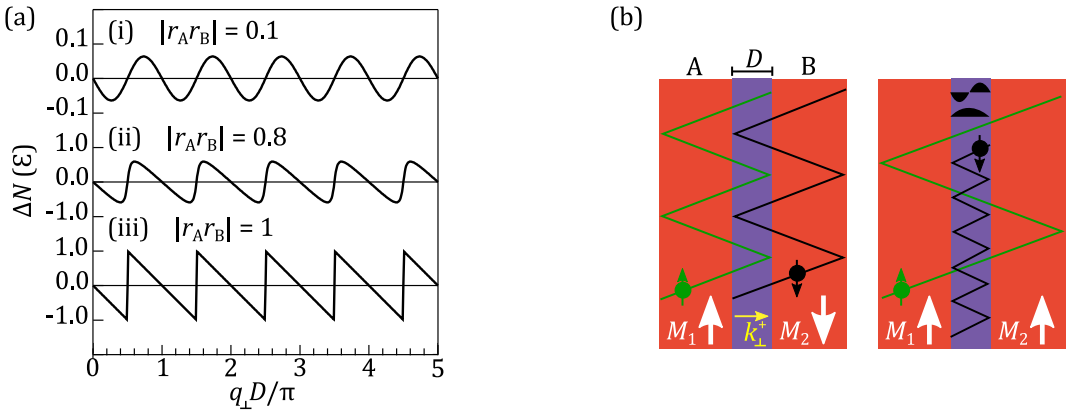

Fig. 2.2.2: (a) Variation of $\Delta N(\epsilon)$ in a quantum well as a function of D for various values of the confinement strength $|r_A r_B|$ along the ordinate axis. (i) $|r_A r_B| = 0.1$, (ii) $|r_A r_B| = 0.8$, (iii) $|r_A r_B| = 1$ (full confinement). Note the different scales. Reproduced from [94]. (b) Spin-dependent interface reflectivity in a layered magnetic structure for antiparallel (left) and parallel (right) alignment. A quantum well state is formed in the parallel alignment in the interlayer. The confinement leads to standing wave modes with discrete energy levels. Adapted from [95].

The essential physics of the model can already be understood in the simplified picture of a one-dimensional quantum well, which represents a spacer layer of width D between two barriers A and B. Electrons with wavevector k^+ in the spacer layer move towards the barrier B, where they get reflected with the reflection amplitude r_B, while electrons with wavevector k^- are reflected at barrier A with amplitude r_A. Interference between the waves leads to a change in the density of states $\Delta N(\epsilon)$. This change depends on the confinement strength $|r_A r_B|$ and is a function of D, as shown in Fig. 2.2.2(a), with $q = k^+ - k^-$. Replacing the barriers to ferromagnetic layers with spin-dependent potential steps introduces the spin-dependent reflection amplitudes $r_A^\uparrow$, $r_A^\downarrow$, $r_B^\uparrow$, and $r_B^\downarrow$. The resulting bound states of discrete energy are shifted with D, with an oscillation of the coupling occurring each time a confined state passes the Fermi energy ϵ_F. The coupling mechanism is illustrated in Fig. 2.2.2(b). The difference in energy between ferromagnetic and antiferromagnetic coupling in a three dimensional layered system is given by [94]

$$E_F - E_{AF} = -\frac{1}{\pi^3}\,\mathrm{Im}\int \mathrm{d}^2\mathbf{k}_{||}\int_{-\infty}^{\infty} f(\epsilon)\Delta r_A \Delta r_B\, \mathrm{e}^{\mathrm{i}q_\perp D}\,\mathrm{d}\epsilon \tag{2.17}$$

with

$$f(\epsilon) = k_B T \ln\left[1 + \exp\left(\frac{\epsilon_F - \epsilon}{k_B T}\right)\right], \tag{2.18}$$

where the factors Δr_A and Δr_B denote the spin asymmetry of the confinement due to the magnetic layers A and B, respectively. With Eq. 2.17, the IEC is a sum of contributions from all occupied electronic states, where the contribution of a state with energy ϵ and in-plane wavevector $\mathbf{k}_{||}$ depends on the spin asymmetry and propagation through the spacer layer ($\mathrm{e}^{\mathrm{i}q_\perp D}$). A noteworthy result is that the IEC coupling strength depends on the degree of matching of the energy bands at the ferromagnet-interlayer interfaces [86].

2.3 Magnetoresistance effects

Magnetoresistance (MR) effects generally denote the change in electric resistivity ρ or resistance R in response to an externally applied magnetic field H, given by

$$\frac{\Delta\rho}{\rho} = \frac{\Delta R}{R} = \frac{R(H) - R_{\min}}{R_{\min}}. \tag{2.19}$$

First discovered by W. Thomson (Lord Kelvin) in 1857 [97], MR effects comprise a major part of spin electronics (spintronics) today. Due to the general definition, many effects of this kind with various physical origins exist. In this chapter, the MR effects which are most relevant for this work are introduced. These are the Giant Magnetoresistance (GMR), Tunnel Magnetoresistance (TMR) and Anisotropic Magnetoresistance (AMR), which in summary are called xMR effects. Other effects include the Colossal Magnetoresistance (CMR) [98], the Spin Hall Magnetoresistance (SMR) [99], and the Extraordinary Magnetoresistance (EMR) [100], to name just a few.

2.3.1 Giant Magnetoresistance

The GMR effect is a change of R depending on the relative alignment of magnetization direction of at least two ferromagnetic materials that are separated by a non-ferromagnetic metal. A parallel alignment leads to a minimized R, whereas R is at its maximum at an antiparallel configuration. It was first observed for Fe/Cr multilayers in 1988 [101, 102] and led to a Nobel prize in physics for P. Grünberg and A. Fert in 2007. In the first systems, the ferromagnetic layers were coupled via the then newly found interlayer exchange coupling (see chapter 2.2), reaching effect strengths up to 65 % at 295 K [103] and 220 % at 1.5 K [104]. In 1991, B. Dieny, V. Speriosu, S.S.P. Parkin et al. used the GMR effect to create a *spin-valve*, where the magnetization of one ferromagnetic layer is fixed through an exchange bias effect [81] and one magnetization is free to rotate with the external magnetic field [105]. This design is still used in GMR sensor concepts today. Typical GMR ratios for spin-valves are well below 10 % [106], with the highest reported GMR ratio of 40.5 % for epitaxial $Co_{50}Fe_{50}$/Cu/$Co_{50}Fe_{50}$ trilayers at room temperature [107].

To model the GMR effect to the extent that quantitative statements can be derived requires a combination of semiclassical Boltzmann transport theory and first-principles quantum mechanical treatment. Depending on the measurement geometry being current in-plane (CIP) or current perpendicular-to-plane (CPP), a nonlocal semiclassical transport approximation or the inclusion of the spin-diffusion length is needed. Derivation approaches are given in detail by X. Zhang and W. Butler [108].

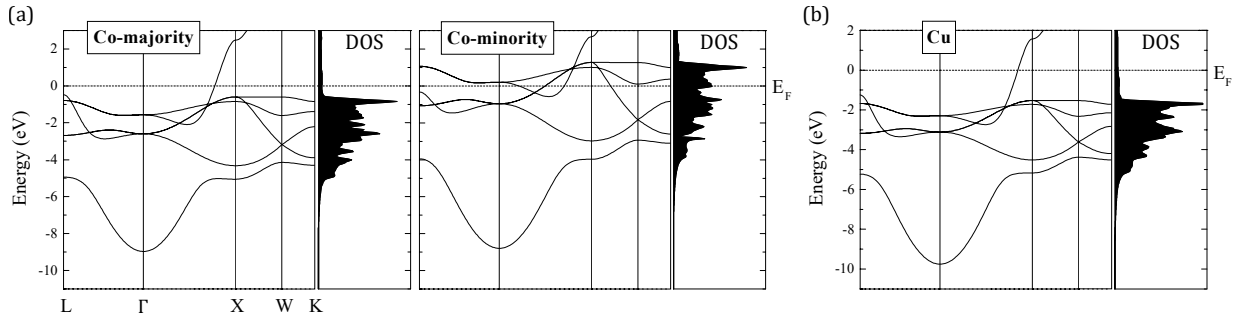

Fig. 2.3.1: Electronic band structure and DOS for (a) fcc Co-majority and Co-minority electrons. Due to *d*-band exchange splitting, the band structures are different, with the Fermi level at the 4*sp* type band for majority electrons, whereas the Fermi level lies at *d* states for minority electrons. This leads to different scattering rates in the bulk and at the interface with (b) Cu. The electron band structure is similar to that of Co-majority electrons. The Co-minority band matches poorly, leading to further scattering. Figure reproduced from [109].

For a qualitative understanding of the GMR effect, however, the two-current model suffices [106]. This model is often affiliated with N.F. Mott, who, long before the GMR effect was discovered, suggested in 1936 that the conductivity in metals can be treated with different scattering rates for *s* and *d* electrons. Mott used the approach of two independent spin state channels to explain the sudden change in the conductivity of ferromagnetic metals as their temperature is decreased below the Curie temperature [110, 111]. The main points of the two-current model for the GMR effects are:

1. The current in metals is separable into two independent spin-channels, corresponding to spin-up and spin-down electrons.

2. Scattering in the bulk and at interfaces is spin-dependent.

Hybridization of spin states is not included in this model, which is one of its major simplifications. To understand why scattering is spin-dependent, one needs to look at the band structure and density of states (DOS) for ferromagnetic materials, here done exemplary for fcc Co in Fig. 2.3.1(a). Generally, only electrons near the Fermi energy E_F contribute to a metal's conductivity, since the Pauli exclusion principle does not allow electrons of lower energy to utilize the energy from a small applied electric field to occupy any higher states that are occupied. Electrons of the type 4*sp* have a high velocity and low DOS (long mean free path). Their band structure is similar to that of a free electron. Electrons of the type 3*d*, on the other hand, are slow and localized within a much narrower energy window with a high DOS (short mean free path). Therefore, the dominating contribution to the conductivity of 3*d* transition metals can be considered to come from 4*sp* electrons near the Fermi level, whereas 3*d* states near E_F introduce additional scattering. In ferromagnetic materials the DOS is different for spin-up and spin-down electrons. Depending on the DOS below E_F, one distinguishes between *majority* and *minority* electrons. In case of the here shown fcc Co, the 3*d* majority electrons are all below E_F with only 4*sd* states at the Fermi level. Whereas for the minority electrons, the Fermi level is within the 3*d* band (here, the *sp* electrons are hybridized with the *d* electrons, reducing their conductivity potential). Thus, the majority channel of fcc Co has a higher conductance than the minority

channel [2)].

Additionally, scattering at the interfaces needs to be considered. This is related to band matching of the two metals at an interface. The better the bands match, the smaller the scattering potential. As seen in the band structure for fcc Cu, shown in Fig. 2.3.1(b), Cu's band structure is similar to that of the Co majority electrons, which adds to the better conductance in the majority channel.

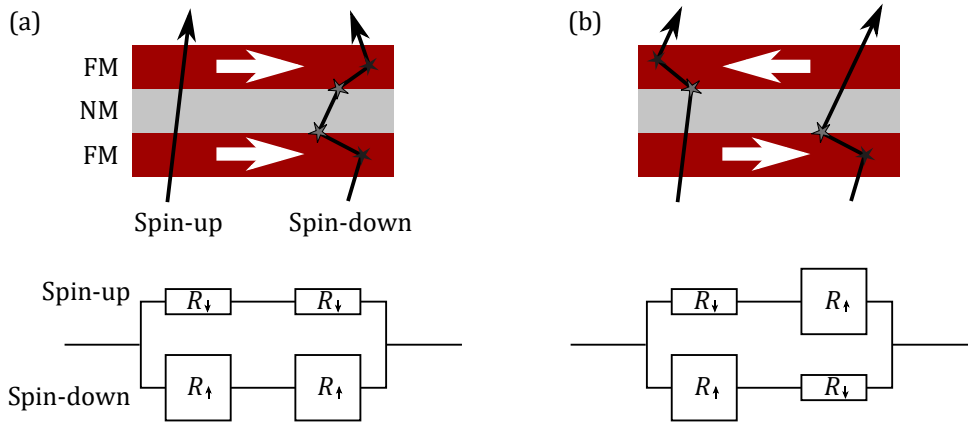

Fig. 2.3.2: Illustration of the two-channel model for the GMR effect and equivalent circuit with two ferromagnetic layers in (a) parallel and (b) antiparallel alignment. Spin-up and spin-down electrons scatter differently in the bulk and at the interfaces, which is represented as different resistances. In total, $R_{\mathrm{AP}} > R_{\mathrm{P}}$.

With this, the ferromagnetic layers, including their interfaces, can be seen as resistors in a circuit with parallel channels for spin-up and spin-down electrons. An illustration is given in Fig. 2.3.2 for a parallel configuration in (a) and antiparallel in (b). Depending on magnetization direction of the ferromagnetic layer and spin direction of the conduction electron, the resistance R at a layer is either $R_\uparrow$, meaning high, or $R_\downarrow$, meaning low, corresponding to the different conductance in the majority and minority channel. The overall resistance in the parallel configuration R_{P} is different than in the antiparallel configuration R_{AP}, with

$$R_{\mathrm{P}} = \frac{2R_\uparrow R_\downarrow}{R_\uparrow + R_\downarrow}, \quad R_{\mathrm{AP}} = \frac{R_\uparrow + R_\downarrow}{2}.$$

This leads to the GMR ratio of

$$GMR = \frac{\Delta R}{R} = \frac{R_{\mathrm{AP}} - R_{\mathrm{P}}}{R_{\mathrm{P}}} = \frac{(R_\uparrow - R_\downarrow)^2}{4R_\uparrow R_\downarrow}. \tag{2.20}$$

Equation 2.20 also shows that $R_{\mathrm{AP}} > R_{\mathrm{P}}$.

Another contribution to CIP GMR that can be deduced from the layer materials' band structure, though going beyond the classical Mott model, is that of the channeling effect [108]. X. Zhang and W. Butler calculated the current densities in a Co/Cu/Co spin-valve for parallel and antiparallel alignments. Since the Co band structure is different for majority and minority electrons, leading

[2)] For Fe the minority electrons have the higher conductance.

to different band structure matching with Cu, also the transmission probabilities from Co to Cu are different for the parallel and antiparallel configurations. Analyzing the Fermi surface of Co and Cu, Zhang and Butler point out that for some wave vectors **k**, states in Cu exist which do not exist in the majority Co band, as shown in Fig. 2.3.3(a). These electrons are then channeled in the Cu layer similar to light waves in a waveguide. This is relevant, since the conductivity of Cu is much higher than of Co. The result is a Giant Magnetoconductance (GMC), visible in Fig. 2.3.3(b).

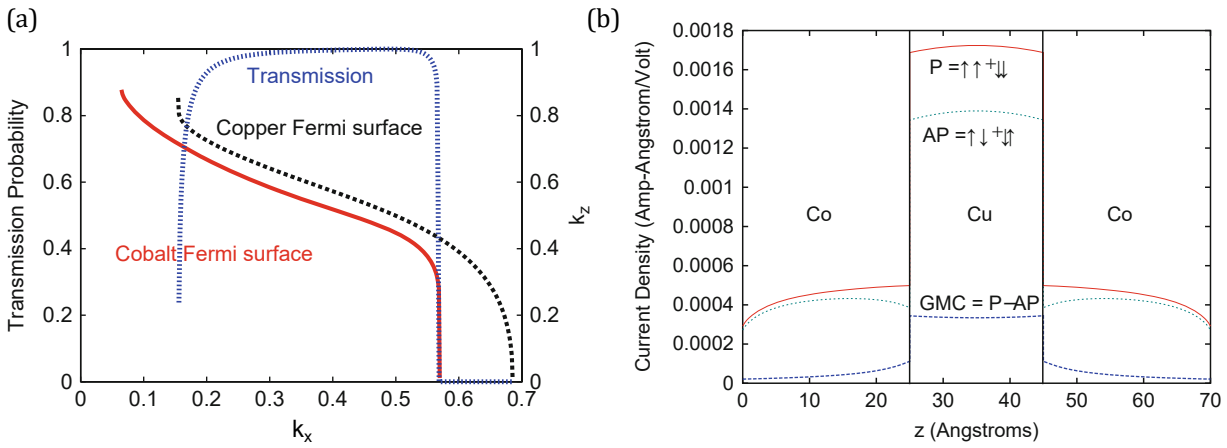

Fig. 2.3.3: (a) Co and Cu Fermi surface, and transmission probability of Co electrons incident on majority Co for a cut through the Fermi surface with $k_y = 0$. For some wave vectors, states in Cu exist, but not for Co-majority electrons. (b) Calculated current densities for a CIP Co/Cu/Co spin-valve in parallel and antiparallel alignment. The difference between current densities shows the Giant Magnetoconductance, stemming partly from the channeling effect in Cu. Figures reproduced from [108].

2.3.2 Tunnel Magnetoresistance

Tunnel Magnetoresistance shares some similarities with GMR. Again, the resistance depends on the relative alignment of two separated magnetic layers, with high resistance at antiparallel alignment and low resistance at parallel alignment. However, these layers are not separated by a normal metal, but by a thin insulator, i.e. a tunnel barrier (TB). Instead of scattering rates affecting the electric resistance, the magnetization alignment changes the overall tunneling current I_T. Therefore, the TMR ratio is defined through the change of electrical conductance G or conductivity σ instead of resistance, with

$$TMR = \frac{\Delta G}{G} = \frac{\Delta \sigma}{\sigma}. \tag{2.21}$$

In 1970, R. Meservey, P.M. Tedrow and P. Fulde discovered that the tunneling current from magnetic materials are spin-polarized [112–114]. Five years later, tunnel magnetoresistance was observed the first time by M. Jullière [115], using Fe/GeO_2/Pb and Fe/GeO_2/Co structures at 4.2 K with a maximum measured TMR ratio of about 14 %. In his paper, Jullière suggests the TMR ratio to be solely a matter of degree of spin-polarization P, with

$$P = 2\chi - 1, \tag{2.22}$$

where χ is the fraction of tunneling electrons near the Fermi level in a metal whose magnetic moments are parallel to the magnetization. This suggestion is derived from the premise of a two-channel model with the assumption that the conductance between the two metals is proportional to the sum of multiplied electron fractions of the same spin. That means for the parallel conductance $G_{\uparrow\uparrow}$ and antiparallel conductance $G_{\uparrow\downarrow}$

$$G_{\uparrow\uparrow} \propto \underbrace{\chi_1\chi_2}_{\text{majority spin}} + \underbrace{(1-\chi_1)(1-\chi_2)}_{\text{minority spin}}$$

and (2.23)

$$G_{\uparrow\downarrow} \propto \chi_1(1-\chi_2) + (1-\chi_1)\chi_2, \tag{2.24}$$

where the indices 1 and 2 each denote the corresponding ferromagnetic layer. Inserting Eqs. 2.22 and 2.24 into Eq. 2.21 yields[3)]

$$TMR = \frac{\Delta G}{G} = \frac{G_{\uparrow\uparrow} - G_{\uparrow\downarrow}}{G_{\uparrow\downarrow}} = \frac{2P_1P_2}{(1-P_1P_2)}. \tag{2.25}$$

Today, this approach is known as the Jullière model. Its key message can be expressed in an easy to understand illustration, as given in Fig. 2.3.4, showing the tunneling rates depending on the DOS and the magnetization alignment of two ferromagnetic layers separated by a tunnel barrier.

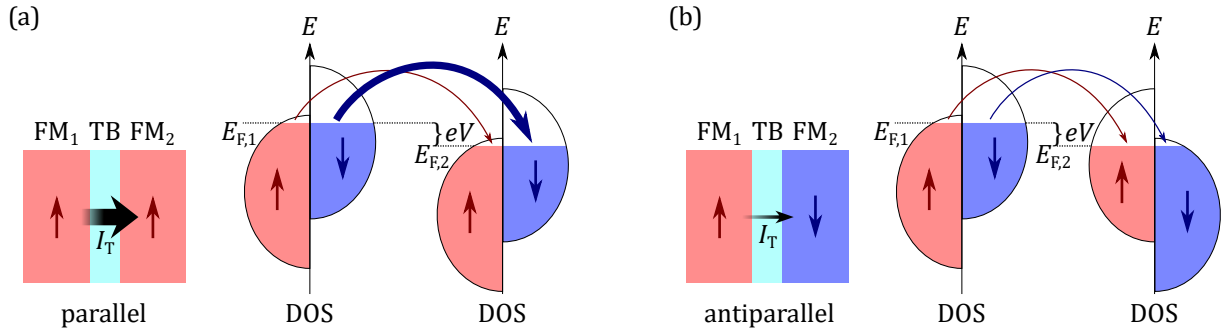

Fig. 2.3.4: Illustration of the TMR effect according to the Jullière model. (a) Parallel and (b) antiparallel alignment of two ferromagnetic (FM) layers separated by a tunnel barrier (TB). Next to the layer system, a simplified version of the DOS is shown. Due to a bias voltage V, a net tunneling current I_T tunnels from FM_1 to FM_2. Here, in case of parallel alignment, the DOS of the minority electrons ($\downarrow$) at the Fermi level is high in both FM layers, enabling a high I_T. At antiparallel alignment, the DOS at the Fermi level for minority and majority spin is low either at FM_1 or FM_2. Consequentially, fewer electrons are able to tunnel through the TB and I_T is lower.

While the Jullière model offers a good first intuition for the TMR effect, it also suffers several disagreements with experimental observations. According to the model, the tunneling current of Co and Ni, which both have a high minority electron DOS at the Fermi level (compare Fig. 2.3.1), should be dominated by minority electrons. However, it is observed that the majority electrons carry the tunneling current [116]. Furthermore, Eq. 2.25 implies an infinite TMR ratio for half-metals with $P = 1$, which to this day has not been reported, and a maximum TMR ratio of only up to ca. 100 % for CoFe(B), of which the polarization has been measured to be around

[3)] In Jullière's original publication [115], a slightly different result is given: $\frac{\Delta G}{G} = \frac{2P_1P_2}{(1+P_1P_2)}$, which comes from the ansatz $\frac{\Delta G}{G} = \frac{G_{\uparrow\uparrow}-G_{\uparrow\downarrow}}{G_{\uparrow\uparrow}}$.

0.6 at 4.2 K [117, 118]. However, the highest TMR ratio found while using CoFe(B) electrodes in fact exceeds even 1000 % at 5 K [119]. Nevertheless, for a long time, the Jullière model worked well with experimental observations. The change came when instead of using AlO_X as a tunnel barrier, researchers started using MgO. The difference is that AlO_X is an amorphous material, so no crystallographic symmetry exists in the TB [120]. Therefore, various electron Bloch states from the crystalline electrode can couple to the evanescent states in AlO_X, which introduces incoherence in the tunneling process. On the other hand, Bloch states are conserved with a crystalline MgO TB, allowing coherent tunneling. Here, the tunneling probabilities of each Bloch state must be considered. An illustration of tunneling through AlO_X and MgO is shown in Fig. 2.3.5(a).

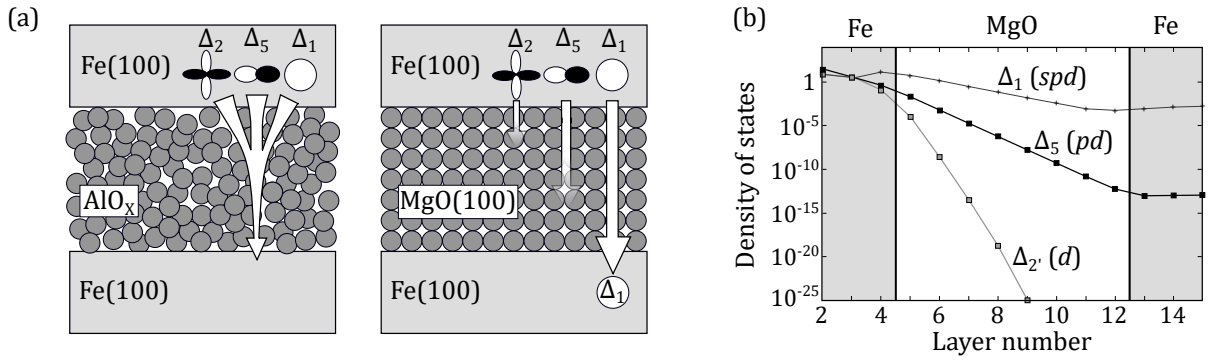

Fig. 2.3.5: (a) Tunneling through an AlO_X and MgO barrier. The amorphous structure of AlO_X allows coupling of various Bloch states to the AlO_X evanescent states, which introduces incoherent tunneling. In an MgO tunnel barrier, Bloch states are conserved, with the Δ_1 state having the slowest rate of decay in the MgO. Figure adapted from [120]. (b) Tunneling DOS for $k_{||} = 0$ for a Fe(100)/MgO(100)/Fe(100) magnetic tunnel junction with magnetizations in parallel alignment. The main contribution to the tunnel current comes from the majority electrons with Δ_1 Bloch state symmetry. Figure adapted from [121]. The results for Co/MgO/Co tunnel junctions are qualitatively the same [122].

W. Butler and X. Zhang have contributed extensive theoretical work on MgO tunnel junctions with Co, Fe, and CoFe electrodes [121–124], where they use first-principles electronic structure techniques to calculate the tunneling between electrodes. From their research it was found that majority electrons with Δ_1 Bloch state symmetry are the main carriers of the tunneling current. The Δ_1 state does not exist for minority electrons. Their results on tunneling DOS of majority-spin states for $k_{||} = 0$ in Fe(001)/MgO(001)/Fe(001) is given in Fig. 2.3.5(b), where the electrodes have parallel magnetization direction. In a study independent from Butler and Zhang, J. Mathon and A. Umerski calculated in 2001 that the TMR ratio can exceed 1000 % using an MgO barrier [125], which, as already mentioned, was indeed measured by S. Ikeda et al. in 2008 [119].

2.3.3 Anisotropic Magnetoresistance

Anisotropic Magnetoresistance was discovered as early as 1857. W. Thomson observed that the electrical resistance of Ni and Fe in a magnetic field is increased when the current and magnetization directions are parallel to each other and diminished when they are orthogonal [97]. As discussed earlier for magnetocrystalline anisotropy (section 2.1.1.2), spin-orbit interaction

causes the charge distribution to take a non-spherical symmetry. In a simple picture, as a result, also the scattering cross section at the charge distribution is non-spherical. Figure 2.3.6 shows that a rotation from parallel to orthogonal geometry of magnetization **M** to current **I** leads to a smaller scattering cross section and therefore smaller resistivity ρ.

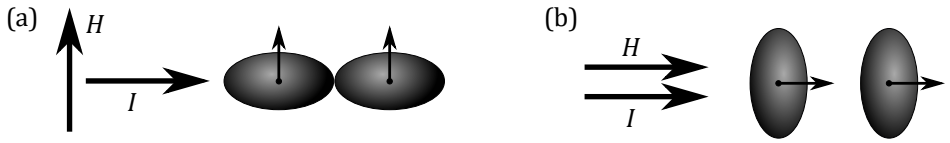

Fig. 2.3.6: Simple illustration of the AMR effect. Spin-orbit interaction in ferromagentic transition metals causes non-spherical charge distributions and anisotropic scattering. Current I flowing (a) perpendicular to the magnetization direction experiences smaller scattering than current (b) parallel to the magnetization.

Popular theoretical models are based, again, on Mott's two-channel model of separate scattering rates for s and d-type electrons. For systems with no d states in the majority spin-channel, such as Co and Ni, s-d scattering of minority electrons are the dominant feature of electronic conductivity. An illustration, including the corresponding resistor model, is shown in Fig. 2.3.7(a). Here, $\rho_{s\updownarrow}$ represents the resistivity within the $4s$ band, and $\rho_{s\downarrow d\downarrow}$ that of s-d scattering of the minority electrons. The anisotropic scattering mechanism is believed to be a result of isotropic scattering potentials with lower-than-cubic-symmetry wavefunctions [126–129]. This is caused by the spin-orbit interaction contributing to the energy of the d states that depends on spin or magnetization direction [129]. s-type electrons can only scatter with empty $3d$ states of compatible momentum. When $\mathbf{I} \parallel \mathbf{M}$ (in xy), empty $3d$ states have orbitals with large components of orbital angular momentum $\mathbf{L} \perp \mathbf{M}$ (e.g. $3d_{x^2-y^2}$). This leads to strong s-d scattering. On the other hand, when $\mathbf{I} \perp \mathbf{M}$, s-d scattering is low.

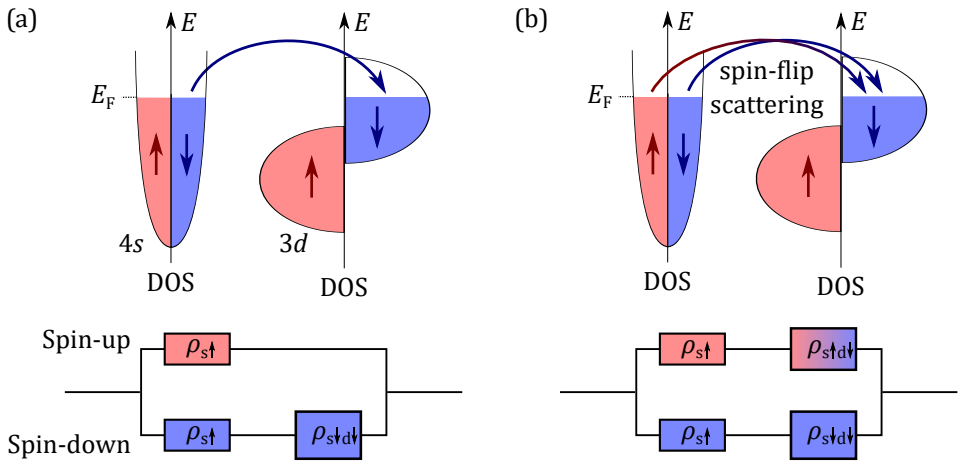

Fig. 2.3.7: Two-channel model for scattering rates in a ferromagnetic $3d$ transition metal with strongly exchange-split d bands. Here, no $3d$ empty states exist for the minority electrons. (a) Without spin-orbit interaction, the electrical resistivity is dominated by s-d scattering of minority electrons ($\rho_{s\downarrow d\downarrow}$). (b) With spin-orbit interaction, an additional spin-flip scattering $\rho_{s\uparrow d\downarrow}$ affects the majority spin channel.

Additionally, spin-flip events have to be considered. The spin-orbit interaction is of the form

$$\begin{aligned} H_{\mathrm{SO}} =& \lambda_{LS} \mathbf{L} \cdot \mathbf{S} \\ =& \lambda_{LS} \left(L_x S_x + L_y S_y + L_z S_z \right) = \lambda_{LS} \left(L_z S_z \frac{L^+ S^- + L^- S^+}{2} \right), \end{aligned} \tag{2.26}$$

with spin magnetic moment $\mathbf{S}$. The spin-flip operator $L^+S^- + L^-S^+$ enables mixing of the spin-up and spin-down states. Therefore, spin-orbit interaction introduces an additional scattering for strongly exchange-split d band systems. For the example of Co, H_{SO} introduces spin-flip scattering for majority $4s$ electrons into minority $3d$ states, as illustrated in Fig. 2.3.7(b) [130].

2.3.3.1 AMR in Pt/Co/Pt sandwiches

For textured ferromagnetic thin films, the AMR effect is phenomenologically described by

$$\rho(\varphi, \theta) = \rho_{\mathrm{t}} + (\Delta\rho_{\mathrm{ip,\ bulk}} + \Delta\rho_{\mathrm{ip,\ interface}}) \sin^2\theta \cos^2\varphi + (\Delta\rho_{\mathrm{op,\ bulk}} + \Delta\rho_{\mathrm{op,\ interface}}) \cos^2\theta. \tag{2.27}$$

Thus, the resistivity is a function of two angles [131–134]: φ represents the angle between current direction and projection of the magnetization in-plane, whereas θ is the angle between magnetization and out-of-plane axis. An illustration of the relevant vectors for a Pt/Co/Pt sandwich is shown in Fig. 2.3.8(a). For an in-plane magnetization with $\theta = 90°$ in orthogonal configuration to the current direction $\varphi = 90°$, the resistivity is minimized with $\rho = \rho_{\mathrm{t}}$ (transverse). The highest resistivity is achieved for a parallel (longitudinal) configuration of magnetization and current direction ($\theta = 90°$, $\varphi = 0°$). Therefore, a rotation of the magnetization from out-of-plane to in-plane (i.e. θ from 0° to 90° with fixed φ) yields a $\cos^2$ function for ρ, where the sign depends on the position of φ (positive for $\varphi = 0°$, negative for $\varphi = 90°$)[4].

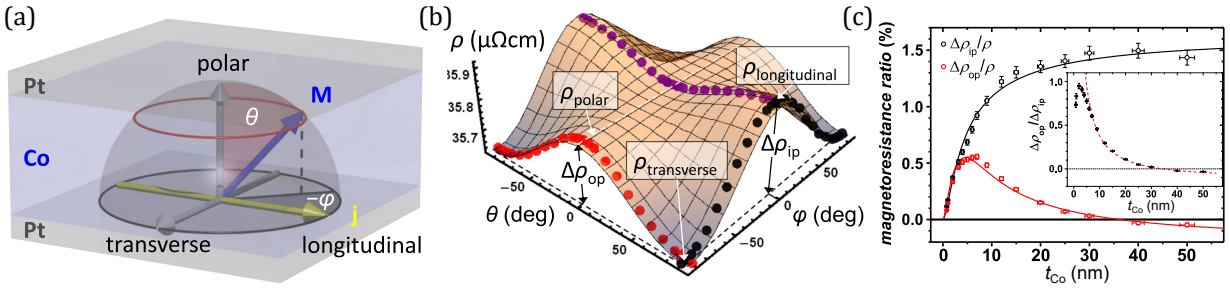

Fig. 2.3.8: AMR effect at textured magnetic thin films, taken from [131,133]. (a) Illustration of angles between magnetization direction M and current direction j in a Pt/Co/Pt sandwich. (b) Measurement of ρ for varying θ and φ. Results are shown as dotted lines for a system with t_{Co}=6 nm. Rotation of M is achieved by rotational external magnetic field with H=60 kOe (sufficient to force $M \parallel H$). (c) Magnetoresistance ratios $\rho_{\mathrm{ip}}/\rho_{\mathrm{t}}$ and $\rho_{\mathrm{op}}/\rho_{\mathrm{t}}$ versus t_{Co}. The inset shows the thickness dependent ratio $\rho_{\mathrm{op}}/\rho_{\mathrm{ip}}$. The smallest t_{Co} is 0.8 nm.

The rotational behavior for ρ is shown in Fig. 2.3.8(b), with the described transfer curves of a θ rotation given in purple and red, respectively. As seen in Eq. 2.27, the out-of-plane con-

[4] $\Delta\rho_{\mathrm{ip}} \sin^2\theta \cos^2\varphi + \Delta\rho_{\mathrm{op}} \cos^2\theta = \Delta\rho_{\mathrm{ip}}(1 - \cos^2\theta)\cos^2\varphi + \Delta\rho_{\mathrm{op}} \cos^2\theta$
$= \underbrace{(\Delta\rho_{\mathrm{op}} - \Delta\rho_{\mathrm{ip}} \cos^2\varphi)}_{\alpha} \cos^2\theta + \underbrace{\Delta\rho_{\mathrm{ip}} \cos^2\varphi}_{const.} \Rightarrow \alpha < 0$ for $\cos^2\varphi > \frac{\Delta\rho_{\mathrm{op}}}{\Delta\rho_{\mathrm{ip}}}$ and $\alpha > 0$ for $\cos^2\varphi < \frac{\Delta\rho_{\mathrm{op}}}{\Delta\rho_{\mathrm{ip}}}$

tribution $\Delta\rho_{\mathrm{op}}$ and in-plane contribution $\Delta\rho_{\mathrm{ip}}$ are each separated into a bulk and an interface term. The magnetoresistance arising from interface effects is also named Anisotropic Interface Magnetoresistance (AIMR). Due to AIMR, the Co thickness t_{Co} in a Pt/Co/Pt is relevant to the overall AMR effect. This is shown in Fig. 2.3.8(c). The interface contribution is particularly important for $\Delta\rho_{\mathrm{op}}$, for which the AMR has a maximum around $t_{\mathrm{Co}} = 5$ to 7 nm. Recently, it has been demonstrated that AIMR is not a new physical effect but a manifestation of the symmetry breaking at the interfaces [134].

Chapter 3

Experimental methods

Several experimental methods are required for the development of spintronic devices, from the production of simple magnetic layers to the characterization of magnetoresistive sensors. In the following, the most relevant methods are presented. There are three categories: Sample fabrication, magnetization measurements, and magnetotransport measurements. The key element of the sample fabrication process is thin film layer deposition. In this thesis, magnetron sputtering is used as the deposition technique. In order to characterize the fabricated samples with regard to their magnetization reversal process, the samples are measured in a superconducting quantum interference device - vibrating sample magnetometer (SQUID-VSM). These measurements are complemented using the magneto-optic Kerr effect (MOKE). Finally, several magnetoresistance (xMR) measurement setups are used to characterize magnetotransport properties of the samples. Depending on the stack of samples measured, the appropriate setup for the detection of giant (GMR), anisotropic (AMR) or tunnel (TMR) magnetoresistance is selected. Since both GMR and TMR depend on the relative magnetization orientation of at least two magnetic layers, these measurements are also used to differentiate between the magnetization contributions of the respective layers.

3.1 Magnetron sputtering

Sputtering is the method of separating the atoms of a target by bombarding the target surface with ions from a plasma [135,136]. The ionizing efficiency of the plasma is increased by utilizing magnetic fields of a magnetron system [137]. The setup of magnetron sputtering is illustrated in Fig. 3.1.1.

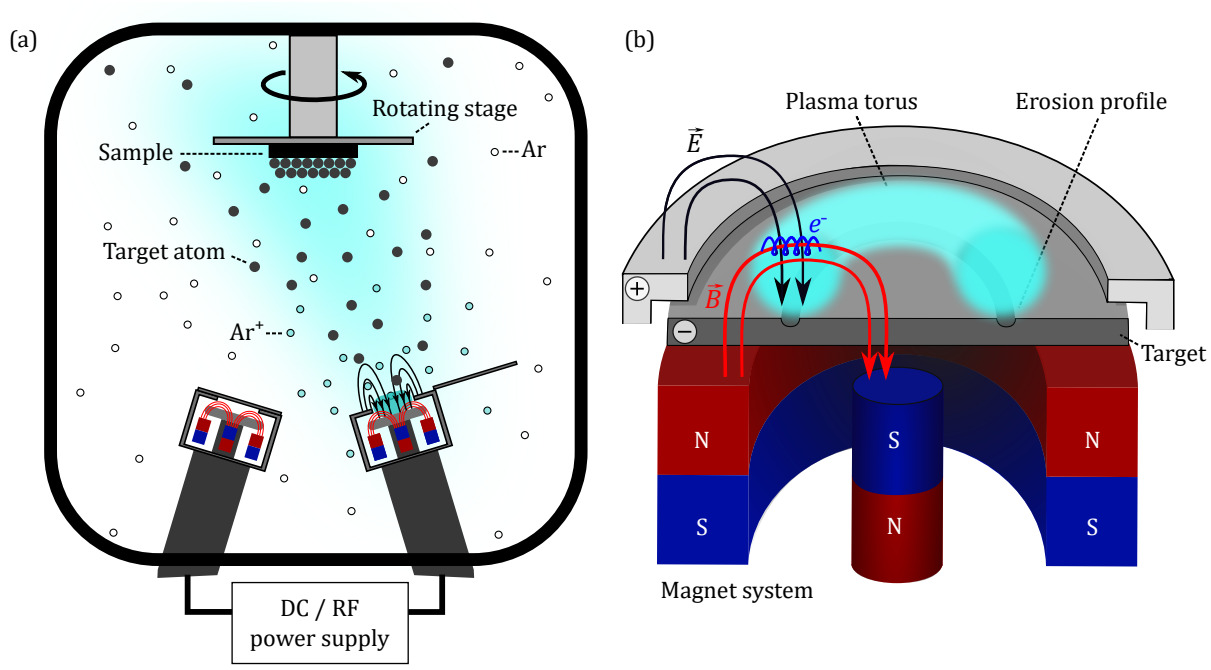

Fig. 3.1.1: Illustration of a magnetron-sputtering system. (a) Ar filled sputter chamber with two exemplary magnetrons. One of these with an open shutter and ignited plasma, illustrated in cyan. (b) Cross section of a magnetron. Electric and magnetic field lines are represented with black and red arrows, respectively. The spiral trajectory of free electrons is illustrated in blue.

Target, magnetron and sample are placed in an ultra-high-vacuum chamber to avoid contamination. The chamber is then filled with a working gas for the plasma. For all fabrications of this work, the working gas is Ar. To establish a plasma at the target, the target is positioned under the edges of a cylinder used as an anode from a DC source (Fig. 3.1.1(b)). The target itself is the cathode, thus electrical field lines are directed perpendicular to the target surface. Ionized Ar atoms and free electrons e^- are accelerated by the electric field **E** above the target, which leads to further ionizing collisions and secondary electron emission from the target. In addition, a magnet is installed underneath the target, which generates a magnetic field **B** in the direction of a cylindrical magnet system surrounding the magnet underneath the target. Due to the positioning of the magnets, magnetic field lines near the target surface move from the target edges to the center of the target. Therefore, besides the electric field, free electrons feel a Lorentz force, which directs the electrons on a spiral trajectory. The result is a longer electron mean free path, consequentially a higher chance of ionizing collisions, and the formation of a plasma torus above this area of the target, with the target center also being the center of the torus. Ionized Ar is accelerated towards the negatively charged target surface, where collisions transfer energy

to target atoms. This leads to the ejection (sputtering) of target atoms near the surface. These, being without charge, can travel away from the electrodes into the surrounding chamber. Since most Ar^+ ions are created in the plasma torus, a circular erosion profile on the target surface underneath the plasma torus appears. The sample is placed in appropriate vicinity on a rotating stage for a homogeneous growth (Fig. 3.1.1(a)). The target atoms collide on their way to the sample with atoms of the Ar gas in the chamber. The average number of these collisions depend, among other things, on the Ar pressure and the distance between target and sample, which has a large impact on the film morphology. Elevated temperatures of the sample during deposition can be used to increase surface diffusion.
Depending on the target material, adjustments to the magnetron sputtering setup may be necessary. In case of ferromagnetic targets, such as Co, the field lines of the magnetron can become distorted. To avoid overwhelming distortion, either relatively thin magnetic targets can be used, or adjustments of the magnetron magnets need to be made. In case of a non-conducting target, such as MgO, a radio frequency (RF) source is used instead of a DC source to establish the plasma [138].
The rate of deposition is determined during a preconfiguration process, for which a quartz crystal is placed at the same position as the sample is for the deposition process. The crystal's resonance frequency shifts with additional mass due to material deposition. Thus, measuring the frequency shift yields the rate of mass deposition per unit time, which can be calibrated to obtain a rate of thickness per unit of time using the density of the target material. The deposition rate is influenced by several parameters, such as the applied power for the plasma, the Ar gas pressure, the distance between target and sample, and the angle of the magnetron with respect to the sample surface. Because of these many influences and the earlier mentioned implications of the target atoms' energy on layer growth, one needs to be careful when samples from different sputtering systems are compared to each other. Even nominally identical samples produced at the same setup but during different deposition sessions may differ from one another (e.g. because of temperature, contamination levels, magnetron-target position, or target thickness).

All samples of this work have been fabricated using the technique of magnetron sputtering. Three different setups have been used. Samples fabricated on a Bestec magnetron-sputtering chamber at the University of Augsburg focus on Co/Pt mulilayer systems. Structures with MgO/CoFeB bilayer systems have been primarily produced in a Canon Anelva magnetron-sputtering chamber at Infineon Technologies AG. The third setup, a Singulus magnetron-sputtering chamber, was used for combined systems of Co/Pt and MgO/CoFeB.

3.2 SQUID-VSM

A very precise instrument for the detection of a sample's magnetic moment is the superconducting quantum interference device - vibrating sample magnetometer (SQUID-VSM) [139, 140], which utilizes magnetic induction. In this work a Quantum Design Magnetic Property Measurement System (MPMS) is used, which employs a DC-SQUID design [141]. A maximal external magnetic field of up to 70 kOe can be applied. Depending on sample insertion geometry, fields are either pointing in-plane or out-of-plane to the sample surface. Measurements can be conducted in temperatures from 1.8 K to 400 K. An illustration of the setup is given in Fig. 3.2.1. The two main components of the working principle of a SQUID-VSM are electromagnetic induction and the Josephson junction [142]. In the following, a brief outline on the functionality of a SQUID-VSM is given. A more detailed discussion can be found from R. Fagaly [143] and in the manual provided by Quantum Design [141].

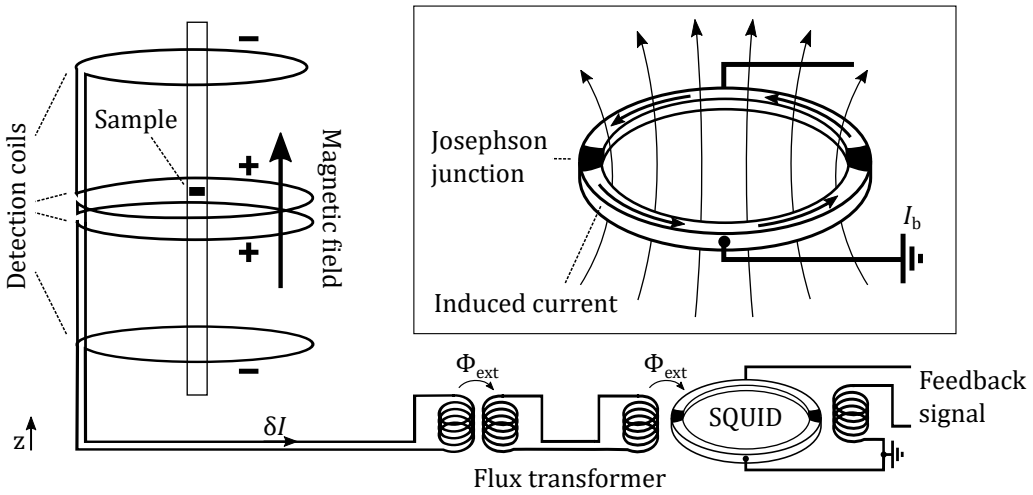

Fig. 3.2.1: Illustration of the SQUID-VSM setup. The sample vibrates inside the detection coils, inducing a current in the gradiometer. Via a flux transformer, the signal is forwarded to a DC-SQUID sensor. The SQUID sensor is operated at a bias current and with a feedback signal for high sensitivities. The inset shows the superconducting ring of the SQUID with two Josephson junctions. Illustrations are based on [141] and [144].

The sample is mounted in the center of superconducting detection coils, which are configured as a second order axial gradiometer, i.e. four symmetric detection coils with the outer coils in the opposite winding direction to that of the inner coils. Ideally, second order axial gradiometers are susceptible to field gradients of second order only, i.e. d^2B_z/dz^2. Uniform magnetic fields and linear magnetic field gradients are strongly suppressed [145]. During a measurement the sample is sinusoidally vibrating perpendicular to the areas of the coils, here defined as the z direction. This induces a current in the detection coils. The amplitude depends on the size of the magnetic moment m_z of the sample. The signal from the detection coils is not directly transferred to the SQUID sensor, but instead forwarded by a flux transformer. One advantage of the flux transformer is that it allows the SQUID sensor to be placed in a different environment than the measured sample. Therefore, high magnetic fields and different temperatures at the

sample don't affect the sensor's performance.

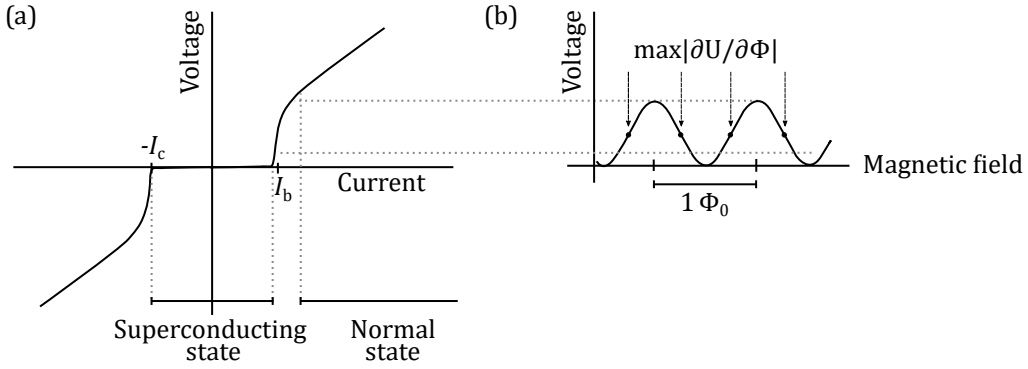

Fig. 3.2.2: (a) Superconducting and normal state of a Josephson junction. A DC-SQUID is operated at bias current between the states. (b) Voltage oscillation of a SQUID sensor with bias current I_b and periodicity Φ_0. The feedback signal locks the SQUID at a magnetic flux that maximizes $\partial U/\partial\Phi$. Figures are adapted from [143].

The heart of the DC-SQUID sensor itself is a superconducting ring with two non-superconducting barriers, i.e. two Josephson junctions. Below a critical current I_C, the conduction particles in a superconducting material (cooper pairs consisting of two coupled electrons) can tunnel through the barrier without a voltage drop. The transition from this superconducting state $I < I_C$ to a normal state $I > I_C$ is not instant, as illustrated in Fig. 3.2.2(a). By inducing a direct bias current I_b, where I_b is slightly higher than $2\,I_C$ (2 times because of 2 Josephson junctions), the SQUID sensor is placed at the transition phase between superconducting and normal state. This way, a change in current δI directly translates into a change of voltage δU. Here, δI stems from the induced current at the detection coils. The level of magnetic flux trapped in a superconducting ring is quantized with $\Phi_0 = h/2e$ (SI), where h is the Planck constant and e the electron charge. The current in the ring with two Josephson junctions, 1 and 2, of the same critical current I_c can be described with

$$I = I_1 + I_2 = I_c \sin\varphi_1 + I_c \sin\varphi_2 = 2I_c \cos\left(\frac{\varphi_1 - \varphi_2}{2}\right) \sin\left(\frac{\varphi_1 + \varphi_2}{2}\right), \tag{3.1}$$

where φ is the respective phase difference between both sides of the junction. With the flux quantization Φ_0 and the condition that the total phase difference along the contour of the ring must be an integer of 2π, Eq. 3.1 evolves to[1)]

$$I = 2I_c \left|\cos\left(\pi \frac{\Phi_{ext}}{\Phi_0}\right)\right|, \tag{3.2}$$

where Φ_{ext} is the external magnetic flux, induced by the magnetic sample. The significance of this is the change of I and therefore U with periodicity Φ_0. Using a feedback current coupled to the SQUID loop, the position of the $U - \Phi_{ext}/\Phi_0$ response can be kept at the steepest (therefore most sensitive) point, i.e. at maximized $\partial U/\partial\Phi$, marked in Fig. 3.2.2(b). With this setup, the necessary feedback indicates the sample's magnetic moment.

[1)] The calculation can be found in more detail in [139] and [145].

Advantages of the SQUID-VSM include its high field range (±70 kOe), its temperature range (1.8 K–400 K), high field sensitivity, and the simple conversion from magnetic moment m to magnetization M via division of the sample volume V. However, complications can arise from measuring the entire sample and its immediate surrounding like the sample holder. Paramagnetic and diamagnetic background can be subtracted if the saturation field of the sample is below 70 kOe. Local artifacts from the sample edges [146] are more difficult to account for, where typically material is deposited with soft magnetic properties.

3.3 Magneto-optic Kerr effect

The magneto-optic Kerr effect (MOKE) [147, 148] describes the polarization rotation of light that has been reflected from a surface with magnetic moment m. It is closely related to the Faraday effect, where the same rotation occurs for light traveling through a medium that is exposed to a magnetic field. The Faraday effect was discovered by Michael Faraday in 1845 [149]. In 1877 John Kerr found the magneto-optic Kerr effect while he studied the polarization of light reflected from a polished electromagnet pole [147]. MOKE can be explained microscopically and macroscopically [150, 151]. Microscopically, the electric field of a light ray generates the motion of electrons in a medium that the light passes through. Circularly polarized electric fields drive electrons in the same circularly motion as that of the electric field. In the absence of a magnetic field the radius of the electron orbit is the same for right-circularly polarized light as it is for left-circularly polarized light. The presence of a magnetic field adds a Lorentz force that disrupts this symmetry. If the direction of field is parallel to the propagation direction of the light, the radius of the electron orbit increases for right-circularly polarization and decreases for left-circularly polarization. Thereby the Lorentz force changes the motion of electrons and with it the optical properties of the material. The source of the magnetic field does not need to be an applied external field, but can also be ferromagnetism of the material itself. Spin-orbit coupling then connects the magnetic and optical properties of the material.
Macroscopically, the magneto-optic effects stem from off-diagonal components of the permittivity tensor. Maxwell explains the rotation of polarization by different propagation velocities of the respective circularly polarization [152]. This leads to a phase shift that results in a rotated net polarization. The magnitude of polarization rotation is proportional to the magnetic moment of the material. Changes in the magnetic moment, e.g. because of an external magnetic field, will result in different polarization rotations. The response of a magnetic material on an external field is therefore detectable by measuring variations in the polarization.

An important difference to the previously presented SQUID-VSM measurement is the spatial resolution limit of the MOKE measurement. The sample's magnetic moment is only measured at the laser spot position. Thus, possible measurement artifacts arising from the sample edges are avoided. Also, due to the finite penetration depth of the laser light, MOKE measurements are surface sensitive. For this work, a 635 nm Coherent® laser diode is used. The magnetic moments of approximately the first 20 nm from the surfaces of this work's samples are detected.

The field range is ca. ±12 kOe in an out-of-plane configuration (polar MOKE).

3.4 xMR measurement setups

For magnetotransport measurements, several setups are utilized in this thesis. These differ in the type of magnetoresistance effect investigated, as well as the setup's contacting capabilities. Samples measured for GMR and AMR effects are examined in setups that are compatible with blanket wafer pieces, whereas different TMR setups are selected for blanket wafers, structured wafers and printed circuit boards (PCB).

3.4.1 Giant and anisotropic magnetoresistance

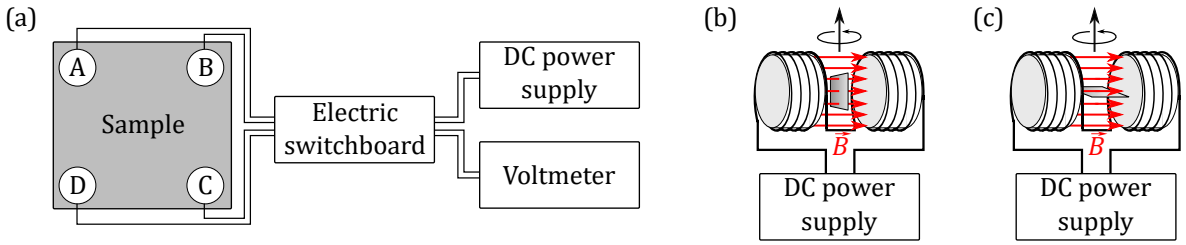

Fig. 3.4.1: Setup for GMR and AMR measurements. (a) Sample contacts in Van der Pauw configuration and electric switchboard for 8 measurements per field value. (b,c) Sample in an electromagnet for (b) out-of-plane and (c) in-plane measurements. The sample holder is rotatable about one axis.

GMR and AMR measurements are conducted in a 4-point Van der Pauw configuration. The setup is illustrated in Fig. 3.4.1. Figure 3.4.1(a) displays four contact points, A, B, C, and D, on the sample surface, near the sample edges. All measurements are performed with current in-plane (CIP). An electric switchboard alternates the applied current I_{ij} from a point i to a point j and voltage measurement points U_{kl}. No diagonal lying points are connected (Hall measurement geometry), which leaves 8 configurations for a pseudo resistance $R_{ij,kl}$, with

$$R_{ij,kl} = \frac{U_{kl}}{I_{ij}}. \tag{3.3}$$

According to Van der Pauw [153], the resistivity ρ of a conducting sample can be determined independent of sample shape and contacting geometry with

$$\rho = \frac{\pi d}{\ln 2} \frac{R_{\mathrm{AB,CD}} + R_{\mathrm{BC,DA}}}{2} f. \tag{3.4}$$

Here, d is the sample's thickness and f a factor which is a function of $R_{\mathrm{AB,CD}}/R_{\mathrm{BC,DA}}$, with

$$\cosh\left[\frac{(R_{\mathrm{AB,CD}}/R_{\mathrm{BC,DA}}) - 1}{(R_{\mathrm{AB,CD}}/R_{\mathrm{BC,DA}}) + 1} \frac{\ln 2}{f}\right] = \frac{1}{2} \exp\left[\frac{\ln 2}{f}\right]. \tag{3.5}$$

A condition is, however, that the contacts are placed at the edges of the sample. Distances introduce deviations from the real resistivity [154]. As illustrated in Fig. 3.4.1(a), the contacts on

the samples are not placed exactly at the edges, therefore deviations are expected. However, this does not present an issue[2)] as the evaluated quantity in this thesis is the (giant) magnetoresistance $(G)MR$, which is the relative change [155] of resistivity in an external magnetic field H:

$$MR(H) = \frac{\rho(H) - \rho_{\min}}{\rho_{\min}}. \tag{3.6}$$

Therefore, most factors in the calculation of ρ do not affect MR. This configuration has the advantage of providing 8 measurement values for an averaged GMR calculation, as well as geometric information relevant for AMR measurements, since 4 measurements are conducted in 90° in-plane rotation to the other 4. In GMR measurements, this also leads to the averaging out of interfering AMR contributions (e.g. stemming from tilted sample installation).

At the University of Augsburg, the external magnetic field is provided by an electromagnet with an iron core, shown in Fig. 3.4.1(b) and (c), at room temperature and normal atmosphere. The magnetic flux density **B** is illustrated with red arrows. Depending on the insertion of the sample, measurements can be conducted with out-of-plane (Fig. 3.4.1(b)) and in-plane fields (Fig. 3.4.1(c)). Furthermore, the sample holder is manually rotatable about one axis, which allows measurements at different field angles. Depending on the sample holder, fields from ±10 kOe to ±12 kOe can be applied.
Additional measurements are conducted at the Institute of Nuclear Physics, Polish Academy of Sciences in Krakow (Poland). The sample is placed in a SQUID setup, which provides fields up to 70 kOe (in-plane and out-of-plane) and temperatures down to 2 K. The electrical configuration is the same as shown in Fig. 3.4.1(a).

3.4.2 Tunnel magnetoresistance

3.4.2.1 Current In-Plane Tunneling

In applications, the contacts of a TMR device are always placed at a conducting layer below and above the tunnel barrier, so that the (change of) conductance through the tunnel barrier can be measured directly. This requires extensive processing, including lithography and precise etching, which is consuming in time and resources. However, for the development stage of TMR structures, Worlegde and Trouilloud [156] invented an alternative measurement system during the MRAM Development Alliance of IBM and Infineon Technologies AG. This method requires no etching for measurements of the MR and the resistance area product (RA), but only surface contacts on blanket wafer level which induce a current in-plane, and is therefore called current in-plane tunneling (CIPT). Its working principle is the variation of contact probe distances, finding the correct spacing for the detection of tunneling conductance. The contacting is shown in Fig. 3.4.2(a) with lines representing the current flow for different probe spacings. The conductance with different spacings through conducting and tunnel barrier can be formalized in an exact differential equation with analytical solution for CIPT. However, the original paper also offers a

[2)] Multiple measurements of the same sample with strongly deviating contacting geometries and edge distances showed no change in GMR results.

simplified model that illustrates the working concept. Here, the system is modeled as a circuit of resistances between two probes of length L and separation x, as shown in Fig. 3.4.2(b). From the contact point of probe and TMR surface, the current can flow along the conducting top layers of resistance $xR_{\mathrm{top/L}}$ to reach the second probe, or deeper into the TMR stack by tunneling through the tunnel barrier with resistance $2RA/xL$, and thereafter through the bottom conducting layers with resistance xR_{bot}/L and back to the surface by tunneling one more time ($2RA/xL$). In case of very small separation x, the resistance of the top layer is much smaller relative to the tunneling resistance so that negligible few electrons take the path of tunneling. In consequence, no current-in-plane magnetoresistance MR_{cip} is detected during field variation, but sheet resistance R_{top} is determined. In case of very large x, the tunnel resistance itself is negligible compared to the resistance of top and bottom layer. Again, no MR_{cip} is detected, but $1/R_{\mathrm{top}} + 1/R_{\mathrm{bot}}$ is determined. For values of x in between these too extremes, however, enough electrons tunnel through the barrier to contribute to the overall conductance, while the resistance of the barrier is substantial enough for changes due to MR to be significant to the measurement [157]. The shape of MR_{cip} as a function of x is shown in Fig. 3.4.2(c) for the simplified model as a dashed line and the exact solution as the solid line (from Worledge and Trouilloud [156]).

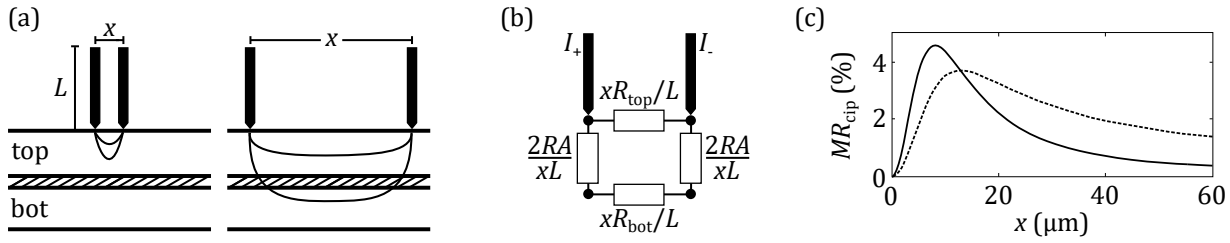

Fig. 3.4.2: CIPT measurement concept. (a) Current flow from two probes through top and bottom conducting layer and through tunnel barrier (shaded) for very small x and very large x. Adapted from [157]. (b) Simplified resistance model for CIPT. (c) MR_{cip} calculation results from Worledge and Trouilloud. The solid line represents the exact solution, whereas the dashed line shows the simplified resistance model. Figures (b) and (c) adapted from [156].

For blanket wafer measurements of this work, a Capres CIPTech®-M200 system is used, with a magnetic field range of ±1.5 kOe in an in-plane configuration. It has to be noted that the system used for this work calculates the MR values based on resistance measurements at ±600 Oe, assuming a parallel and antiparallel magnetization alignment of the magnetic layers (below field values that affect the reference layer magnetization). However, it is often the case that TMR free layers of this work are not yet fully saturated at these field values. CIPT measurements are therefore only used for preliminary characterization.

3.4.2.2 Probe station

At Infineon Technologies AG fully structured wafers with TMR stacks are fabricated. On each wafer are multiple dies with several different module structures. The TMR elements used in this thesis are all of circular shape with a diameter of the order of 1 µm. Connected in parallel and in series, these elements comprise a TMR resistor. Modules differ in several parameters, such as the diameter of the TMR elements, the distance between them and the overall used number of

elements in parallel and series for one resistor. Furthermore, the modules are categorized into different types with regard to their electric circuitry. For instance, some modules are configured in Wheatstone bridge circuits of varying geometries, whereas other modules only allow measurements at single resistors. The composition of a structured wafer is illustrated in Fig. 3.4.3, showing wafer, die, module, resistor, and TMR element. Even though this thesis does not focus on the impact of circuitry but on the TMR stacks itself, structured wafer measurements still provide two advantages. First, the measurements of modules with different TMR element geometries give an indication of the elements' sensitivity toward these. This is of particular interest because for some applications TMR sensors with perpendicular magnetic anisotropy (PMA) may be an alternative to TMR sensors with vortex anisotropy, where element geometry is a defining parameter [158]. Secondly, measurement statistics can be created with structured wafers, for there are tens of dies and hundreds of modules on a wafer.

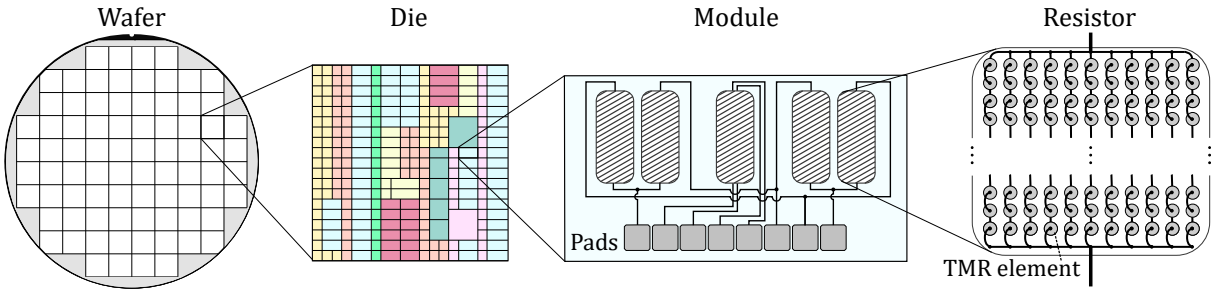

Fig. 3.4.3: Composition of a structured wafer. The wafer is divided into dies, which consists of several modules. The same colors represent modules of the same type. In this example, the shown module type features a Wheatstone bridge and a centered direct resistor. A resistor is built from multiple circular TMR elements connected in parallel and series. Element diameter, separation, and number vary between modules, among other differences.

For the measurements of these modules, a UF-200 probe station from TSK is used. After configuration, the probe station is able to automatically change positions on the wafer and contact the module pads with probing needles. Furthermore, the setup features a heat chuck for temperatures between 35 °C and 150 °C. For the magnetic fields, two different electromagnetic setups are used. One is a quadrupole magnet for in-plane measurements up to 2 kOe. The other, a single coil, generating out-of-plane fields up to approximately 180 Oe.

3.4.2.3 Printed Circuit Board

After measurements at the probe station, selected modules are cut out of the wafer and connected onto printed circuit boards (PCB). This allows further TMR measurements at an electromagnet with a 70 A Lakeshore® power supply providing 10 kOe magnetic fields in-plane and 6 kOe magnetic fields out-of-plane. Additionally, measurements are possible from −40 °C to 150 °C due to an attached ThermoStream® system. With an automated stepper motor, rotational measurements in in-plane fields can be conducted, used for TMR angle sensors.

Chapter 4

Perpendicular antiferromagnetic reference system

In this chapter, the development of magnetoresistance (xMR) sensors is presented, where a perpendicular synthetic antiferromagnet (p-SAF) acts as reference system, whereas the free layer (FL) has an in-plane effective magnetic anisotropy K_{eff}. The aim is the understanding, design, and fabrication of Giant Magnetoresistance (GMR) and Tunnel Magnetoresistance (TMR) sensors with an out-of-plane field sensitivity of several kOe.

First, Co/Pt multilayers (ML) with perpendicular magnetic anisotropy (PMA) are fabricated and studied. To that end, fabrication and post processing parameters are investigated. The MLs are then used to construct different types of p-SAFs. Since MLs and p-SAFs are the basic structures for the desired xMR sensors, the respective sections 4.2 and 4.3 also form a documentation of the optimization process. Furthermore, measurements show spin-canting effects within the p-SAF, which is subject to further research, including micromagnetic simulations in this chapter. Besides their magnetization properties, magnetoresistance effects in p-SAF structures are explored and modeled. Finally, GMR and TMR sensors are developed, while investigating methods to control the FL K_{eff}.

Sample fabrication as well as measurements are primarily conducted at the University of Augsburg, with the exception of one TMR wafer lot deposited by Singulus Technologies AG, which is processed and measured at Infineon Technologies AG. For characterization purposes, several measurement methods are conducted: M-H hysteresis loops in a SQUID-VSM and polar MOKE, GMR resistivity measurements in Van der Pauw configuration, and TMR conductivity on wafer and printed circuit board (PCB) level.

4.1 Sample fabrication

In this section, the sample fabrication of MLs, p-SAFs, GMR and TMR sensors is presented. All samples in this chapter, if not stated otherwise, were fabricated at room temperature. Films were deposited onto 1.5 cm×1.5 cm thermally oxidized silicon (100) wafer pieces in a Bestec magnetron-sputtering chamber with a base pressure of 1×10^{-8} mbar. Argon was used as a sputter gas during the deposition process with a pressure of 5×10^{-3} mbar. Table 4.1.1 shows every material that was used and their respective sputtering rate. The only exception is MgO, which was sputtered with a constant power P rather than sputtering rate, which fluctuates between 0.01 and 0.02 Å/s depending on the target position within the sputtering chamber. For MOKE and GMR measurements, no further treatment of the samples was undertaken. For SQUID-VSM measurements, the wafer pieces were cut manually with a diamond cutter and broken into appropriate pieces of a few mm^2 for insertion. In a few cases, which will later be mentioned in more detail, samples were post annealed in a tube oven at 250 to 310 °C for 1 h in a low pressure Ar atmosphere of 1 mbar.

Material	Ta	Ru	Pt	Co	CoFe	Cu	MgO
Rate [Å/s]	0.4	0.2	0.4	0.2	0.2	0.4	$P = 60$ W

Table 4.1.1: Sputtering deposition rates of all materials used in this chapter. MgO was sputtered at constant power P. During deposition Ar pressure is set to 5×10^{-3} mbar.

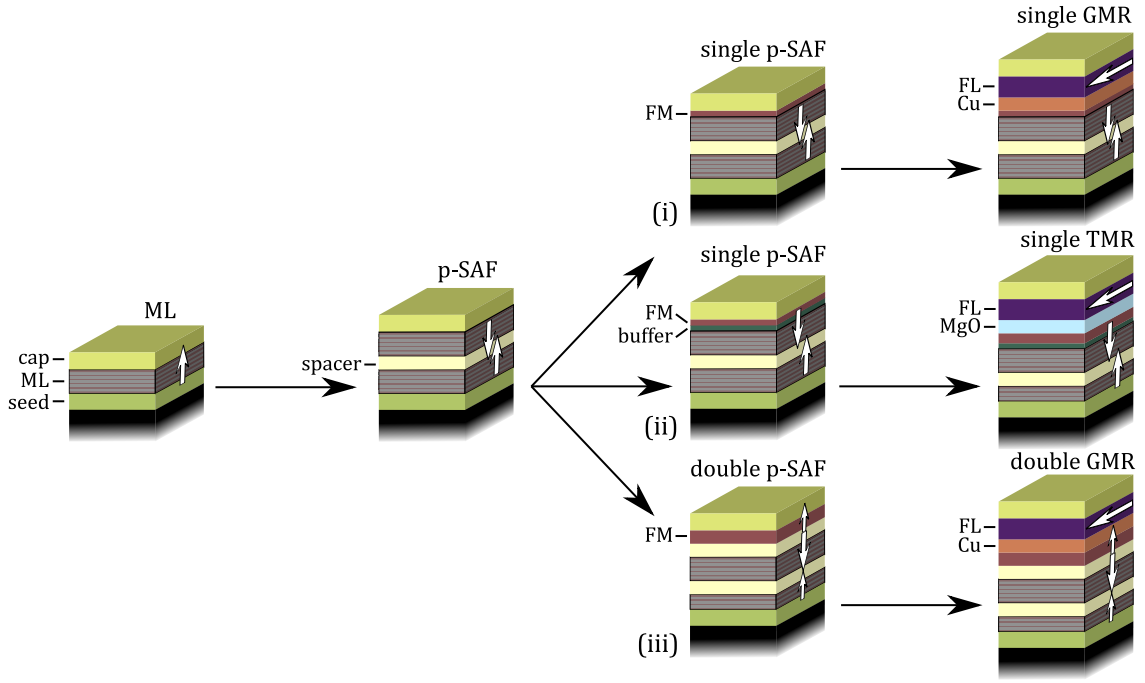

Fig. 4.1.1: Flow of development from ML via p-SAFs to GMR and TMR sensors. The different stack variations for the deposition of the top FM layer (acting as reference layer in xMR sensors) are shown from (i) – (iii). Free layers (FL) are separated from the p-SAFs by Cu in GMRs and an MgO tunnel barrier in TMRs. White arrows indicate magnetization directions at zero magnetic field.

Figure 4.1.1 illustrates the flow of development from Co/Pt MLs to GMR or TMR sensor. Each

development step requires an understanding of the fabrication parameters and, accordingly, an optimization process.

At first, Co/Pt ML systems were fabricated and optimized towards high PMA by varying the layer repetition N, layer thicknesses and seed layer composition using Ta, Ru, and Pt. The basic structure of the MLs is Si/SiO_2/seed layer/[Co(t_{Co})/Pt(t_{Pt})]$_N$/capping layer, where t_{Co} and t_{Pt} denote the layer thicknesses of Co and Pt, respectively. As a next step, two MLs with a Ru spacer layer were used to construct a simple p-SAF structure (ML/Ru/ML), where the optimization process focuses on the interlayer exchange coupling (IEC) by varying the materials adjacent to the Ru spacer layer and the Ru layer thickness t_{Ru} [82–86]. Having in mind to use these p-SAFs as a reference system for GMR and TMR sensors, a ferromagnetic (FM) layer was coupled to the top ML of the p-SAF. This FM layer consists of Co, CoFe, or CoFeB. Three different variations were used:

(i) direct deposition on top of the multilayer,

(ii) deposition of a buffer layer (Ta) and a FM layer on top, and

(iii) adding a second spacer layer (i.e. Ru) before deposition of the FM layer.

Variation (i) and (ii) comprise single p-SAF structures, of which (ii) is needed for systems that use a FM with boron and different crystallography than that of fcc (111) Co/Pt (i.e. amorphous CoFeB crystallizing into bcc CoFe upon annealing) [55, 59, 60, 159, 160]. Variation (iii) leads to a double p-SAF with the top (L_{top}) and bottom layer (L_{bot}) having parallel magnetization directions antiferromagnetically aligned to the magnetization of the middle layer (L_{mid}) via IEC, when spacer thicknesses are chosen accordingly.

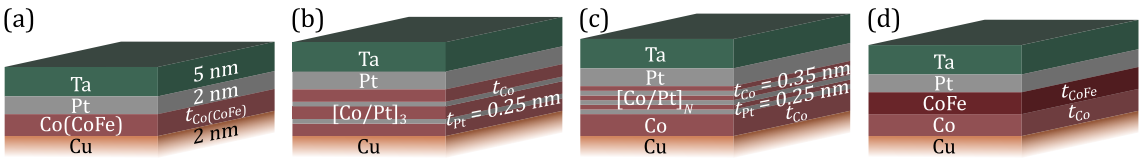

Fig. 4.1.2: Free layer design with capping layers used for GMR sensors: (a) Single FM layer Co(t_{Co}) or CoFe(t_{CoFe}), (b) ML [Co(t_{Co})/Pt(0.25)]$_3$, (c) single layer coupled to a ML Co(t_{Co})/Pt(0.25)/[Co(0.35)/Pt(0.25)]$_N$, and (d) bilayer Co(t_{Co})/CoFe(t_{CoFe}).

As a last step, a FL is added that is magnetically decoupled by a Cu spacer layer in case of GMR sensors and an MgO tunnel barrier in that of TMR sensors. In the GMR construction, four different FL designs have been used, illustrated in Fig. 4.1.2:

(a) a single FM layer with either Co(t_{Co}) or CoFe(t_{CoFe}),

(b) a ML with [Co(t_{Co})/Pt(0.25)]$_3$,

(c) a single layer coupled to a ML with Co(t_{Co})/Pt(0.25)/[Co(0.35)/Pt(0.25)]$_N$, and

(d) a bilayer with Co(t_{Co})/CoFe(t_{CoFe}).

N denotes the number of Co/Pt bilayers of the FL (c). All thicknesses are given in nm.

4.2 Co/Pt multilayer

In order to achieve the fabrication of a well functioning magnetoresistive sensor, creating a hard magnetic reference layer with a high coercive field H_c and a high magnetic anisotropy field H_k is essential, as the reference layer needs to be unaffected from an external field within the operation range of the sensor. Furthermore, the preferred magnetic orientation must show a distinct direction – in this case, perpendicular – since otherwise in-plane stray fields can induce disturbances in the signal such as magnetic hysteresis. Even though Co/Pt MLs have been extensively studied by other groups [20, 26, 28, 34, 38, 50, 161–173], significant differences can be found concerning optimal fabrication parameters. The reason for this is that the strength of PMA in Co/Pt multilayers is attributed to a number of different factors, such as film roughness, texture and microstructure, formation of interface alloys, and mechanical stress [20, 53, 161, 163–165, 169, 170]. This suggests the need for an optimization process on the individual sputter chamber setup. In the following, results are presented for the magnetic optimization of the basic Co/Pt ML system.

4.2.1 Seed layer

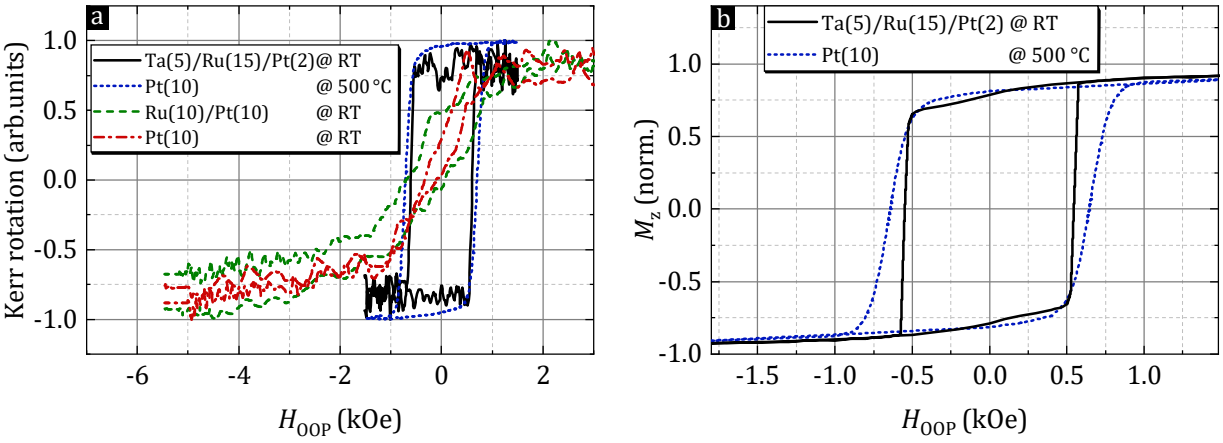

Fig. 4.2.1: *M-H* hysteresis loops from (a) polar MOKE and (b) SQUID-VSM measurements of $[Co(0.25)/Pt(0.20)]_7$ multilayer samples with different seed layers and seed layer deposition temperatures.

The stack system is based on previous works by the group of Yasuo Ando [6, 31, 32, 77] and Kay Yakushiji et al. [35, 174]. In their studies, a combination of Ta/Ru is used as seed layer to promote ideal crystal growth conditions of fcc (111) [164, 168], whereas a publication by Mancoff et al. (2000) [22] abstains from using these materials and works with high deposition temperatures for a Pt seed layer instead. Figure 4.2.1 shows the results of this thesis regarding the seed layer material and deposition temperature. In all cases the ML system above the seed layer is $[Co(0.25)/Pt(0.20)]_7$ with thicknesses given in nm. In Fig. 4.2.1(a) one can see the Kerr rotation of polar MOKE measurements. A seed layer with Ta(5)/Ru(15)/Pt(2) sputtered at room temperature (RT) and a seed layer with Pt(10) sputtered at 500 °C show a similar out of plane

(OOP) behavior with H_c at around 0.6 kOe. However, if the seed layer is sputtered without Ta and at RT, with or without a Ru(10) layer, MOKE measurements suggest the sample's hard axis to be OOP, therefore failing to achieve PMA. To understand which method – high temperature deposition or additional Ta/Ru layers – should be pursued further in this work, SQUID-VSM measurements were conducted, as shown in Fig. 4.2.1(b). Generally, the results are similar. While the Pt(10) at 500 °C sample shows a higher H_c at 640 Oe than that of the Ta(5)/Ru(15)/Pt(2) sample with 550 Oe, it also has a less well defined transition from positive to negative magnetization and vice versa, indicating the formation of magnetic domains [175]. This behavior is undesirable since these MLs are later used as reference systems for GMR sensors and therefore need to have a clearly defined magnetization direction. Additionally, practical reasons speak against the high temperature deposition method: first, it takes several hours for the sputter chamber to cool down from 500 °C, and secondly, both Ta and Ru are already installed targets for their use in other functions, such as capping and/or spacer layer. Therefore, their further use as seed layer costs only little additional time and effort.

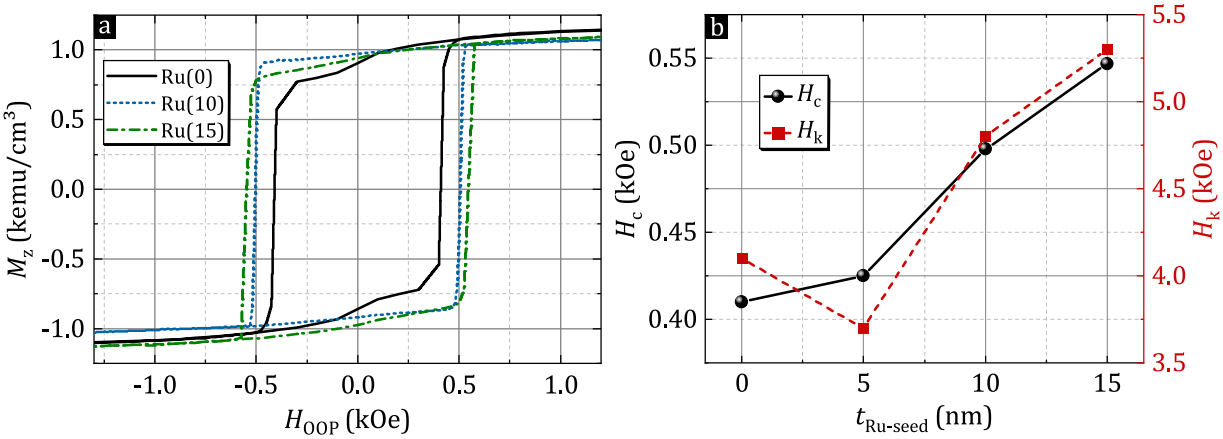

Fig. 4.2.2: ML samples (Si/SiO_2/Ta(5)/Ru($t_{Ru\text{-}seed}$)/Pt(2)/[Co(0.25)/Pt(0.2)]$_7$/cap) with varying Ru seed layer thickness $t_{Ru\text{-}seed}$. (a) M-H hysteresis loops from SQUID-VSM measurements. (b) H_c and H_k values against $t_{Ru\text{-}seed}$.

Because of ruthenium's brittleness, sputtering of Ru tends to produce Ru flakes that create electrical short circuits at the magnetron plasma position, if they fall between target area and magnetron cylinder. Therefore, reducing the amount of Ru sputtered per sample is still desirable. The influence of Ru thickness in the seed layer on H_c and H_k is shown in Fig. 4.2.2. M-H hysteresis loops for ML systems of the stack [Co(0.25)/Pt(0.20)]$_7$ with $t_{Ru\text{-}seed}$ from 0 to 15 nm are plotted in Fig. 4.2.2(a). Figure 4.2.2(b) shows H_c and H_k values, extracted from magnetometer measurements. The results suggest an increase in H_c of 10 Oe per 1 nm of Ru, accompanied with an increase in H_k of about 0.1 kOe for Ru thicknesses $t_{Ru\text{-}seed} \leq 15$ nm. For the rest of this work, Ru is sputtered as a seed layer with $t_{Ru\text{-}seed} = 10$ nm, chosen as an appropriate value in the tradeoff between PMA and risk of electrical short circuit.

4.2.2 $[Co/Pt]_N$ multilayer design

In this section, the influence of layer thicknesses and number of Co/Pt bilayer repetition within the Co/Pt multilayer is examined for the stack $Si/SiO_2/Ta(5)/Ru(10)/Pt(2)/[Co(t_{Co})/Pt(t_{Pt})]_N/Pt(2)/Ta(5)$.

4.2.2.1 Co layer thickness t_{Co}

As discussed in chapter 2.1.2, the PMA in Co/Pt ML systems arises from interface effects, contributing to the interface anisotropy K_S. For the calculation of the effective magnetic anisotropy K_{eff}, the term with K_S is given by $2K_S/t$, where t is the ferromagnetic layer thickness (see Eq. 2.10). Therefore, the Co thickness t_{Co} is a key parameter for the design of perpendicular magnetized MLs. Experimental results of other groups generally show PMA dominance emerging for $t_{Co} \leq 1.0\,nm$ [38,53,161,168,170]. For this study a sample series with $0.15\,nm \leq t_{Co} \leq 1.0\,nm$ was prepared, with Pt thickness $t_{Pt} = 0.20\,nm$ and the number of bilayers $N = 7$. H_c and H_k values are summarized in Fig. 4.2.3(a). As expected, both values increase for $t_{Co} \leq 1.0\,nm$, since interface effects become more dominant for thinner layers. H_c reaches its highest values of up to 880 Oe between $t_{Co} = 0.3$ and 0.5 nm. Similarly, the highest values for H_k lie between $t_{Co} = 0.3$ and 0.6 nm with H_k up to 9.5 kOe. However, both values significantly decrease for $t_{Co} < 0.3\,nm$. This is likely because of deposition thicknesses being too small for a continuous Co layer to form, thus resulting in irregularities at the Co/Pt interface and reducing PMA.

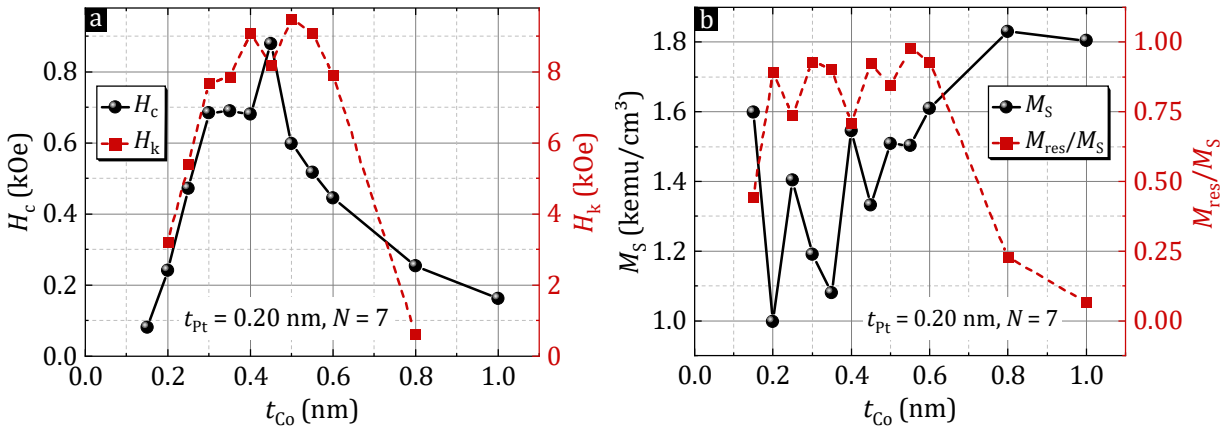

Fig. 4.2.3: a) H_c and H_k, and b) M_S and M_{res}/M_S for $[Co(t_{Co})/Pt(0.20)]_7$ ML samples.

Figure 4.2.3(b) shows the saturation magnetization M_S and the squareness of the hysteresis curves, calculated as ratio of the remanence or residual magnetization M_{res} over M_S. Note that, due to Pt polarization in Co/Pt multilayers [50,163,167], t_{Pt} is included in the multilayer volume V for the calculation of the magnetization M from the measurement of the magnetic moment m with

$$M = m/V. \tag{4.1}$$

Similarly to Fig. 4.2.3(a), the squareness is high for $t_{Co} \leq 0.6\,nm$ but decreases for higher thicknesses to $M_{res}/M_S \leq 0.25$, indicating the formation of magnetic domains [175]. M_S is

between 1.0 and 1.9 kemu/cm^3 for all samples, with a general tendency of increasing M_S at thicker t_{Co}.

Figure 4.2.4(a) shows an exemplary graphical determination of the effective magnetic anisotropy K_{eff} for the Co/Pt ML systems. In this thesis, K_{eff} is calculated from the enclosed area of IP and OOP M-H hysteresis loops. It should be noted that the calculation of H_k from the M-H hysteresis loop along the magnetic hard axis is done independently from the determination of K_{eff}, which means that the approximation given in Eq. 2.3 ($K_{eff} = \pm\mu_0 H_k M_S/2$) is not used in this thesis. The determined values of K_{eff} and $K_{eff}\,t_{Co}$ are plotted against t_{Co} in Fig. 4.2.4(b).

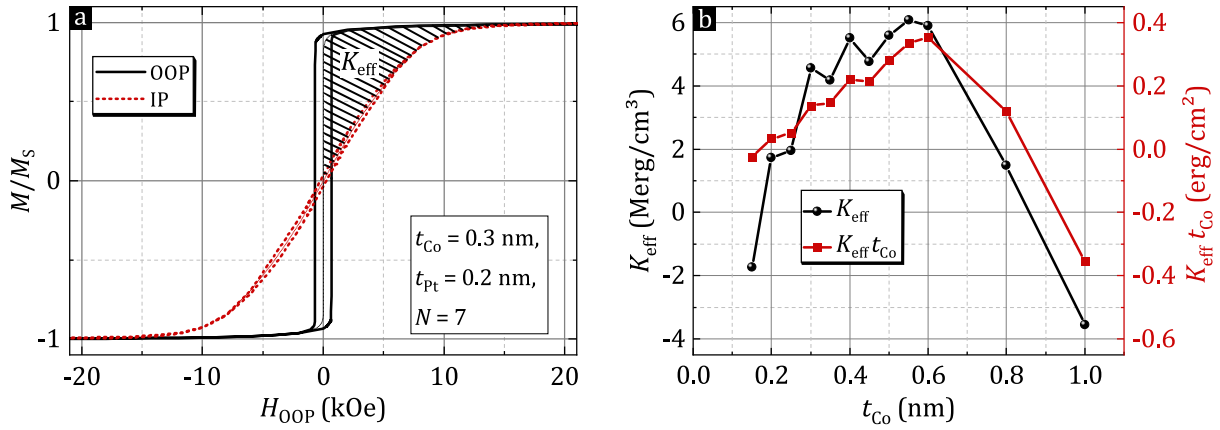

Fig. 4.2.4: (a) Exemplary OOP and IP M-H hysteresis loops (SQUID-VSM) of a sample with $t_{Co} = 0.30$ nm for K_{eff} calculation. (b) K_{eff} for $[Co(t_{Co})/Pt(0.20)]_7$ ML samples.

Similar to H_c and H_k, K_{eff} is maximized between $t_{Co} = 0.3$ and 0.6 nm with values up to $K_{eff} = 7$ Merg/cm^3. Shown in Fig. 4.2.4(b), at $t_{Co} = 0.15$ and 1.0 nm, K_{eff} is distinctively negative at about -2 Merg/cm^3 and -3.5 Merg/cm^3. From Eq. 2.10 and Fig. 4.2.4(b), the interface contribution K_S can be approximated to be around 0.8 erg/cm^2 and the volume contribution K_V to be around -22 Merg/cm^3, which is in good agreement with literature values [20].

In conclusion, the Co/Pt ML samples of this thesis show a dominant PMA for 0.2 nm $\leq t_{Co} \leq$ 0.8 nm, and a maximized PMA for 0.3 nm $\leq t_{Co} \leq$ 0.5 nm. These results are in agreement with the conclusions drawn by other groups [38, 53, 161, 168, 170].

4.2.2.2 Layer repetition N

Similar investigations are conducted to optimize N and t_{Pt}. Figure 4.2.5 shows H_c and H_k in subfigure (a), and M_S and M_{res}/M_S in subfigure (b) for ML samples with varying N and fixed $t_{Co} = 0.25$ nm and $t_{Pt} = 0.20$ nm.

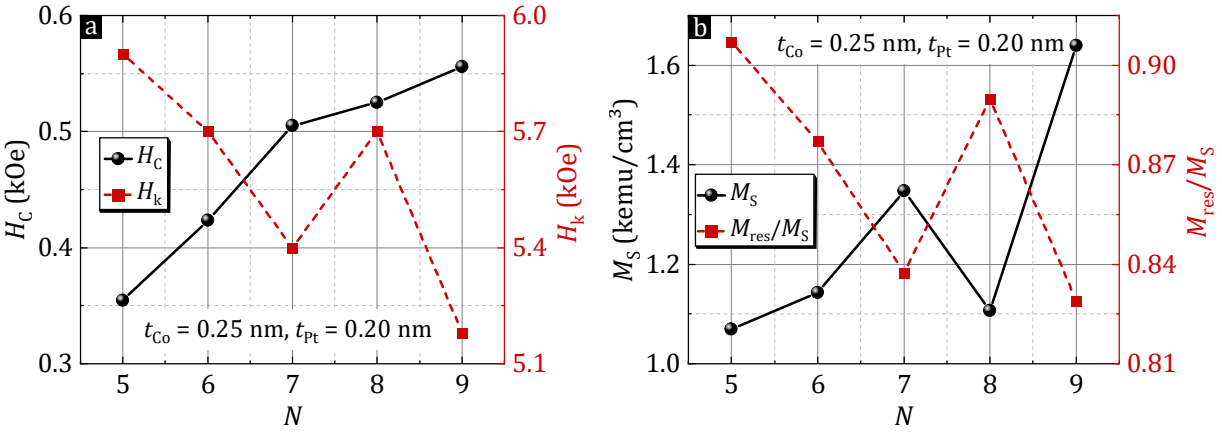

Fig. 4.2.5: (a) H_c and H_k, and (b) M_S and M_{res}/M_S for $[Co(0.25)/Pt(0.20)]_N$ ML samples.

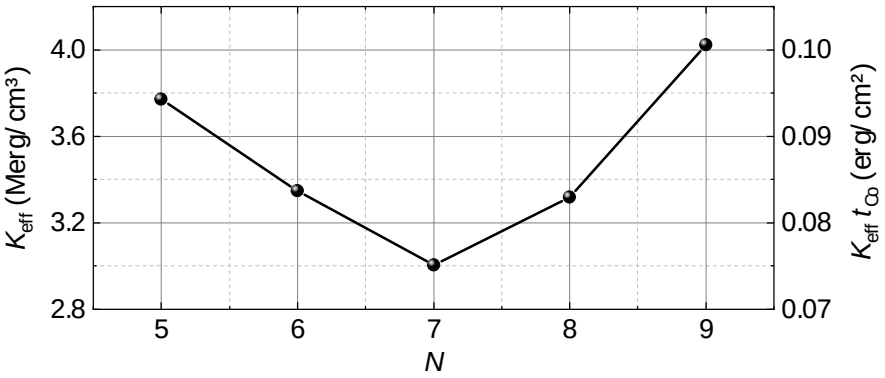

Fig. 4.2.6: K_{eff} for $[Co(0.25)/Pt(0.20)]_N$ ML samples.

While H_c and M_S increase with N, suggesting the use of higher N to optimize PMA, H_k and M_{res}/M_S decrease, suggesting the opposite. This result can also be found in the values for K_{eff}, plotted in Fig. 4.2.6, since both the decrease of H_k as well as the increase of M_S have an influence on K_{eff}. The impact of N is not significantly strong, giving values between 3 and 4 Merg/cm^3, with no clear trend either as K_{eff} decreases towards $N = 7$ but then increases again for higher N. A possible reason for this is the formation of magnetic domains as the stack thickness increases [175].

In a similar study by Lin et al. [161], an increase of H_c and decrease in squareness was measured when N was increased from $N = 4$ to $N = 77$ with 4 intermediate steps. It is suggested that the multilayers experience an increase of roughness, but also improved texture with higher N. While they also measured an increase in K_{eff}, their measurement results don't disagree with the findings of this thesis, as their measured deviations in K_{eff} suggest that no clear trend might be observed in the range of $5 \leq N \leq 9$. In a study by Yakushiji et al. [34], increasing N from $N = 3$ to $N = 6$ yields higher M_S and a small decrease of H_k, which, however, resulted in an overall increase of K_{eff}. In their study, the increase in M_S with N is attributed to the smaller impact of magnetic dead layers at the buffer and capping interfaces.

4.2.2.3 Pt thickness t_{Pt}

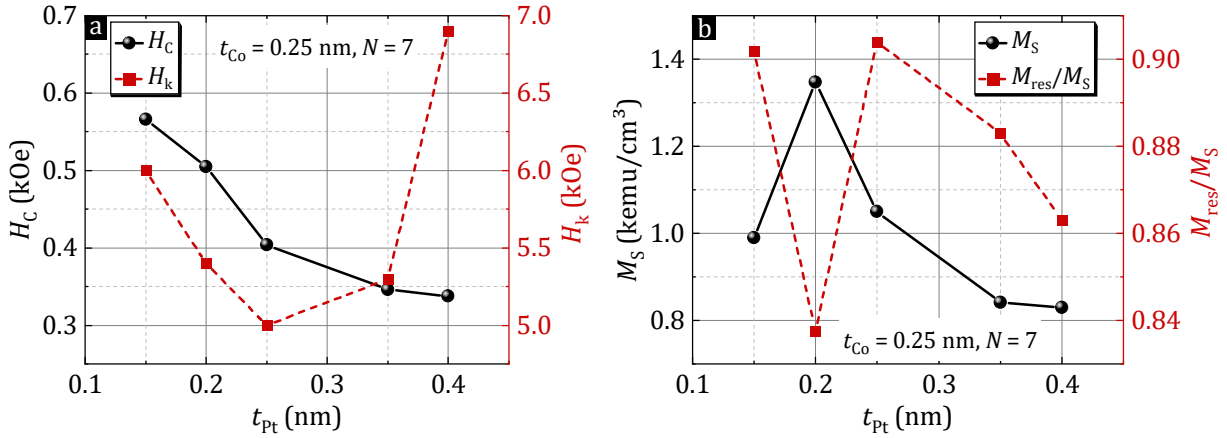

Fig. 4.2.7: (a) H_c and H_k, and (b) M_S and M_{res}/M_S for [Co(0.25)/Pt(t_{Pt})]$_7$ ML samples.

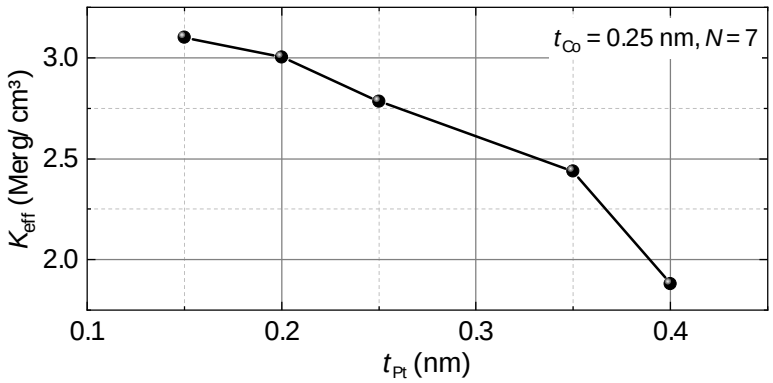

Fig. 4.2.8: K_{eff} for [Co(0.25)/Pt(t_{Pt})]$_7$ ML samples.

The results for the Pt thickness give a clearer picture, suggesting smaller t_{Pt} to be preferable. Figure 4.2.7, once more, shows H_c, H_k, M_S and M_{res}/M_S. Both M_S and M_{res}/M_S show a tendency of decreasing with increasing t_{Pt}, with, however, strong deviations. H_c significantly decreases with increasing t_{Pt}. Figure 4.2.8 shows K_{eff} as a function of t_{Pt}, also decreasing with t_{Pt}.

4.2.3 Post annealing stability

Finally, measurements after post annealing are conducted. Annealing the ML system might cause interdiffusion, which can lead to a decreasing PMA [166, 176, 177], or, on the other hand, ordering of the crystal structure, improving PMA. Since the fabrication of TMR sensors requires post annealing processes, temperature instabilities of the ML systems need to be understood, if they are to be used in TMR reference systems. The results are given in Fig. 4.2.9. The samples show no performance degradation up to 275 °C post annealing temperatures for 1 h in a low pressure Ar atmosphere, and even show increased H_c values of approximately 50 Oe.

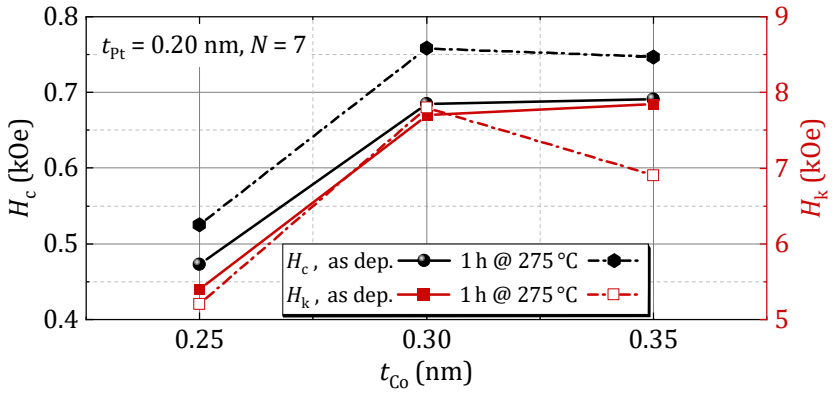

Fig. 4.2.9: Post annealing effect after 1 h at 275 °C in a low Ar atmosphere on H_c and H_k for samples with different Co layer thickness (Si/SiO_2/Ta(5)/Ru(10)/Pt(2)/[Co(t_{Co})/Pt(0.2)]$_7$/cap).

4.2.4 Summary

To summarize, the fabrication parameters for Co/Pt multilayers with PMA were investigated in this section. For the seed layer material, a Ta(5)/Ru(10)/Pt(2) stack (thicknesses in nm) sputtered at room temperature was found to be the preferred choice. While the Ru seed layer thickness may be increased, 10 nm were found to suffice, considering fabrication difficulties connected to the brittleness of Ru. For a high PMA, the Co thickness t_{Co} shows maximized values in H_c, H_k, M_{res}/M_S, and K_{eff} for $0.3\,\text{nm} \leq t_{Co} \leq 0.5\,\text{nm}$. This range agrees well with the thicknesses used in the literature [27, 28, 169, 178, 179]. Increasing the layer repetition N also increases H_c and M_S, but decreases H_k and M_{res}/M_S, with an inconclusive result for K_{eff}. Pt thickness t_{Pt} yields the best results for small thicknesses, i.e. $t_{Pt} < 0.25\,\text{nm}$. A post annealing process of 1 h at 275 °C increases H_c by approximately 50 Oe in ML systems with $0.25\,\text{nm} \leq t_{Co} \leq 0.35\,\text{nm}$.

4.3 Perpendicular synthetic antiferromagnets

Perpendicular synthetic antiferromagnets (p-SAFs) are essential for the performance of an out-of-plane xMR sensor. The dynamic magnetic field range of such a sensor is limited only by the reference layer's range of stability, i.e. the field range of the p-SAF's antiferromagnetic alignment [32]. In this chapter, p-SAFs are developed and investigated with regard to the influence of several structural design parameters, such as the composition of the seed layer as well as magnetic and non-magnetic layer thicknesses. A "double" p-SAF structure with three antiferromagnetically interlayer exchange coupled magnetic layers is studied and compared to regular "single" p-SAFs with two magnetic layers. *M-H* hysteresis loops are measured by SQUID-VSM and MOKE, and in some cases accompanied with resistance measurements in Van der Pauw configuration. While giant magnetoresistance (GMR) sensors are investigated in a later chapter, the GMR effect is already exploited in this section to reveal the behavior of the underlying p-SAF reference systems. Furthermore, micromagnetic simulations of single and double p-SAFs are carried out, in order to understand the magnetic reversal processes and emerging spin-canting effects.
P-SAFs with up to 10 kOe exchange fields at room temperature are fabricated, and an understanding is established on the influence of design parameters on p-SAF performance as well as on the influence of magnetic layer properties on the p-SAF's magnetic reversal behavior.

4.3.1 Measurement evaluation

Before the results are discussed, the measurement evaluation is explained at an example presented in Fig. 4.3.1, which shows *M-H* hysteresis loops for (a) p-SAF and (b) GMR structures.

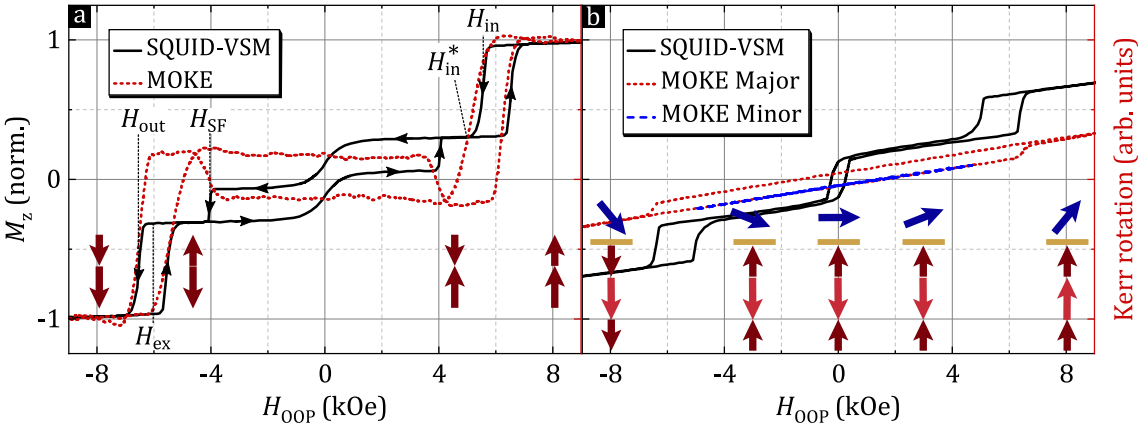

Fig. 4.3.1: *M-H* hysteresis loops of (a) a p-SAF structure and (b) a GMR sensor. (a) shows the definition of the characteristic fields H_{in}, H_{in}^*, H_{SF}, H_{out}, and H_{ex}. SQUID measurements reveal an additional artifact around 0 Oe, that is not visible in MOKE measurements. Red arrows illustrate the magnetization directions of the p-SAF layers (red) and the in-plane free layer (dark blue).

The out-of-plane magnetization as obtained by SQUID-VSM is plotted as M_z normalized to M_S. In addition, MOKE measurements show the Kerr rotation in arbitrary units. In a field

sweep of the p-SAF structure, three switching fields occur: switching from a saturated state into the antiferromagnetically coupled p-SAF state at H_{in}, switching out of the p-SAF state into a saturated state at H_{out}, and a reversal of the antiparallel alignment of the moments (state flip) at H_{SF}. The latter only appears in case of imbalanced p-SAF layer moments. The mean of H_{in} and H_{out} is defined as the exchange field H_{ex}. Since the p-SAF is developed with the purpose of serving as a GMR reference system, the field at which the antiferromagnetic alignment of the p-SAF is stable in both field directions is of interest, which is the field range up to $\pm H_{\mathrm{in}}^{*}$. All characteristic fields are mentioned in Fig. 4.3.1(a). Black arrows act as a guide for the sweep direction of the external magnetic field H_{OOP}.

Figure 4.3.1(b) shows M-H hysteresis loops of a double p-SAF GMR structure, where a linear magnetization increase of the free layer is superimposed on that of the double p-SAF. The nature of double p-SAFs will be explored in detail later in this chapter. Note, that both a SQUID-VSM as well as a polar MOKE measurement show the sample's M-H hysteresis loop. However, around 0 Oe the SQUID measurements of p-SAF and GMR structure display a behavior not seen with polar MOKE. The reason for this is a magnetic soft phase originating from the samples edges [146]. The SQUID, measuring the samples globally, detects these artifacts, which the locally measuring MOKE does not. For this thesis, the disordered structures at the sample edges are considered as artifact to be subtracted from the measurement data, when analyzing the sample's magnetization behavior. Later, when the focus shifts from p-SAFs to GMR sensors, the additional magnetization profile of the in-plane free layer can, in some cases, make the subtraction of the p-SAFs soft phase difficult. Therefore, magnetoresistance measurements, which expectedly also do not detect edge effects, will prove to be an important measurement tool.

Another difference is the MOKE's higher sensitivity to layers closer to the surface. This feature helps identifying the order of the individual p-SAF layer switching.

4.3.2 Seed layer

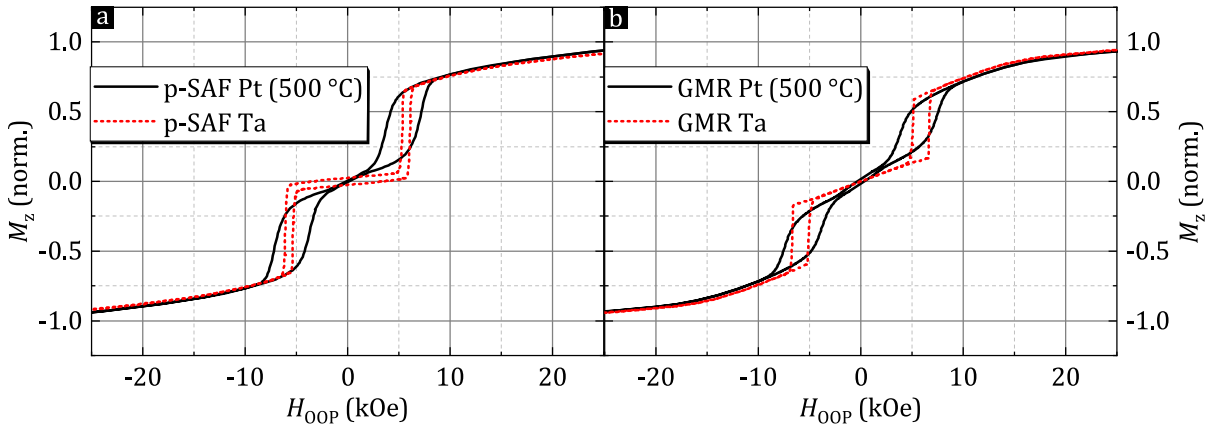

Fig. 4.3.2: Out-of-plane M-H hysteresis loops for (a) p-SAF and (b) GMR structures. Dotted red lines show structures with the standard seed layer stack Ta(5)/Ru(10)/Pt(2) sputtered at room temperature, solid black lines show the sample structures using a seed layer Pt(10) sputtered at 500 °C.

In section 4.2, Fig. 4.2.1, it was determined that Ta is essential as a seed layer for PMA in Co/Pt multilayers, although high temperature deposition of Pt also resulted in a strong PMA but with less well defined magnetization transitions. In Fig. 4.3.2 this is explored for (a) a p-SAF and (b) a GMR structure. The results confirm the first observations. The GMR sample with Ta (Si/SiO_2/Ta(5)/Ru(10)/Pt(2)/ML/Ru(0.4)/ML/Cu(2)/Free Layer (FL)/cap) has very well defined transitions. That is not the case for the GMR sensor without Ta but with a high deposition temperature of Pt in the seed layer (Si/SiO_2/Pt(10)@500 °C/ML/Ru(0.4)/ML/Cu(2)/FL/cap). The same is true for the p-SAF structure, which additionally shows a change in magnetization in between H_{in} and H_{out}, indicating instability. In conclusion, the lack of Ta can provide a similar H_{ex} but only a much smaller H_{in}^* and is therefore no alternative for this work.

4.3.3 Co layer thickness

Because of its importance, the Co layer thickness in the multilayer systems, discussed in sec. 4.2, is revisited in Fig. 4.3.3 for p-SAF structures with stack $[Co(t_{Co})/Pt(0.2)]_6/Co(t_{Co})/Ru(0.4)/[Co(t_{Co})/Pt(0.2)]_7$/cap. In sec. 4.2 the ideal Co thickness in the ML systems was found to be between $t_{Co} = 0.3$ and 0.5 nm. In Fig. 4.3.3 *M-H* hysteresis loops for p-SAFs and GMR samples show higher H_{ex} values for t_{Co} towards lower thicknesses, i.e. $t_{Co} = 0.3$ nm. This nominal thickness agrees well with the 0.24 nm to 0.3 nm used by Yakushiji et al. in their work on Co/Pt superlattices for p-SAFs [34, 35, 174, 180]. With H_{ex} values up to 10 kOe, their exchange fields for Co/Pt based single p-SAF structures rank among the highest found in the literature [35].

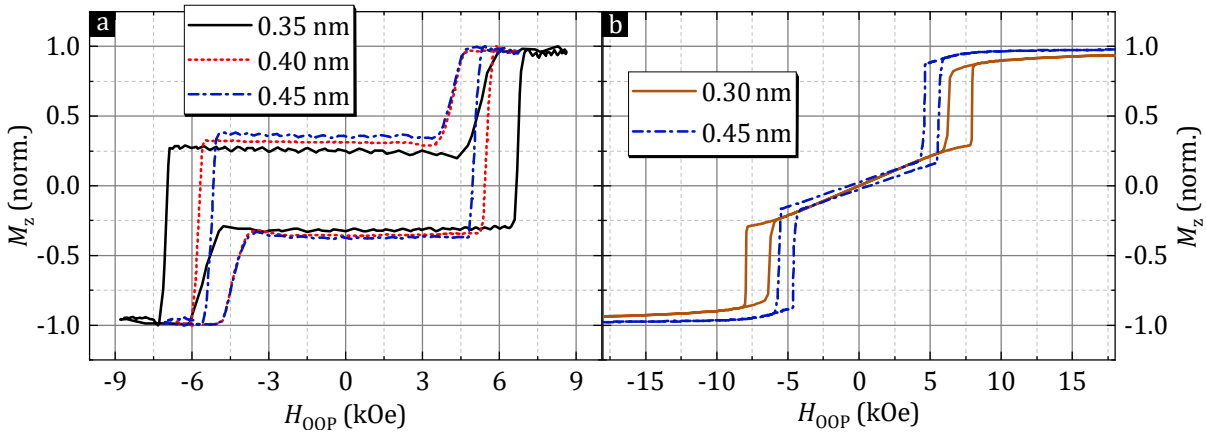

Fig. 4.3.3: Influence of Co thickness in ML systems for (a) p-SAFs in MOKE measurements and (b) GMR sensors in SQUID-VSM measurements. Lower Co thicknesses yield higher p-SAF exchange fields.

4.3.4 Ru spacer layer thickness

For all p-SAF and GMR samples in this work, the spacer layer material for interlayer exchange coupling is Ru. In most modern devices, the second rather broad IEC oscillation peak around 0.9 nm is used [74, 181–183]. In this work the slimmer first oscillation peak at around 0.4 nm is preferred [35, 179, 184, 185], which provides a stronger IEC. The advantage is presented in Fig. 4.3.4(a) and (b), where *M-H* hysteresis loops of a 0.4 nm p-SAF display a significantly

higher H_{ex} than a 0.9 nm sample. The stacks are seed/[Co(0.35)/Pt(0.2)]$_7$/Co(0.35)/Ru(t_{Ru})/[Co(0.35)/Pt(0.2)]$_7$/Co(0.35)/cap. However, due to the smaller range of suitable t_{Ru} around the first oscillation peak, the possible damage caused by interdiffusion at high post annealing temperatures is increased [35]. When the p-SAF structures of this work are used for reference systems in TMR sensors, post annealing for 1 h at 250 °C or higher is necessary for the crystallization of the CoFeB layers and MgO tunnel barrier [120,186–189]. Therefore, the post annealing performance for a sample with $t_{Ru} = 0.4$ nm is investigated, plotted in Fig. 4.3.4(b). After post annealing for 1 h at 260 °C at low Ar pressure, no change in magnetization behavior is apparent. Only for a post annealing temperature of 310 °C a slight decrease in H_{ex} becomes visible, with which H_{ex} is still significantly higher than that of the $t_{Ru} = 0.9$ nm sample in Fig. 4.3.4(a) and (b).

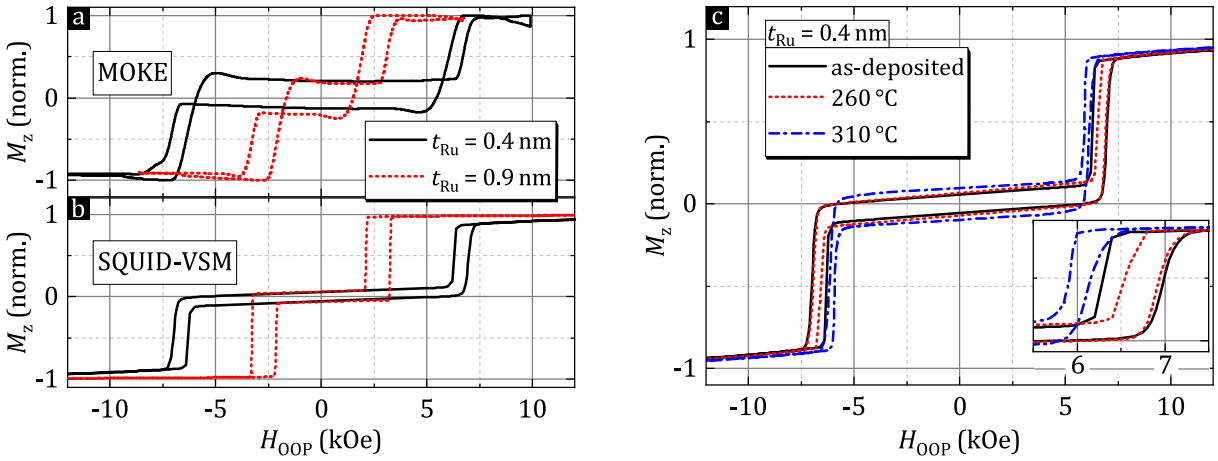

Fig. 4.3.4: (a) Polar MOKE and (b) SQUID-VSM hysteresis loops of p-SAFs with $t_{Ru} = 0.4$ nm and 0.9 nm. (c) *M-H* hysteresis loops (SQUID-VSM) for a $t_{Ru} = 0.4$ nm p-SAF after different states of post annealing.

To find the optimal Ru thickness in the fabrication process, two sample series are used to investigate the change of characteristic fields with t_{Ru}. In Fig. 4.3.5(a) the single p-SAFs are of the form ML/Ru(t_{Ru})/ML, which entails that Ru is sandwiched between a layer of Pt from the bottom ML and a layer of Co from the top ML. All characteristic field values, including H_{in}^*, peak at $t_{Ru} = 0.40$ nm, which is close to literature values, peaking at around $t_{Ru} = 0.45$ nm [35,175,179].

In Fig. 4.3.5(b) an additional Co layer was deposited on top of the first ML, so that Ru is now sandwiched between two Co layers. Furthermore, the t_{Ru} range was narrowed down to $t_{Ru} = 0.40$ nm ± 0.025 nm. The results show that characteristic fields are significantly higher with the additional Co layer, which is consistent with the results of model calculations that state energy band matching as a key factor for interlayer exchange coupling strength (see chapter 2.2). The maximum of the plot is not at exactly $t_{Ru} = 0.40$ nm, but, according to Fig. 4.3.5(b), at slightly lower nominal t_{Ru}. In a study by Yakushiji et al. [35], a shift towards higher t_{Ru} values with post annealing temperature, regarding optimized H_{ex} was found.

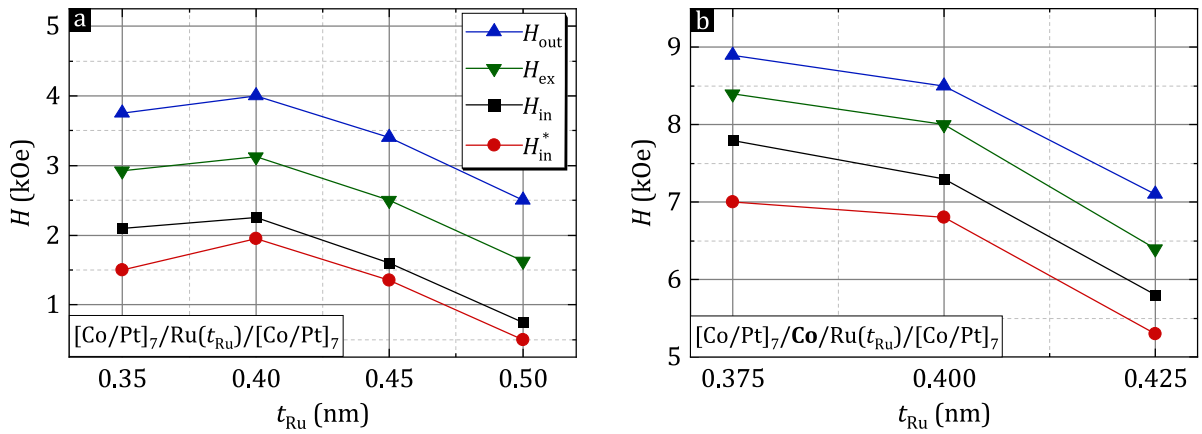

Fig. 4.3.5: Characteristic field analysis for p-SAFs of different Ru spacer layer thickness. (a) shows the results of a p-SAF with ML/Ru/ML configuration containing a Pt/Ru/Co stack, whereas (b) shows the results for a ML/Co/Ru/ML p-SAF. The MLs have the stack [Co(0.35)/Pt(0.2)]$_7$.

For this work, a nominal Ru thickness of 0.40 nm is chosen, which yields high H_{ex} fields and is slightly thicker than the optimal Ru thickness, providing a higher temperature stability [35].

4.3.5 Number of Co/Pt bilayers N

Finally, the reduction of bilayer number N can further increase H_{ex} of single p-SAF structures. The highest H_{ex} achieved in this work is that of a p-SAF with $t_{Co} = 0.3$ nm, $t_{Pt} = 0.2$ nm, $t_{Ru} = 0.4$ nm, and $N = 5$ with an additional Co(0.3) layer on top of each [Co/Pt] multilayer. At 300 K the p-SAF has an exchange field of $H_{ex} = 8.4$ kOe and at 4 K $H_{ex} = 9.2$ kOe. The M-H hysteresis loops are shown in Fig. 4.3.6 for these two temperatures. The linear increase of M is due to the in-plane free layer as the p-SAF is already embedded in a GMR structure. The full stack is Si/SiO$_2$/Ta(5)/Ru(10)/Pt(2)/[Co(0.3)/Pt(0.2)]$_5$/Co(0.3)/Ru(0.4)/[Co(0.3)/Pt(0.2)]$_5$/Co(0.3)/Cu(2)/FL/Pt(2)/Ta(5). The FL is of the structure [Co(1.5)/Pt(0.2)]$_3$.

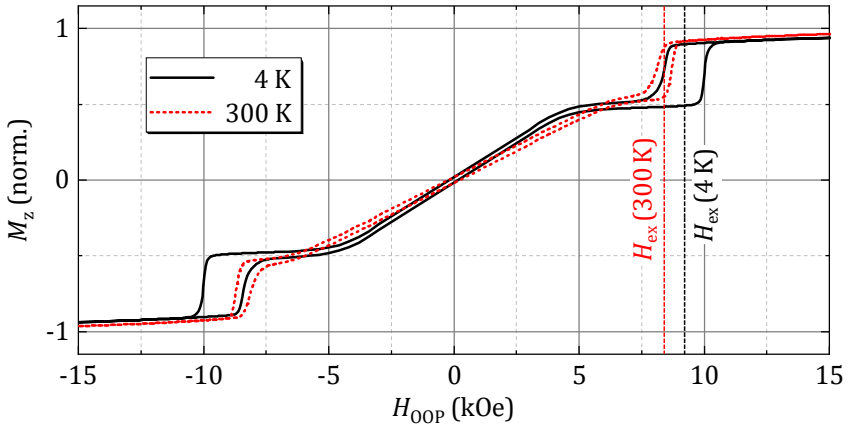

Fig. 4.3.6: M-H hysteresis loops of a GMR structure with p-SAF reference system of highest H_{ex} achieved in this work. Low temperatures further increase H_{ex}.

4.3.6 Double p-SAF structures

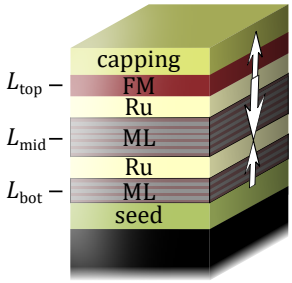

Fig. 4.3.7: Double p-SAF structure. The FM layer may be Co, CoFe or a Co/Pt ML.

In the following, the concept of double p-SAF structures is discussed and compared to simple single p-SAFs. For this purpose, the design of a double p-SAF structure (first shown in Fig. 4.1.1 in section 4.1) is presented again in Fig. 4.3.7 with additional details. Note the three magnetic layers L_{bot}, L_{mid} and L_{top}. In this work, the ferromagnetic material (FM) in L_{top} is either Co or CoFe. In Fig. 4.3.8(a) SQUID-VSM measurements show the M-H hysteresis loop of a single and a double p-SAF with the stacks seed/ML_7/Ru/ML_7/capping, and seed/ML_6/Ru/ML_9/Ru/FM/capping, respectively. The ML of the single p-SAF is of the form ML_7 = [Co(0.3)/Pt(0.2)]$_7$/Co(0.3). In the double p-SAF, the magnetic layers are ML_6 = [Co(0.3)/Pt(0.2)]$_6$/Co(0.3) and ML_9 = [Co(0.3)/Pt(0.2)]$_9$/Co(0.3) and FM = Co(1). All thicknesses are given in nm.

Noteworthy observations for the double p-SAF include the higher H_{ex} and a lower degree of magnetization saturation at H_{out}. Generally, double p-SAF structures yield a similar stability during the antiferromagnetic state, i.e. $-H_{in} < H < +H_{in}$, but require much higher fields to reach M_S. For example in the case of the p-SAFs shown in Fig. 4.3.8(a), magnetic saturation is reached at about 18 kOe for the single p-SAF, whereas the double p-SAF is not saturated below a magnetic field of 50 kOe.

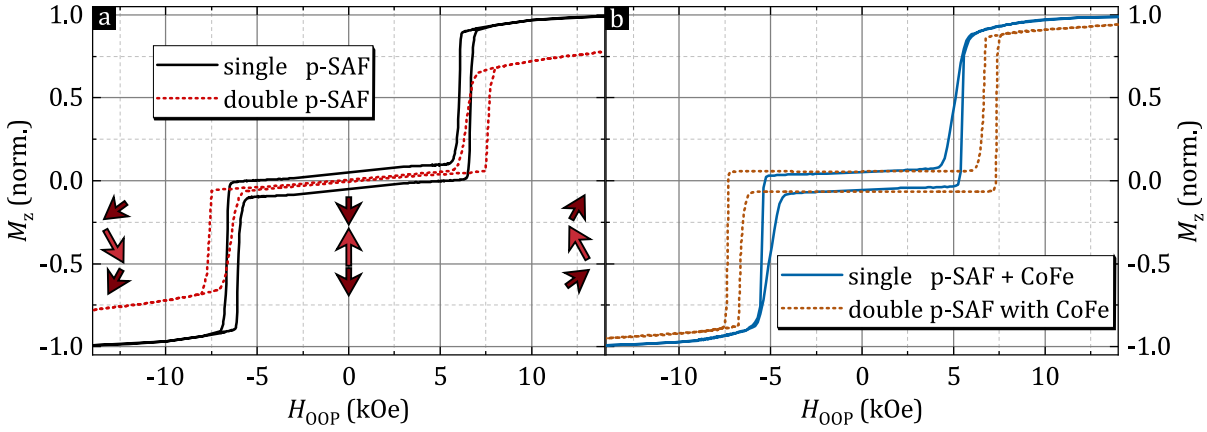

Fig. 4.3.8: M-H hysteresis loops (SQUID-VSM) of single and double p-SAFs. Structures in (a) only contain Co for the ferromagnetic material. Arrows illustrate the magnetization directions in the double p-SAF. (b) shows M-H hysteresis loops of a single p-SAF that couples to a CoFe(1) layer via exchange interaction, and a double p-SAF that couples to a CoFe(1) layer via interlayer exchange interaction.

Besides higher H_{ex}, another advantage of double p-SAFs is a stronger coupling to a CoFe layer. Figure 4.3.8(b) shows M-H hysteresis loops of a single and a double p-SAF, which both contain a CoFe layer as the top magnetic layer L_{top}. While the CoFe layer is coupled to the single p-SAF via exchange interaction, interlayer exchange coupling is used in the case of the double p-SAF. The respective stack structures are seed/ML_9/Ru/ML_6/CoFe(1)/capping, and seed/ML_6/Ru/

ML_9/Ru/CoFe(1)/capping. Generally, the CoFe layer destabilizes the p-SAFs since it has an in-plane effective magnetic anisotropy for 1 nm [190]. The motivation in coupling the p-SAFs to a CoFe layer lies in the high spin polarization. CoFe is routinely used in industrial GMR sensors to reach high GMR effects. In a research project by Fathoni et al. [107], a GMR effect of 40.5 % has been achieved using an epitaxially grown $Co_{50}Fe_{50}$/Cu/$Co_{50}Fe_{50}$ trilayer. The destabilization is much more pronounced in single p-SAFs than in double p-SAF structures. The double p-SAF in Fig. 4.3.8(b) yields significantly better defined transitions into the antiparallel alignment of layer magnetizations, a higher H_{ex}, and higher saturation fields than the single p-SAF. Possibly responsible for the latter observation are spin-canting effects, which are discussed later in more detail (chapter 4.3.8).

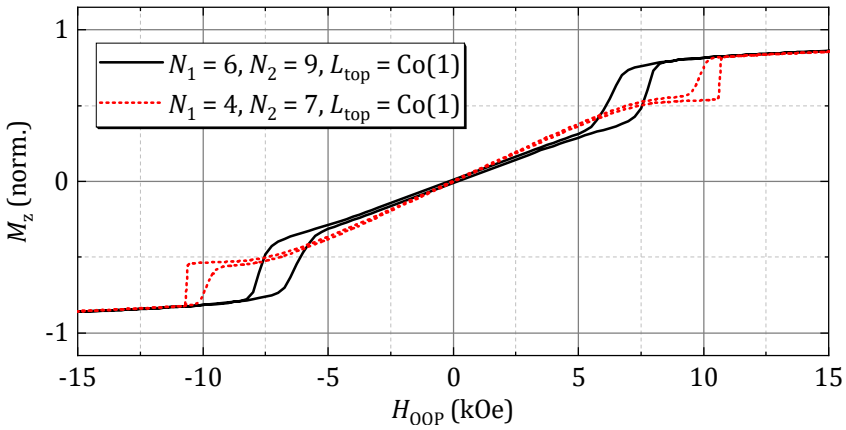

Fig. 4.3.9: *M-H* hysteresis loop of two GMR sensor structure with p-SAF reference systems with different N_1 and N_2 values. The structure with $N_1 = 4$, and $N_2 = 7$ yields the highest H_{ex} achieved for a double p-SAF structure in this work.

The numbers of Co/Pt bilayers for double p-SAFs N_1 and N_2 influence H_{ex} similarly as it was observed earlier for single p-SAFs in section 4.3.5. Here, N_1 denotes the number of bilayers in the multilayer in L_{bot}, and N_2 the number of bilayers in L_{mid}. The highest achieved H_{ex} value of this work for a double p-SAF sensor is $H_{ex} = 10.3$ kOe at room temperature. Like the best single p-SAF structure of this work, its thicknesses are $t_{Co} = 0.3$ nm, $t_{Pt} = 0.2$ nm, and $t_{Ru} = t_{Ru2} = 0.4$ nm. The bilayer numbers are $N_1 = 4$, $N_2 = 7$ with a Co(1 nm) layer as L_{top}. The *M-H* hysteresis loop is shown in Fig. 4.3.9 in comparison with a p-SAF structure of the same stack but with $N_1 = 6$, and $N_2 = 9$. Since both p-SAFs are already embedded in a GMR sensor stack, a linear change of M is visible due to the respective free layers. The full stacks are Si/SiO_2/Ta(5)/Ru(10)/Pt(2)/$[Co(0.3)/Pt(0.2)]_{N1}$/Co(0.3)/Ru(0.4)/$[Co(0.3)/Pt(0.2)]_{N2}$/Co(0.3)/Ru(0.4)/Co(1)/Cu(2)/FL/Pt(2)/Ta(5).

4.3.7 Double p-SAF switching behavior

While an approximate equilibrium of magnetic moments in a single p-SAF is simply achieved by designing the top and bottom multilayer with the same or similar layer thicknesses and layer repetitions, double p-SAF designs require more balancing to avoid magnetization reversal events. Some investigation is necessary in particular for double p-SAFs with CoFe as L_{top}.

For design examples, Fig. 4.3.10 shows double p-SAFs with different numbers of Co(0.3)/Pt(0.2) bilayers N_1 and N_2 in L_{bot} and L_{mid}, respectively, as well as different CoFe thicknesses t_{CoFe} in L_{top} with $t_{\mathrm{CoFe}} = 1.0$ and 1.5 nm. A well balanced double p-SAF is shown as the solid black line with $N_1 = 6$, $N_2 = 9$, and $t_{\mathrm{CoFe}} = 1.0$ nm. Increasing the CoFe thickness to 1.5 nm, shown as a dashed red line, doesn't significantly change the value of H_{ex}, but adds a continuous change of magnetization throughout the field sweep, indicating the occurrence of spin-canting. Additionally, the saturation field is strongly increased. Finally, an example for an imbalanced p-SAF is plotted as a dashed-dotted blue line with $N_1 = 9$, $N_2 = 6$, and $t_{\mathrm{CoFe}} = 1.0$ nm. While H_{ex} is very high at about 12.5 kOe, there is also a magnetization reversal at $H_{\mathrm{SF}} = 1.8$ kOe, drastically reducing the dynamic range for GMR sensor applications.

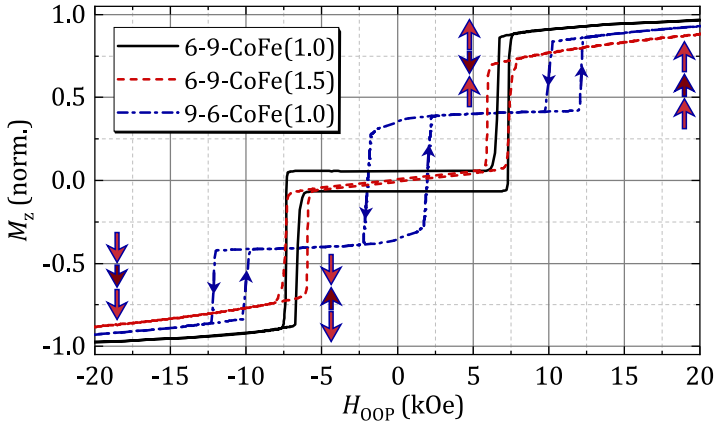

Fig. 4.3.10: M-H hysteresis loops of double p-SAF structures with different balancing of magnetic moments in L_{bot}, L_{mid} and L_{top}. A change in magnetic moment is achieved by choosing $N_1 = 6$ and $N_2 = 9$ (black and red line) or $N_1 = 9$ and $N_2 = 6$ (blue line) and by changing the CoFe layer thickness in L_{top}. Arrows denote the magnetization directions of the magnetic layers in the unbalanced sample with $N_1 = 6$ and $N_2 = 9$ (blue line).

Depending on the magnetic moments within the double p-SAF structures, either L_{mid} or the outer layers, L_{bot} and L_{top}, switch first. The difference is shown in Fig. 4.3.11, where two consecutively fabricated double p-SAF GMR sensors yield a different switching behavior due to a change of $M_{\mathrm{S}}t_{\mathrm{ML}}$ in L_{mid} by design, with t_{ML} being the total film thickness of the ML. This increase of $M_{\mathrm{S}}t_{\mathrm{ML}}$ is achieved by using a higher number of Co/Pt bilayers $N_2 = 9$ instead of $N_2 = 8$ [34] (see Fig. 4.2.5(b)). In both cases, $N_1 = 6$ and $L_{\mathrm{top}} = \mathrm{Co}(1)$. In Fig. 4.3.11(a) it is visible that the total magnetization reversal and the underlying magnetization profile is similar for both samples, however, with the difference of the $N_2 = 9$ sample showing a significantly higher hysteresis width ΔH, which is here defined as the field difference of p-SAF switching fields H_{in} and H_{out}.

A further difference emerges in the comparison of GMR transfer curves in Fig. 4.3.11(b). While the results for GMR sensor measurements are discussed in section 4.5 in more detail, the GMR effect is already used here as a tool for the investigation of p-SAF structures. In a magnetoresistance measurement, the GMR effect denotes the relative change of the samples resistance R in an out-of-plane external magnetic field H_{OOP} with

$$GMR(\%) = 100 \times \frac{R(H_{\mathrm{OOP}}) - R_{\mathrm{min}}}{R_{\mathrm{min}}}, \tag{4.2}$$

where R_{min} is the minimum resistance within the measurement range.

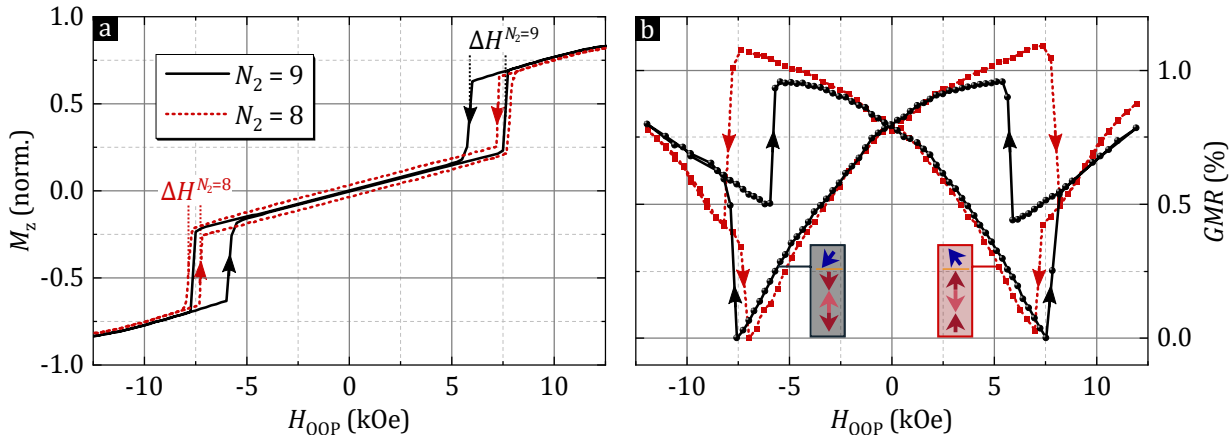

Fig. 4.3.11: (a) M-H hysteresis loops of two double p-SAF GMR sensors with $N_1 = 6$ and $N_2 = 9$ (solid black line) or $N_2 = 8$ (dotted red line). $L_{\mathrm{top}} = \mathrm{Co}(1)$. Arrows indicate the sweep direction. (b) Corresponding GMR transfer curves with illustrations of the layers' magnetization directions.

The GMR transfer curves of the two samples reveal different switching behaviors in the GMR measurements shown in Fig. 4.3.11(b). In a sweep from positive to negative fields, the $N_2 = 8$ sample of lower L_{mid} magnetization jumps from a spin-canted state (discussed in the next section 4.3.8) into a configuration of low GMR, with L_{top} and L_{bot} dominating the p-SAF, pointing parallel to the external magnetic field, and L_{mid} pointing antiparallel (see illustration of magnetization in the right inset). Towards smaller and eventually negative fields, the GMR increases as the FL magnetization rotates into an antiparallel alignment with L_{top}. For the $N_2 = 9$ sample the opposite p-SAF behavior occurs, with L_{mid} dominating the p-SAF, leading to a decrease of GMR in a field sweep from positive to negative fields (magnetization directions illustrated in the left inset).

4.3.8 Spin-canting effects

In previously shown M-H hysteresis loops of single and particularly double p-SAF structures, it was observed that the samples' magnetization at fields above H_{out} is still far away from full saturation. For example, the normalized magnetization at 8 kOe for the single p-SAF structure in Fig. 4.3.8(a) is $M_{\mathrm{z}}/M_{\mathrm{S}}(8\,\mathrm{kOe}) = 0.80$, while for the double p-SAF it is only $M_{\mathrm{z}}/M_{\mathrm{S}}(8\,\mathrm{kOe}) = 0.69$. The reason for this is that the macroscopic spins of the magnetic layers enter a spin-canted state, in which the externally applied field only partially overcomes the interlayer exchange coupling between the MLs or, in case of the double p-SAF, between L_{bot}, L_{mid} and L_{top}, before reaching full magnetic saturation. To further investigate this hypothesis, the GMR effect is used again as an indicator for the top magnetic layer in single and double p-SAF structures. Figure 4.3.12 shows GMR measurements and M-H hysteresis loops of GMR sensors with a single p-SAF structure in the reference system in Fig. 4.3.12(a) and a double p-SAF structure in Fig. 4.3.12(b). In both cases the magnetic free layer is designed to saturate at fields lower than H_{in} (free layer magnetic anisotropy will be further discussed in section 4.5). The GMR measurements agree with the assumption of spin-canting effects, taken from M-H hysteresis loops. In the following, the results are discussed, starting from positive field saturation.

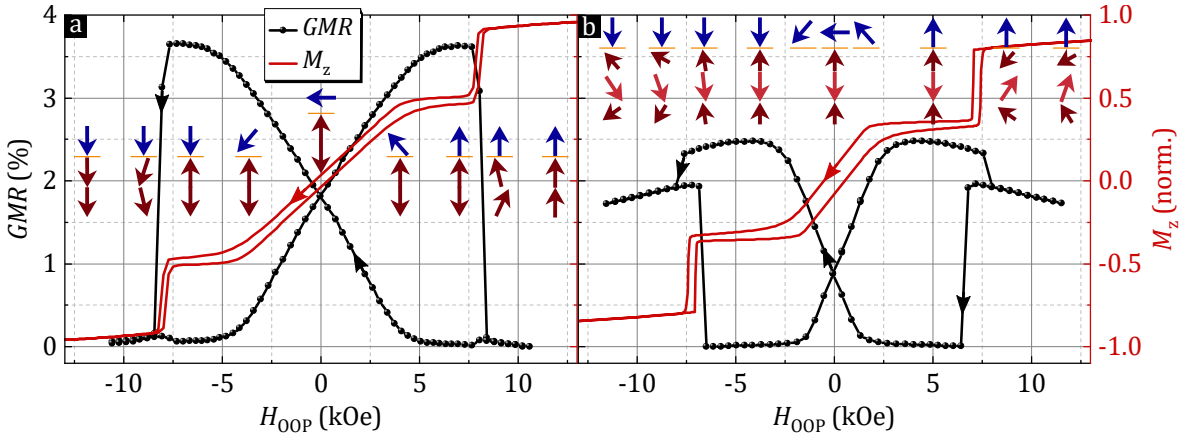

Fig. 4.3.12: GMR and M-H hysteresis loops for a (a) single p-SAF GMR sensor and a (b) double p-SAF GMR sensor. Arrows along the transfer curves indicate the magnetic sweep direction. Stacked red arrows indicate the magnetization of the respective p-SAF layer, while the blue arrow above the orange line (representing the Cu layer) indicates the magnetization direction of the magnetic free layer.

In Fig. 4.3.12(a), M_{z} at 11 kOe is already close to M_{S}, namely $0.94M_{\mathrm{S}}$. Therefore, it can be assumed that the magnetization directions of the single p-SAF layers and the free layer are in approximate parallel alignment and magnetoresistance is low. This is indeed the case with GMR values at ± 11 kOe being around 0 %, i.e. the lowest values of the measurement cycle. Slightly lower values at even higher external fields are likely, but is limited by the available field range of the used measurement equipment. As the external field decreases, spin-canting increases, increasing slightly the GMR. At $H_{\mathrm{in}} = 7.5$ kOe, the GMR decreases again, which shows that the top p-SAF layer moved from a canted to a parallel alignment with the free layer. As H_{OOP} further decreases, the free layer rotates along its magnetic hard axis, and the GMR increases. The linear change of the GMR from +5 kOe to −5 kOe matches the linear change in M_{z} very

well. Note that the GMR measurement does not show the magnetic soft phase from the sample edges discussed earlier in this chapter in section 4.3.1. When the antiferromagnetic state of the p-SAF is overcome by the external field at $H_{\mathrm{out}} = -8\,\mathrm{kOe}$, the GMR rapidly decreases, indicating a change from antiparallel to nearly parallel alignment of magnetic reference and free layer.

The *M-H* hysteresis loop of the double p-SAF GMR structure in Fig. 4.3.12(b) is qualitatively similar to the one of the single p-SAF GMR structure, whereas the GMR transfer curve displays significant differences. This difference can be explained by strong spin-canting effects in the double p-SAF reference system. At 11 kOe, $M_{\mathrm{z}}/M_{\mathrm{S}}$ has a value of only 0.8 and the GMR is unexpectedly high (1.7 %) – higher even than at zero field (0.9 %). Therefore, the double p-SAF must be canted so strongly that the magnetization direction of L_{top} is tilted in a more antiparallel than parallel alignment with the free layer, as illustrated with the arrows in Fig. 4.3.12(b). With decreasing H_{OOP} spin-canting and GMR increase further. At $H_{\mathrm{in}} = 7\,\mathrm{kOe}$, the magnetization direction of the free layer and L_{top} become parallel and the GMR drops to its minimum. When the free layer magnetization rotates between +2 kOe and −4 kOe, the GMR increases to 2.5 %. The differing field values of 2 kOe and 4 kOe, and the fact that $GMR(0\,\mathrm{kOe}) < GMR^{\mathrm{max}}/2$, stem from magnetic hysteresis in the free layer, which is also visible in the *M-H* hysteresis loop. After the free layer reaches magnetization saturation at around −4 kOe, the GMR decreases towards −7.5 kOe. Since the free layer magnetization is already saturated, this change in GMR must originate in small spin-canting of the p-SAF reference system, as it was also seen in *M-H* hysteresis loops of p-SAFs in Fig. 4.3.8. At $H_{\mathrm{out}} = -7.5\,\mathrm{kOe}$, the double p-SAF becomes heavily spin-canted again and the GMR drops. Interestingly, the maximum GMR effect (2.5 %) is significantly smaller than that of the single p-SAF GMR structure (3.6 %). Because of the higher thickness of the double p-SAF, the resistance at the Cu layer, which is subject to the GMR effect, accounts for a smaller part of the total resistance in comparison to the resistance at the Cu layer of single p-SAF structure. Another possible reason for the smaller GMR ratio is the typically thick L_{mid} in the double p-SAF and its impact on the spin direction, since the spin-diffusion lengths of the materials above L_{mid} (Ru and Co) are several nanometers larger than their thicknesses in the Ru interlayer and in L_{top} [106, 191–193]. This might lead to a smaller spin-polarization in double p-SAF GMR structures.

In order to confirm these findings and to unravel the underlying reversal processes, micromagnetic simulations are carried out and discussed in the next chapter.

4.3.9 Micromagnetic simulations on p-SAF structures

The content of the following section is the result of a collaboration with Christoph Vogler and Dieter Suess (Faculty of Physics, University of Vienna; Christian Doppler Laboratory for Advanced Magnetic Sensing and Materials), and has been published in [194].

	L_{bot}	L_{mid}	L_{top}
K_{eff} (Merg/cm^3)	4.49	4.49	−0.01
M_{S} (kemu/cm^3)	1.43	1.15	1.75
A_{ex} (µerg/cm)	1.00	1.00	1.00
J_{iex} (erg/cm^2)	−2.5	−2.5	
α	1.00	1.00	1.00
a (Å)	10	10	10
t (Å)	33	43	10

Table 4.3.1: Material parameters of the simulated double p-SAF systems for all involved layers. K_{eff} is the effective magnetic anisotropy constant, M_{S} is the saturation magnetization, A_{ex} is the bulk exchange constant within the layers, J_{iex} is the interface exchange coupling between the layers, α is the dimensionless damping constant, a is the lateral side length of the simulated nanorod and t is the thickness of the layers.

To understand the experimentally obtained magnetization reversal processes in Figs. 4.3.10–4.3.12, and the corresponding GMR transfer curve of Fig. 4.3.12, the finite-element software package magnum.fe [195] was used to simulate the field dependence of the magnetization of the introduced p-SAF systems and GMR sensors by means of a spin-chain model. This model consists of a nanorod with a square basal plane of side length $a = 10$ Å and a discretization length in x and y of also 10 Å. Along the easy-axis direction (z direction) the model uses the given nominal thicknesses of the ferromagnetic material with discretization lengths of the individual layers (L_{bot}, L_{mid}, L_{top}). The reference material parameters are based on the experimental data and are summarized in Table 4.3.1. For simplicity, temperature fluctuations are disregarded.
In the micromagnetic simulations single ferromagnetic layers with the properties of the p-SAF multilayers are computed. The modeling is started with a positive external saturation field of 30 kOe with all layers pointing in the +z direction. The field is applied with an angle of 5° with respect to the easy axis to avoid metastable states. Then, the magnetic field magnitude is decreased stepwise in −0.5 kOe increments to −30 kOe and back to +30 kOe. After each field-step the micromagnetic state of the system is relaxed for 100 ns. The variation of the applied field in the modeling work is performed much faster than that used during the acquisition of the measurement data. However, because a high damping constant ($\alpha = 1.0$) is used in the modeling work, a stationary state is obtained within 100 ns, such that the modeled M-H loops are representative for the experimental ones.
In the following a systematic analysis of the influences of the most important parameters for the double p-SAF structures are presented to uncover the layer magnetizations' impact on differing switching behavior, as seen experimentally in Figs. 4.3.10–4.3.11 (paragraph 4.3.7). Starting from the experimental data of the saturation magnetization of the layers, M_{S} of L_{top} is varied in the

range of 1.19 kemu/cm^3 to 1.95 kemu/cm^3 as well as M_S of L_{mid} in the range of 0.88 kemu/cm^3 to 1.39 kemu/cm^3, while keeping the properties of L_{bot} constant. In both cases a step size of $\Delta M_S = 0.02$ kemu/cm^3 is used.

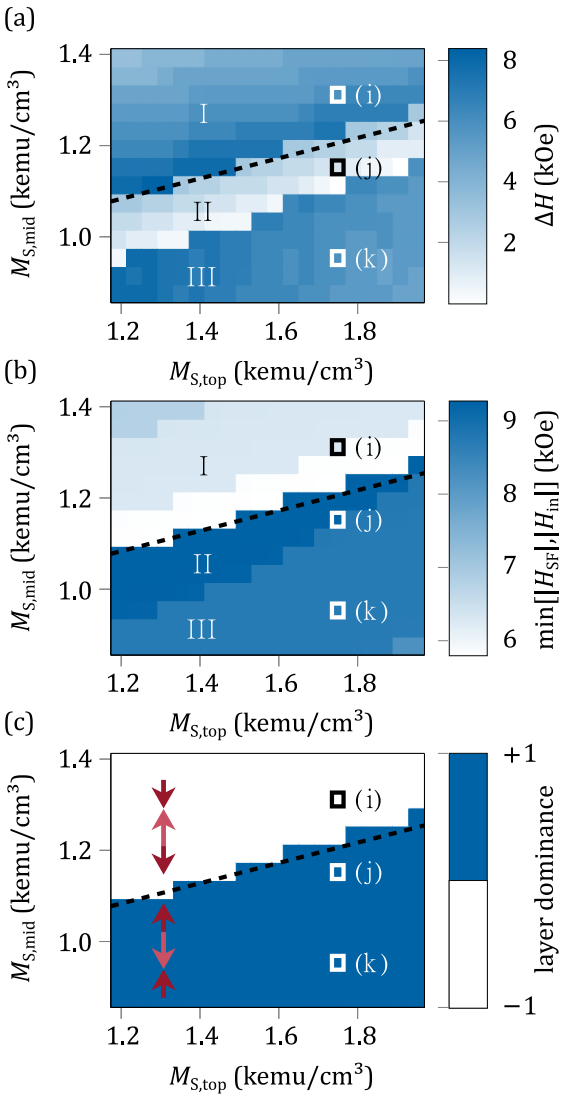

Fig. 4.3.13: Characteristic properties of the hysteresis loops of the double p-SAF system for variations of the saturation magnetizations of the top and the middle p-SAF layer. All material parameters that are not varied are taken from Tab. 4.3.1. The properties are (a) the hysteresis loop width ΔH, (b) the linear range of the sensor stack defined as min[$|H_{SF}|$, $|H_{in}|$] and (c) the layer dominance with respect to the external field. The arrows illustrate the meaning of the dominance by showing the reversal mechanism of the layers for a decreasing external field coming from positive saturation. The dashed line illustrates the border between the regions of dominance.

Figure 4.3.13 displays three interesting properties of the resulting hysteresis loops, namely the hysteresis width ΔH, the linear range, which is defined as min[$|H_{SF}|$, $|H_{in}|$] (see Fig. 4.3.1), and the layer dominance of the p-SAF with respect to the external field. As shown in the inset of Fig. 4.3.13(c), a value of -1 means that, when coming from (positive field) saturation, the top layer switches into an antiparallel direction with respect to the external magnetic field, while a value of $+1$ means that the middle layer switches, which leaves the top layer magnetization direction and external field in a parallel configuration. In contrast to Fig. 4.3.13(b) and (c) three regions appear (labeled with I, II and III) in the minor loop hysteresis width of Fig. 4.3.13(a). While the border between regions I and II is identical to that of Fig. 4.3.13(c), it is not a priori clear why there is an additional border between regions II and III. To gain deeper insights into the magnetization behavior, three phase points of Fig. 4.3.13 are investigated in more detail. Figure 4.3.14 illustrates the hysteresis loops of phase points (i), (j) and (k). In detail, the normalized magnetization of the full double p-SAF is shown in the first column and that of L_{mid} is shown in the last column. To lower the complexity of the system L_{top} and L_{bot} are reduced to a single layer with the following properties:

$$\begin{aligned} K_{eff,red} &= \frac{K_{eff,top}t_{top} + K_{eff,bot}t_{bot}}{t_{top} + t_{bot}} \\ M_{S,red} &= \frac{M_{S,top}t_{top} + M_{S,bot}t_{bot}}{t_{top} + t_{bot}} \end{aligned} \tag{4.3}$$

This reduction implicitly assumes a parallel alignment of L_{top} and L_{bot}, which is not strictly true at least during the reversal.

But this simplified picture is much more instructive and most importantly it is sufficient to characterize the magnetization reversal correctly.
In the middle column of Fig. 4.3.14 the dynamics of this reduced layer is displayed. A typical hysteresis loop for region I in Fig. 4.3.13 with high $M_{S,mid}$ and low $M_{S,top}$, and thus low $M_{S,red}$ is shown in Fig. 4.3.14(i). In agreement with Fig. 4.3.13(c), it can be seen that L_{mid} dominates the magnetization process. Hence, the switching field of L_{mid} determines the outer part of the hysteresis loop (vertical line with label H_{out} in Fig. 4.3.14) and the field at which the reduced p-SAF layer switches back to an antiparallel state determines the inner part of the hysteresis loop (vertical line with label H_{in} in Fig. 4.3.14). Since the switching fields are inversely proportional to the saturation magnetization, an increase of H_{in} is observed for lower values of $M_{S,top}$ at fixed $M_{S,mid}$ in Fig. 4.3.13(a). This results in an increasing linear range and a decrease of ΔH.

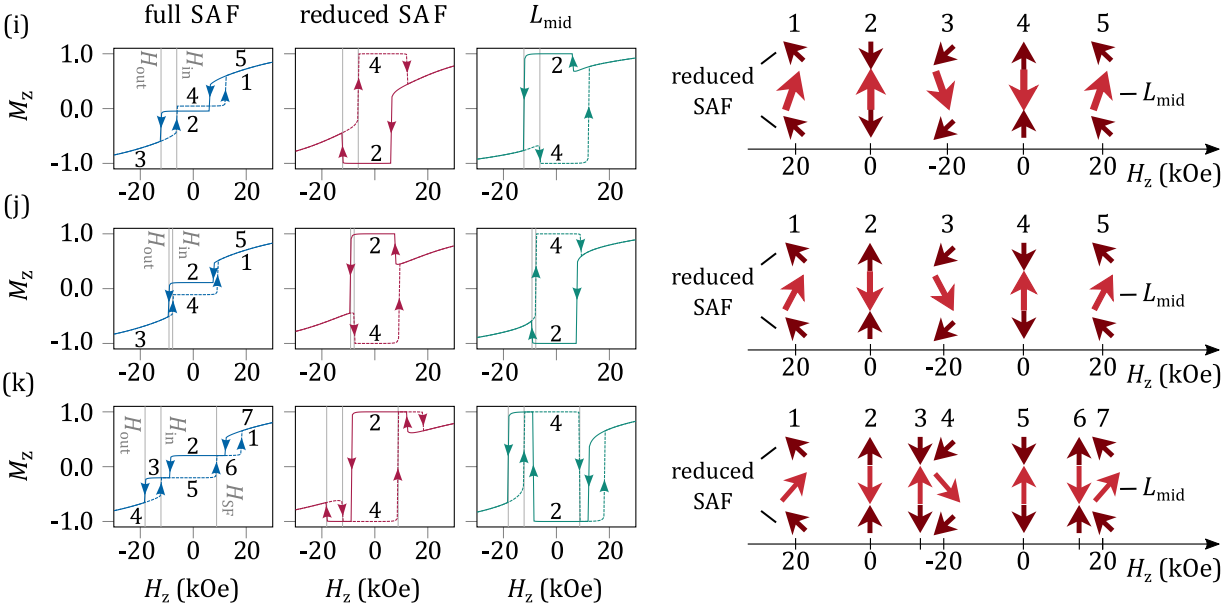

Fig. 4.3.14: Normalized z component of the magnetization of the full double p-SAF system, the middle p-SAF layer L_{mid} and a reduced p-SAF layer as introduced in Eq. 4.3. (i), (j) and (k) refer to the phase points marked in Fig. 4.3.13. The vertical lines indicate the switching fields H_{in} and H_{out} and the magnetization reversal (state-flip) field H_{SF} (introduced in Fig. 4.3.1). The arrows on the right illustrate the magnetization directions at the respective magnetic fields, as numbered in the hysteresis loops.

If $M_{S,mid}$ decreases from 1.31 kemu/cm^3 to 1.11 kemu/cm^3 and the saturation magnetization of the reduced layer remains fixed, one arrives at phase point (j) and the hysteresis loops of Fig. 4.3.14(j). Here, the reduced p-SAF layer is dominating the reversal. Since it has a higher magnetic moment its switching field H_{out} is much lower than that of L_{mid} in region I. It is slightly higher than the backswitching field H_{in} of L_{mid} resulting in a very small ΔH. Due to the change of dominance H_{in} is now determined by L_{mid}. Hence, the linear range in region II is significantly higher than that in region I. The effect of the decrease of $M_{S,mid}$ from region I to region II can also be clearly seen experimentally in the SQUID-VSM measurements of Fig. 4.3.11, where the decrease is caused by changing the layer numbers in L_{mid}. For even lower $M_{S,mid}$ an abrupt increase of ΔH in Fig. 4.3.13(a) can be observed. The reason is illustrated in Fig. 4.3.14(k). At the switching field of the dominating reduced p-SAF layer a magnetization reversal occurs.

The reason is that the switching field of L_{mid} is much larger than that of the reduced layer. Therefore, the reduced layer becomes dominant after the magnetization reversal and determines both the fields H_{out} and H_{in}. Also this change in ΔH is observed in the experimentally acquired Fig. 4.3.11.

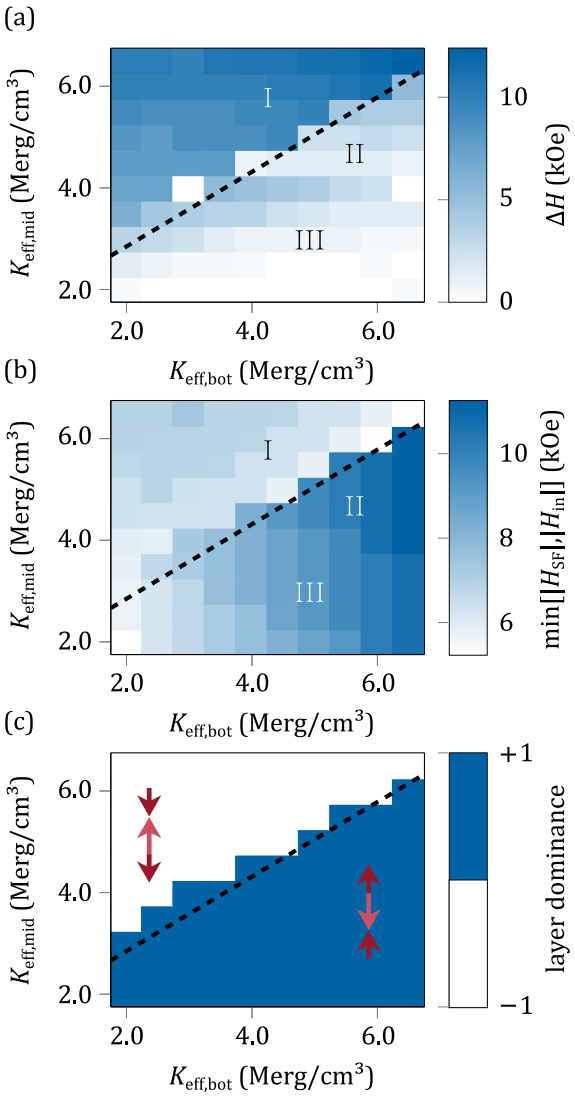

Fig. 4.3.15: Characteristic properties of the hysteresis loops of the double p-SAF system for variations of the effective magnetic anisotropy of the top and the middle p-SAF layer. All material parameters that are not varied are taken from Tab. 4.3.1. The properties are (a) the hysteresis loop width ΔH, (b) the linear range of the sensor stack defined as $\min[|H_{\mathrm{SF}}|, |H_{\mathrm{in}}|]$ and (c) the layer dominance with respect to the external field. The arrows illustrate the meaning of the dominance by showing the reversal mechanism of the layers for a decreasing external field coming from positive saturation.

But not only the saturation magnetization has an influence on the hysteresis of the double p-SAF. In the following the variation of the effective magnetic anisotropies of the bottom and the middle layer with fixed $K_{\mathrm{eff,top}} = -0.01\,\mathrm{Merg/cm^3}$ is discussed.

Figure 4.3.15 displays the hysteresis loop width, the linear range and the layer dominance for K_{eff} of both layers in the range of $1.99\,\mathrm{Merg/cm^3}$ to $6.49\,\mathrm{Merg/cm^3}$ with steps of $0.5\,\mathrm{Merg/cm^3}$. Again, three regions appear that represent the same types of hysteresis loops as those in Fig. 4.3.13. In region I, L_{mid} dominates the reversal process under an applied magnetic field, while in regions II and III the reduced p-SAF layer dominates. Region II again shows magnetization reversal processes. Figure 4.3.15 again proves that the magnetic anisotropy is as important as the saturation magnetization of the individual layers if one wants to describe the reversal mechanism of the double p-SAF.

In the following, spin-canting effects, which were experimentally observed in Fig. 4.3.12, are investigated using micromagnetic simulations. For the double p-SAF GMR structure, the parameters are summarized in Tab. 4.3.1. Single p-SAF GMR structure parameters are given in Tab. 4.3.2. For simplicity the free layer magnetization is not simulated. Instead it is modeled with a generic tanh function, where the thickness, the saturation field and the saturation magnetization of the free layer are chosen according to the measured sensor stacks (see Fig. 4.3.12).

To qualitatively model the GMR [105] from the simulated hysteresis loops, an enclosed magnetization angle γ is used of the free layer and the top p-SAF layer per:

$$\mathrm{GMR}^{\ddagger} = 1 - \cos(\gamma). \tag{4.4}$$

With the spin-chain model and the material parameters of Tab. 4.3.1 and 4.3.2, an excellent qualitative agreement with the measurements in both the magnetization data as well as in the GMR data is obtained, as illustrated in Fig. 4.3.16. The spin-canting of the p-SAF layers obtained from the simulations also agrees well with that extracted from the GMR measurements of Fig. 4.3.12.

	L_{bot}	L_{top}
K_{eff} (Merg/cm^3)	3.49	3.99
M_{S} (kemu/cm^3)	1.15	1.35
A_{ex} (µerg/cm)	1.00	1.00
J_{iex} (erg/cm^2)	-2.5	
α	1.00	1.00
a (Å)	10	10
t (Å)	28	29

Table 4.3.2: Material parameters of the simulated single p-SAF system for all involved layers.

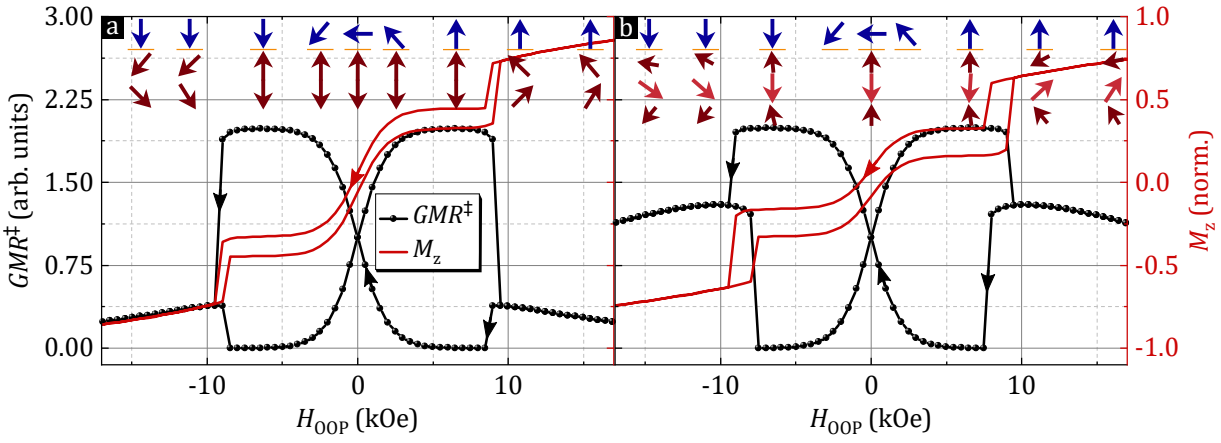

Fig. 4.3.16: Micromagnetic simulations of GMR and magnetization for a (a) single p-SAF GMR sensor and a (b) double p-SAF GMR sensor. Arrows along the transfer curves indicate the magnetic sweep direction. Stacked red arrows show the simulated magnetization of the respective p-SAF layer, while the blue arrow above the orange line (representing the Cu layer) shows the magnetization direction of the magnetic free layer.

4.3.10 Summary

In this chapter, fabrication parameters of p-SAF structures were systematically varied to optimize the p-SAF's performance, which was characterized by its switching behavior and its exchange field H_{ex}. First, it was shown that a Ta seed layer is needed to achieve well defined p-SAF reversal, even though substituting the Ta seed layer with a Pt layer deposited at a high deposition temperature of 500 °C yields a similar H_{ex}. A variation of the Co thickness t_{Co} in the multilayers revealed that smaller thicknesses in the previously found preferable range of $0.3\,\text{nm} \leq t_{Co} \leq 0.5\,\text{nm}$ (from the multilayer investigation in section 4.2.2) yield the highest H_{ex} values. A nominal thickness of $t_{Co} = 0.3\,\text{nm}$ approaches the 0.24 nm used by Yakushiji et al. in their work on Co/Pt superlattices for p-SAFs [34,35,174]. In further agreement, it was found that the first Ru interlayer exchange coupling (IEC) peak around $t_{Ru} = 0.4\,\text{nm}$ yields significantly higher H_{ex} than the second peak around $t_{Ru} = 0.9\,\text{nm}$. Stacks of Co/Ru/Co sandwiches show stronger coupling than Pt/Ru/Co stacks. Furthermore, the structure of double p-SAFs was explored, which generally yields higher exchange fields than single p-SAFs. A graphical summary of the p-SAF optimization is given in Fig. 4.3.17.

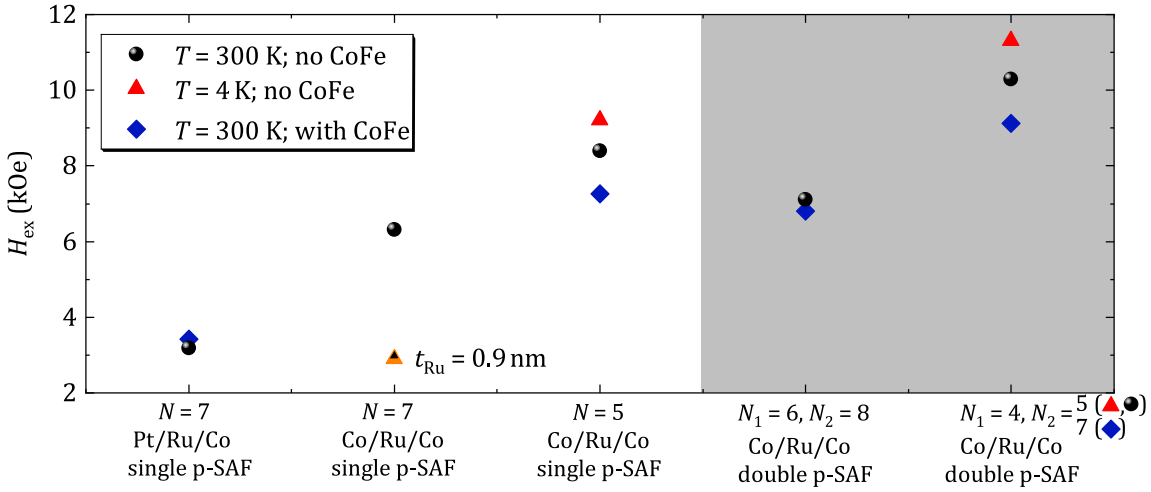

Fig. 4.3.17: Summary of the most important steps for the p-SAF optimization process. CoFe is used in GMR sensor structures for high spin polarization but add instability to the p-SAF structure due to its in-plane magnetic anisotropy. $t_{Ru} = 0.4\,\text{nm}$ if not stated otherwise.

While double p-SAFs show higher H_{ex}, they also require greater external fields for saturation. Related to this, the magnetic reversal process was investigated, focusing on spin-canting effects in the p-SAF magnetic layers. The magnetoresistance of GMR sensors with single and double p-SAFs was measured, where double p-SAFs show unexpected GMR transfer curves that can be explained by spin-canting effects. Micromagnetic simulations confirm the strong spin-canting and further disclose phase diagrams for the characteristics of the magnetic reversal process with regard to individual layer saturation magnetization M_S and effective magnetic anisotropy K_{eff}.

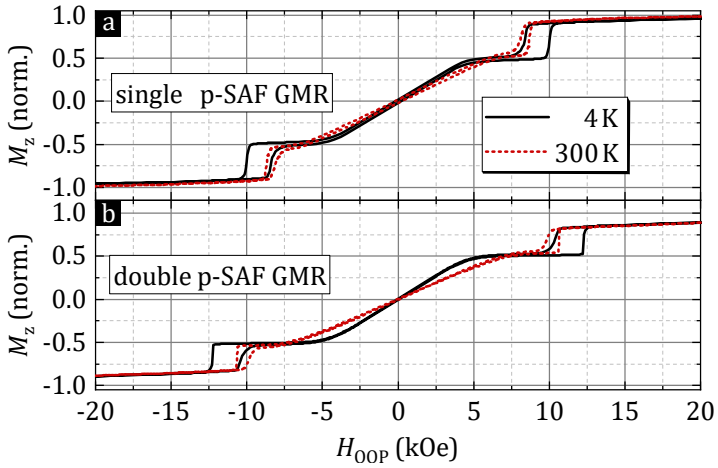

Fig. 4.3.18: *M-H* hysteresis loops of a (a) single and (b) double p-SAF GMR structure with the highest exchange fields achieved in this work.

Besides establishing a general understanding of the influences at hand, one goal of this chapter was the development of a p-SAF reference system for magnetoresistance (xMR) sensors that yields a range of several kOe in which the p-SAF shows a stable antiferromagnetically coupled behavior. To that end, single p-SAFs up to $H_{ex} = 8.4\,\text{kOe}$ at room temperature and 9.2 kOe at 4 K were developed, as well as double p-SAFs up to $H_{ex} = 10.3\,\text{kOe}$ at room temperature and 11.3 kOe at 4 K. Respective *M-H* hysteresis loops are presented in Fig. 4.3.18.

4.4 Magnetoresistance effects in p-SAFs

At this point, it has become evident that the GMR effect at the RL/Cu/FL sandwich is the overwhelmingly dominant feature of the magnetoresistance for GMR structures in this work (see for instance Fig. 4.3.12). Nevertheless, it is expected that there is also a GMR effect at the Ru interface [82] of the p-SAF structure as well as an AMR effect for any ferromagnetic layer present. The AMR effect in Pt/Co/Pt sandwiches has been a subject of recent research, as discussed in chapter 2.3.3.1, with the resistivity given by [133]

$$\rho(\varphi,\theta) = \rho_\mathrm{t} + \Delta\rho_\mathrm{ip}\sin^2\theta\cos^2\varphi + \Delta\rho_\mathrm{op}\cos^2\theta. \tag{4.5}$$

Here, θ denotes the angle between the magnetization direction and the out-of-plane axis, and φ the angle between the in-plane component of the magnetization and the current direction. The out-of-plane and in-plane contributions are defined as

$$\Delta\rho_\mathrm{op} = \rho_\mathrm{p} - \rho_\mathrm{t} \tag{4.6}$$

and

$$\Delta\rho_\mathrm{ip} = \rho_\mathrm{l} - \rho_\mathrm{t}, \tag{4.7}$$

where ρ_p denotes the resistivity at $\theta = 0°$ (polar), ρ_t at $\theta = 90°$ with $\varphi = 90°$ (transverse), and ρ_l at $\theta = 90°$ with $\varphi = 0°$ (longitudinal). The contributions of the AMR effect to a Co/Pt based p-SAF, as well as the GMR effect in such a p-SAF, however, have not yet been investigated. Using different field geometries, these effects will be studied in this chapter. An illustration of the relevant angles for the AMR and GMR effect is given in Fig. 4.4.1(a) and (b), respectively.

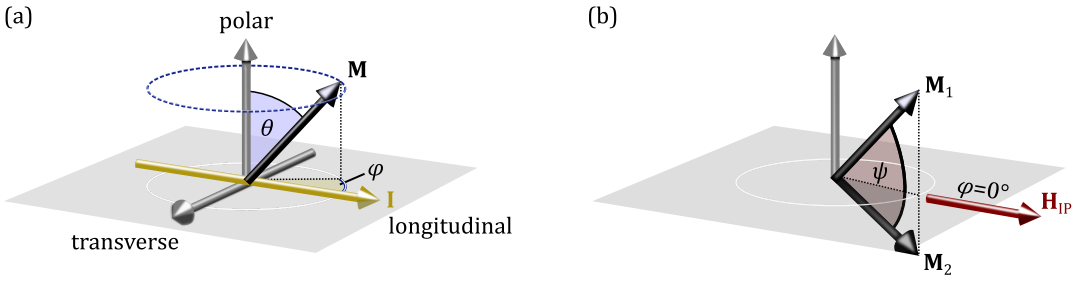

Fig. 4.4.1: Illustrations of vectors and angles for the magnetization **M** of Co/Pt multilayers with perpendicular magnetic anisotropy. (a) The AMR effect depends on the magnetization angle θ to the polar axis, as well as the angle φ between the projection of **M** to the sample plane and the current **I**. (b) The GMR effect depends on the angle ψ, which is the angle of magnetizations between neighboring multilayers in a p-SAF structure.

4.4.1 Magnetoresistance effects in [Co/Pt] multilayer systems

Before p-SAFs are measured, magnetoresistance effects in a Co/Pt multilayer – the essential building block of the p-SAFs – need to be understood. The magnetoresistance in a PMA multilayer is determined by the direction of the current **I** and the direction of the magnetization **M**

(among other factors). The latter is given by the sample's effective magnetic anisotropy and the applied field **H**. There are three distinct configurations:

(i) $\mathbf{H}_{\mathrm{IP}} \perp \mathbf{I}$,

(ii) $\mathbf{H}_{\mathrm{IP}} \parallel \mathbf{I}$, and

(iii) $\mathbf{H}_{\mathrm{OOP}}$, which is orthogonal to any in-plane current direction.

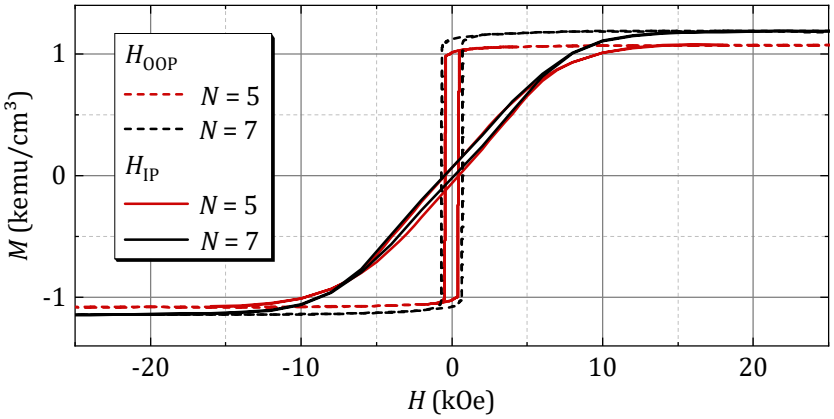

Fig. 4.4.2: M-H hysteresis loops for $[\mathrm{Co}(0.3)/\mathrm{Pt}(0.2)]_N$ multilayer samples in in-plane and out-of-plane fields at 300 K.

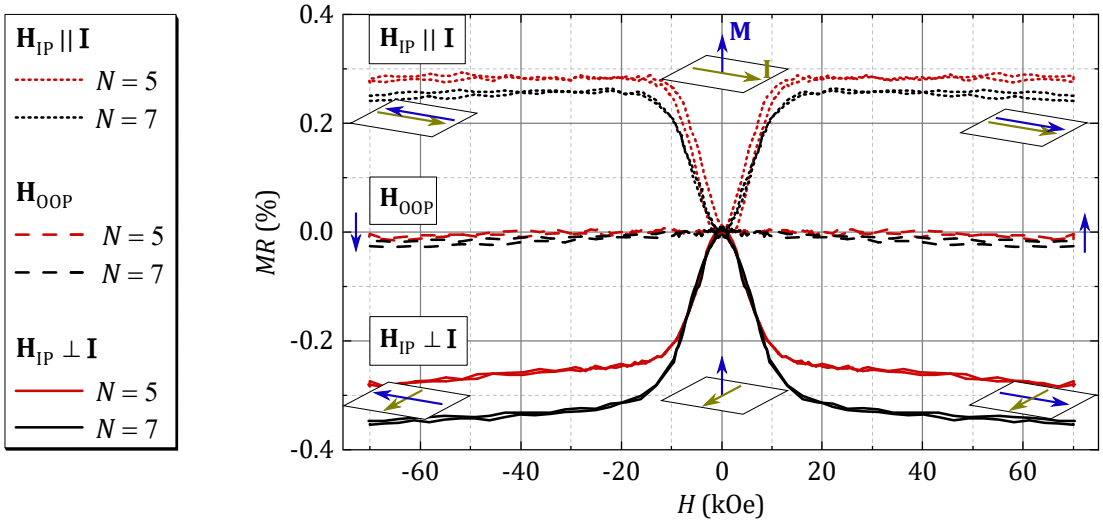

Fig. 4.4.3: Magnetoresistance measurements for two $[\mathrm{Co}(0.3)/\mathrm{Pt}(0.2)]_N$ multilayer samples in different field-to-current configurations at 300 K. At zero field, the magnetization points along the polar direction ($\theta = 0°$). Depending on the current direction, the applied in-plane field forces the magnetization in a longitudinal or transverse geometry with the current, yielding a resistivity increase and decrease, respectively.

M-H hysteresis loops for a $[\mathrm{Co}(0.3)/\mathrm{Pt}(0.2)]_5$ and $[\mathrm{Co}(0.3)/\mathrm{Pt}(0.2)]_7$ multilayer are shown in Fig. 4.4.2. The corresponding magnetoresistance measurements are plotted in Fig. 4.4.3. In the following, the MR effects from case (i) and case (ii) are distinguished as $MR_{\perp}$ and $MR_{\parallel}$, respectively. At zero field, the magnetization is directed out-of-plane ($\theta = 0°$). In accordance

with Philippi-Kobs et al. [133], the resistivity at zero field is here referred to as polar resistivity ρ_p. In case (iii), the magnetization direction stays out-of-plane, i.e. perpendicular to **I**, for any field strength. Since there is no GMR spacer layer, no significant magnetoresistance is measured, as expected. For the other two field configurations, the direction of **M** changes with field strength. At magnetization saturation (here reached at around ±15 kOe), the magnetization is either in a transverse state (i) $\mathbf{M} \perp \mathbf{I}$ or in a longitudinal state (ii) $\mathbf{M} \parallel \mathbf{I}$. Accordingly, the resistivities at in-plane magnetization saturation are the longitudinal resistivity ρ_l and transverse resistivity ρ_t. Note that, in order to project an accurate comparison, here the magnetoresistance MR is not necessarily defined by its change from the minimum resistivity, but from the resistivity at zero field, i.e. ρ_p, thus

$$MR(H) = \frac{\Delta\rho(H)}{\rho} = \frac{\rho(H) - \rho_\mathrm{p}}{\rho_\mathrm{p}}. \tag{4.8}$$

The results in Fig. 4.4.3 agree with the expectation for the anisotropic magnetoresistance effect in Co/Pt multilayers [133]. $MR_{||}$ increases until saturation magnetization is reached, with maximum values $MR_{||} = 0.29\,\%$ for the $N = 5$ multilayer and $MR_{||} = 0.26\,\%$ for the $N = 7$ multilayer. On the other hand, $MR_\perp$ decreases, yielding in this case a higher amplitude for $N = 7$. At magnetization saturation, the values for $MR_\perp$ are around $MR_\perp = -0.24\,\%$ for the $N = 5$ multilayer and $MR_\perp = -0.32\,\%$ for the $N = 7$ multilayer. With further increasing magnetic field strengths, the $MR_\perp$ continues to linearly decrease. Since this continuing decrease is relatively small (approx. $-0.45 \times 10^{-3}\,\%$/kOe) and occurs above magnetic saturation fields, it is likely related to another magnetoresistance effect, e.g. *s-d* Mott scattering [202].

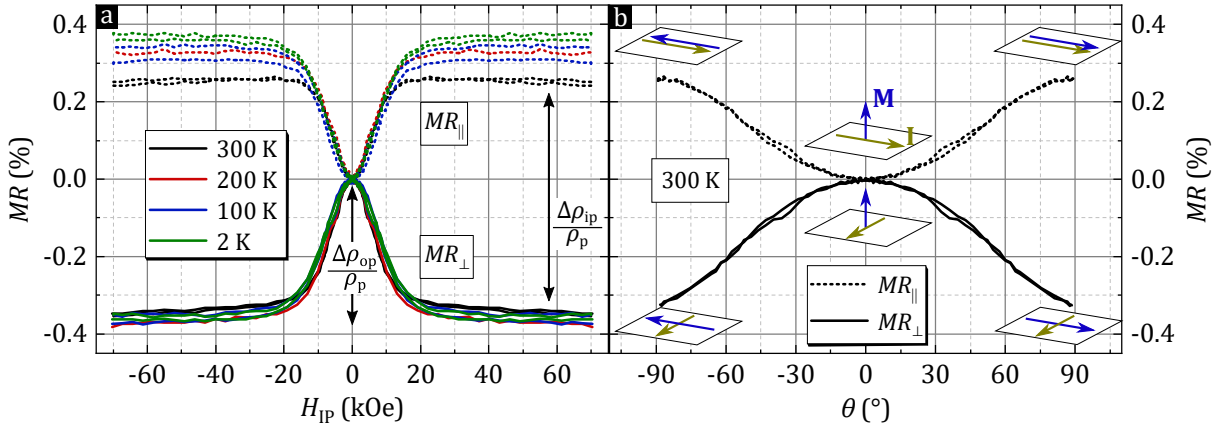

Fig. 4.4.4: AMR measurements in a field sweep with fixed field direction. (a) MR for various temperatures as a function of H_IP. (b) 300 K measurement mapped onto the polar angle θ using H_IP, Eq. 4.9, and data from an M-H in-plane hysteresis loop. The results show the expected $\sin^2$ and $\cos^2$ behavior for the longitudinal and transverse measurement, respectively.

Figure 4.4.4(a) shows exemplary the temperature dependent magnetoresistance for the $[\mathrm{Co}(0.3)/\mathrm{Pt}(0.2)]_7$ sample. While lower temperatures increase the amplitude for $MR_{||}$, no significant influence can be observed for $MR_\perp$. In Fig. 4.4.4(b) the 300 K measurement is mapped onto the change of the polar angle θ between **M** and the out-of-plane axis. This is achieved by taking the

in-plane M-H hysteresis loop from Fig. 4.4.2 and using the trigonometric relation

$$\sin\theta\,(H_{\mathrm{IP}}) = \frac{M_{\mathrm{IP}}\,(H_{\mathrm{IP}})}{M_{\mathrm{S}}}. \tag{4.9}$$

The change in resistivity fits the phenomenological description of AMR, given in Eq. 4.5, very well. $\Delta\rho/\rho$ follows the expected $\sin^2\theta$ function on the longitudinal ($\varphi = 0°$) path and the $\cos^2\theta$ function on the transverse ($\varphi = 90°$). With Eqs. 4.6 and 4.7 for $\Delta\rho_{\mathrm{op}}$ and $\Delta\rho_{\mathrm{ip}}$ one can calculate the relative change in resistivity for the $[\mathrm{Co}(0.3)/\mathrm{Pt}(0.2)]_7$ sample with [133]

$$MR_{\mathrm{op}} = \frac{\Delta\rho_{\mathrm{op}}}{\rho_{\mathrm{p}}} = 0.32\,\% \tag{4.10}$$

and

$$MR_{\mathrm{ip}} = \frac{\Delta\rho_{\mathrm{ip}}}{\rho_{\mathrm{p}}} = 0.58\,\% \tag{4.11}$$

for $T = 300\,\mathrm{K}$. This leads to the ratio $\Delta\rho_{\mathrm{op}}/\Delta\rho_{\mathrm{ip}} = 0.57$ (for the $[\mathrm{Co}(0.3)/\mathrm{Pt}(0.2)]_5$ sample, $\Delta\rho_{\mathrm{op}}/\Delta\rho_{\mathrm{ip}} = 0.45$). While direct comparison to the literature is limited, a measurement series by Philippi-Kobs et al. [131, 133] for a $\mathrm{Pt/Co}(t_{\mathrm{Co}})\mathrm{/Pt}$ sandwich suggests agreeable values. Their results are shown in the inset of Fig. 2.3.8(c).

For the majority of this chapter, the differentiation between a polar to transverse and polar to longitudinal field sweep is more relevant than comparing MR_{op} to MR_{ip}. Therefore, the following expressions for the AMR contributions are introduced:

$$A_{\perp} = \frac{\rho_{\mathrm{p}} - \rho_{\mathrm{t}}}{\rho_{\mathrm{p}}} = MR_{\mathrm{op}} \tag{4.12}$$

$$A_{||} = \frac{\rho_{\mathrm{l}} - \rho_{\mathrm{p}}}{\rho_{\mathrm{p}}} = MR_{\mathrm{ip}} - MR_{\mathrm{op}}. \tag{4.13}$$

Thus, for the $N = 7$ ML above at 300 K one obtains

$$A_{\perp} = 0.32\,\%,\ A_{||} = 0.26\,\%. \tag{4.14}$$

To verify the AMR behavior of the sample, rotational measurements have been conducted. Note that with a maximum field of $H = 10\,\mathrm{kOe}$ at the available setup, in-plane magnetization saturation cannot be reached for this measurement. Therefore, even though the geometry for in-plane measurements is set to an angle $\theta' = 90°$ between $\mathbf{H}$ and the out-of-plane axis, the maximum θ between $\mathbf{M}$ and out-of-plane axis is only around 65° (calculated from in-plane M-H hysteresis loops). The rotational measurement in-plane is shown in Fig. 4.4.5(a) with $\varphi = \angle\,(\mathbf{M}_{\mathrm{ip}}, \mathbf{I})$. The measurement data adequately follows the expected $\cos^2\varphi$ fit.

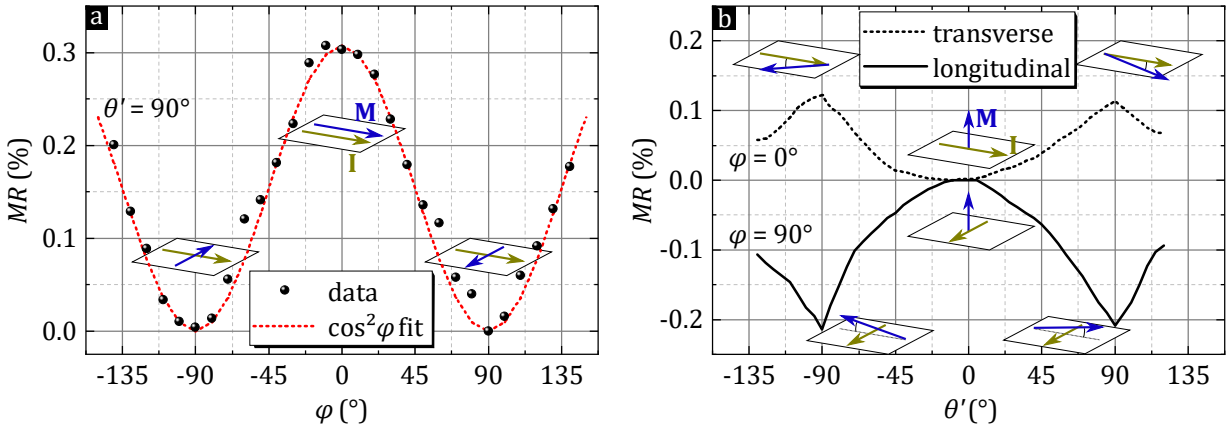

Fig. 4.4.5: Rotational measurements of a $[Co(0.3)/Pt(0.2)]_7$ multilayer in a magnetic field of 10 kOe. (a) In-plane rotation with set $\theta' = 90°$. (b) Rotation from an out-of-plane field ($\theta' = \theta = 0°$) to in-plane field ($\theta' = 90° \neq \theta$). Switching features at ±90° are attributed to the unsaturated in-plane magnetization.

The AMR effect amplitude is around 0.3 %, and thus smaller than the $MR_{ip} = 0.58\,\%$ previously measured in Fig. 4.4.4(a). This is due to the applied field of 10 kOe not fully saturating the in-plane magnetization. Figure 4.4.5(b) shows the rotation of θ', similar to Fig. 4.4.4(b), but with fixed field strength. Again, the $\sin^2\theta'$ behavior is observed for $\varphi = 0°$ and $\cos^2\theta'$ for $\varphi = 90°$. However, this time also a sudden change is observed at $\theta' = \pm 90°$. The reason is once more the limited field strength: At $\theta' = +90°$ an out-of-plane field component is still present with $\theta = +65°$. Therefore, when $\theta' = +90°$ is passed, the out-of-plane magnetization component will not smoothly transition, but instead jumps into the position of $\theta = 180° - 65° = 115°$ (i.e. the magnetization is never fully in-plane).

4.4.2 Magnetoresistance in a single p-SAF

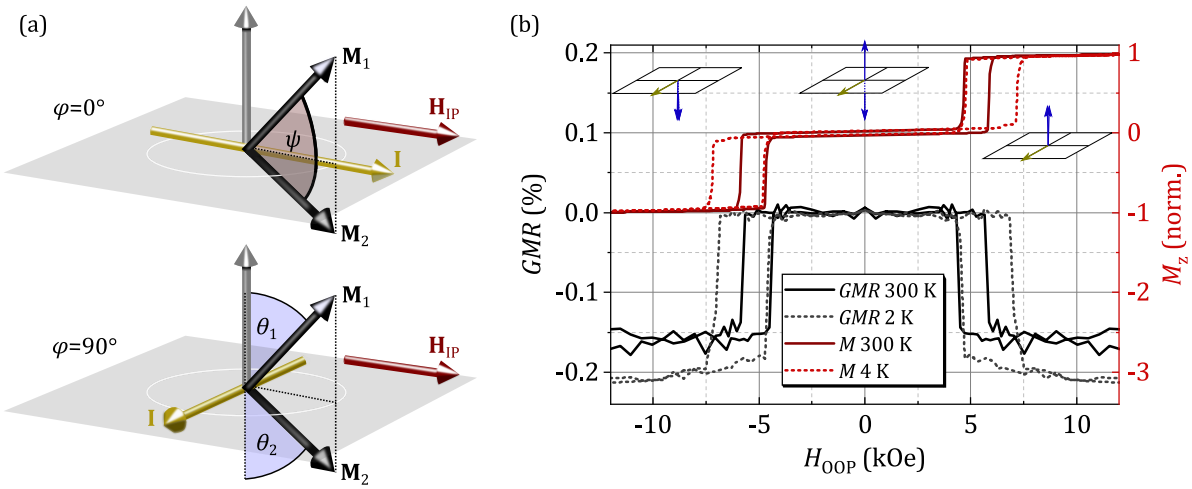

Fig. 4.4.6: (a) Vector geometries for a single p-SAF structure in an in-plane field. The current direction is either perpendicular ($\varphi = 90°$) or parallel ($\varphi = 0°$) to the applied in-plane field. (b) GMR and M-H hysteresis loops of a p-SAF with $[Co(0.3)/Pt(0.2)]_7$ multilayers in an out-of-plane field sweep. Switching fields in GMR and magnetization are in good agreement.

With the expansion to a single p-SAF structure of the form seed/[Co(0.3]/Pt(0.2)]$_7$/Co(0.3)/Ru(0.4)/[Co(0.3]/Pt(0.2)]$_7$/cap, it is essential to be aware of the angles between relevant vectors. Figure 4.4.6(a) shows a schematic of a single p-SAF structure with two ferromagnetic layers of magnetization $\mathbf{M}_1$ and $\mathbf{M}_2$. ψ is the angle between these magnetization vectors. Due to the antiferromagnetic interlayer exchange coupling, $\psi = 180°$ at zero field. At saturated magnetization, $\psi = 0°$, i.e. parallel alignment. Note that ψ is the relevant angle for GMR contributions. When an in-plane field is applied, $\mathbf{M}_1$ and $\mathbf{M}_2$ will rotate away from the out-of-plane axis by the angles θ_1 and θ_2, respectively. As before, the in-plane component of the magnetization and the current direction form the angle φ, with φ being either 0° or 90°, depending on the current direction set by an electric switchboard. The angles θ and φ determine the AMR contributions. An out-of-plane field sweep should produce only a GMR contribution, as no other significant MR effect is expected for the multilayer sample. This is indeed the case, as presented in Fig. 4.4.6(b), showing the GMR and out-of-plane magnetization M_z for low temperature and room temperature. The switching fields H_{in} and H_{out} from magnetization and GMR measurement are in good agreement. Low temperatures of 2 K increase the value of H_{out} and of the GMR signal from approx. -0.16 % at 300 K to -0.2 %. Note that the magnetoresistance is set to 0 % at zero field to simplify the comparison of GMR and AMR effect as well as the mathematical addition of the two effects.

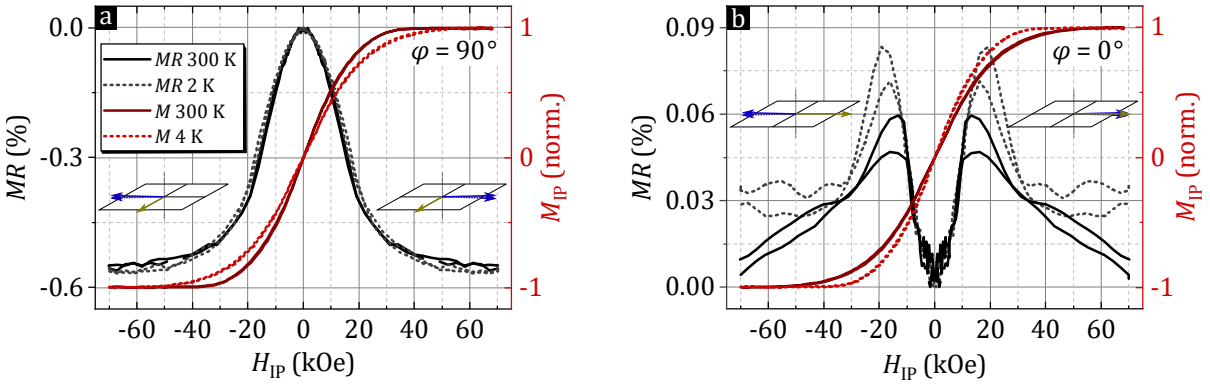

Fig. 4.4.7: In-plane field sweeps for a single p-SAF with [Co(0.3)/Pt(0.2)]$_7$/Co(0.3) multilayers. Depending on the field direction yielding either (a) $\varphi = 90°$ or (b) $\varphi = 0°$. The magnetoresistance of GMR and respective AMR contribution add up or subtract each other.

In-plane field sweeps are a subject to both GMR and AMR contributions simultaneously. The results are presented in Fig. 4.4.7(a) and (b) for $\mathbf{M}_{IP} \perp \mathbf{I}$ ($\varphi = 90°$) and $\mathbf{M}_{IP} \parallel \mathbf{I}$ ($\varphi = 0°$), respectively. In the case of $\mathbf{M}_{IP} \perp \mathbf{I}$, the resistance of the system drops by approx. 0.55 % in a somewhat bell-shaped curve. While lower temperatures don't affect the MR amplitude, the curve is slightly widened as saturation magnetization is reached at higher fields. In the case of $\mathbf{M}_{IP} \parallel \mathbf{I}$ in Fig. 4.4.7(b), the MR amplitude is strongly diminished to only 0.08 %. After a parabolic increase in MR as a function of field, the resistance decreases again for fields above approx. 17 kOe. For low temperatures the result is very similar with the only difference of the resistance decreasing slightly earlier, which overall leads to a smaller maximum magnetoresistance.

4.4.3 A simple model to describe magnetoresistance in p-SAF systems

While understanding the out-of-plane field measurement is straightforward to interpret as GMR effect of the Co/Ru/Co trilayer, the in-plane measurements require a discussion in more detail. To construct a very simple model for p-SAFs with any number of Ru spacer layers N_{Ru}, the following assumptions are made with regard to the geometries given in Fig. 4.4.6(a):

1. The contributions of GMR and AMR effect to the total magnetoresistance are a matter of simple addition
2. $|\varphi| = 0° \wedge 90°$
3. $\theta := \theta_1 = \theta_2 = ... = \theta_{N_{\mathrm{Ru}}+1}$
   $\psi := \psi_1 = \psi_2 = ... = \psi_{N_{\mathrm{Ru}}}$
4. $\hat{G} := -GMR(M_{\mathrm{S}}^{\mathrm{OOP}}) = -GMR(M_{\mathrm{S}}^{\mathrm{IP}})$, i.e. the GMR amplitude $\hat{G}$ from out-of-plane GMR measurements can be used to model in-plane transfer curves

Using the definitions for $\Delta\rho_{\mathrm{op}}$ and $\Delta\rho_{\mathrm{ip}}$ (Eqs. 4.6, 4.7), the phenomenological description of the AMR resistivity (Eq. 4.5) can be rewritten as follows:

$$\begin{aligned}
\rho(\varphi,\theta) &= \rho_{\mathrm{t}} + \Delta\rho_{\mathrm{ip}} \sin^2\theta \cos^2\varphi + \Delta\rho_{\mathrm{op}} \cos^2\theta \\
&= \rho_{\mathrm{t}} \left(1 - \sin^2\theta\cos^2\varphi - \cos^2\theta\right) + \rho_{\mathrm{l}} \sin^2\theta\cos^2\varphi + \rho_{\mathrm{p}} \cos^2\theta \\
&= \rho_{\mathrm{t}} \sin^2\theta \left(1 - \cos^2\varphi\right) + \rho_{\mathrm{l}} \sin^2\theta\cos^2\varphi + \rho_{\mathrm{p}} \left(1 - \sin^2\theta\right) \\
&= -\left[(\rho_{\mathrm{p}} - \rho_{\mathrm{t}}) + (\rho_{\mathrm{t}} - \rho_{\mathrm{l}})\cos^2\varphi\right] \sin^2\theta + \rho_{\mathrm{p}}
\end{aligned}$$

Insertion into this chapter's definition of magnetoresistance (Eq. 4.8) and using the expressions of $A_\perp$ and $A_{||}$ (Eqs. 4.12, 4.13) yield

$$\begin{aligned}
AMR(\varphi,\theta) &= \frac{\rho_{\mathrm{p}} - \rho(\varphi,\theta)}{\rho_{\mathrm{p}}} \\
&= \left[A_\perp - \left(A_{||} + A_\perp\right)\cos^2\varphi\right] \sin^2\theta
\end{aligned} \tag{4.15}$$

The GMR effect is calculated as [105]

$$GMR(\psi) = -\hat{G}\,(1 + \cos\psi)\,/2 = -\hat{G}\cos^2\frac{\psi}{2}. \tag{4.16}$$

With the first assumption, adding the AMR effect to the GMR effect, the total magnetoresistance can be written as

$$\begin{aligned}
MR(\varphi,\theta,\psi) &= AMR(\varphi,\theta) + GMR(\psi) \\
&= \left[A_\perp - \left(A_{||} + A_\perp\right)\cos^2\varphi\right] \sin^2\theta - \hat{G}\cos^2\frac{\psi}{2}
\end{aligned} \tag{4.17}$$

Using the second assumption of $\varphi = 0° \wedge \pm 90°$, the two cases for $\mathbf{M}_{\mathrm{IP}} \parallel \mathbf{I}$ and $\mathbf{M}_{\mathrm{IP}} \perp \mathbf{I}$ directly follow from Eq. 4.17 with

$$MR_{||}(\theta, \psi) = AMR_{||}(\theta) + GMR(\psi) = -A_{||} \sin^2 \theta - \hat{G} \cos^2 \frac{\psi}{2} \tag{4.18}$$

$$MR_{\perp}(\theta, \psi) = AMR_{\perp}(\theta) + GMR(\psi) = A_{\perp} \sin^2 \theta - \hat{G} \cos^2 \frac{\psi}{2} \tag{4.19}$$

Using Eqs. 4.18 and 4.19 to model the magnetoresistance still requires a short discussion of the parameters and variables in these equations. For the GMR term, $\hat{G}$ is known from out-of-plane GMR measurements. Even though $A_{||}$ and $A_{\perp}$ are unknown, their approximate size is known as well, measured for multilayer structures in Fig. 4.4.4 ($N = 5$: $A_{||} = 0.29\,\%$, $A_{\perp} = 0.24\,\%$; $N = 7$: $A_{||} = 0.26\,\%$, $A_{\perp} = 0.32\,\%$). In an appropriate fit, their values should be in that vicinity.
This leaves the choice for θ and ψ. With regard to the geometry of the measurement, as shown in Fig. 4.4.6(a), it is tempting to further simplify Eqs. 4.18 and 4.19 by expressing ψ with $\psi = 180° - 2|\theta|$. This, however, would be an oversimplification, rendering the model attempted inaccurate. It can already be seen by considering the results for $MR_{||}(\theta, \psi)$ in Fig. 4.4.7(b). With an angle $\tilde{\theta}$, defined by $\psi = 180° - 2|\tilde{\theta}|$, Eq. 4.18 can be written as

$$MR_{||}\left(\theta, \tilde{\theta}\right) = -A_{||} \sin^2 \theta - \hat{G} \cos^2 \left(90° - \tilde{\theta}\right) = -A_{||} \sin^2 \theta - \hat{G} \sin^2 \tilde{\theta}. \tag{4.20}$$

If $\tilde{\theta} = \theta$ were used, the expression for $MR_{||}$ would become $-(A_{||} + \hat{G}) \sin^2 \theta$, which does not match the experimental results. In consequence, ψ and θ have to be chosen independently. This necessity is likely to arise from this model's third assumption of equal angles $\theta_{1 \ldots N_{\mathrm{Ru}}+1}$ and equal angles $\psi_{1 \ldots N_{\mathrm{Ru}}}$. Experimentally, however, a perfect balance of magnetic moments is not possible to achieve. In-plane field exposure therefore leads to (slightly) different angles towards the film plane surface, meaning $\theta_1 \neq \theta_2$. With that differentiation it follows that also the AMR amplitudes need individual parametrization, i.e. $A_{||,1} \neq A_{||,2} \neq A_{\perp,1} \neq A_{\perp,2}$, which further complicates the treatment of the system. Instead, the here used simple model does not account for differences between the individual layers, but sufficiently compensates this by the independent angle choice.
In summary, in the proposed model, magnetization directions of the p-SAF layers cannot be deduced from measured in-plane M-H hysteresis loops (θ_{meas}, ψ_{meas}), but require to be treated as fit parameters (θ_{fit}, ψ_{fit}). Nevertheless, measured angles can act as reference. The angle calculation is as follows:

$$\theta_{\mathrm{meas}} = \arcsin\left(M_{\mathrm{IP}}/M_{\mathrm{S}}\right) \tag{4.21}$$

$$\theta_{\mathrm{fit}} = 90° \times \tanh(\beta_{\theta}\ H_{\mathrm{IP}}/H_{\mathrm{max}}) \tag{4.22}$$

$$\psi_{\mathrm{meas}} = 180° - 2|\arcsin\left(M_{\mathrm{IP}}/M_{\mathrm{S}}\right)| \tag{4.23}$$

$$\psi_{\mathrm{fit}} = 180° \times (1 - |\tanh(\beta_{\psi}\ H_{\mathrm{IP}}/H_{\mathrm{max}})|), \tag{4.24}$$

where H_{max} is the maximum applied field (here 70 kOe), and the factors β_{θ} and β_{ψ} are the respective angle fit parameters.

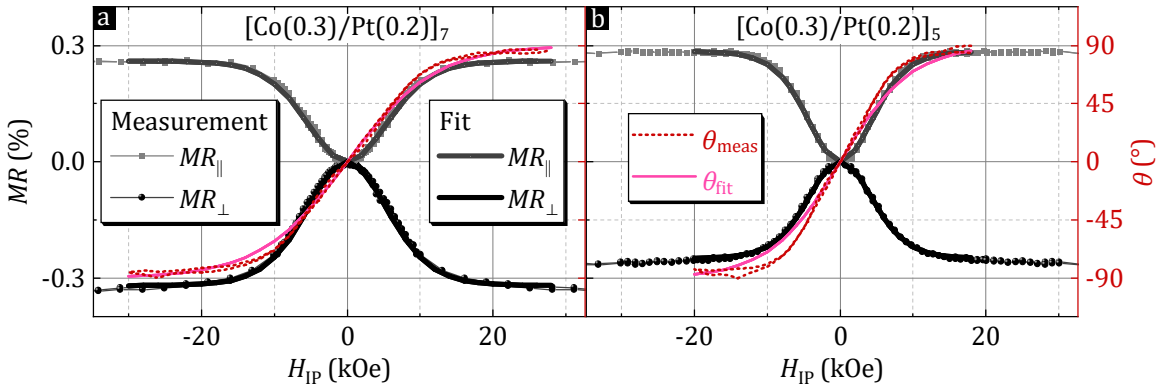

Fig. 4.4.8: In-plane field measurements of Co/Pt multilayer systems with (a) $N = 7$ and $N = 5$. Fits are calculated with Eq. 4.18 for $MR_{||}$ and Eq. 4.19 for $MR_{\perp}$. With a chosen angle θ_{fit} from Eq. 4.22 the fit matches the data nearly perfectly.

To observe the match of the modeled magnetoresistance in the simplest structure, it is first applied for the previously shown Co/Pt multilayer systems, where $\hat{G} = 0$. Furthermore, in this case the fit parameters $A_{||}$ and $A_{\perp}$ can be directly taken from the measurements. The results are shown in Fig. 4.4.8. In both cases, the fit tracks the measurement data accurately. θ_{fit} and θ_{meas} are not perfectly matched. The deviation might have multiple causes, including geometrical imprecision of current flow direction or sample installation in the magnetic field (tilt). Note that M-H hysteresis loops were conducted on a different measurement setup, using a different piece of the same sample. Therefore, direct comparison is inherently flawed.

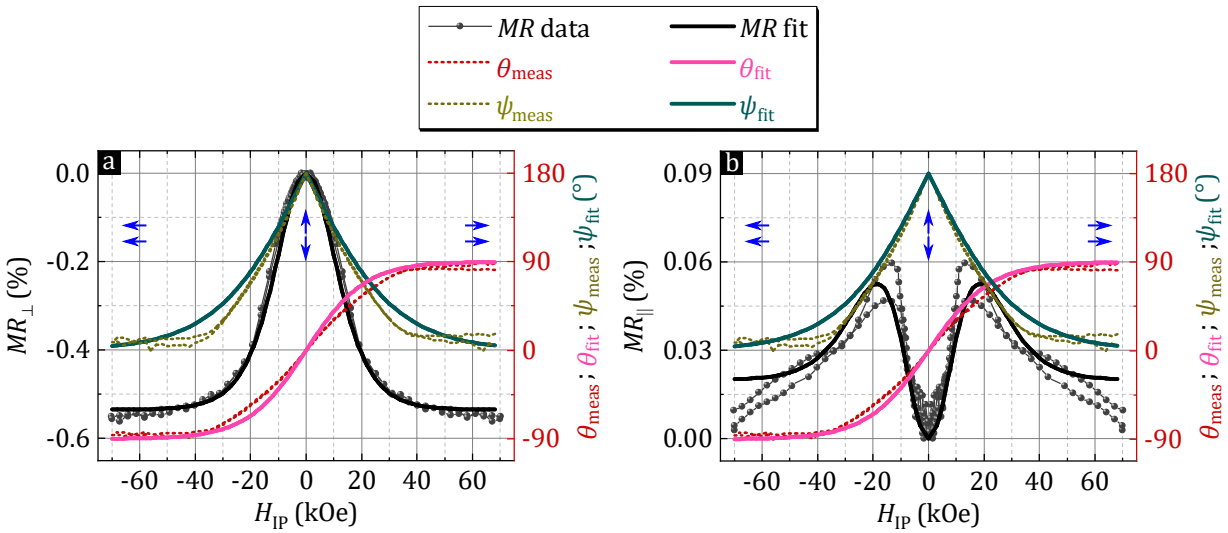

Fig. 4.4.9: In-plane magnetoresistance measurement of a single p-SAF with $[\text{Co/Pt}]_7$/Co/Ru/$[\text{Co/Pt}]_7$/Co stack for (a) $\mathbf{M}_{\text{IP}} \perp \mathbf{I}$, and (b) $\mathbf{M}_{\text{IP}} \parallel \mathbf{I}$. Overlaying the measurement data is a fit using the model given by Eqs. 4.18 and 4.19. θ_{meas} and ψ_{meas} are not used for the fit, but plotted for comparison to θ_{fit} and ψ_{fit}. Fit parameters are $\hat{G} = 0.16\,\% \pm 0.02\,\%$ (measured), $A_{||} = 0.18\,\% \pm 0.02\,\%$, and $A_{\perp} = 0.38\,\% \pm 0.02\,\%$. The blue arrows represent the configuration of magnetic moments for the constituent Co/Pt multilayers.

As it can be seen in Fig. 4.4.9, the model matches the results of magnetoresistance measurements with a single p-SAF structure very well. The exemplary p-SAF that is shown has the layer stack

$[Co/Pt]_7/Co/$ Ru$/$ $[Co/Pt]_7/Co$. The fit parameters are $\hat{G} = 0.16\,\% \pm 0.02\,\%$ (from out-of-plane measurements), $A_{||} = 0.18\,\% \pm 0.02\,\%$, and $A_{\perp} = 0.38\,\% \pm 0.02\,\%$, where the uncertainties are estimated based on the measurement noise and fit uncertainty. Consequently, this simple model can be used to determine the AMR amplitude contributions $A_{||}$ and $A_{\perp}$.

4.4.4 Influence of p-SAF stacking on magnetoresistance

In the following, the magnetoresistance effects in stacked p-SAF structures with multiple Ru layers are further discussed. First, the double p-SAFs stack with a Co(1 nm) layer in the top p-SAF layer from the previous chapter is considered.

Figure 4.4.10 shows magnetoresistance and M-H hysteresis loops in an out-of-plane field. The here measured double p-SAF has the structure seed/$[Co/Pt]_6$/Co/Ru/$[Co/Pt]_8$/Co/Ru/Co(1)/ capping, with the thickness of Co and Pt in the multilayers of 0.3 nm and 0.2 nm, respectively. The Ru spacer layer has a thickness of 0.4 nm. With about 0.31 %, the GMR amplitude is roughly twice as high as for the single p-SAF structure. The effect of spin-canting is clearly visible at fields above $H_{\mathrm{out}}^{300\,\mathrm{K}} = 7.5\,\mathrm{kOe}$, both in magnetization as well as GMR measurements.

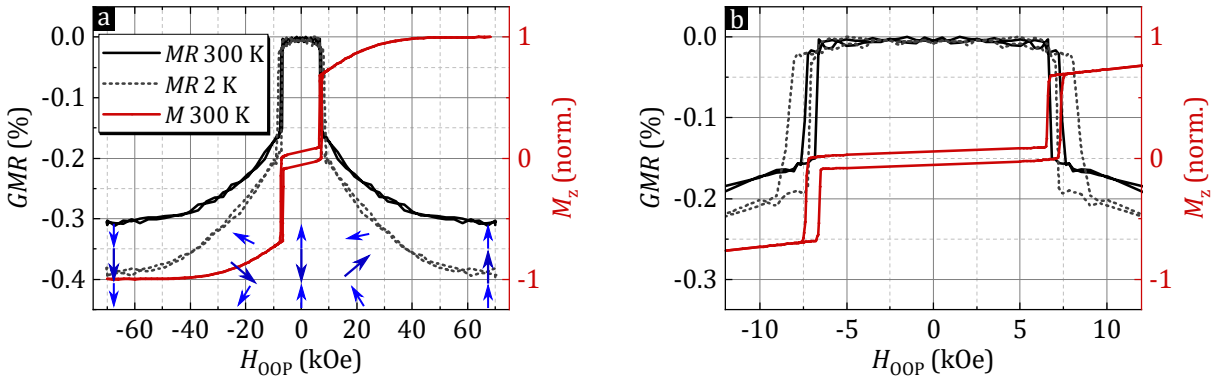

Fig. 4.4.10: (a) GMR and M-H hysteresis loops of a double p-SAF in an out-of-plane field sweep at 300 K and 2 K. Switching fields in GMR and magnetization, shown in (b), are in good agreement. For fields above H_{out}, the effects of spin-canting within the system are well visible in both GMR as well as magnetization. Blue arrows illustrate the magnetization directions of the respective layers.

The results for in-plane fields are given in Fig. 4.4.11, with the fit model overlapping the measurement data. From the model, the AMR amplitude contributions yield $A_{\perp} = 0.38\,\% \pm 0.04\,\%$, and $A_{||} = 0.17\,\% \pm 0.04\,\%$, and therefore a total $AMR = A_{\perp} + A_{||} = 0.56\,\% \pm 0.06\,\%$. The $MR_{||}$ measurement for this sample features a less pronounced dip around 0 kOe. This is due to the GMR amplitude being twice as high for the double p-SAF, thus being the dominating contribution to $MR_{||}$.

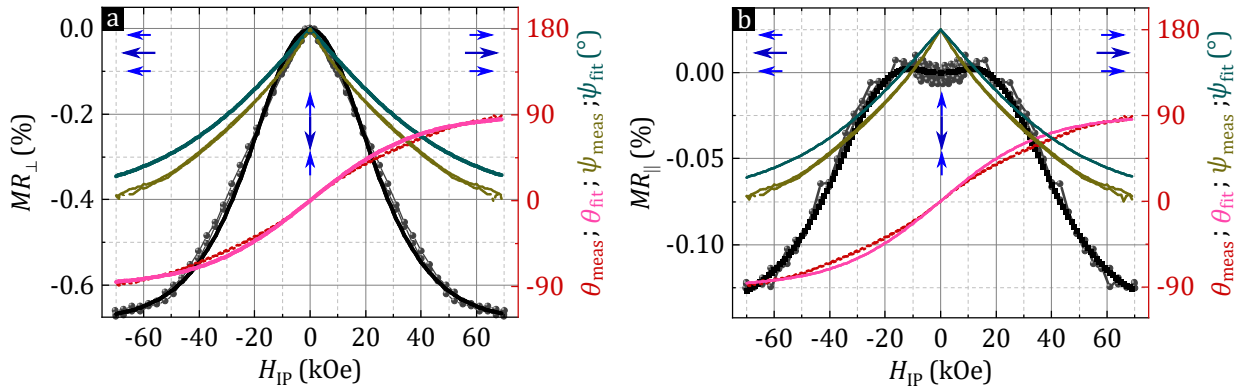

Fig. 4.4.11: In-plane magnetoresistance measurement of a double p-SAF system for (a) $\mathbf{M}_{IP} \perp \mathbf{I}$, and (b) $\mathbf{M}_{IP} \parallel \mathbf{I}$. Overlaying the measurement data is a fit using the model given by Eqs. 4.18 and 4.19, and using the fit parameters θ_{fit} and ψ_{fit}.

To systematically investigate the influence of p-SAF stacking on magnetoresistance and magnetization behavior, measurements are conducted for a series of similar p-SAFs with increasing numbers of multilayers. For the fabrication of such p-SAFs, a distinction between p-SAFs with an odd number of Ru layers N_{Ru}, and an even number of N_{Ru} has to be considered. The reason for this distinction stems from the balance of multilayer magnetization. With odd numbered N_{Ru}, an even number of magnetic multilayers is present in the p-SAF structure. Choosing a multilayer repetition with 5 Co layers, the odd numbered N_{Ru} stack structures can be simply summarized with:

N_{Ru} = odd: seed/{[Co(0.3)/Pt(0.2)]$_4$/Co(0.3)/Ru(0.4)}$_{NRu}$/[Co(0.3)/Pt(0.2)]$_4$/Co(0.3)/capping.

Even numbered N_{Ru}, however, result in odd numbered Co/Pt multilayer quantities, which require different Co layer repetitions in each layer. Here, the multilayers contain 5, 7, and 9 Co layers to balance the total magnetization at zero field:

$N_{Ru} = 2$: seed/ [Co/Pt]$_4$/Co/ Ru/ [Co/Pt]$_8$/Co/ Ru/ [Co/Pt]$_4$/Co/ capping

$N_{Ru} = 4$: seed/ {[Co/Pt]$_4$/Co/ Ru/ [Co/Pt]$_6$/Co}$_3$/ Ru/ [Co/Pt]$_4$/Co/ capping

$N_{Ru} = 6$: seed/ {[Co/Pt]$_4$/Co/ Ru/ [Co/Pt]$_6$/Co}$_5$/ Ru/ [Co/Pt]$_4$/Co/ capping

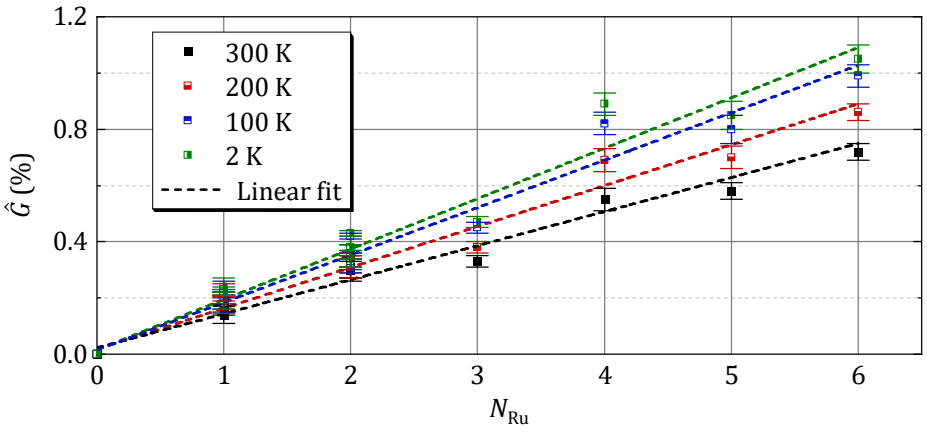

Fig. 4.4.12: GMR amplitudes over number of Ru spacer layers in p-SAF structures. The amplitudes increase linearly with N_{Ru} and decrease for increasing measurement temperatures.

The results for the GMR amplitude of each structure are plotted in Fig. 4.4.12. Independent of N_{Ru} being even or odd, the GMR amplitude increases linearly with increasing N_{Ru}. Measurements were conducted at 2 K, 100 K, 200 K and 300 K, revealing increasing amplitudes with decreasing temperatures, as expected. On average, the GMR ratio is 0.12 % per Ru layer for 300 K and 0.18 % for 2 K. This yields a relative change as a function of temperature of $(-0.06/0.18)/(300\,\mathrm{K} - 2\,\mathrm{K}) = -0.11\,\%/\mathrm{K}$.

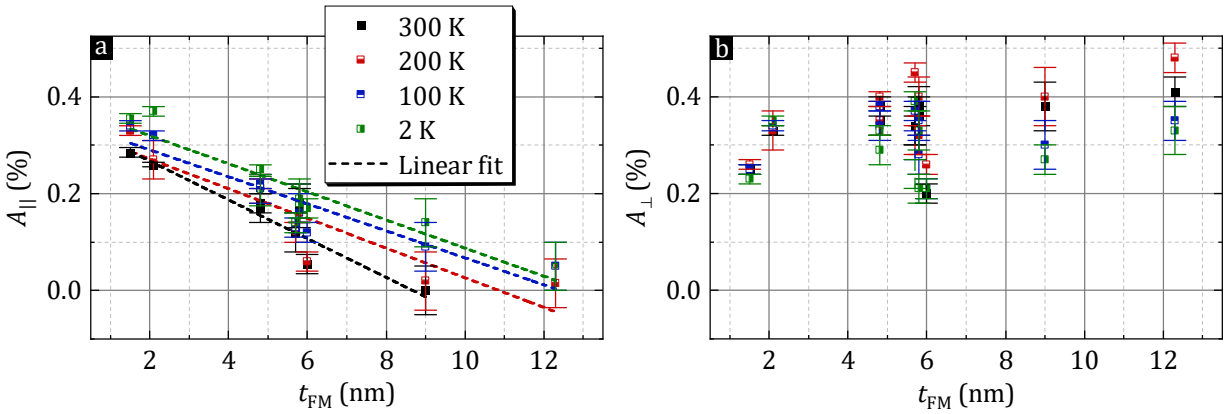

Fig. 4.4.13: AMR contributions (a) $A_{||}$ and (b) $A_{\perp}$ as a function of total ferromagnetic layer thickness t_{FM}. $A_{||}$ decreases with increasing t_{FM} and temperature, whereas no correlation is observed for $A_{\perp}$.

The AMR contributions $A_{||}$ and $A_{\perp}$, extracted from fitting the proposed model onto the experimental data, are shown in Fig. 4.4.13. Instead of N_{Ru}, the amplitudes are plotted against the total thickness t_{FM} of ferromagnetic materials (i.e. Co) in the p-SAF stack. A decrease over t_{FM} is observed for the longitudinal AMR contribution $A_{||}$, which can be approximated with a linear fit[1)]. Furthermore, $A_{||}$ decreases with increasing temperatures, as was already seen for the ML sample in Fig. 4.4.4.

[1)] Since in this sample fabrication series t_{FM} and N_{Ru} are correlated, a somewhat linear decrease of $A_{||}$ as a function of N_{Ru} also occurs, even though the physical origin of the AMR effect is unrelated to the Ru spacer layers. However, deviations from linear fits are more pronounced than for t_{FM}.

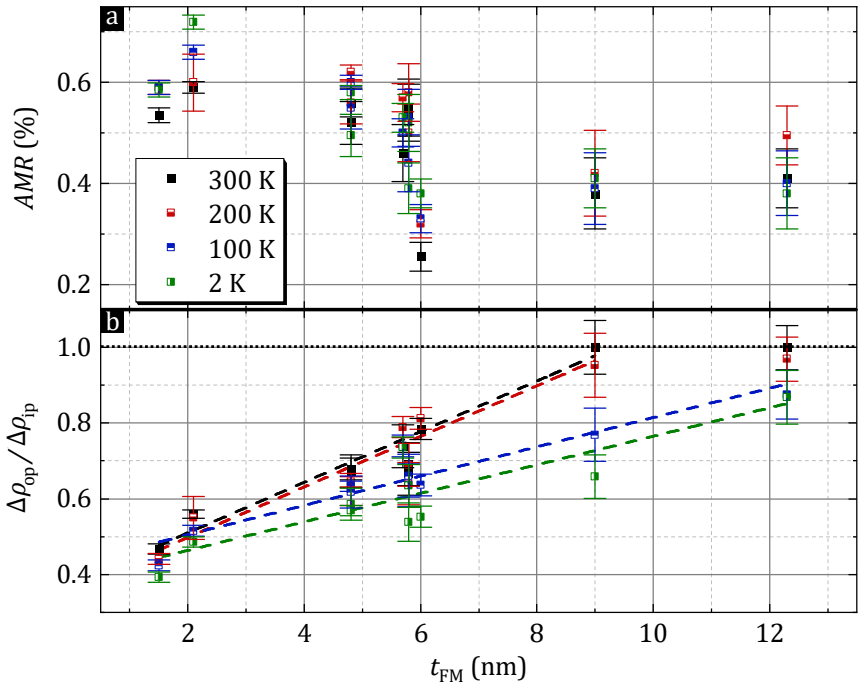

Fig. 4.4.14: (a) AMR amplitude ($= A_{||} + A_{\perp}$) as a function of t_{FM}. (b) $\Delta\rho_{op}/\Delta\rho_{ip}$ ($= A_{\perp}/(A_{\perp} + A_{||})$) showing an increase with t_{FM}, due to the decrease of $A_{||}$. The $\Delta\rho_{op}/\Delta\rho_{ip}$ ratio is capped at a value of 1, per definition.

On the other hand, neither a clear temperature nor t_{FM} dependence is observed for the transverse contribution $A_{\perp}$, shown in Fig. 4.4.13(b). Using $A_{||}$ and $A_{\perp}$, the total AMR amplitude as well as the ratio $\Delta\rho_{op}/\Delta\rho_{ip}$ ($= A_{\perp}/(A_{\perp} + A_{||})$) are plotted in Fig. 4.4.14. As a consequence of the decreasing $A_{||}$ contribution, the AMR amplitude overall decreases with t_{FM} as well, whereas $\Delta\rho_{op}/\Delta\rho_{ip}$ increases. $\Delta\rho_{op}/\Delta\rho_{ip}$ is capped at 1, per definition. However, to understand the decrease of the longitudinal AMR contribution, further research is necessary. While a thickness dependent change in $\Delta\rho_{op}$ and $\Delta\rho_{op}$ was also observed by Kobs et al. [131, 133], including an increase of $\Delta\rho_{op}/\Delta\rho_{ip}$ to a ratio of 1 for low thicknesses, their samples consisted of a single Pt/Co/Pt trilayer with various Co thicknesses, whereas the individual Co thickness in the samples of this chapter were kept at 0.3 nm. Thus, a direct comparison cannot be made.

4.4.5 Influence of p-SAF stacking on the magnetic layer switching

While the shape of the in-plane magnetoresistance curve as a function of field was already discussed and modeled above, the response in out-of-plane fields has so far only been briefly examined for the single and double p-SAFs. However, since out-of-plane fields are directed along the magnetic easy axis of the p-SAF structures, the number of Ru spacer layers and magnetic multilayers have a significant impact on the shape of the transfer curve. In the following it is shown that the switching behavior of the p-SAFs' layers can be deduced using both the results of M-H hysteresis loops as well as magnetoresistance measurements.

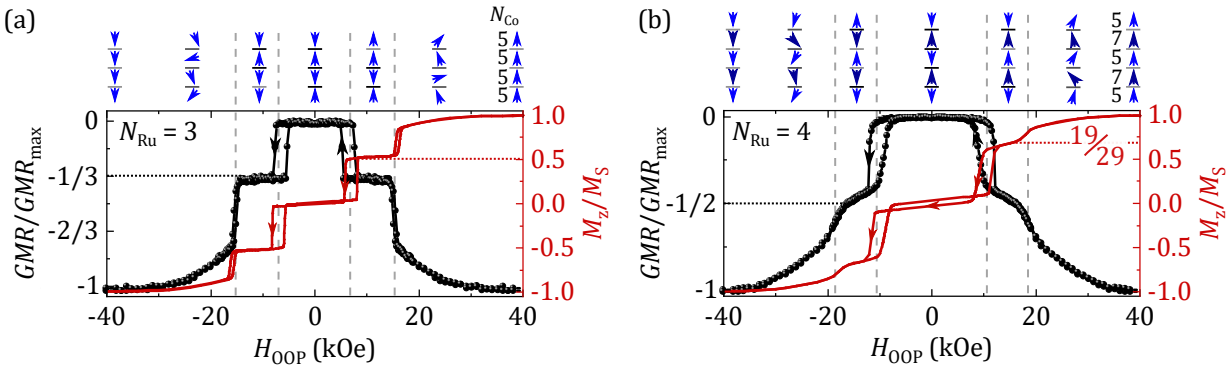

Fig. 4.4.15: GMR and *M-H* hysteresis loops of a p-SAF with (a) 3 and (b) 4 Ru spacer layers in an out-of-plane field sweep at 300 K. The GMR and magnetization are normalized to their respective maximum values GMR_{max} and M_S. Switching fields in GMR and magnetization are in good agreement. Blue arrows illustrate the magnetization directions of the respective layers, which can be estimated from the magnetization and magnetoresistance behavior. The Ru spacer layers in between the multilayers are illustrated as black in case of antiferromagnetic alignment, light gray in case of ferromagnetic alignment, or dark gray in case of spin-canting.

The measurements of a p-SAF with 3 Ru layers is presented in Fig. 4.4.15(a). Magnetization and GMR measurement are in good agreement. Both measurements indicate an intermediate switching step at ca. 7 kOe between complete antiparallel and parallel alignment. The nature of this intermediate switching can be concluded by considering the change in M_z from 0 kOe to 10 kOe by $0.5M_S$, whereas the GMR dropped by only a third of its total amplitude. As the number of Co layers in each multilayer is the same $N_{Co} = 5$, the measurement results indicate the reversal of only one outer magnetization layer. At higher fields around 15 kOe, the p-SAF transitions into a spin-canted state until it saturates with complete parallel alignment at around 35 kOe.

Similarly, the magnetization reversal process can be analyzed for a p-SAF with $N_{Ru} = 4$, shown in Fig. 4.4.15(b). For simplicity, the contribution of a multilayer to the total magnetization is assumed to scale linearly with N_{Co}. Therefore, a magnetization of $19/29\,M_S$ (19 being the number of Co layers with parallely aligned magnetization direction along the applied field and 29 being the total number of Co layers in the structure) and a GMR ratio of $1/2\,GMR_{max}$ corresponds to an antiparallel alignment of the outer two multilayers with respect to the inner three multilayers, as illustrated. Less well defined transitions to and out of the intermediate step at 10 kOe and 18 kOe, as well as a non-zero slope of the GMR and M_z signal, suggest the occurrence of spin-canting effects throughout the measurement range. The magnetic remanence at zero field is due to the imperfect magnetization balance.

The same analysis was done for an $N_{Ru} = 5$ stack in Fig. 4.4.16(a) and $N_{Ru} = 6$ stack in Fig. 4.4.16(b). For the latter, a second intermediate step is observed. The first occurs at approx. 7.5,kOe, where an outer multilayer becomes parallel to its neighbor. The second intermediate switching happens around 10 kOe, where the second outer multilayer adopts the same magnetization direction.

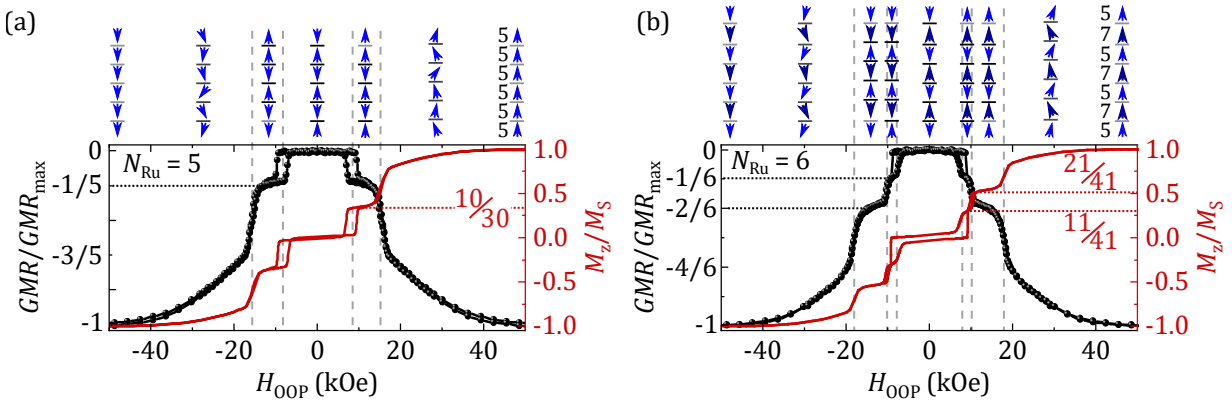

Fig. 4.4.16: GMR and M-H hysteresis loops of a p-SAF with (a) 5 and (b) 6 Ru spacer layers in an out-of-plane field sweep at 300 K. For the $N_{Ru} = 6$ sample, two intermediate switching events occur.

4.4.6 Summary

In summary, the anisotropic and giant magnetoresistance effects in Co/Pt based p-SAF structures were investigated in this chapter. First, measurements were conducted on a simple Co/Pt multilayer, using out-of-plane, in-plane, and rotational in-plane fields. No magnetoresistance effect is present in out-of-plane fields, as expected. The magnetoresistance found in in-plane field configurations match the expected AMR effect in Co/Pt bilayers. It was distinguished between the transverse AMR contribution $A_\perp$, and the longitudinal contribution $A_{||}$. The former denotes the change in resistivity from a polar magnetization at zero field to a saturated in-plane magnetization direction that is transverse to the current direction. The latter denotes the change from a polar to a longitudinal current direction.
In p-SAFs, a GMR effect was measured that scales linearly with the number of Ru spacer layers in the system. Lower temperatures yield higher GMR amplitudes, as expected. Later in this chapter, magnetoresistance measurements and M-H hysteresis loops were used to understand the magnetic switching of the individual multilayer structures in stacked p-SAF systems. A key feature of the magnetization reversal process of stacked p-SAFs is the occurrence of intermediate switching steps, as was also observed by Hellwig et al. [175].

The in-plane magnetoresistance in p-SAFs yield a superposition of AMR and GMR effect. A model of simple summation of the GMR and AMR terms was proposed, which is able to accurately reproduce the measurement results and enables the extraction of the AMR amplitude contributions $A_{||}$ and $A_\perp$. Plotted as a function of the total thickness of ferromagnetic layers in the stacked p-SAF structured, measurements revealed a decrease of $A_{||}$ with thickness and measurement temperature, whereas no distinct correlation can be determined for $A_\perp$.
While the proposed model appeals for its simplicity, its treatment of the individual multilayer magnetization rotation as unified rotation angles θ and ψ may lead to inaccuracies in between zero field and magnetization saturation. A possible further improvement is therefore the implementation of micromagnetic simulations for individual and more precise rotation angles.

4.5 GMR sensors

In this chapter giant magnetoresistance (GMR) sensors are investigated. Since the reference system has already been discussed in chapters 4.3 and 4.4, the focus of this chapter lies on the free layer (FL). In that respect, CoFe as a material for the FL is discussed. Furthermore, the four FL systems first presented in chapter 4.1 (*Sample fabrication*) are analyzed with respect to the correlation of Co thickness t_{Co} and magnetic anisotropy field H_k and to the correlation of H_k and GMR sensitivity S. Using the different FL systems and varying t_{Co}, H_k of the FL can be fully controlled. Finally, the previously investigated single and double p-SAF systems are combined with ferromagnetic layers revealing different H_k values to understand the M-H hysteresis loops and GMR transfer curves.

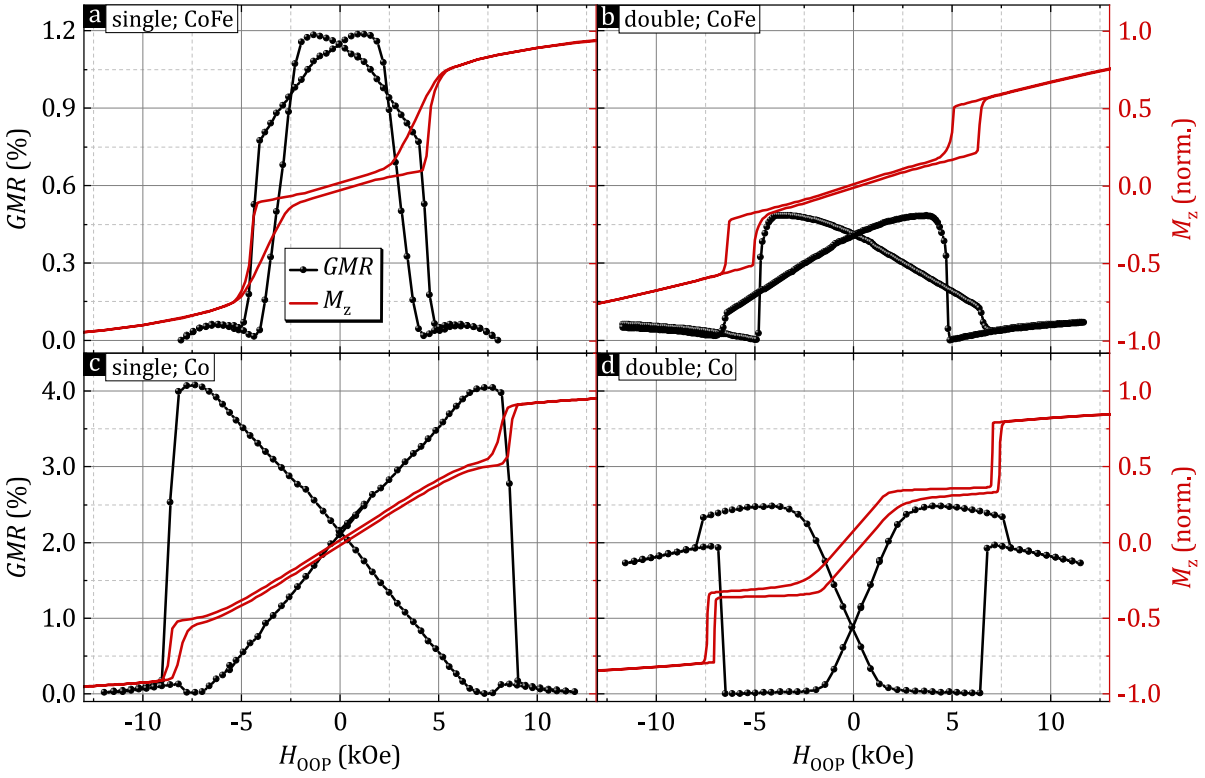

Fig. 4.5.1: GMR transfer curves and M-H hysteresis loops for GMR sensors with (a,b) a CoFe/Cu/CoFe configuration and (c,d) a Co/Cu/Co configuration. (a) and (c) contain a single p-SAF reference system, while (b) and (d) contain a double p-SAF.

4.5.1 CoFe in out-of-plane GMR sensors

When p-SAF structures were discussed in section 4.3, it was mentioned that CoFe is an attractive choice as a material for the reference layer due to CoFe's high spin-polarization [107]. However, the destabilization of the p-SAF reference system, which is caused by CoFe's in-plane magnetic anisotropy, is a significant disadvantage. The question remains, if the expected gain in GMR effect with CoFe compensates for the disadvantage of destabilization. Interestingly, however, when CoFe is in both reference layer and free layer, the opposite behavior is observed.

Figure 4.5.1 shows GMR measurements and M-H hysteresis loops for four GMR sensors. The GMR effect in CoFe/Cu/CoFe structures, given in Fig. 4.5.1(a) and (b), is considerably lower than it is in Co/Cu/Co GMR structures, given in Fig. 4.5.1(c) and (d). In fact, the measurement shown in Fig. 4.5.1(a) yields the highest GMR signal of 1.2 % among all single p-SAF GMR structures with a CoFe/Cu/CoFe configuration that were fabricated in this work (ML/Co/Ru/ML/CoFe(1)/Cu/CoFe(3)). The single p-SAF GMR sensor from Fig. 4.5.1(c) with Co reaches a GMR effect of over 4 % (ML/Co/Ru/ML/Co/Cu/[Co(1.5)/Pt(0.25)]$_3$). Furthermore, while the overall GMR effect in Fig. 4.5.1(a) is about 1.2 %, the GMR effect within the dynamic magnetic field range is only $\Delta GMR = 0.2\,\%$. Additionally, the p-SAF's lack of stability is well visible in the relatively low H_{ex} and poorly defined transitions from ferromagnetic to antiferromagnetic alignment. This lack of stability was discussed in section 4.3.6 in connection with coupling the CoFe reference layer via the interlayer exchange coupling in double p-SAF systems compared to the exchange interaction in single p-SAFs. Accordingly, the stability is increased using a double p-SAF structure in Fig. 4.5.1(b) (ML/Co/Ru/ML/Co/Ru/CoFe(1)/Cu/CoFe(3)). With that, however, the GMR effect decreases significantly, which relates to the generally observed superior GMR effect in single compared to double p-SAF GMR sensors, for which the possible influence of L_{mid} was already discussed in section 4.3.8. The same is visible for a double p-SAF GMR structure with Co in Fig. 4.5.1(d) (ML/Co/Ru/ML/Co/Ru/Co(1)/Cu/[Co(1)/Pt(0.25)]$_3$). With 2.5 %, its GMR effect is still significantly higher than that of the single p-SAF GMR structure using CoFe.

The main reason for the smaller GMR effect in CoFe systems is the high out-of-plane saturation field, i.e. the effective magnetic anisotropy field H_{k} of the in-plane free layer. In the following the influence of H_{k} is discussed in more detail.

4.5.2 Free layer magnetic anisotropy field H_{k}

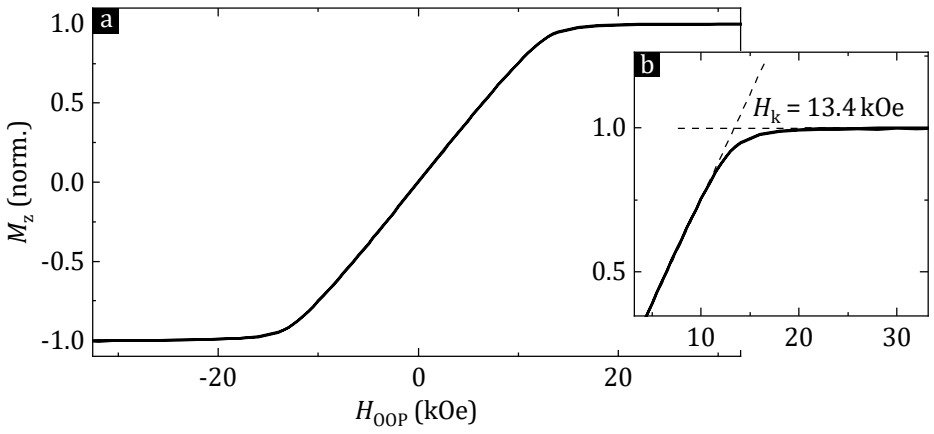

Fig. 4.5.2: M-H hysteresis loop of an in-plane Co(3 nm) layer in an out-of-plane field H_{OOP}. (a) shows the full loop, while the inset (b) shows only the area around H_{k}. H_{k} is the field at which a linear extension from the slope around 0 kOe intercepts M_{S}, i.e. $M_{\mathrm{z}}\,(\mathrm{norm.}) = 1$.

An exemplary graphical determination of H_{k} is given in Fig. 4.5.2, showing an M-H hysteresis loop of a (free) layer with an in-plane easy axis of magnetization in an out-of-plane field H_{OOP}.

Since the GMR effect is measured as a relative change in resistivity and mainly stems from the interfaces of the free layer, Cu spacer layer and reference layer [108, 203], the difference in magnetization angles between free and reference layer is crucial. In consequence, a maximum GMR effect in the field range $-H_{\mathrm{in}}^{*} < H < H_{\mathrm{in}}^{*}$ is achieved, if the free layer magnetization direction rotates from a completely parallel to a completely antiparallel alignment with the reference layer ($H_{\mathrm{k}} \leq H_{\mathrm{in}}^{*}$) (see Fig. 4.5.1(c) and (d)). Likewise, the GMR effect is small, if H_{k} of the free layer is significantly higher than H_{in}^{*} with accordingly little change in the alignment of magnetization directions from $-H_{\mathrm{in}}^{*}$ to $+H_{\mathrm{in}}^{*}$ (see Fig. 4.5.1(a) and (b)).

In the more commonly found in-plane GMR and TMR sensors the low field free layer saturation of approximately 50 Oe limits the dynamic field range of the sensor. More sophisticated free layer magnetic anisotropies, such as the magnetic vortex anisotropy [7, 155, 158], can enlarge the dynamic range up to 500 Oe. On the other hand, free layer saturation fields for GMR sensors with the concept of an out-of-plane reference system, i.e. out-of-plane field operation, are much higher. H_{k} of a commonly used CoFe layer with a thickness of several nanometers is in the range of 20 kOe and is therefore a disadvantage in this work, as argued above. Hence, the endeavor in this work is not to increase the saturation field of the free layer, but to sufficiently decrease it. For TMR structures with an MgO barrier and a CoFeB free layer this can be achieved by choosing CoFeB to be appropriately thin so that orbital hybridization at the MgO/CoFeB interface adds perpendicular magnetic anisotropy to the FL system [30, 32]. For the here presented GMR sensors, four different free layer systems are used to change the free layer's magnetic anisotropy:
S_a: Co(t_{Co}),
S_b: [Co(t_{Co})/Pt(0.25)]$_3$,
S_c: Co(t_{Co})/Pt(0.25)/[Co(0.35)/Pt(0.25)]$_{N_{\mathrm{Sc}}}$
S_d: Co(t_{Co})/CoFe(3).
The number of bilayers N_{Sc} in system S_c is chosen to be either 3 or 5. For every FL system a Pt(2)/Ta(5) bilayer serves as a capping layer. An illustration of these systems is shown in chapter 4.1 (*Sample fabrication*) in Fig. 4.1.2. H_{k} values for these four systems were investigated in both stand-alone free layers as well as free layers in complete single p-SAF GMR structures. In order to get similar growth conditions, stand-alone free layers were deposited on a Ta/Ru/Pt/Cu seed layer stack. Results are presented in Fig. 4.5.3(a). Note the reciprocal scales for the layer thickness, which is in accordance with the expected dependence of

$$H_{\mathrm{k}} \propto -K_{\mathrm{V}} - 2K_{\mathrm{S}}/t \tag{4.25}$$

from Eqs. 2.10 and 2.3[2)]. For every FL system, stand-alone and embedded free layers yield very similar H_{k} values. For the simplest FL system S_a, H_{k} strongly depends on t_{Co} with H_{k} values between 5 kOe for $t_{\mathrm{Co}} = 1$ nm and 15.5 kOe for $t_{\mathrm{Co}} = 6$ nm. Similarly to S_a, the saturation field of a FL with multilayer system design of type S_b can be easily adjusted via the specific Co thickness

[2)] H_{k} is defined for a measurement along the magnetic hard axis, i.e. out-of-plane, therefore giving the equation the negative signs. With that negative sign, the volume anisotropy of Co K_{V} contributes a positive term, whereas the interface anisotropy K_{S} contributes a negative term, hence decreasing H_{k} with higher thicknesses t.

t_{Co} in the ML. The effective magnetic anisotropy favors an in-plane easy axis magnetization for $t_{Co} \geq 1\,\text{nm}$ [38], due to the large contribution of magnetic shape anisotropy. With growing t_{Co} the magnetic shape anisotropy increases, leading to a FL saturation at higher out-of-plane fields. In comparison to S_a, S_b free layer systems yield somewhat smaller H_k values for the same t_{Co}, while both systems show a reciprocal behavior of H_k as a function of t_{Co}. In case of a sample with a type S_c FL, where a layer of Co(2) or Co(3) with strong in-plane magnetic anisotropy is coupled to a ML with PMA, H_k is strongly decreased by 5 kOe for $N_{Sc} = 3$ and by 7 kOe for $N_{Sc} = 5$. Lastly, adding a CoFe(3) layer to a Co(3) layer in the S_d FL, significantly increases H_k from 12.5 kOe to approximately 17 kOe, which is partly due to the CoFe layer acting as a spacer between the Co free and the Pt capping layer, thus preventing PMA at the Co/Pt interface.

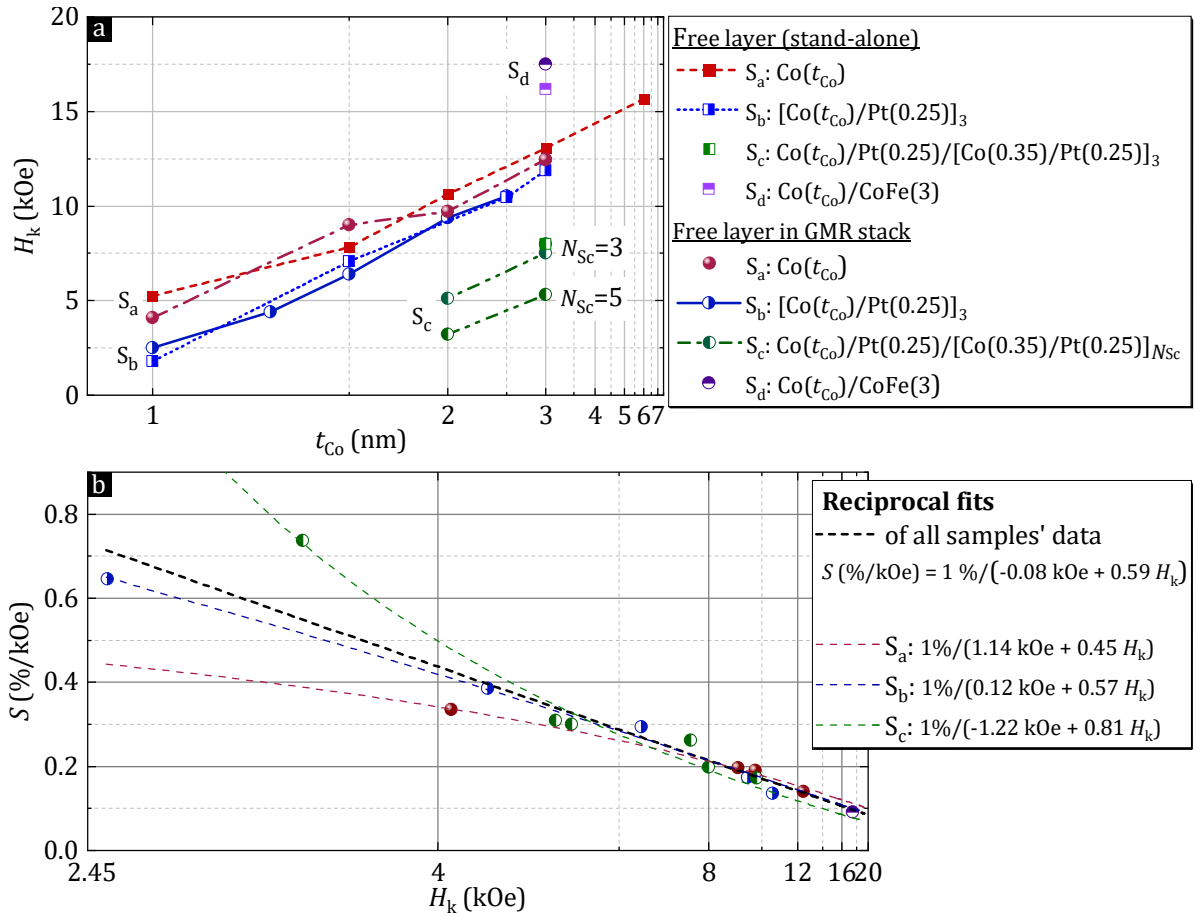

Fig. 4.5.3: Free layer anisotropy field H_k for different free layer structures $S_{a\text{-}d}$. (a) H_k in relation to t_{Co} on reciprocal scale, with stand-alone free layer structures represented by squares and free layers embedded in GMR sensors represented as circles. (b) Single p-SAF GMR sensitivities around 0 kOe following reciprocal fits as a function of H_k. The scale of H_k is reciprocal with an offset of −0.08 kOe. Reciprocal fits with other offsets therefore appear curved.

Similar magnetic anisotropy fields can be achieved by using different FL systems, choosing t_{Co} accordingly. From this follows the question which benefit the more complicated S_b and S_c structures have. One answer to this is related to the reciprocal behavior of H_k as a function of t_{Co}, observed in Fig. 4.5.3(a). For the design of smaller H_k values, the accuracy of t_{Co} during fabrication becomes increasingly important. The risk of undesired fabrication results is mitigated when instead of S_a a FL system is used that yields a smaller H_k at the same t_{Co},

i.e. an S_b or S_c structure. Another argument for abstaining from the use of a S_a FL with thin t_{Co} is the correlation of t_{Co} and *GMR*. For thin film systems, it is observed that the GMR amplitude decreases for smaller Co thicknesses [27,204–206], often showing the decline starting at $t_{Co} < 2\,\text{nm}$ [207,208]. For the GMR sensors in this work, comparing the GMR amplitudes is not sufficient and would be deceiving. That is because it rapidly decreases when $H_k > H_{in}^*$, i.e. when the full spectrum of parallel to antiparallel alignment with the reference layer is not achieved anymore due to switching of the p-SAF reference system. Thus, to compare the GMR sensors that have an $H_k > H_{in}$ with those that have an $H_k < H_{in}$, the GMR sensitivity S is investigated, here defined as[3)] [155]:

$$S = \left(\frac{\Delta R}{\Delta H}\right)_{\text{linear}} / R_0 \tag{4.26}$$

With this, the predominant factor for the GMR amplitude is found to be the free layer magnetic anisotropy field. This is shown in Fig. 4.5.3(b). For $H_k > 7\,\text{kOe}$, all GMR sensitivities show the same $S(H_k)$ behavior, independent of their free layer system. For smaller H_k, however, the reciprocal fits for S_a, S_b and S_c diverge from one another (the respective reciprocal fits appear curved on the reciprocal scale due to different offsets in the fit formulas). This difference can be explained by H_k's correlation to t_{Co} in the respective cases of S_a, S_b, and S_c. With this in mind, the expectation is that of a decrease in GMR amplitude – and thereby a decrease of sensitivity – with decreasing $t_{Co} < 2\,\text{nm}$ for any FL system [207,208]. While the available data for the shown GMR sensors in that specific range of t_{Co} and H_k is limited, the observed behavior matches the expectation: An S_a FL yields smaller sensitivities for small H_k values than an S_b FL, whereas the highest S is achieved with an S_c FL.

Generally, the GMR sensitivity follows a reciprocal behavior as a function of H_k, which agrees with the work of Van Dijken et al. (2005) [23] and Nakano et al. (2015) [5]. While their xMR sensors differ in that the reference layer has an in-plane effective magnetic anisotropy and it is the free layer that has an out-of-plane magnetic anisotropy, their findings are supported by calculations, which are based on the generally applicable Stoner-Wohlfarth (SW) model [37], using the expression for the resistance R being

$$R = \frac{R_{AP} + R_P}{2} + \frac{R_{AP} - R_P}{2} \sin\left[\tan^{-1}\left(\frac{H}{H_k}\right)\right], \tag{4.27}$$

with R_{AP} and R_P being the resistance in antiparallel and parallel alignment, respectively. For small angles $\alpha = \tan^{-1}\left(\frac{H}{H_k}\right)$, the equation simplifies to

$$R = \frac{R_{AP} + R_P}{2} + \frac{R_{AP} - R_P}{2} \frac{H}{H_k}. \tag{4.28}$$

Van Dijken et al. [23] have utilized a GMR sensor with CoFe layers in their study, whereas Nakano et al. [5] worked with magnetic tunnel junctions (MTJ). In a consecutive study [209], they added the Slonczewski model [210] for the conductance of MTJs to their calculation, which

[3)] The definition $S = \left(\frac{\Delta R}{\Delta H}\right)_{\text{linear}} / R_{\min} = \frac{GMR}{(\Delta H)_{\text{linear}}}$ can also be found in the literature [9]. This definition results in higher values for S by the factor $\frac{R_0}{R_{\min}}$.

yields

$$R = \frac{R_0}{1 + P^2 H / H_\mathrm{k}}, \tag{4.29}$$

where P is the effective spin polarization value at the ferromagnet/barrier interface. As a comparison to the work of this thesis, their calculation and measurement data is given in the plot 4.5.4, adapted from Fig. 3(a) in their work [5]. It has to be noted, however, that even though the Stoner-Wohlfarth model gives a satisfactory qualitative description to some degree, quantitatively the calculations yield significant differences to the experimental observations of Fig. 4.5.4. Besides other magnetization processes, such as domain-wall motion, the calculation also lacks the dependence of magnetoresistance ratio on the magnetic layer thickness, i.e. TMR ratio on t_CoFeB [5, 186, 211] and GMR ratio on t_Co [207, 208], as observed above for S in S_a, S_b, and S_c GMR structures.

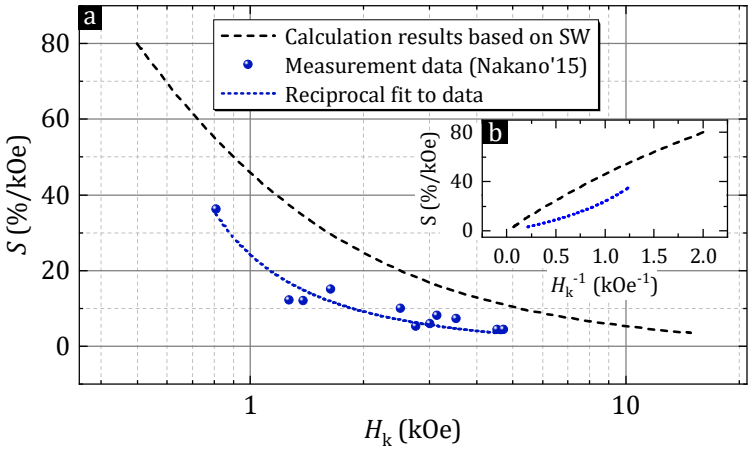

Fig. 4.5.4: Calculation plot and measurement data of MTJs with OOP FL and IP reference layer, taken from the work of Nakano et al. (2015) [5]. Reciprocal fits disclose the relation of S and free layer H_k, which agrees to measurement results for samples of this thesis. (a) shows the data on a logarithmic scale as given in [5], (b) shows a reciprocal scale. The curvature is due to non-zero offsets in the reciprocal fits.

4.5.3 Layer magnetization directions in GMR sensors

In order to fully understand the M-H hysteresis loops and GMR transfer curves of all GMR sensors fabricated in this work, the results on p-SAF structures of section 4.3, especially regarding emerging spin-canting effects, and the results on free layer magnetic anisotropy, have to be taken into account. A systematic variation in free layer H_k values for both single and double p-SAF structures is shown in Fig. 4.5.5, with single p-SAFs in Fig. 4.5.5(a-c) and double p-SAFs in Fig. 4.5.5(d-f). GMR transfer curves, both minor (red) and major loops (black), as well as normalized M-H hysteresis loops from SQUID-VSM measurements are plotted. GMR major and M-H hysteresis loops from positive to negative fields are shown in solid lines, negative to positive field sweeps in dashed lines. The arrows illustrate the assumed magnetization direction of the respective magnetic layers (from positive saturation to negative). From the measurements, three distinct configurations regarding the relation of FL H_k to p-SAF H_ex are visible for both single and double p-SAF GMRs in order of appearance in Fig. 4.5.5: (a,d) $H_\mathrm{k} \leq H_\mathrm{ex}$, (b,e) $H_\mathrm{k} > H_\mathrm{ex}$, and (c,f) $H_\mathrm{k} \gg H_\mathrm{ex}$. The plots of Fig. 4.5.5(a) and (d) were already shown earlier in section 4.3.8

in the investigation of spin-canting effects. Generally, the decrease in sensor sensitivity S with increasing H_k is well visible, as expected. The single p-SAF GMR sensors in Fig. 4.5.5(b) and 4.5.5(c) show their smallest resistance for $H_{OOP} > H_{ex}$, when the FL saturation is reached at H_k. Spin-canting effects in the p-SAF system aren't visible, due to the change of magnetization in the FL. An exception is the sample shown in Fig. 4.5.5(a) with $H_k < H_{ex}$. Here, a small increase in R is visible at H_{ex}, followed by a decrease in R for $H_{OOP} > H_{ex}$. This indicates a very small spin-canting of the p-SAF reference system for $H_{OOP} > H_{ex}$.

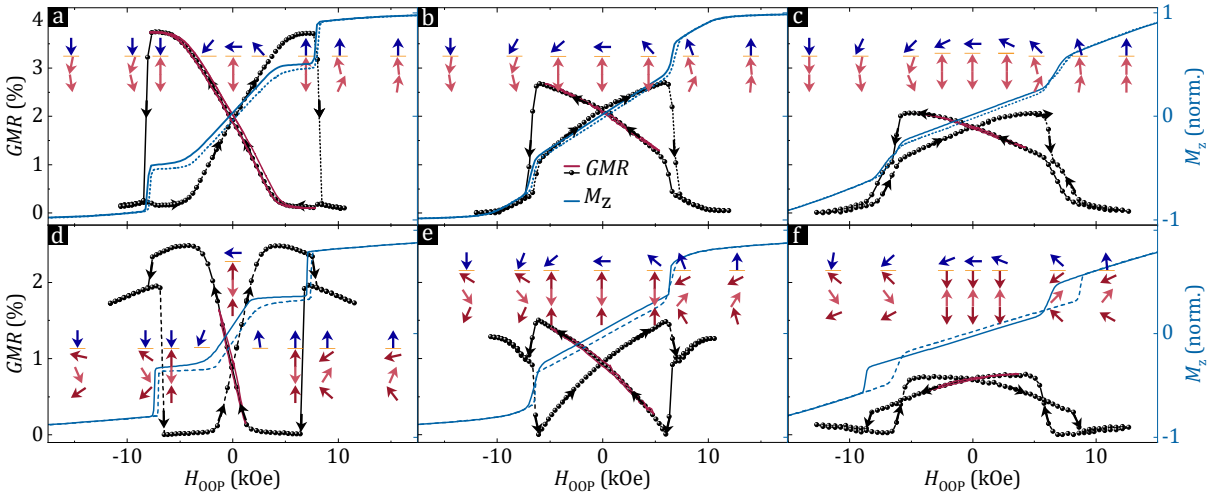

Fig. 4.5.5: GMR signals and normalized magnetizations for GMR sensors in out-of-plane fields. GMR sensors with (a-c) single ($N = 5$) and (d-f) double p-SAF reference system (N_1=6, N_2=8), and free layer (a,c) $H_k \leq H_{ex}$, (b,e) $H_k > H_{ex}$, and (c,f) $H_k \gg H_{ex}$. The respective FL systems are (a) S_b (t_{Co}=1.25 nm), (b) S_b (t_{Co}=2.5 nm), (c) S_d (t_{Co}=t_{CoFe}=3 nm), (d) S_b (t_{Co}=1.0 nm), (e) S_c (t_{Co}=3.0 nm, N_{Sc}=3), and (f) S_d (t_{Co}=t_{CoFe}=3 nm). The arrows illustrate possible magnetization directions of the respective layers, with blue representing the free layer and red representing the layers of the p-SAF reference system. Solid lines represent a field sweep from positive to negative saturation, dashes lines from negative to positive saturation. Published in [194].

The double p-SAF GMR sensors in Fig. 4.5.5(d-f), on the other hand, show an unexpected high R at $H_{OOP} > H_{ex}$. The resistance in Fig. 4.5.5(d) gradually decreases for increasing $H_{OOP} > H_{ex}$. Since the FL of the sample saturates already before H_{ex}, this decrease is caused by a spin-canted state of the p-SAF reference system and its gradual magnetic alignment with the FL magnetization at higher fields. In Fig. 4.5.5(e), the resistance further increases for increasing $H_{OOP} > H_{ex}$, until the FL saturation magnetization is reached. A different GMR behavior can be seen in Fig. 4.5.5(f), where $H_k \gg H_{ex}$. Here, R is smaller for $H_{OOP} > H_{ex}$, indicating a more parallel configuration of FL and reference layer magnetization direction than for $H_{OOP} < H_{ex}$. However, with further increasing $H_{OOP} > H_{ex}$, the magnetization directions rotate to an increasingly antiparallel alignment, owed to the strong spin-canting of the p-SAF reference system. This leads to an increase in R for high fields, in contrast to the decrease that is observed in the case of the same FL but with a single p-SAF reference system, as shown in Fig. 4.5.5(c). At even higher fields, the resistance is expected to decrease again, as the spin-canted reference system approaches magnetization saturation and parallel alignment with the free layer. However, these field strengths are out of range for the measurement setup.

The GMR minor loops in red give an indication of the sensors' hysteresis. Generally, only a

small hysteresis is measured that is similar to the measurement noise level. The most noticeable hysteresis effects occur in samples with small FL H_k, identifying the FL magnetization as main contributor for hysteresis effects for $H_{OOP} < H_{in}$.

Summarized, by systematically varying the FL effective magnetic anisotropy, only a small spin-canting behavior for single p-SAF GMR sensors is observed, but strong spin-canting for double p-SAF GMR samples at fields above H_{ex}, which yields significantly different GMR transfer curves.

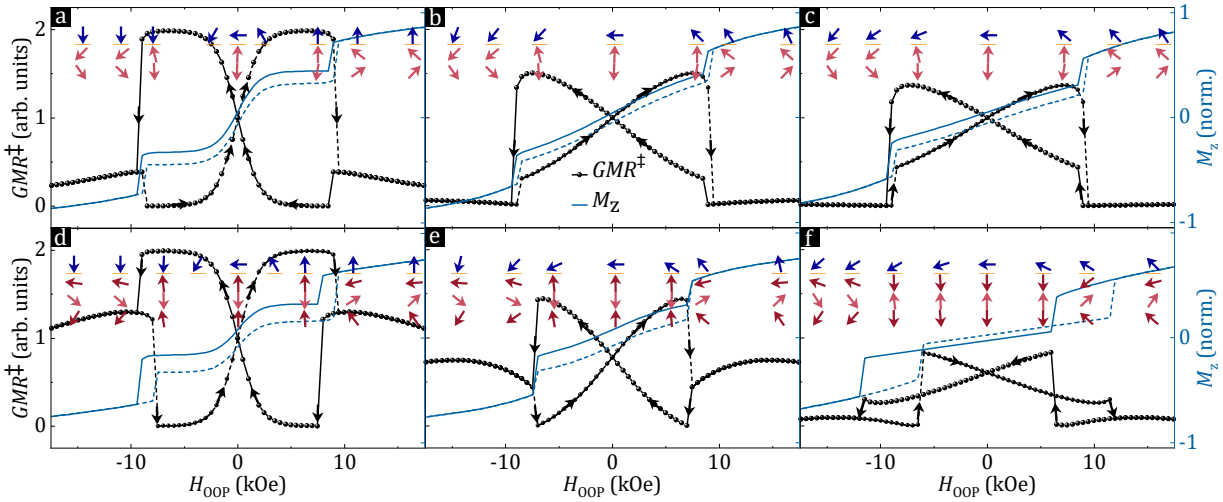

Fig. 4.5.6: Simulation results for GMR‡ signals and normalized magnetizations for GMR sensors in out-of-plane fields. GMR sensors with (a-c) single and (d-f) double p-SAF reference system, and free layer (a,c) $H_k \leq H_{ex}$, (b,e) $H_k > H_{ex}$, and (c,f) $H_k \gg H_{ex}$. The arrows illustrate simulated magnetization directions of the respective layers, with blue representing the free layer and red representing the layers of the p-SAF reference system. Published in [194].

To confirm these results, micromagnetic simulations, as described in section 4.3.9, were performed. Again, excellent qualitative agreement with the measurements in both the magnetization data as well as in the GMR curves is obtained, as presented in Fig. 4.5.6. To achieve this agreement, some, at this point, seemingly arbitrary variations are made to the material parameters of the individual layers of the double p-SAF system. The parameter variations are given by the superscripts, containing the corresponding reference figure to which they refer, in Tab. 4.5.1.

	single p-SAF		double p-SAF		
	L_{bot}	L_{top}	L_{bot}	L_{mid}	L_{top}
$K_{\text{eff}}\,(\text{Merg/cm}^3)$	3.49	3.99	$2.99^{4.5.6e}$/ $4.49^{4.5.6d,f}$	$3.99^{4.5.6e}$/ $4.49^{4.5.6d,f}$	-0.01
$M_{\text{S}}\,(\text{kemu/cm}^3)$	1.15	1.35	1.43	$1.15^{4.5.6d,e}$/ $1.31^{4.5.6f}$	$1.75^{4.5.6d,e}$/ $1.67^{4.5.6f}$
$A_{\text{ex}}\,(\mu\text{erg/cm})$	1.0	1.0	1.0	1.0	1.0
$J_{\text{iex}}\,(\text{erg/cm}^2)$	-2.5		-2.5		-2.5
α	1.0	1.0	1.0	1.0	1.0
$a\,(\text{Å})$	10	10	10	10	10
$t\,(\text{Å})$	28	29	33	43	10

Table 4.5.1: Material parameters of the simulated single p-SAF and double p-SAF systems for all involved layers. K_{eff} is the effective magnetic anisotropy constant, M_{S} is the saturation magnetization, A_{ex} is the bulk exchange constant within the layers, J_{iex} is the interface exchange coupling between the layers, α is the dimensionless damping constant, a is the lateral side length of the simulated nanorod and t is the thickness of the layers. The superscript symbols in the values of K_{eff} and M_{S} refer to the used parameters in the subplots of Fig. 4.5.6. The underlined parameters indicate the basis parameters that are used unless otherwise specified.

4.5.4 Summary

In summary, free layer (FL) systems were investigated in respect to their magnetic anisotropy fields H_k and impact on GMR sensor sensitivity S. While CoFe is a popular material for in-plane sensitive GMR sensors, it is disadvantageous for out-of-plane GMR sensors, because of its strong in-plane magnetic anisotropy, which destabilizes the p-SAF reference system and requires high fields for magnetic saturation in the FL. A reciprocal correlation between FL H_k and GMR sensitivity S was measured. Furthermore, systems that allow higher Co thicknesses t_{Co} than others while yielding the same H_k (e.g. S_c) also yield higher S, which becomes increasingly significant for $t_{Co} < 2\,nm$. Using the FL H_k control and the previously introduced single and double p-SAF designs, M-H hysteresis loops and GMR transfer curves of systematically varied GMR designs were investigated experimentally and supported by micromagnetic simulations.

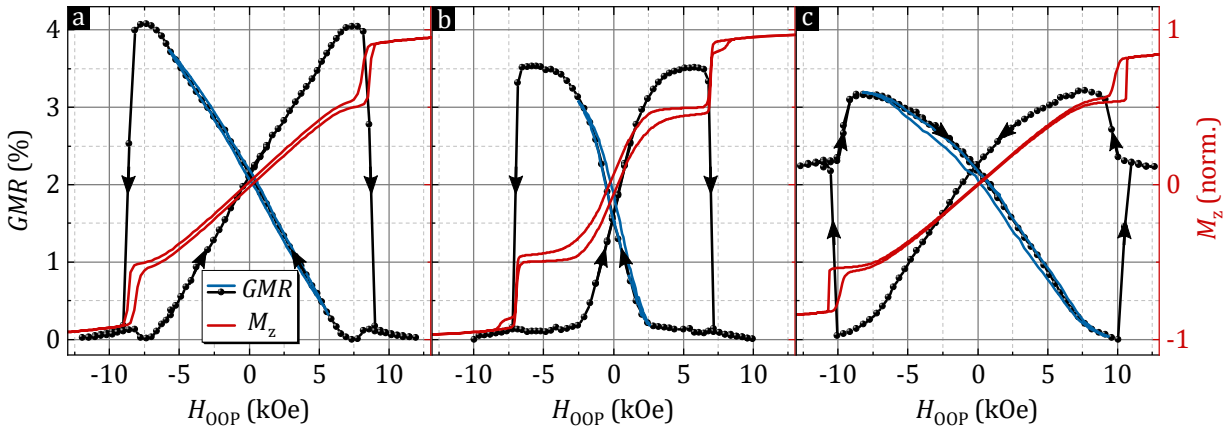

Fig. 4.5.7: GMR measurements and M-H hysteresis loops for (a) a single p-SAF GMR structure with the highest achieved GMR ratio, (b) a single p-SAF GMR structure with the highest achieved sensitivity, and (c) a double p-SAF GMR structure with the highest achieved dynamic range achieved in this work.

To conclude, the findings of this chapter provide a good understanding about the underlying magnetization processes in p-SAF and GMR structures, which in return allows for a custom GMR sensor design. As an example, a sensor designed for high GMR ratio and good linearity is shown in Fig. 4.3.18(a). The sensor is designed with a single p-SAF reference system (N=5) that provides a high stability and an exchange field $H_{ex} = 8.4\,kOe$, which amounts to a dynamic field range of 7 kOe. Its FL is an S_b multilayer system with $[Co(1.5\,nm)/Pt(0.3\,nm)]_3$ with a magnetic anisotropy field $H_k = 7.4\,kOe$. The GMR ratio of 4 % is maximized in this sensor, yielding a sensitivity of $S = 0.29\,\%/kOe$. The GMR sensor with the highest S is shown in Fig. 4.3.18(b). Here, H_k is reduced to only 3.2 kOe. The FL is of the type S_c with $Co(2)/Pt(0.25)/[Co(0.35)/Pt(0.25)]_5$ and the sensitivity $S = 0.74\,\%/kOe$. The highest dynamic magnetic range was achieved with the double p-SAF GMR shown in Fig. 4.3.18(c). The double p-SAF reference system with $N_1 = 4$, $N_2 = 7$ and reference layer $L_{top} = Co(1\,nm)$ achieves an $H_{ex} = 10.3\,kOe$, providing a dynamic field range of 9 kOe. However, the double p-SAF system is less stable within the dynamic range, which can be seen in the poor linearity.

4.6 TMR sensors

In this chapter, tunnel magnetoresistance (TMR) sensors with out-of-plane reference system are studied.
First, *M-H* hysteresis loops of p-SAF reference systems with a CoFeB reference layer and MgO capping layer are analyzed, followed by the investigation of full TMR systems. A TMR wafer lot with 9 wafers (pre-structured at Infineon Technologies AG, with layer deposition conducted by Singulus Technologies AG, and post-processing by Infineon) is characterized on wafer level and printed circuit board (PCB) level, using TMR minor and major loop measurements from temperatures $T = -50\,°C$ to $150\,°C$. The focus of investigation is on the influence of post annealing temperature T_{PA}, free layer thickness t_{FL}, and reference layer thickness t_{RL}.
It is found that t_{FL} and T have the strongest impact on sensitivity S and that the reference layer stability significantly impairs the sensor performance with further improvements to be made.

4.6.1 Unstructured TMR sensor stacks (Augsburg)

The first TMR structures of this work were fabricated and measured at the University of Augsburg. The measurements are limited to *M-H* hysteresis loops of the underlying p-SAF reference system as well as the full TMR stack. Furthermore, first post annealing effects are observed. P-SAF structures are designed with a CoFeB reference layer and MgO capping layer:
$Si/SiO_2/Ta(5)/Ru(20)/Pt(2)/[Co(0.35)/Pt(0.2)]_9/Co(0.35)/Ru(0.4)/[Co(0.35)/Pt(0.2)]_6/Co(0.35)/Ta(0.3)/Co_{40}Fe_{40}B_{20}(t_{RL})/MgO(2)/Ta(5)$.

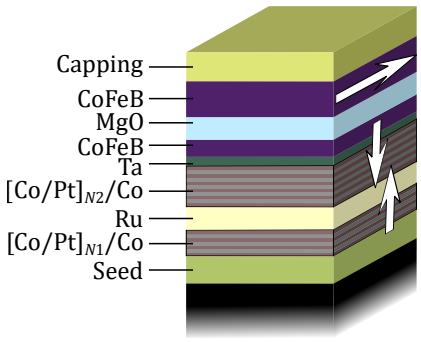

Fig. 4.6.1: TMR stack structure with p-SAF in the reference system and in-plane CoFeB free layer. White arrows indicate the magnetization directions at zero magnetic field.

Illustrations of the p-SAF and TMR stack are given in chapter 4.1 (*Sample fabrication*) in Fig. 4.1.1 as well as in Fig. 4.6.1 with additional details. The Ta spacer layer between the p-SAF and the CoFeB RL serves two purposes. For a high PMA and TMR effect, the CoFeB layer needs to adopt the bcc crystal structure of the MgO tunnel barrier (or capping layer in case of a p-SAF structure) upon post annealing [120, 186–189]. Therefore, the Ta layer serves as buffer layer. Furthermore, as CoFeB is amorphous and crystallizes with boron diffusion, the second purpose of Ta is that of a boron acceptor [212, 213], as boron diffusion into the MgO tunnel barrier would result in a decrease of the TMR effect [214,215]. While post annealing is expected

to increase the PMA in CoFeB, it also poses the risk of deterioration of the Co/Pt multilayers via interdiffusion.

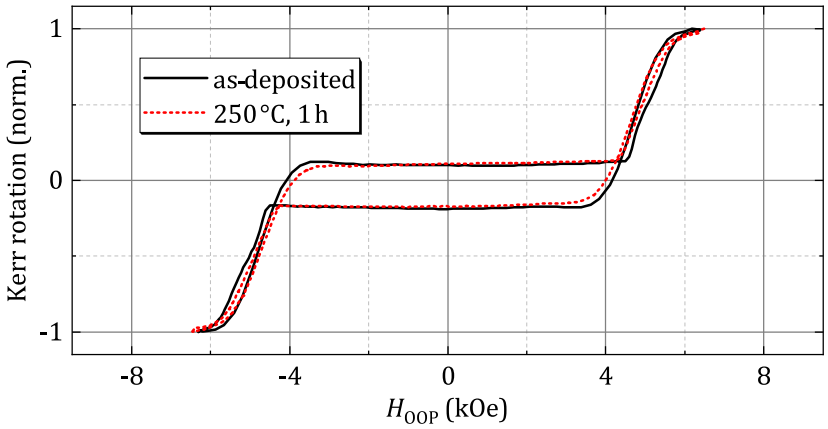

Fig. 4.6.2: MOKE measurement of a p-SAF structure with CoFeB RL and MgO capping layer in an out-of-plane magnetic field. No significant difference is measured between a measurement of the sample as-deposited (solid black line) and a measurement after post annealing for 1 h at 250 °C.

Figure 4.6.2 shows the normalized Kerr rotation in an out-of-plane field H_{OOP} for such a p-SAF structure before and after post annealing for a 1 h at 250 °C in a low pressure Ar atmosphere. In both cases, the p-SAF exchange field H_{ex} of the p-SAF is around 6 kOe with a wide transition from parallel to antiparallel layer alignment (i.e. $H_{out} \rightarrow H_{in}^{*}$). The p-SAF's magnetization appears stable in a range of ±3 kOe. An important observation is that post annealing has not changed the magnetic properties. The CoFeB layer may have still been altered with respect to its crystal structure and PMA, but is not detected due to its small thickness of only 0.9 nm in comparison to the Co/Pt multilayers. This result further confirms the post annealing stability, previously measured for Co/Pt multilayers in chapter 4.2.3 (Fig. 4.2.9) and for p-SAF structures in chapter 4.3.4 (Fig. 4.3.4).

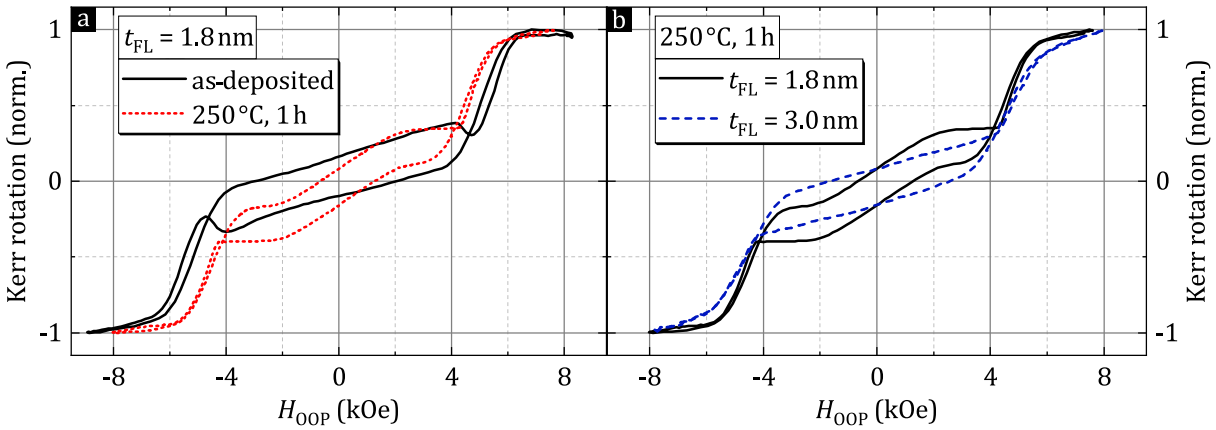

Fig. 4.6.3: MOKE loops of TMR sensor stacks. (a) TMR structure with $t_{FL} = 1.8$ nm as-deposited and after annealing for 1 h at 250 °C. (b) Post annealed TMR structures with $t_{FL} = 1.8$ nm and 3.0 nm.

For TMR structures, a $Co_{40}Fe_{40}B_{20}$ free layer with thickness t_{FL} is deposited on top of the MgO tunnel barrier and capped with a 5 nm Ta layer. MOKE measurements are shown in Fig. 4.6.3.

In Fig. 4.6.3(a) the impact of post annealing is visible for a sample with $t_{FL} = 1.8\,nm$. A linear increase in Kerr rotation around 0 Oe is present for both samples, caused by the in-plane magnetic FL. After post annealing, the slope is increased and the magnetic saturation (or the magnetic anisotropy field H_k) of the FL is visible at around 2 kOe. Hence, post annealing significantly increased the PMA of the FL. The layer thickness determines the effective magnetic anisotropy of the FL [61,212,216,217] (see Eq. 4.25), which is demonstrated in Fig. 4.6.2(b), showing the Kerr rotation of a sample with $t_{FL} = 1.8\,nm$ and of a sample with $t_{FL} = 3.0\,nm$ after post annealing for 1 h at 250 °C. In contrast to the former sample, the latter sample shows no FL saturation within the present measurement range (±8 kOe).

4.6.2 Structured TMR sensor stacks (Singulus)

To be able to measure the TMR effect, one needs either a Current In-Plane Tunneling setup (CIPT) or install contacts to both free and reference layer (or rather to the adjacent conductive layers) using etching methods. For the TMR sensors of this work with an out-of-plane reference layer, the latter option was applied, which allows the use of multiple setups (i.e. setups on wafer level and on printed circuit board (PCB) level). Ten pre-structured 200 mm Si wafers were provided and sent to Singulus Technologies AG for layer deposition. Post processing, including etching processes and post annealing, were performed at Infineon Technologies AG.

Wafer	t_{RL} (nm)	t_{FL} (nm)	T_{PA} (°C)
1	0.9	2.4	275
2	0.9	2.4	275
3	0.9	3.0	275
4	0.9	1.8	275
5	0.9	2.4	300
6	- -	- -	- -
7	0.7	2.4	275
8	1.1	2.4	275
9	0.9	2.4	325

Table 4.6.1: Distinguishing fabrication and post processing parameters of comparable wafers deposited by Singulus Technologies AG.

Of the 9 wafers fabricated, 8 use a layer stack inspired by the earlier results of this chapter, fabricated and measured at the University of Augsburg:
Si/ SiO_2/ Ta(5)/ Ru(20)/ Pt(2)/ $[Co(0.35)/Pt(0.2)]_9$/ Co(0.35)/ Ru(0.4)/ $[Co(0.35)/Pt(0.2)]_6$/ Co(0.35)/ Ta(0.3)/ $Co_{40}Fe_{40}B_{20}(t_{\mathbf{RL}})$/ MgO(1)/ $Co_{40}Fe_{40}B_{20}(t_{\mathbf{FL}})$/ Ta(20)/ Ru(5).
The p-SAF reference system is purposely not designed for highest possible exchange fields H_{ex}, so that the available measurement setups are able to sweep through the p-SAF switching fields. For the investigation of the free layer thickness t_{FL}, the reference layer thickness t_{RL}, and the post annealing temperature T_{PA}, these three parameters vary among the 8 wafers and are listed in table 4.6.1. The final wafer 10 is based on the experience of Singulus with regard to layer deposition of magnetoresistive random-access memory (MRAM) devices. The reference system differs

strongly from the other 8 wafers. The free layer is capped with W adjacent to the CoFeB instead of Ta. Wafer 10 has the stack $Si/SiO_2/Ta(3)/Ru(20)/Ta(0.7)/Pt(1.5)/[Co(0.5)/Pt(0.35)]_6/Co(0.6)/Ru(0.8)/Co(0.6)/[Pt(0.35)/Co(0.5)]_3/Pt(0.25)/Ta(0.2)/Co(1.2)/Ta(0.25)/Co_{40}Fe_{40}B_{20}(0.9)/MgO(1)/Co_{40}Fe_{40}B_{20}(2.4)/\mathbf{W(0.3)}/Pt(1.5)/Ta(20)/Ru(5)$.

4.6.3 Measurements on wafer level

The first measurements of the Singulus TMR sensors are conducted on wafer level using a probe station (UF200) at 35 °C. The available setup can reach only 180 Oe out-of-plane magnetic fields, but is capable of measuring multiple devices on the wafer in a timely manner. Thus, it provides an overview of the influence of device position on the wafer, and of the device module. Before measurements are performed, each wafer is exposed to a 10 kOe out-of-plane field. Before the exposure, the p-SAF reference system is in an undefined state and likely contains multiple magnetic domains. This results in a lower TMR effect as seen in Fig. 4.6.4, where the TMR effect of wafer 1 ($t_{FL} = 1.8$ nm) is measured before and after the wafer is exposed to the 10 kOe out-of-plane field. After the p-SAF was saturated, the TMR effect is increased, which indicates a more aligned synthetic antiferromagnetic state.

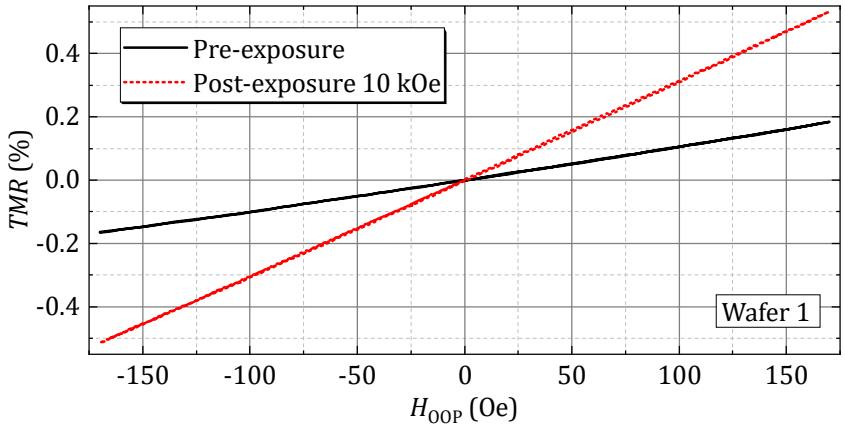

Fig. 4.6.4: TMR minor transfer curves of wafer 1 before and after it is exposed to an out-of-plane field of 10 kOe. After exposure, a higher TMR effect is achieved, likely caused by a better alignment of the p-SAF layer magnetization.

As already discussed, after the layer deposition of a TMR sensor stack, post annealing is required to increase the TMR signal. Besides the mentioned purpose of boron diffusion from CoFeB, also the crystal structure of the MgO tunnel barrier is improved during the process of annealing. For in-plane TMR sensors the preferred post annealing temperature is around 350 °C for 1 h [55]. Since the CoFeB layers in this chapter are relatively thin in comparison to standard in-plane TMR sensors, lower post annealing temperatures are potentially favorable, as they are likely sufficient for both MgO crystallization as well as boron diffusion and thus reduce the risk of undesired diffusion from Ta.

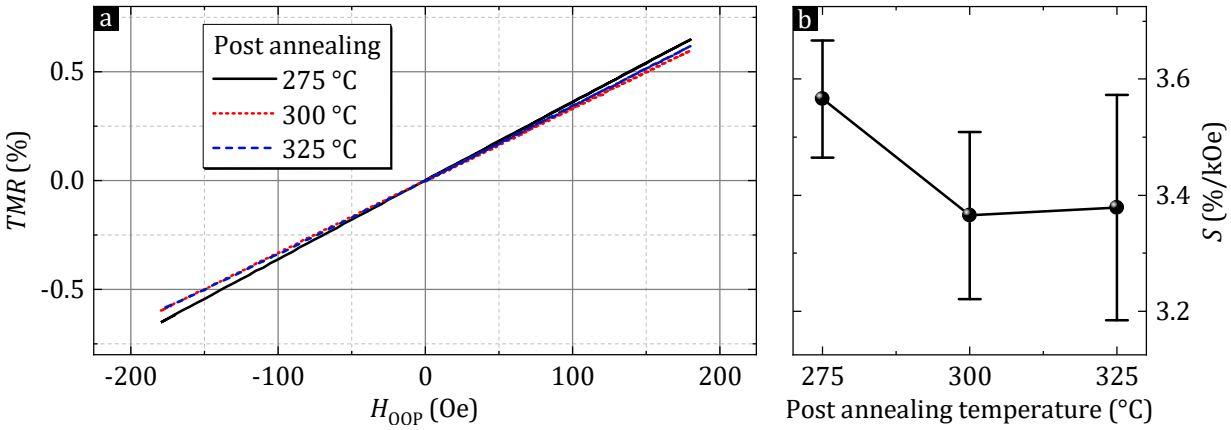

Fig. 4.6.5: Measurement results on wafer level for three identical wafers, post annealed at different temperatures for 1 h (no magnetic field during annealing). (a) Exemplary TMR transfer curves for a ±180 Oe magnetic field range. (b) S as a function of post annealing temperature with standard deviation of the same device module on different wafer positions used as error bars.

Before every wafer is committed to post annealing, only three wafers, identical in their nominal layer deposition, are annealed for 1 h at 275 °C, 300 °C, and 325 °C, respectively. No external magnetic field is applied during the annealing process. Exemplary measurement results of minor transfer curves are given in Fig. 4.6.5(a), showing the TMR signal as a function of an out-of-plane field with the TMR signal set to 0 % at 0 Oe. It is already visible that the post annealing temperature in this range has only minor effects with the lowest temperature of 275 °C yielding the highest sensitivity S, as summarized in Fig. 4.6.5(b). The error bars represent the standard deviation across the measurement of multiple devices on different position on the wafer. Note that for TMR structures, not the resistivity but the conductance σ is considered for S with [155]

$$S = \left(\frac{\Delta\sigma}{\Delta H}\right)_{\text{linear}} / \sigma_0. \tag{4.30}$$

For an easier comparison, only one module type, named PT07, is shown in Fig. 4.6.5(b), but is representative for the general behavior. The other Singulus wafers have been post annealed with a temperature of 275 °C for 1 h.

The MgO tunnel barrier is sandwiched between a CoFeB free layer (FL) and a CoFeB reference layer (RL). The FL thickness t_{FL} is sufficiently thick (≥ 1.8 nm) to ensure an in-plane effective magnetic anisotropy K_{eff} [61,212,216,217]. However, depending on t_{FL} the FL saturates at lower or higher out-of-plane fields [32], similar to the influence of t_{Co} on the magnetic anisotropy field H_{k} observed earlier in GMR systems (see Fig. 4.5.3(a)). It is therefore expected that t_{FL} has a significant impact on S, which is observed in the measurements shown in Fig. 4.6.6(a), where the measured S follows a reciprocal decay with increasing t_{FL}.

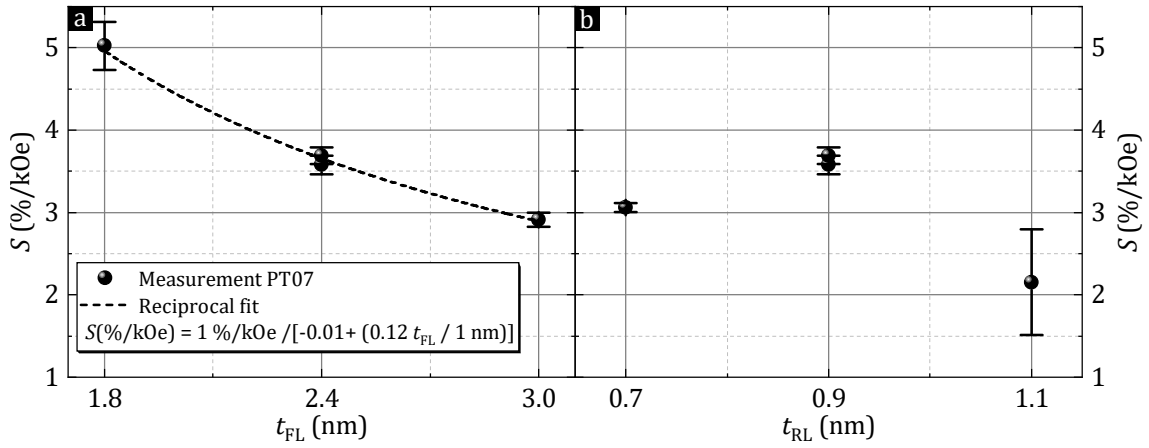

Fig. 4.6.6: Sensitivity measurements of multiple samples with the same module (PT07) for different (a) t_{FL} and (b) t_{RL}.

The RL is coupled to the p-SAF reference system and therefore forced into an out-of-plane magnetization direction. Additionally, the out-of-plane interface anisotropy from spin-orbit hybridization at the CoFeB/MgO interface dominantly contributes to K_{eff} of a CoFeB/MgO bilayer for CoFeB thicknesses smaller than 1 nm [61, 212, 216, 217]. While a higher RL thickness t_{RL} is expected to yield higher TMR amplitudes, RLs with $t_{\mathrm{RL}} > 1\,\mathrm{nm}$ may also introduce dominant in-plane magnetic anisotropies (as shown previously in Fig. 4.6.3(b)), thereby destabilizing the TMR's reference system. Measurement data of TMRs with $t_{\mathrm{RL}} = 0.7$, 0.9, and 1.1 nm, shown in Fig. 4.6.6(b), suggest the occurrence of this expected behavior. The TMR samples with $t_{\mathrm{RL}} = 0.9\,\mathrm{nm}$ perform with a higher S than the sample with $t_{\mathrm{RL}} = 0.7\,\mathrm{nm}$. The sensitivity of the $t_{\mathrm{RL}} = 1.1\,\mathrm{nm}$, however, is significantly reduced with a broad distribution of values. This may be an indication for a less stable reference system that experiences a stronger spin-canting effect even in the low magnetic field range.

As stated above, the wafer level probe station setup (UF200) is suitable to investigate the influence of device modules and of device position on the wafer. Figure 4.6.7 shows the measurement results for 18 different positions on the wafers in terms of TMR sensitivity (due to the limited magnetic field range). The plot presents sensitivity S for every Singulus wafer, including its interquartile range (25 % to 75 %, IQR), range within 1.5 IQR, median, mean, and outliers. The tick labels on the abscissa provide the distinguishing information for each wafer. Results on post annealing for wafers 1, 5, and 9 were presented earlier in Fig. 4.6.5, as were the results on t_{FL} for wafers 1, 2, 3, and 4, and on t_{RL} for wafers 1, 2, 7, and 8 in Fig. 4.6.6.

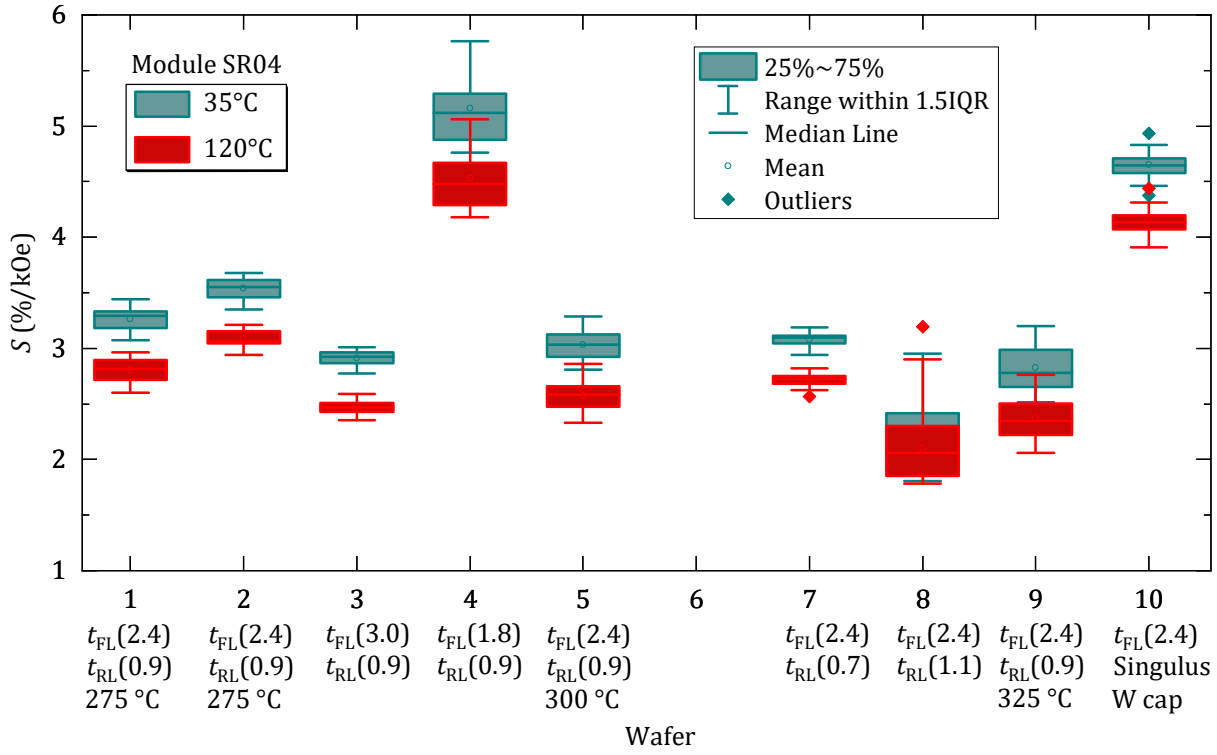

Fig. 4.6.7: Box chart plot showing S for all wafers measured at two different temperatures. Characteristic features of the respective TMR structures on the wafers are given below the abscissa.

The remaining wafer 10 shows a relatively high S, even though its FL has a thickness of 2.4 nm. Since its stack involves several major differences to the other wafers, discussing the origin of a higher S is rather speculative. The Ta/Co/Ta sandwich below the CoFeB RL may give a more favorable growth condition for the RL, thus leading to a higher TMR effect and S. Since it was shown that the FL magnetic anisotropy is most relevant for S, it is also very likely that the FL design of wafer 10 is responsible for the relatively high sensitivity. The FL is capped by a W(0.3 nm) layer, which might have an influence on the FL's crystal structure and magnetic anisotropy. W is used as an alternative boron acceptor during the post annealing process [214, 218–220]. Its use may have lead to a better boron diffusion and consequentially improved electron transport properties [214] as well as a stronger spin-orbit hybridization at the CoFeB/MgO interface [221, 222], reducing the FL's H_k. To verify this, further sample fabrication with the intent of capping layer investigation is needed, as well as measurements of the respective H_k values.

Measurements at an elevated temperature of 120 °C result in a decrease of sensitivity for all wafers. This behavior is generally expected for TMR sensors [187–189, 223] and can be attributed to direct elastic tunneling with a Bloch law dependent polarization and a spin-independent tunneling dominated by hopping mechanisms [187]. Besides the general phenomenon, the individual structure of the FL plays an important role in the TMR temperature dependence [224]. In the case of the TMR sensors presented in Fig. 4.6.7, the elevated temperature also reduces the PMA at the CoFeB/MgO interface [217] at the FL, which increases H_k and decreases S.

4.6.4 PCB measurements

Based on the results of the measurements at the probe station, four wafers were selected for further investigation. Since the most significant difference was detected in correlation with the FLs, the selected wafers are wafer 2 ($t_{\mathrm{FL}} = 2.4\,\mathrm{nm}$), 3 (3.0 nm), 4 (1.8 nm), and 10 ($t_{\mathrm{FL}} = 2.4\,\mathrm{nm}$ with W capping layer). Three PT07 modules (see Fig. 4.6.6) were cut from each wafer and soldered onto a printed circuit board (PCB), enabling measurements in a setup with an out-of-plane magnetic field range of more than 6 kOe and a temperature range from −40 °C to 150 °C. Major loop TMR measurements of these PCBs, shown in Fig. 4.6.8, reveal the respective switching behavior of the p-SAF reference system. The p-SAFs of wafers 2–4 transition out of antiferromagnetic coupling at fields above $H_{\mathrm{OOP}} > 2\,\mathrm{kOe}$ with a long transition until $H_{\mathrm{OOP}} = 3.5\,\mathrm{kOe}$. Exchange fields of approximately $H_{\mathrm{ex}} = 2.75\,\mathrm{kOe}$ are significantly smaller than those of p-SAFs fabricated at the University of Augsburg. This is understandable, since no stack optimization for these structures has been done at the Singulus layer deposition setup. More significantly, the poorly defined reversal transition indicates strong spin-canting in the p-SAF structure. This p-SAF instability even at low magnetic fields is likely to have a negative impact on the performance of TMR minor loops. The TMR major loop measurement of wafer 10, shown in Fig. 4.6.8(b), unexpectedly shows an asymmetric behavior of the p-SAF reference system. Further measurements of the magnetization reversal process are needed to determine if this asymmetric behavior is a consequence of the asymmetric p-SAF structure or merely an artifact from the measurement, e.g. due to erroneous sample insertion.

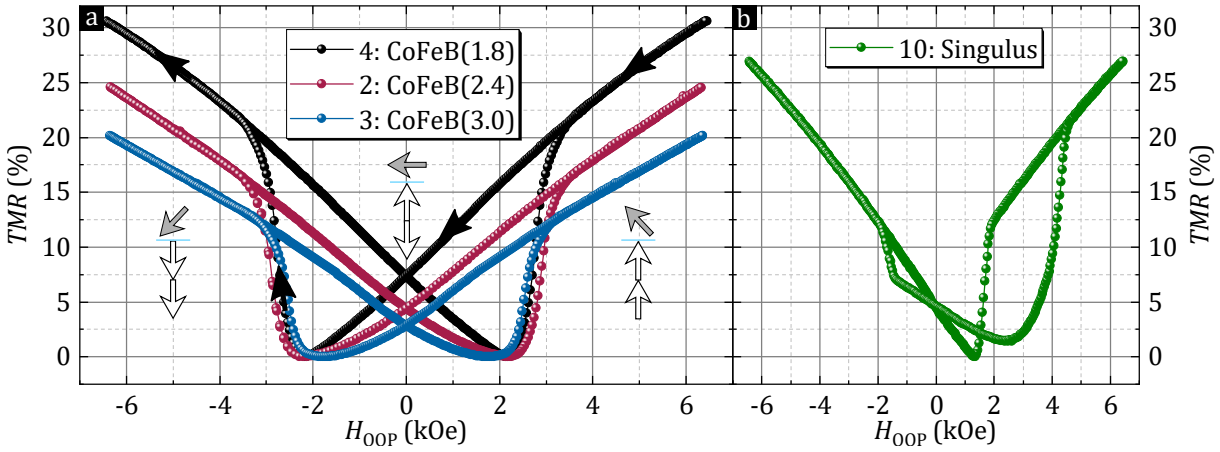

Fig. 4.6.8: TMR major transfer curves on PCB level at room temperature. (a) Three wafers with the same magnetic reference system but different t_{FL}. White arrows illustrate the magnetization direction of the p-SAF layer for a sweep from positive to negative fields with L_{bot} switching first. The gray arrays are only an approximation of the FL magnetization direction, as H_{k} has not been measured. (b) Singulus TMR stack with distinct reference system and W capping layer, showing a strong asymmetry.

All four wafer samples reveal FL saturation fields above the measurable magnetic field range. Therefore, no H_{k} values can be deduced. In terms of applicability, these high H_{k} values are problematic, since the rotation of the FL magnetization direction cannot be exploited above H_{ex}. For future sample fabrications this implies the possibility of a substantial gain in sensitivity when the FL is designed such that H_{k} is close to the p-SAF's H_{ex}, as discussed for GMR sensors

in section 4.5.2.

In the following, wafers 2, 3, and 4 are further investigated regarding hysteresis, non-linearity and temperature dependence in 1.5 kOe TMR minor transfer curve measurements. Figures 4.6.9(a) and (b) present the raw data of TMR signal measurements at 0 °C for all 3 wafers, and of wafer 4 ($t_{\mathrm{FL}} = 1.8$ nm) for 4 different temperatures, respectively. Besides the expected drop in TMR signal with increasing t_{FL} and temperature, it is also already visible that the samples experience hysteresis and non-linear transfer curves within the ±1.5 kOe magnetic field range (most noticeably for wafer 2 at 0 °C).

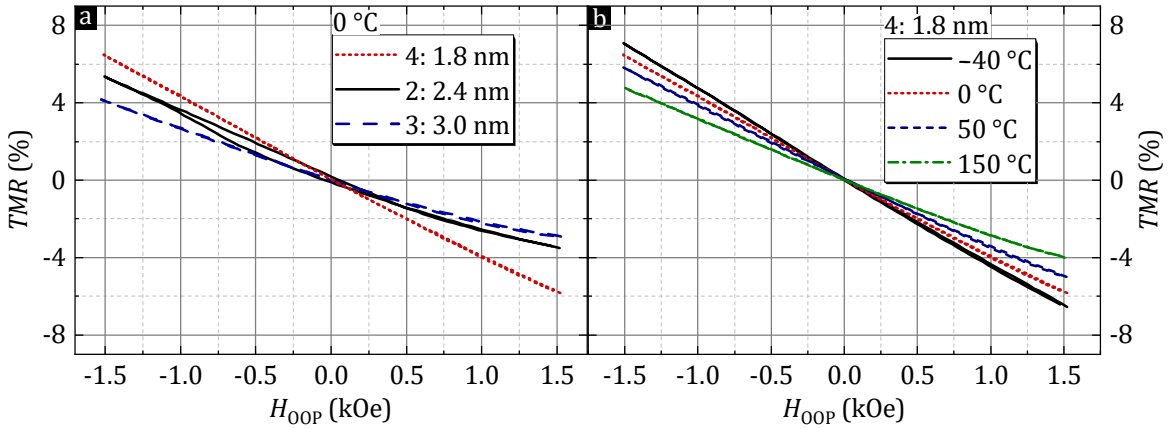

Fig. 4.6.9: Exemplary TMR minor transfer curves (±1.5 kOe) of (a) wafers 2, 3, and 4 with different t_{FL} at 0 °C, and (b) wafer 4 with t_{FL}=1.8 nm at different temperatures.

Figure 4.6.10(a) exemplary shows σ in millisiemens (mS) measured at 0 °C of a wafer 4 sample with visible hysteresis. Figure 4.6.10(b) shows the extracted hysteresis parameter and non-linearity (NL) for this measurement. The hysteresis parameter is calculated as

$$\mathrm{Hysteresis}\,(H_{\mathrm{OOP}}) = \frac{\sigma_-\,(H_{\mathrm{OOP}}) - \sigma_+\,(H_{\mathrm{OOP}})}{\Delta\sigma_{\mathrm{FS}}}, \tag{4.31}$$

where σ_- is the conductance in decreasing magnetic field direction, σ_+ the conductance in increasing magnetic field direction and $\Delta\sigma_{\mathrm{FS}}$ the range of conductance at the full scale (FS) of the measurement. The non-linearity is calculated as

$$NL\,(H_{\mathrm{OOP}}) = \frac{\mathrm{mean}\,[\sigma_-\,(H_{\mathrm{OOP}})\,;\sigma_+\,(H_{\mathrm{OOP}})] - \sigma_{\mathrm{fit}}\,(H_{\mathrm{OOP}})}{\Delta\sigma_{\mathrm{FS}}}, \tag{4.32}$$

where σ_{fit} is a linear fit function of the mean conductance (mean$[\sigma_-;\sigma_+]$) around 0 Oe. It is important to note that neither hysteresis nor non-linearity are symmetric around 0 Oe, but are increased towards positive fields. That is because both quantities are dominated by the reference layer, not the free layer. The reference layer in the measurement of Fig. 4.6.10 is pointing towards a negative out-of-plane direction, as seen in the major loop measurement of Fig. 4.6.8(a). The hysteresis and non-linearity observed in the minor loop measurement of Fig. 4.6.10 is therefore a product of early spin-canting effects in the reference layer.

For further investigation, the mean and the standard deviation of the maximum values of hysteresis and non-linearity in the ±1.5 kOe magnetic range are taken from three samples per wafer.

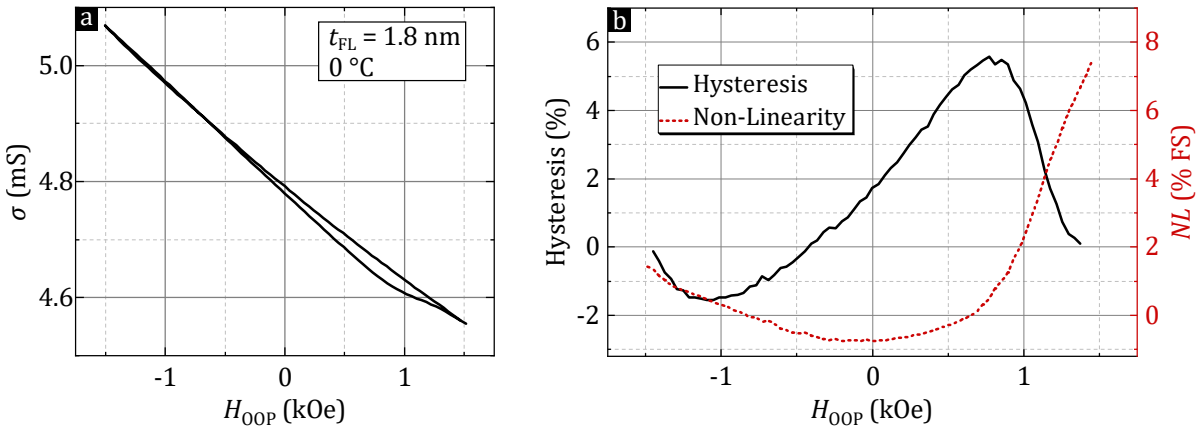

Fig. 4.6.10: TMR minor transfer curves of wafer 4 with $t_{FL} = 1.8$ nm at 0 °C. (a) Conductance in millisiemens. (b) Extracted hysteresis parameter and non-linearity.

The measurement on PCB samples reveal a similar drop of S with increasing t_{FL}, shown in Fig. 4.6.11(a) for 0 °C, as it was observed on wafer level in Fig. 4.6.6(a). In contrast to S, neither a correlation between hysteresis and t_{FL} nor between non-linearity and t_{FL} can be observed in Fig. 4.6.11(b). This is a further indication that both values are mainly caused by the reference layer of the TMR structure.

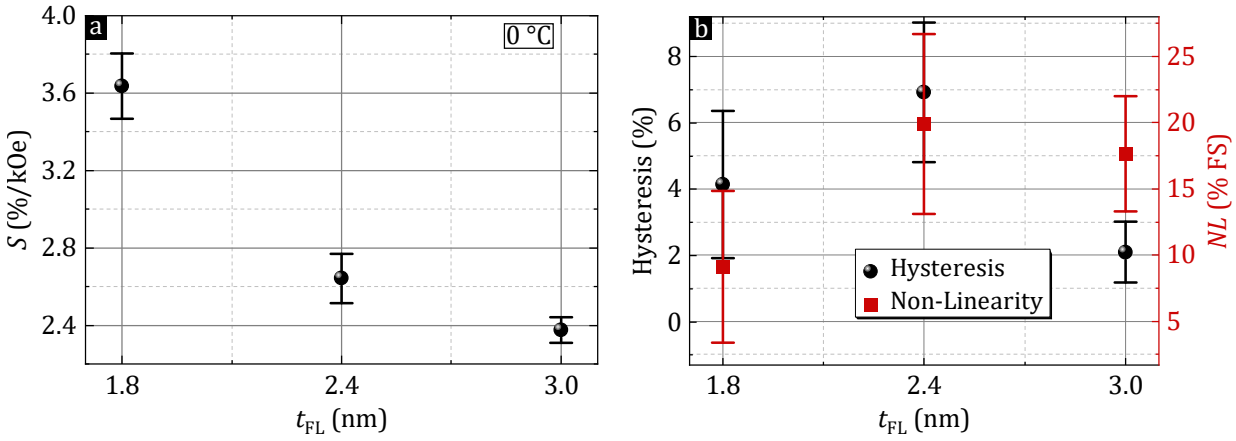

Fig. 4.6.11: TMR minor transfer curves at 0 °C, showing (a) sensitivity, (b) hysteresis and non-linearity for the wafers 2, 3 and 4 with $t_{FL} = 2.4$, 3.0, and 1.8 nm, respectively. Error bars represent the standard deviation for 3 samples of each wafer on a PCB.

Similar results are obtained for measurements at different temperatures T. The sensitivity, shown in Fig. 4.6.12(a) for wafer 4 ($t_{FL} = 1.8$ nm), reveals the expected decline with elevated temperatures, which among other factors is caused by the temperature dependent PMA and the consequential increase of H_k with T, as discussed earlier for Fig. 4.6.7. The temperature coefficient T_k, i.e. the relative change in $S(T)$, is about $T_k = -0.15\,\%/°C$. For hysteresis and non-linearity, shown in Fig. 4.6.12(b), no significant impact of temperature is observed.

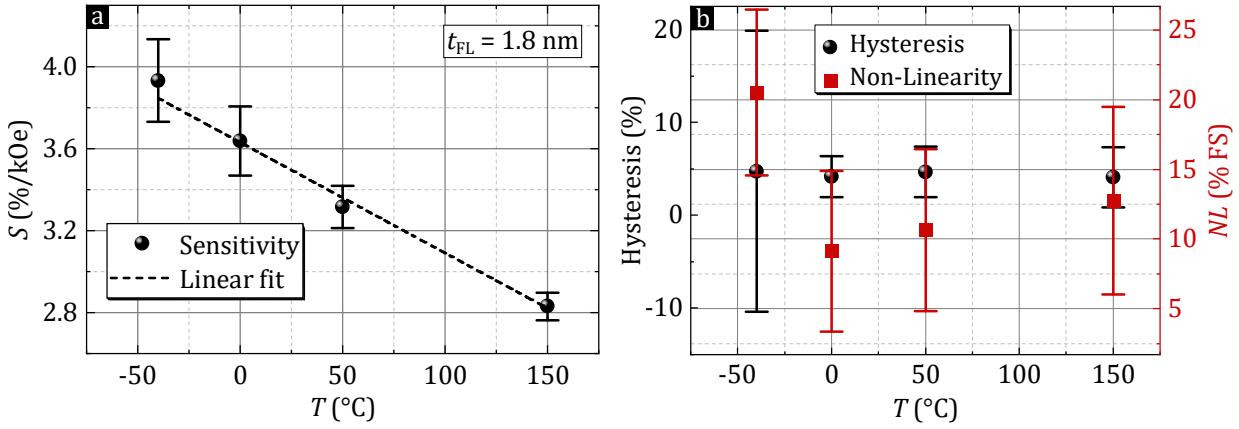

Fig. 4.6.12: TMR minor transfer curves of wafer 4 with $t_{FL} = 1.8$, showing (a) sensitivity, (b) hysteresis parameter and non-linearity for different temperatures. Error bars represent the standard deviation for 3 samples of the wafer on a PCB.

4.6.5 Summary

In summary, out-of-plane p-SAF structures were developed and used for out-of-plane sensitive TMR sensor designs. Several fabrication parameters and temperature influences were investigated.

Already for unstructured p-SAF and TMR stacks fabricated in Augsburg it was found that post annealing at $T_{\mathrm{PA}} = 250\,^{\circ}\mathrm{C}$ for 1 h at low pressure has minor to no effect on the p-SAF structure, but affects the effective magnetic anisotropy of the CoFeB free layer (FL). Due to boron diffusion and crystallization, the perpendicular magnetic anisotropy (PMA) at the MgO/CoFeB interface strengthens [214, 218, 219], which leads to a lower magnetic anisotropy field H_{k} of the in-plane free layer in an out-of-plane field. Furthermore, H_{k} is higher for greater free layer thicknesses t_{FL}.
Structured wafers were measured in TMR minor loops, where a significantly higher TMR ratio is observed, if the wafers have previously been exposed to high out-of-plane fields, likely because of a better magnetic alignment in the p-SAF reference system. Post annealing in the range of 275 °C to 325 °C shows only small effects with wafers that were annealed at 275 °C yielding slightly higher sensitivities S. S decreases with increasing t_{FL}, following a reciprocal fit function. The reference layer (RL) thickness t_{RL} shows a small increase in S for $t_{\mathrm{RL}} = 0.9\,\mathrm{nm}$ in comparison to $t_{\mathrm{RL}} = 0.7\,\mathrm{nm}$, but decreases significantly for $t_{\mathrm{RL}} = 1.1\,\mathrm{nm}$ with a higher error, which is attributed to the increased in-plane magnetic anisotropy for CoFeB layer thicknesses above 1.0 nm [61, 212, 216, 217]. TMR major loop measurements reveal H_{k} values for all FLs with $1.8\,\mathrm{nm} < t_{\mathrm{FL}} < 3.0\,\mathrm{nm}$ to be out of the measurement range up to 6.5 kOe. Furthermore, the p-SAF reference system is found to be relatively unstable with an exchange field H_{ex} of around 2.5 kOe and a wide magnetization transition from parallel to antiparallel alignment compared to optimized p-SAFs of the previous chapters. Hysteresis parameter and non-linearity calculations further confirm the instability of the reference layer to be the major contributor for flaws in the TMR sensor performance. S decreases with t_{FL} and T as expected, whereas hysteresis and non-linearity are not significantly affected and show a strong asymmetry, which matches the p-SAFs' magnetization reversal behavior.

In conclusion, the concept of an out-of-plane TMR sensor was presented and an understanding regarding the different parameters of influences established. While TMR minor loops disclose linear and hysteresis-free transfer curves in the field range of at least ±170 Oe, further improvements are necessary to achieve sufficient linearity in the range of kOe. These improvements may include an optimization of t_{FL} and a stabilization of the reference system. The latter may be achieved by reducing the number of bilayers in the Co/Pt multilayers, as seen in chapter 4.3, and exploring the option of an interlayer exchange coupling of the CoFeB reference layer (i.e. double p-SAFs).

4.7 Discussion and outlook

The aim of the research in this chapter was divided into three interdependent parts: Understanding the influences of fabrication parameters on the performance and magnetic behavior of perpendicular synthetic antiferromagnets (p-SAF), the development of a giant magnetoresistance (GMR) sensor with a dynamic field range of several kOe in an out-of-plane magnetic field, and the equivalent of the latter for a tunneling magnetoresistance (TMR) sensor. The following is a discussion of the most important results of this chapter. A brief outlook is given for possible future research on the topic of magnetoresistance sensors with a p-SAF as reference system and an in-plane free layer (FL). The discussion is divided into the design of the p-SAF system, of the GMR sensor, and of the TMR sensor.

4.7.1 Co/Pt based p-SAF structures

In the chapters 4.2 and 4.3 the fabrication of Co/Pt based multilayer (ML) systems and thereafter of p-SAF structures was optimized at the University of Augsburg. Optimization parameters included the seed layer composition, layer thicknesses of Ru (seed $t_{\text{Ru-seed}}$ and spacer t_{Ru}), Co t_{Co}, and Pt t_{Pt}, the bilayer repetition number N, and the order of materials in the ML/(Co)/Ru/ML stack in p-SAFs. The design of a double p-SAF structure, consisting of three antiferromagnetically coupled magnetic layers with two Ru spacer layers, was presented and investigated regarding magnetization balance and the related magnetization reversal process. The coupling of a CoFe reference layer (RL) was compared for single and double p-SAFs. Furthermore, micromagnetic simulations were performed to analyze spin-canting effects and the influence on the magnetization reversal process by the double p-SAF's individual layer saturation magnetization M_{S} and by the individual effective magnetic anisotropy K_{eff}.
Generally, the results on ML and p-SAF fabrication are in good agreement with similar research projects found in the literature. The most influential parameter for K_{eff} in Co/Pt ML systems is the Co thickness t_{Co}. In the literature, the preferred t_{Co} ranges from 0.20 nm [34] to 0.60 nm [168, 170, 172], which exactly matches the range in which perpendicular magnetic anisotropy (PMA) was found in this work. With magnetic anisotropy fields H_{k} up to 8.5 kOe, coercive fields H_{c} up to 0.8 kOe and K_{eff} values up to 6 Merg/cm^3, the ML systems perform very well in comparison to the literature [27, 28, 163, 168, 179]. However, there is still potential for stronger PMA, as the highest values have been achieved by Yakushiji et al. [34] with $H_{\text{c}} = 3$ kOe, $H_{\text{k}} = 20$ kOe, and $K_{\text{eff}} = 7$ Merg/cm^3. In their study, a $[\text{Co}(0.2)/\text{Pt}(0.2)]_6$ multilayer formed an fcc (111) oriented Co/Pt superlattice with monatomic layer-by-layer stacking. Thus, the group managed to minimize t_{Co} while maximizing texture and smoothness. In order to replicate this result, further optimization should be accompanied by transmission electron microscopy (TEM) to understand how fabrication parameters influence the ML's microstructure. Besides further reducing t_{Co}, additional parameters to investigate include the deposition temperature and the Ar pressure during sputter deposition [225].

For GMR and TMR sensors to operate in a wide magnetic field range, the switching fields of the p-SAF structure in the p-SAF reference system need to be accordingly high. The highest exchange fields H_{ex} were achieved in this thesis by using the first oscillation peak of the Ru mediated interlayer exchange coupling (IEC) at around 0.4 nm, having two Co layers sandwiching the Ru spacer layer, and reducing the Co/Pt multilayer repetition number N. For single p-SAF structures, $H_{ex} = 8.4\,\text{kOe}$ was achieved at room temperature, where $t_{Co} = 0.3\,\text{nm}$, $t_{Pt} = 0.2\,\text{nm}$, and $N = 5$ was utilized. The only p-SAF structure of the same design scheme found in the literate that outperforms this value was created by Yakushiji et al. [35] with $H_{ex} = 10\,\text{kOe}$. While their fabrication parameters are very similar to the ones of this thesis, slightly smaller thicknesses ($t_{Co} = 0.24\,\text{nm}$, $t_{Pt} = 0.16\,\text{nm}$) suggest that the higher performance can be attributed to their perfected Co/Pt superlattice, presented in their earlier work [34].

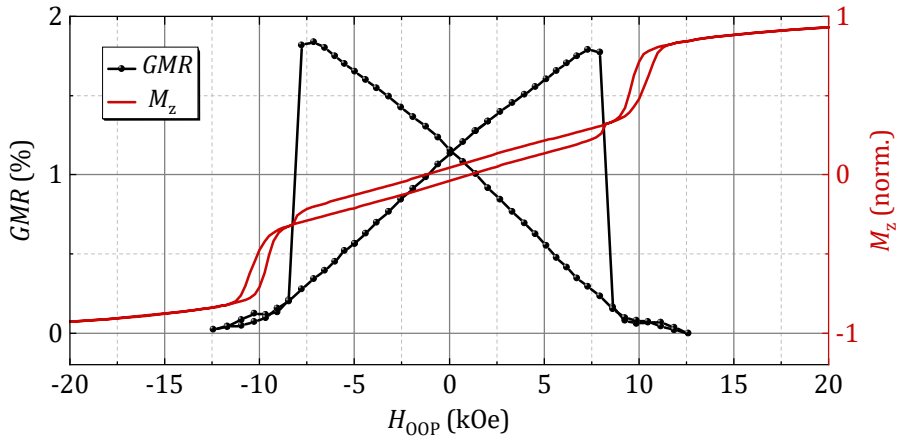

Fig. 4.7.1: Magnetoresistance measurement and M-H hysteresis loops of a GMR sensor with double p-SAF reference system. The GMR transfer curve yields a promising linearity up to the magnetization reversal of the p-SAF at 7.5 kOe.

Through the design of a double p-SAF, however, an even higher $H_{ex} = 10.3\,\text{kOe}$ was achieved. These structures evidently show potential for high exchange fields but also for stronger coupling to ferromagnetic layers with in-plane magnetic anisotropy, i.e. CoFe, than single p-SAFs. On the other hand, double p-SAF systems are more sensitive to unbalanced magnetic moments, which results in magnetization reversals and generally stronger spin-canting effects. Therefore, even though double p-SAFs yield higher exchange fields, they need to be carefully designed to provide stability at fields below the switching fields. One path to this, fairly unexplored in this thesis, might be the design of a purposefully unbalanced double p-SAF sensor, with a rigid antiferromagnetic alignment until a magnetization reversal occurs, i.e. minimization of spin-canting at low magnetic fields. In a GMR sensor with double p-SAF reference system, a dynamic field range with good linearity is achieved up to a magnetization reversal event at 7.5 kOe, shown in Fig. 4.7.1. Furthermore, micromagnetic simulations have shown that the loss of dynamic field range due to a magnetization reversal is expected to be in the range of 0 kOe to 1 kOe only (see Fig. 4.3.13). Another approach for more stable p-SAF systems is the implementation of iridium layers [36, 226]. In a further study by Yakushiji et al. [36] substituting iridium for the Ru spacer layer increased H_{ex} from 10 kOe to 12 kOe.

4.7.2 GMR sensors

In chapter 4.5 GMR sensors with out-of-plane reference layer and in-plane free layer were investigated, focusing on the free layer magnetic anisotropy field H_k. In that respect, CoFe was discussed as a material for sensors of this design. While it is commonly used for in-plane sensitive GMR sensors [107, 155], its destabilizing effect on the p-SAF systems of this work and its high H_k in the FL proved to be disadvantageous. However, there are reports by other groups of thin CoFe layers showing perpendicular magnetic anisotropy (PMA) [23, 190]. Therefore, additional studies on the prospects of CoFe implementation into out-of-plane GMR sensors might be useful. Further, four different FL systems were presented in chapter 4.5. These systems, labeled $S_{a\text{-}d}$, consist of Co layers, Co/Pt MLs, and Co/CoFe bilayers. Their respective H_k fields were studied in a single p-SAF GMR sensor setup and correlated to their Co thicknesses t_{Co}. A reciprocal behavior was found, matching the expected change in $K_{eff} = K_V + 2K_S/t$. Besides t_{Co}, the FL system design plays an important role for H_k, which allows the fabrication of low H_k values with relatively thick t_{Co} values (see Fig. 4.5.3(a)). Systems with ML design ($S_{b,c}$) generally yield smaller H_k values at the same t_{Co}. Furthermore, the relation of H_k to the GMR sensors' sensitivity S was investigated. GMR sensors of all FL designs follow a reciprocal fit over H_k, which agrees with the Stoner-Wohlfahrth model [37] and the results of other research groups [5, 23]. Because of the decreasing GMR effect for $t_{Co} < 2\,\text{nm}$ [207, 208], FLs with ML systems reach the highest sensitivities. The highest S was measured for a GMR sensor with a FL design S_c: Co(2)/Pt(0.25)/$[$Co(0.35)/Pt(0.25)$]_5$, yielding $H_k = 3.2\,\text{kOe}$, and $S = 0.74\,\%/\text{kOe}$.
At last, p-SAF switching and spin-canting results of the previous chapter were combined with this chapters' H_k manipulation to fully understand the magnetization reversal process and GMR transfer curves of single and double p-SAF GMR sensors with different FL designs. The results were supported by micromagnetic simulations. Besides the established understanding, GMR sensors with different characteristics were developed, with GMR amplitudes up to 4 %, sensitivities up to $S = 0.74\,\%/\text{kOe}$, and dynamic field ranges up to 9 kOe. The GMR sensors of this work have the highest magnetic field range of GMR or TMR sensors reported in the literature.

A next step should be the characterization of FL designs with respect to their non-linearity and hysteresis. First minor loop measurements in Fig. 4.5.5 suggest a higher hysteresis with smaller H_k. However, no correlation to the FL system types $S_{a\text{-}d}$ has been investigated so far. In addition, temperature dependencies should be further explored. *M-H* hysteresis loops of GMR sensors presented in Fig. 4.3.18 show the expected increase of PMA [227, 228] and IEC [175] at lower temperatures. In that regard, future measurements of interest include magnetoresistance measurements at low and elevated temperatures, which includes the investigation of the temperature dependence of non-linearity, hysteresis, and sensitivities for GMR sensors employing different FL systems ($S_{a\text{-}d}$).

4.7.3 TMR sensors

In chapter 4.6 TMR sensor stacks were fabricated and characterized. Preliminary stack development was done at the University of Augsburg. Thereafter, nine TMR stacks were deposited on structured Si wafers at Singulus Technologies AG and post-processed as well as measured at Infineon Technologies AG. Later, devices from four wafers were installed on printed circuit boards (PCBs) for measurements at higher magnetic fields with temperatures ranging from $-40\,°C$ to $150\,°C$.
It was found that post annealing at temperatures around $300\,°C$ for 1 h had only minor effects on the p-SAF system, matching with post annealing measurements of ML systems in chapter 4.2.3 and of p-SAF structures in chapter 4.3.4. Further, post annealing was found to increase PMA at the CoFeB FL, attributed to boron diffusion, crystallization and a stronger spin-orbit hybridization at the MgO/CoFeB interface. The FL H_k increases with increasing FL thickness t_{FL}, leading to a higher sensitivity S. Hence, matching the observations made for GMR sensors in chapter 4.5. A variation in reference layer thickness t_{RL} disclosed a decline in S with increased deviations, suggesting emerging instabilities of the p-SAF reference system. Higher temperatures lead to a decrease in S as generally expected for TMR sensors [187] and, in particular, for sensors of this design due to the temperature dependent magnetic anisotropy of the free layer [217, 224]. The decrease in S is about $T_k = -0.15\,\%/\mathrm{kOe}$.

Even though the general working principle of out-of-plane TMR sensors with a dynamic magnetic field range of several kOe was shown successfully, the TMR sensors at hand have two problematic shortcomings that need to be addressed.
TMR major loops revealed free layer H_k fields far higher than the operable dynamic range, set by the p-SAF reference system. Therefore, the sensitivity is unnecessarily reduced. An intuitive improvement is the design of thinner CoFeB free layers to reduce H_k. However, since ultrathin CoFeB layers are more likely to be discontinuous and fall into a superparamagnetic state [75], another approach could be the adoption of the free layer systems developed in chapter 4.5.2. Specifically system S_c, with, in this case, $\mathrm{CoFeB}(t_{\mathrm{CoFeB}})/\mathrm{Ta}(0.3)/[\mathrm{Co}(0.35)/\mathrm{Pt}(0.25)]_{N_{Sc}}$.
Secondly, the lack of p-SAF stability is evident from wide alignment transitions visible in magnetization and TMR measurements, and from hysteresis and non-linearity results. To gain stability, less bilayer repetitions N in the multilayer should be used. Most likely, however, the instability is also due to the CoFeB reference layer. Again, it is unclear, if further thinning of the reference layer improves the stability, or if a superparamagnetic state may form [75]. Instead, the use of interlayer exchange coupling from the multilayer systems of the p-SAF to the CoFeB RL might be of interest (i.e. double p-SAFs), as it was seen to yield better coupling to CoFe layers in chapter 4.3.6. In fact, in a study by Chatterjee et al. [185], IEC coupling of a Co/Pt ML to a CoFeB RL was used for magnetoresistive random access memory stacks (MRAM). With a Ru(0.4)/W(0.2) spacer bilayer, stable p-SAFs up to 3 kOe were achieved. Generally, tungsten has become a popular alternative to Ta as a boron sink adjacent to CoFeB [214, 217–220].

Chapter 5

Perpendicularly magnetized free layer

In this chapter, tunnel magnetoresistance (TMR) sensors are developed, consisting of a reference layer (RL) with an in-plane effective magnetic anisotropy and a free layer (FL) with a perpendicular magnetic anisotropy (PMA). The aim is to identify the influences of fabrication parameters on the perpendicularly magnetized FL, and to characterize the sensor performance with regard to its sensitivity, linear range, hysteresis, and other performance criteria.
Concerning the free layer, a distinction between two sensor types is made: TMR sensors with a superparamagnetic FL, and TMR sensors with a ferromagnetic FL. Starting with blanket wafer measurements of superparamagnetic $Co_{60}Fe_{20}B_{20}$ (60:20:20) FL sensors, the correlation of sensor sensitivity S, linear range (LR), and FL thickness t_{CoFeB} is discussed. Furthermore, the effect of post annealing is investigated. In this regard, two capping layer stacks are considered, which differ in their materials' tendency towards interdiffusion. Structured TMR sensors allow a more quantitative analysis of the sensor performance, including hysteresis measurements and the influence of measurement temperature. These results are compared to measurements of another stack variation, using a 40:40:20 CoFeB composition as FL.
Subsequently, TMR sensors with ferromagnetic free layers are discussed and compared to the superparamagnetic free layers. Here, a stronger focus is put on the behavior at high magnetic fields and the non-linear change in sensitivity as a function of measurement temperature.

5.1 Sample fabrication

The samples of this chapter are fabricated using magnetron sputtering on 200 mm silicon wafers. Superparamagnetic TMR sensors stacks are deposited at Infineon Technologies AG (IFX), whereas TMR stacks with ferromagnetic free layer stacks are deposited at a demo vendor. Figure 5.1.1(a) shows the general concept of cross-geometric magnetic anisotropies of reference and free layer, separated by a tunnel barrier (TB). The reference layer is magnetized along the direction which is here defined as the x axis. Figure 5.1.1(b) illustrates the full layer stack. The reference system consists of several magnetic layers. At the bottom, an antiferromagnet (AFM) is deposited,

above which a ferromagnetic layer is pinned via exchange bias (pinned layer, PL). With a spacer layer, the reference trilayer FM/Ta/CoFeB above is antiferromagnetically interlayer exchange coupled to the PL, with FM denoting a ferromagnetic material. The Ta in the trilayer serves as a buffer layer and boron sink for the CoFeB reference layer. MgO is used as the TB. The FL is a thin CoFeB layer, for which different compositions are used in this chapter:
(i) 60:20:20
(ii) 40:40:20
(iii) 20:60:20

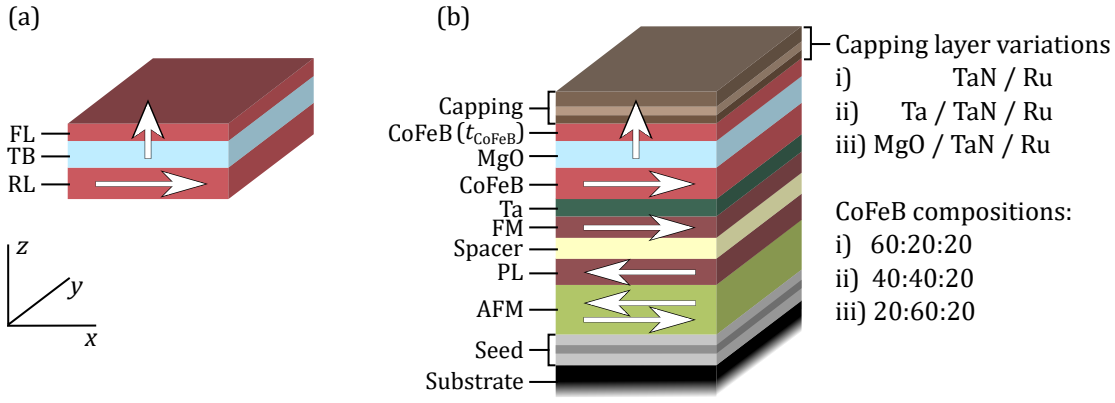

Fig. 5.1.1: Illustrations of TMR sensor stacks, employing a CoFeB free layer with perpendicular magnetic anisotropy. (a) General concept for the magnetic anisotropy of free layer and reference layer. The magnetization directions at zero field are represented with white arrows. The FL magnetization is directed out-of-plane. The RL magnetization is directed in-plane, here defined as the x-direction. (b) Full TMR sensor stack. The reference layer consists of a FM/Ta/CoFeB trilayer that is magnetically coupled to the pinned layer via interlayer exchange coupling. The pinned layer is exchange biased to an antiferromagnet. For the capping layer, three configurations are used which mainly differ in the layer adjacent to the FL being TaN, Ta or MgO. TMR structures with various CoFeB compositions are fabricated: 60:20:20, 40:40:20, and 20:60:20.

The sensors are capped with different variations of capping layer stacks:
(i) TaN(20 nm)/Ru(5 nm)
(ii) Ta(3 nm / 1 nm)/TaN(20 nm)/Ru(5 nm)
(iii) MgO(0.8 nm)/TaN(20 nm)/Ru(5 nm)

All wafers are post processed at Infineon, including 1 h post annealing in an in-plane magnetic field of 10 kOe. The post annealing temperature T_{PA} is set to 300 °C if not stated otherwise. Blanket wafer measurements are performed on wafers with no further processing. Measurements on the probe station (wafer level) are conducted on structured wafers (compare chapter 3.4.2.2). For high magnetic field measurements ($H > 2$ kOe) and measurements involving out-of-plane magnetic fields, TMR modules are cut out of structured wafers and soldered onto printed circuit boards (PCB).

5.2 Superparamagnetic free layers

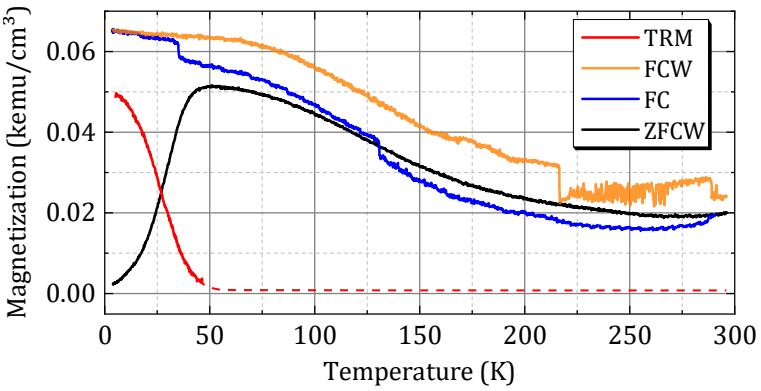

Fig. 5.2.1: M-T measurements of a 60:20:20 (0.9 nm) free layer grown on top of an MgO(1 nm) tunnel barrier, post annealed at 300 °C for 1 h. The results for thermoremanent magnetization (TRM), field cooled warming (FCW), zero field cooled warming (ZFCW), and field cooled (FC) measurements strongly indicate the presence of superparamagnetism in the sample (compare section 2.1.3.1). The blocking temperature lies at approx. $T_\mathrm{b} = 40\,\mathrm{K}$.

All IFX deposited free layers with PMA are superparamagnetic. A distinct characteristic of superparamagnetism is its strong magnetization M dependence on temperature T with a specific blocking temperature T_b. Above T_b thermal energy disorders the uniform spin direction at a higher rate than the measurement rate of the setup. This leads to M-T measurement results that depend on the initial magnetization state and temperature, as described in more detail in chapter 2.1.3.1. Figure 5.2.1 exemplary shows the results of an M-T measurement for a 60:20:20 (0.9 nm) FL, deposited on top of an MgO(1 nm) tunnel barrier and capped with TaN. From thermoremanent magnetization (TRM) and zero field cooled warming (ZFCW) measurements in a SQUID-VSM, T_b can be estimated to be around 40 K. The low magnetization values and general temperature dependence agree with the expectation for superparamagnetic behavior.
In the following, results for superparamagnetic TMR sensors are presented and discussed. Measurements of TMR sensors with 60:20:20 free layers are followed by a comparison to results from TMR structures with a 40:40:20 FL.

5.2.1 $Co_{60}Fe_{20}B_{20}$ free layers

5.2.1.1 Blanket wafer measurements

With the reference layer having an effective magnetic anisotropy directed along the x-axis, the magnetoresistance (MR) is measured as a function of an externally applied field H_x in x. The magnetic range, in which the conductance depends on the external field, is determined by the FL effective magnetic anisotropy K_eff. Higher PMA in the FL means that stronger fields are needed to saturate the FL along the x-axis. The field at which the FL magnetization is saturated along its magnetic hard axis is the magnetic anisotropy field H_k. Figure 5.2.2 presents the described behavior. Measurements are obtained from blanket wafer samples in a current in-

plane tunneling (CIPT) setup. The TMR sensor stacks have 60:20:20 CoFeB free layers of various thicknesses t_{CoFeB}, TaN/Ru capping and were post annealed at 280 °C for 1 h in a 10 kOe in-plane field. K_{eff} in MgO/CoFeB bilayers is thickness dependent, as shown in Fig. 5.2.2(a). The scale of the conductance G is normalized to show the measured data from -1 to $+1$, obtained by implementing the equation

$$G_{\mathrm{norm}} = 1 + 2\frac{G - \max(G)}{\max(G) - \min(G)}. \tag{5.1}$$

The purpose of this being an easier visual comparison of samples with different t_{CoFeB}. As shown, G_{norm} for $t_{\mathrm{CoFeB}} = 0.9\,\mathrm{nm}$ depends on H_x for the entire measurement field range of $\pm 1.5\,\mathrm{kOe}$, whereas the high localization of field dependence for the $t_{\mathrm{CoFeB}} = 1.5\,\mathrm{nm}$ sample suggests an in-plane K_{eff} of the FL. Besides the field range, also the signal amplitude depends on t_{CoFeB}, as shown in Fig. 5.2.2(b).

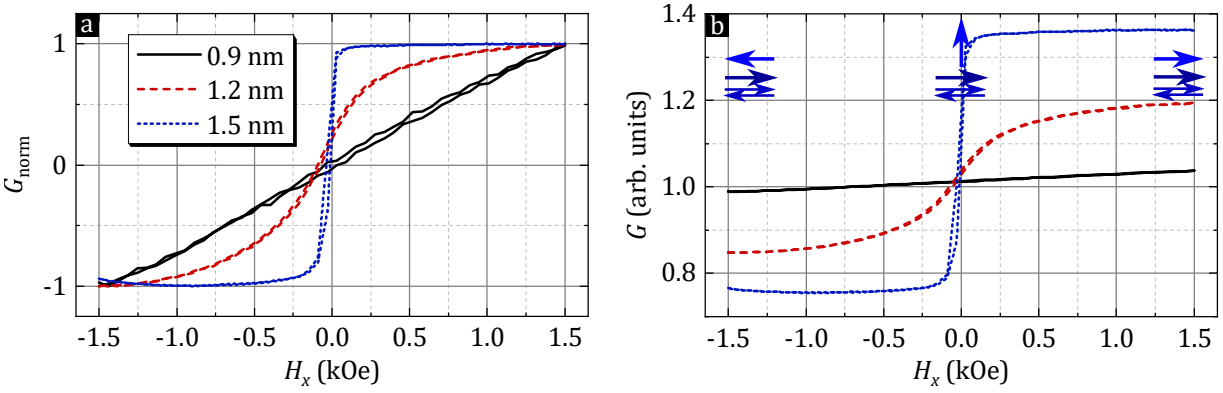

Fig. 5.2.2: CIPT measurements at room temperature of a TMR structure with in-plane reference layer on blanket wafer level. The externally applied magnetic field is aligned along the axis of the reference layer magnetization direction, here defined as x direction. (a) shows the conductance in the normalized scale defined in Eq. 5.1. With increasing FL t_{CoFeB} the change in conductance as a function of field is more localized around 0 kOe, indicating the thickness dependent magnetic anisotropy of the FL. (b) shows the same measurement with the conductance given in the arbitrary units of the CIPT setup. Here, the dependence of measurement signal on t_{CoFeB} is well visible. Blue arrows illustrate the configuration of magnetization directions of reference system and free layer, where the free layer is rotated from its perpendicularly magnetized state at zero field to an in-plane magnetization direction.

Thus, while the TMR amplitude increases with t_{CoFeB}, the linear range (LR) decreases. The LR is here defined as the magnetic range at which the non-linearity (NL) remains below 1 % of the full scale (% FS). NL is defined as

$$NL\,(H) = \frac{G\,(H) - G_{\mathrm{fit}}\,(H)}{\max(G) - \min(G)}, \tag{5.2}$$

where G_{fit} is the conductance from a linear fit to the measured conductance around zero field. Besides its use in applications, the LR also provides a substitution for the effective anisotropy field H_{k} in the measurement evaluation. For most structures in this chapter, H_{k} cannot be determined, since either the applied magnetic fields are too low to achieve magnetization saturation, or the superposed magnetization change of the reference layer distorts the measured transfer curves. The evaluation of the linear range, on the other hand, is also constrained by the maximum applied

field, but without the need to know the saturation fields. The limit for the smallest linear ranges that can be determined is given by the field step size of the measurement (the sensor detectivity is discussed later in this chapter).

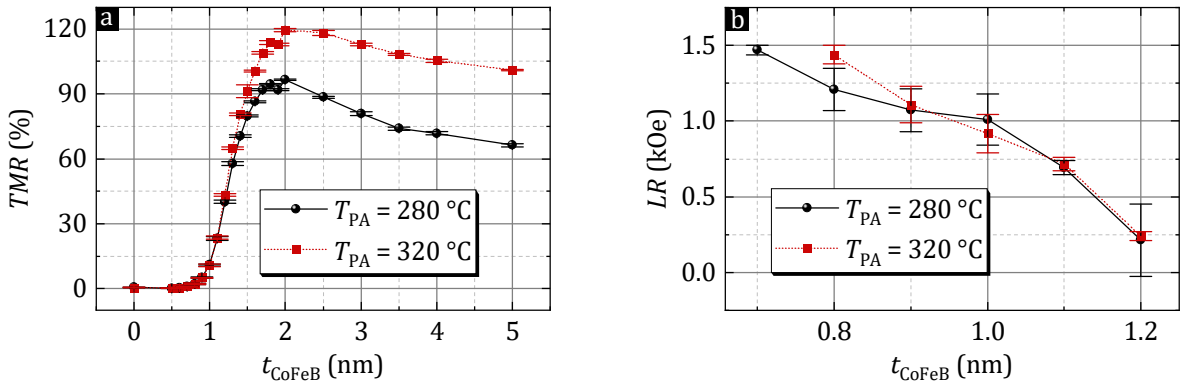

Fig. 5.2.3: (a) TMR amplitudes and (b) linear range as a function of t_{CoFeB} at room temperature, extracted from CIPT measurements for TMR structures that were processed with two different post annealing temperatures T_{PA}. Error bars represent the standard deviation at different wafer positions.

The results for TMR amplitude and LR as a function of t_{CoFeB} are shown in Fig. 5.2.3. Below a thickness of 1.2 nm, the TMR amplitude increases quickly with increasing t_{CoFeB}, but generally remains small with a TMR amplitude below 25 % for $t_{CoFeB} = 1.1$ nm. This low amplitude can be explained by the FL being superparamagnetic. Besides the low magnetization, superparamagnetism also means that CoFeB is divided into nanostructures instead of being a continuous crystalline layer. This hinders the coherent tunneling that is usually responsible for high TMR amplitudes in CoFeB/MgO/CoFeB layers. For higher thicknesses, the FL becomes ferromagnetic. Consequentially, TMR amplitudes are an order of magnitude higher, with a saturation at $t_{CoFeB} = 2$ nm. The LR decreases linearly with increasing t_{CoFeB} (Fig. 5.2(b)). For small thicknesses, the FL has a perpendicular magnetic anisotropy, which transitions to an in-plane magnetic anisotropy when t_{CoFeB} is increased. This leads to the change in LR. Additionally to t_{CoFeB}, the post annealing temperature T_{PA} is varied for this measurement series, featuring 280 °C and 320 °C for 1 h. In the low thickness regime, no significant difference emerges. For higher thicknesses, the 320 °C annealed samples show higher TMR amplitude than the 280 °C samples, which is likely due to a better crystallization of the MgO and CoFeB layers.
The thickness dependence of TMR amplitude and effective magnetic anisotropy is also reflected in the sensitivity S, here defined as the relative change of the conductance over applied field within the range of linearity, i.e.

$$S = \left(\frac{\Delta G}{\Delta H}\right)_{\text{linear}} / G_0, \tag{5.3}$$

with G_0 being the conductance at zero field. Figure 5.2.4 shows the results for S, extracted from CIPT measurements. While S follows an exponential increase with t_{CoFeB}, the sensitivity and linear range show a reciprocal relation, which will be further quantified later in this chapter, when more precise measurements on structured TMR sensors are obtained.

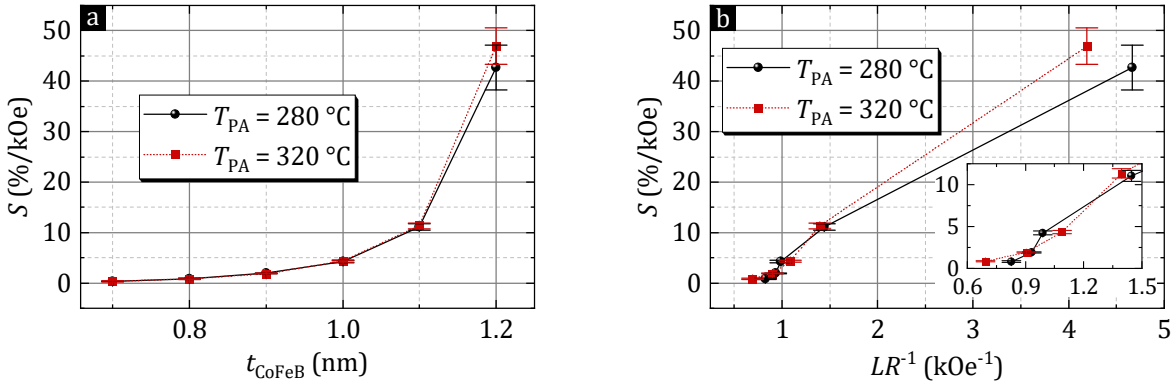

Fig. 5.2.4: Sensitivities as a function of (a) t_{CoFeB} and (b) LR^{-1}, extracted from CIPT measurements at room temperature. The latter displays a somewhat linear behavior.

In the literature, a more commonly used capping layer for MgO/CoFeB bilayers with PMA is the use of Ta [55, 119, 229, 230]. However, the measurement results shown thus far were obtained from structures with a TaN capping layer, which is found to be the preferred choice. The reason for this is the difference of diffusion tendency, which is discussed in the following.

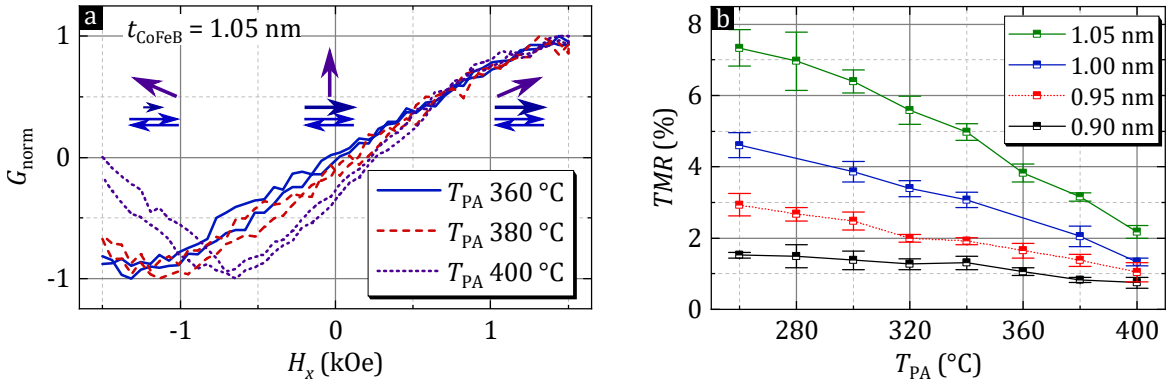

Fig. 5.2.5: CIPT measurement results for a TMR structure on blanket level with Ta capping layer. (a) Field dependence of G_{norm} for a FL with $t_{\mathrm{CoFeB}} = 1.05\,\mathrm{nm}$ and various post annealing temperatures from 360 °C to 400 °C. Blue arrows illustrate the reference system magnetization directions with an instability emerging for fields below approx. 750 Oe, depending on T_{PA}. This instability is visible as change in magnetization along the x-axis of the reference layer, here in the case of $T_{\mathrm{Pa}} = 400\,°\mathrm{C}$. The free layer on top is drawn in purple. (b) TMR amplitude as a function of T_{PA} for several t_{CoFeB}, showing a decline in both increasing T_{PA} and decreasing t_{CoFeB}.

Figure 5.2.5(a) shows G_{norm} as a function of field from CIPT measurements for TMR structures on blanket wafers with a Ta(3 nm)/TaN(20 nm)/Ru(5 nm) capping layer stack. Exemplary, three different post annealing temperatures are presented. Even though a FL with $t_{\mathrm{CoFeB}} = 1.05\,\mathrm{nm}$ has a linear range of only 0.75 kOe when no Ta capping layer is used, the here shown samples with Ta capping layer display a somewhat linear behavior up to the measurement range of 1.5 kOe. An analysis of the linear range is not possible due to the dominant noise that is obscuring the low signal. At negative fields, however, the conductance transfer curve reveals a clear non-linear behavior at fields below −0.5 kOe. The higher T_{PA}, the smaller are the fields at which this is observed. This is related not to the free layer, but to a change in reference layer magnetization along the x-axis, as illustrated by the blue arrows. The TMR amplitudes for several FL thicknesses are shown in Fig. 5.2.5(b) as a function of T_{PA}. The *TMR* declines with

decreasing t_{CoFeB} and increasing T_{PA}. The same behavior occurs for the sensitivity, as shown in Fig. 5.2.6(a). In Fig. 5.2.6(b), the sensitivities of the earlier shown TaN capped structures are compared to the Ta capped TMR stacks. While the qualitative behavior is similar, the Ta capped structures have significantly lower S values at the same nominal t_{CoFeB}. A possible reason is the diffusion of Ta. Ta is known to diffuse into the CoFeB free layer, creating so called magnetic dead layers, effectively thinning the FL [231]. The real CoFeB FL thickness of the Ta capped structures is significantly reduced. TaN, on the other hand, is a diffusion barrier [232]. Post annealing temperatures, that are driving the diffusion process, therefore have a smaller impact in TaN structures.

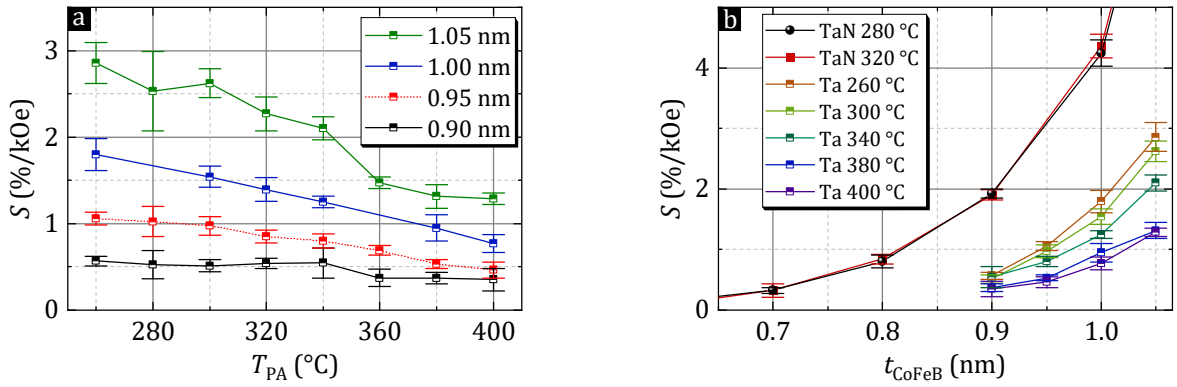

Fig. 5.2.6: Sensitivities of TMR structures with various FL t_{CoFeB} and T_{PA}, extracted from CIPT measurements. (a) shows a linear decrease of S for increasing T_{PA}. (b) shows an increase with increasing t_{CoFeB}. A comparison to TMR structures with TaN capping reveals a qualitatively similar behavior, with the difference of a higher post annealing temperature sensitivity and a shifted S-t_{CoFeB} curve for structures with a Ta capping layer.

5.2.1.2 Structured wafer measurements

Because of the higher resilience against diffusion effects, the here fabricated structured wafers of 60:20:20 CoFeB samples are capped with TaN(5 nm)/ Ru(20 nm), i.e. without Ta. T_{PA} is set to 300 °C for 1 h. The results from probe station TMR measurements are generally consistent with the previously shown blanket wafer measurements. The shape of the transfer curves are presented in Fig. 5.2.7(a), showing G_{norm} and the measurement hysteresis. Because of the higher applied magnetic fields in the probe station, reference layer instabilities become more visible at negative fields. In Fig. 5.2.7(b), the extracted maximum hysteresis of each measurement as a function of t_{CoFeB} gives a good indication of the thickness dependent transition from PMA ($t_{\mathrm{CoFeB}} < 1.1\,\mathrm{nm}$) to in-plane magnetic anisotropy ($t_{\mathrm{CoFeB}} > 1.1\,\mathrm{nm}$). Shown are the averaged hysteresis values for measurements of multiple modules of a wafer, with the standard deviation used as error bars.

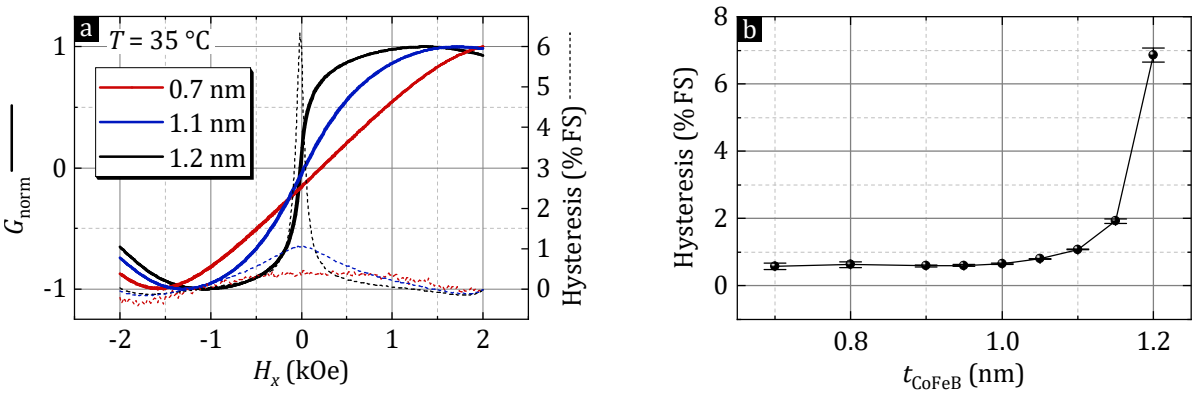

Fig. 5.2.7: Probe station measurements of structured TMR sensors with various FL t_{CoFeB}. (a) Normalized tunneling current and hysteresis for three exemplary FL thicknesses as a function of H_x at 35 °C. The hysteresis, shown in (b), stays below 1 % FS for $t_{\mathrm{CoFeB}} < 1.1$ nm, above which the hysteresis rapidly increases. Error bars represent the standard deviation from measurements of various wafer dies.

TMR amplitudes and linear ranges for measurement at 35 °C are shown in Fig. 5.2.8(a). Consistent with the CIPT measurements, the TMR amplitude increases with t_{CoFeB}, whereas the linear range decreases. That yields the reciprocal relation of sensitivity as a function of linear range, shown in Fig. 5.2.8(b), which can be approximated by

$$S_{60:20:20} = \frac{1}{12.7 \times LR} - 0.08\,\mathrm{kOe}^{-1}. \tag{5.4}$$

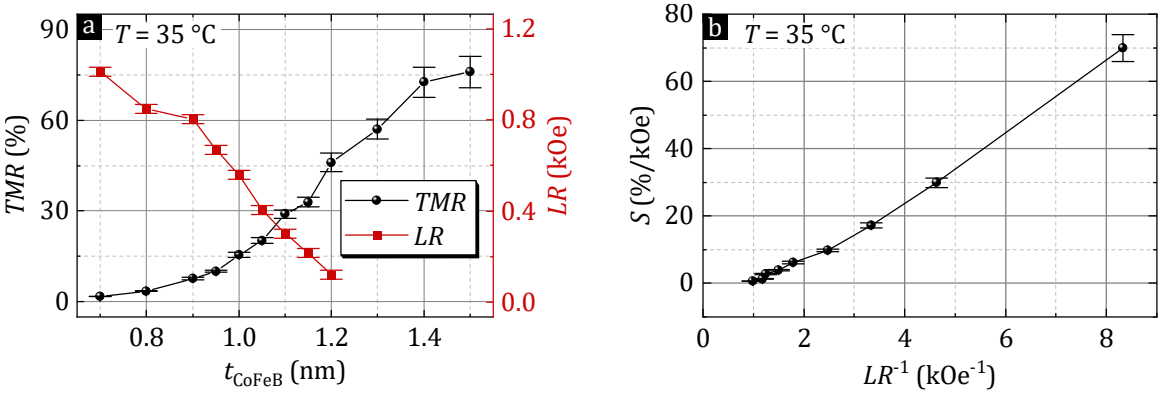

Fig. 5.2.8: (a) TMR amplitude and LR of structured TMR sensors at 35 °C. With higher t_{CoFeB}, TMR amplitude increases, while the LR decreases. (b) Reciprocal plot of sensitivity for TMR sensors of various FL t_{CoFeB}.

In Fig. 5.2.9(a), the transfer curves for two different measurement temperatures are shown. The shape of the curve remains the same, whereas the amplitude is decreased for a higher measurement temperature. As a result, the sensitivity decreases. This temperature dependent change in sensitivity is quantified as the temperature coefficient T_{k}, here defined as

$$T_{\mathrm{k}} = \frac{\Delta S}{\Delta T} / S_{T=35\,^{\circ}\mathrm{C}}. \tag{5.5}$$

Typical values for T_{k} for TMR sensors are around −0.1 to −0.2 %/°C [233], whereas the temperature coefficient for the here measured superparamagnetic 60:20:20 sensors is $T_{\mathrm{k}} = -0.5$ %/°C.

The higher value is expected, since superparamagnetic structures are strongly temperature sensitive by their nature (compare Fig. 5.2.1). The temperature effect on the linear range is only minor with

$$|T_{LR}| = \left| \frac{\Delta LR}{\Delta T} / LR_{T=35\,^\circ\mathrm{C}} \right| < 0.15\,\%/^\circ\mathrm{C} \tag{5.6}$$

for any FL thickness.

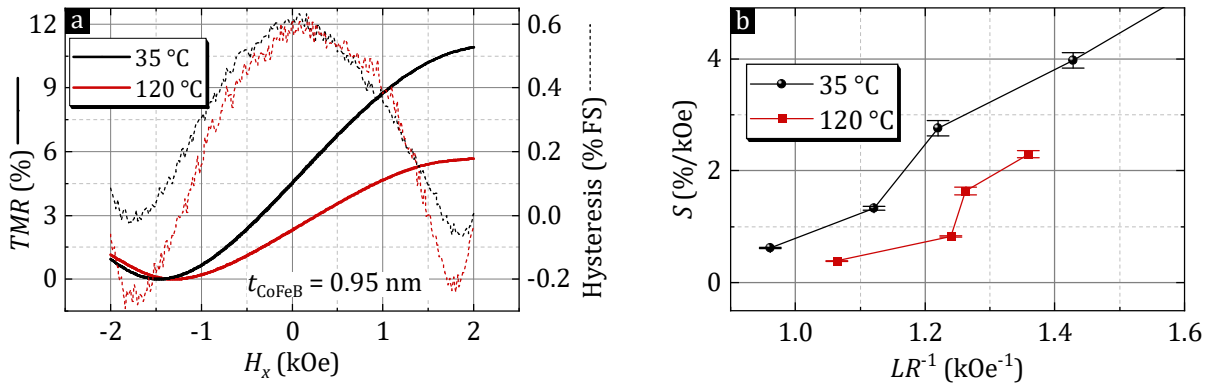

Fig. 5.2.9: (a) TMR amplitude and hysteresis for two different measurement temperatures $T = 35\,^\circ\mathrm{C}$ and $120\,^\circ\mathrm{C}$. (b) Decreasing sensitivity as a function of linear range.

5.2.2 $Co_{40}Fe_{40}B_{20}$ free layers

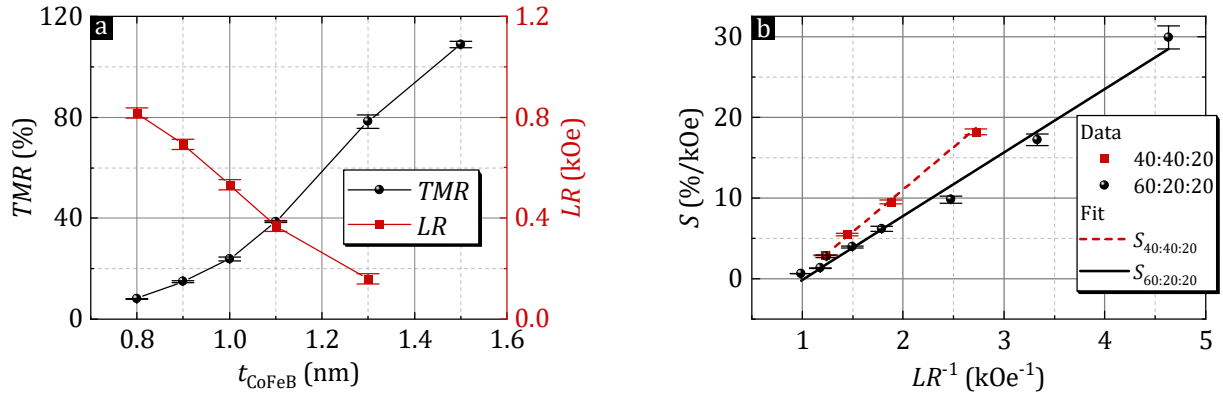

Fig. 5.2.10: (a) TMR amplitude and LR as a function of t_{CoFeB}, extracted from probe station measurements of a TMR sensor with 40:40:20 (t_{CoFeB}) free layer at 35 °C. The increasing TMR amplitude and decreasing LR yields (b) a reciprocal behavior of sensitivity over LR. A comparison to 60:20:20 samples reveals qualitatively the same behavior but, for 40:40:20 samples with high PMA, higher sensitivities at the same linear ranges.

In the following, TMR sensors of the same stack structure, but with a 40:40:20 free layer instead of 60:20:20 are discussed. The CoFeB composition has been reported to affect its magnetic properties and to have a strong impact on the crystal structure and can therefore influence the superparamagnetic behavior of the nanostructures [14, 33, 58, 59, 119, 234]. TMR amplitudes and LR are plotted in Fig. 5.2.10(a) for $T = 35\,^\circ\mathrm{C}$. The reciprocal S as a function of LR behavior is shown in Fig. 5.2.10(b), where also a comparison to the 60:20:20 samples is given. The sensitivity

for 40:40:20 samples is evidently higher with a higher slope in the plot. The data follows the fit

$$S_{40:40:20} = \frac{1}{9.5 \times LR} - 0.1\,\mathrm{kOe}^{-1}. \tag{5.7}$$

Furthermore, measurements at elevated temperatures yield a smaller temperature coefficient of $T_\mathrm{k} = -0.4\,\%/°\mathrm{C}$. The linear range decreases in the same small rate of $|T_{LR}| < 0.15\,\%/°\mathrm{C}$. The hysteresis (not shown here) is not affected by the change of CoFeB composition.

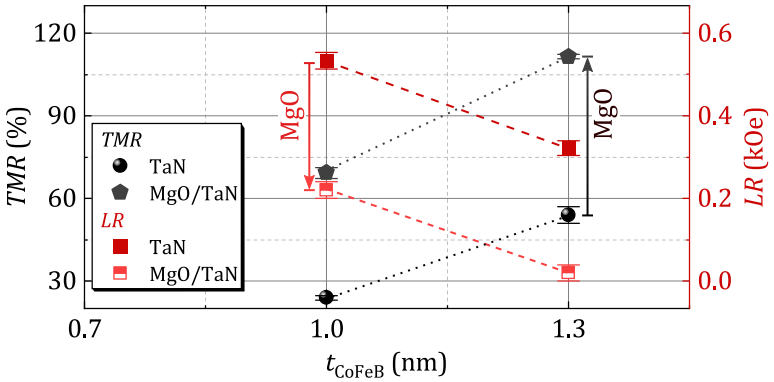

Fig. 5.2.11: Change of TMR amplitude and LR for TMR sensors with additional MgO capping on top of the 40:40:20 FL. For both here shown nominal thicknesses $t_{\mathrm{CoFeB}} = 1.0$ and 1.3 nm, the additional MgO layer shifts the TMR and LR values in accordance to approx. +0.25 nm t_{CoFeB} as shown in Fig. 5.2.10(a)

These results indicate that the above change in CoFeB composition reduces the superparamagnetic nature of the free layer, but still does not yield ferromagnetism. Another step to avoid superparamagnetism, i.e. the formation of nanostructures, might be the utilization of an additional MgO layer on top of the free layer. Besides adding an additional contribution to the PMA at the CoFeB/MgO interface, without reducing the FL thickness, the additional MgO may provide a protection to the CoFeB layers from Ta bombardment during the deposition process. The effect of the additional MgO layer for TMR sensors with a 40:40:20 FL is shown in Fig. 5.2.11. In comparison to $t_{\mathrm{CoFeB}} = 1.1$ and 1.3 nm without an MgO cap, the TMR amplitude significantly increases with MgO, whereas the LR significantly decreases. The reason, however, is unlikely to be due to the avoidance of nanostructures. Instead, it might be caused by the prevention of magnetic dead layers. Without the MgO cap, Ta particles might penetrate the CoFeB layer during the deposition of TaN. This would create magnetic dead layers that effectively thin the free layer down. This picture agrees well with the measurement, since the decrease of TMR amplitude and increase of LR corresponds to a gain in t_{CoFeB} of +0.25 nm for both here presented t_{CoFeB} cases (compare Fig. 5.2.10(a)). Thus, the MgO capped samples still follow the superparamagnetic fit from Eq. 5.7.

5.3 Ferromagnetic free layers

To compare the Infineon (IFX) deposited superparamagnetic samples with ferromagnetic samples, the same nominal stacks (with minor changes in the reference system) but with ferromagnetic free layers were provided by a demo vendor and further processed by Infineon. Two sensors are available, using either 40:40:20 or 20:60:20 CoFeB. Both free layers are $t_{\mathrm{CoFeB}} = 1\,\mathrm{nm}$ thick, are capped by a Ta(1 nm)/TaN(20 nm)/Ru(5 nm) stack and were post annealed for 1 h at 300 °C and 10 kOe in-plane magnetic field. The ferromagnetic behavior can be observed in a magnetoresistance measurement in an out-of-plane field, shown in Fig. 5.3.1. While the superparamagnetic IFX samples are hysteresis-free without any coercive fields of the PMA free layer, the *TMR* of the demo sample jumps at around ±0.2 kOe, caused by the coercive field of the ferromagnetic free layer. The corresponding magnetization directions of the respective layers in the demo sample are illustrated in purple (FL, top arrow) and blue (reference system) for a field sweep from positive to negative magnetic fields.

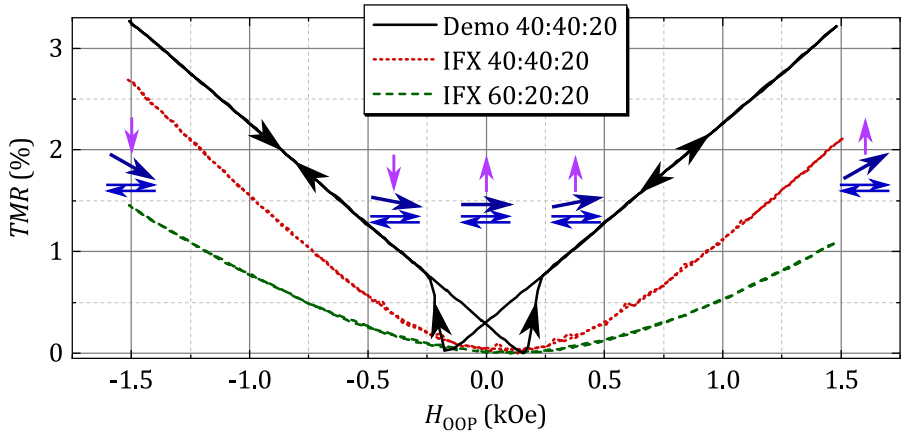

Fig. 5.3.1: Out-of-plane magnetic field measurements, comparing the TMR effect of the demo and IFX produced TMR sensors with $t_{\mathrm{CoFeB}} = 1\,\mathrm{nm}$. The IFX sensors show a hysteresis-free behavior, typical for superparamagnetism. Demo sensor measurements indicate a hysteresis of the perpendicularly magnetized free layer with a coercive field around 200 Oe. Magnetization directions of reference and free layer of the demo sensor are illustrated by the blue and purple arrows.

Magnetic in-plane measurements are shown in Fig. 5.3.2, where the *MR* and *NL* are plotted for (a) minor and (b) major loops. Here, the *MR* is set to 0 % at zero field to provide an easier comparison with an IFX sample in Fig. 5.3.2(a). The IFX TMR sensor with the highest available *LR* is chosen for the comparison. From the *MR* transfer curves it is already visible that, while similar instabilities of the reference layers occur in negative fields, the TMR amplitudes (and thereby sensitivities) of the demo wafers are significantly higher than that of the here shown 40:40:20 (0.8 nm) IFX sample. At the same time, however, the non-linearity increases faster with field for the IFX sensor than it does for the demo samples. That means that the demo samples yield both higher sensitivities as well as linear ranges, which is in contrast to the earlier observed reciprocal tradeoff between the two (see Fig. 5.2.10(b)). In fact, the major loop measurement of the 40:40:20 demo sample on PCB level in Fig. 5.3.2(b) even indicates a free layer saturation

at around 6 kOe external magnetic field. The linear range is thus significantly reduced only by the reference layer, which begins to destabilize at around $H_x = -2$ kOe when the applied field is directed antiparallel to the reference layer. At positive fields, the non-linearity takes an upward turn, peaking around 4 kOe. This behavior does not match the expected magnetization curve of the free layer, which would (and for higher H_x eventually does) cause a downward turn when the saturation magnetization is approached, and must thus be again related to reference layer instabilities. Even though the magnetic field is applied parallel to the initial state of the reference layer, destabilization may still occur due to the oppositely magnetized pinned layer, which is interlayer exchange coupled to the reference layer. Therefore, the linear range may be significantly higher than 2 kOe for this sample, if the reference system were to withstand higher magnetic fields.

In conclusion, the utilization of a ferromagnetic instead of superparamagnetic free layer increases both the sensitivity as well as linear range of a TMR sensor with perpendicularly magnetized free layer.

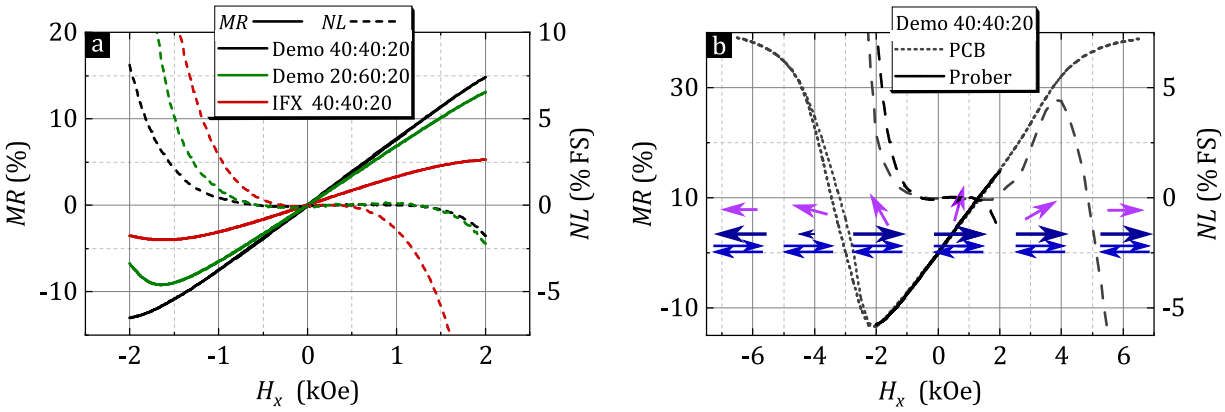

Fig. 5.3.2: Magnetoresistance measurements of TMR sensors with $t_{\mathrm{CoFeB}} = 1$ nm produced by a demo vendor. The magnetoresistance *MR* is scaled to zero at zero field for an easier comparison. The *NL* is given in percentage to full scale (% FS). (a) Measurements on wafer level at the probe station, comparing demo sensors with 40:40:20 (1 nm) and 20:60:20 (1 nm) free layers to an Infineon fabricated sensor with 40:40:20 (0.8 nm) free layer. Despite the earlier found tradeoff between sensitivity and linear range, the vendor produced sensors outperform the here shown IFX sample. A measurement in high magnetic fields on PCB level, shown in (b), reveals the linear range of the demo sensor to be primarily limited by the stability of the reference layer. The transfer curve at positive fields indicates a linear free layer magnetization rotation up to approx. 4 kOe, whereas at negative fields, the *MR* behavior is dominated by the in-plane magnetization change of the reference layer. The magnetization directions are illustrated by the purple and blue arrows, respectively.

In the following the demo TMR sensors are further investigated with respect to their behavior under temperature on PCB level. Figure 5.3.3 shows the (a) hysteresis and (b) sensitivity for temperatures between −40 °C and +150 °C. For the hysteresis of the 40:40:20 sample, no temperature dependence can be observed. While the variation across multiple samples is up to 0.4 % FS, all samples remain below a hysteresis value of 1 % FS. The hysteresis of the 20:60:20 demo sample lies below the detection range of the setup (0.3 %). The sensitivity of the 40:40:20 sample, on the other hand, follows an exponential increase with temperature that can be expressed with

$$S_{40:40:20} = [1.31\,\mathrm{E}{-5} \times \exp\left(T/53.79\,\mathrm{K}\right) + 0.064]\ \mathrm{kOe}^{-1}. \tag{5.8}$$

The sensitivity for the 20:60:20 demo sample with temperature increases up to 100 °C only. At 150 °C, the sensitivity drops.

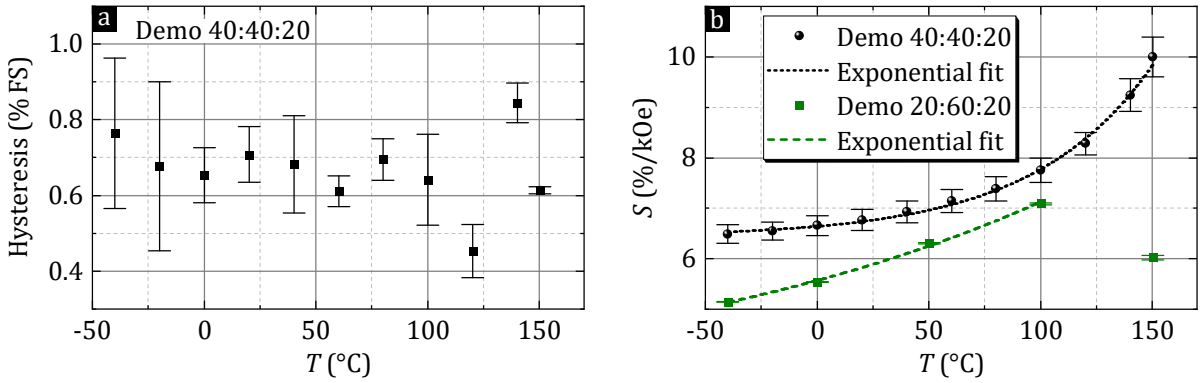

Fig. 5.3.3: Influence of measurement temperature on demo vendor produced TMR sensors. (a) The hysteresis is not significantly affected, staying below 1 % full scale for any temperature, whereas (b) the 40:40:20 sensor sensitivity follows an exponential fit with T. The 20:60:20 follows an exponential fit up to 100 °C only. At 150 °C the S decreases again.

The temperature dependence of S for the 40:40:20 demo sample being not only positive but even exponential strongly differs from the constant negative dependence found in previously discussed TMR sensors. However, it can be explained by the temperature dependent PMA. Generally, the interface PMA in MgO/CoFeB bilayers increases at lower temperatures [235]. That means, when measurement temperatures increase, the magnetic anisotropy field H_k of the free layer decreases, which affects the slope of the *TMR* transfer curve. As a result, even if the total TMR amplitude decreases with temperature, the sensitivity increases. The described behavior can be observed in Fig. 5.3.4 where the *MR* and *NL* are plotted for major loops with various measurement temperatures. *MR* slope, amplitude and saturation are all influenced by the temperature of the measurement. At negative fields, also the reference layer stability shows an expected earlier decline with higher temperatures.

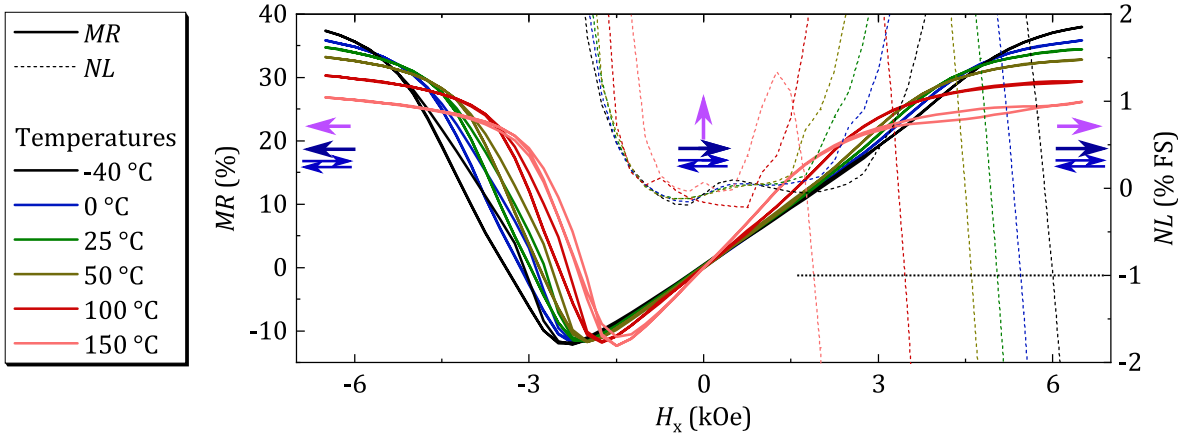

Fig. 5.3.4: *MR* and *NL* major loop measurements for the 40:40:20 demo sample on PCB level. Measurement temperatures influence the *MR* amplitude, slope, and saturation field.

The absolute TMR amplitudes as a function of temperature for the 40:40:20 and 20:60:20 samples

are plotted in Fig. 5.3.5(a). Note that a stable reference layer (i.e. allowing a full rotation from parallel to antiparallel alignment) would increase these amplitudes by 10-20 %. For both samples, the TMR decreases with increasing measurement temperature. While the decrease is very linear for the 40:40:20 sample with approximately $-0.07\,\%/°C$, the curve of the 20:60:20 sample is slightly curved with a stronger decrease for higher temperatures. To put the results for the ferromagnetic free layers in context to the superparamagnetic samples, the demo samples' linear range needs to be approximated. For this, the increase in *NL* due to the reference layer is disregarded and thus the linear range is defined as the field at which the *NL* is at $-1\,\%\,\mathrm{FS}$ (see Fig. 5.3.4). The results is shown in Fig. 5.3.5(b). For both samples, the *LR* decreases substantially with increasing T. While this decrease slightly accelerates with temperature for the 40:40:20 sensor, it slows down for the 20:60:20 sample, which explains its decrease in sensitivity at 150 °C observed in Fig. 5.3.3(b). Note that the decrease of the linear range for superparamagnetic samples is less than $|T_{LR}| = 0.15\,\%/°C$ (i.e. $< 1\,\mathrm{Oe}/°C$), whereas the *LR* of the ferromagnetic samples change with an approximate rate of $T_{LR} = -0.6\,\%/°C$ ($\widehat{=} -25\,\mathrm{Oe}/°C$).

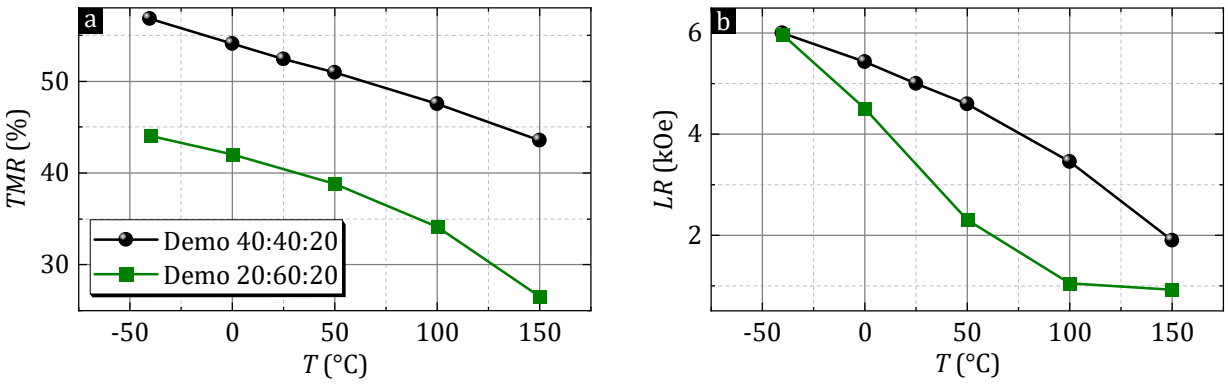

Fig. 5.3.5: (a) TMR amplitude of the ferromagnetic demo samples as a function of temperature. The 40:40:20 sample's TMR amplitude follows a linear decrease of $-0.07\,\%/°C$. (b) Linear range as a function of temperature, with the linear range defined as the field at which the *NL* is at $-1\,\%\,\mathrm{FS}$ (see Fig. 5.3.4). Here, reference layer instabilities are ignored.

The sensitivity and linear range values again form a reciprocal correlation (with a small deviation for the high temperature measurement at $T = 150\,°C$) for the 40:40:20 sample, shown in Fig. 5.3.6(a). The relation for the 20:60:20 sample is more complicated, since its TMR amplitude decreases faster at higher temperatures, where the linear range decreases slower. A direct comparison with the results of the superparamagnetic IFX sensors should be handled with caution, since the data from the demo sensors was obtained by varying the temperature for one FL thickness (1 nm), whereas the IFX data features various thicknesses at a fixed temperature (35 °C). Nevertheless, the substantial difference in S as a function of LR^{-1} for the 40:40:20 demo sample, shown in Fig. 5.3.6(b), is clearly visible.

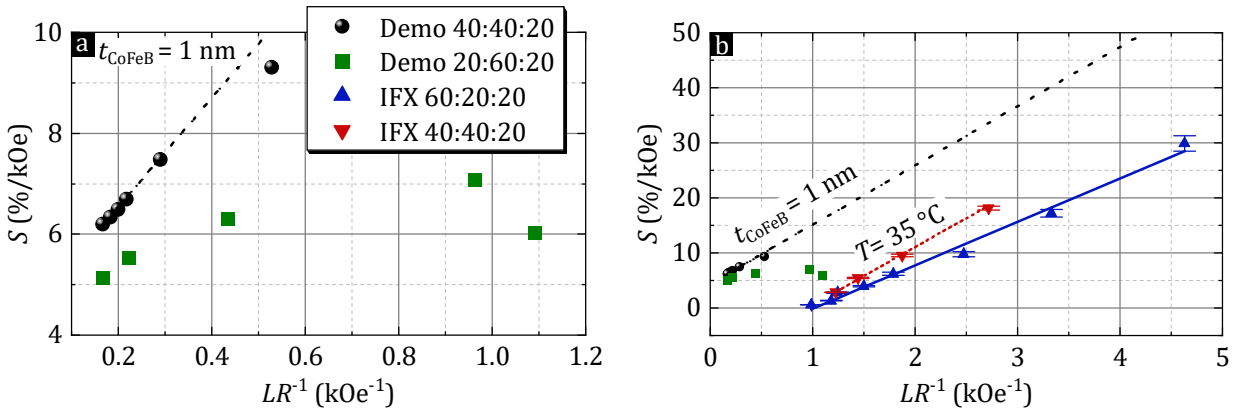

Fig. 5.3.6: Sensitivity as a function of linear range on a reciprocal scale for the (a) 40:40:20 demo sample with $t_{\mathrm{CoFeB}} = 1\,\mathrm{nm}$ and various measurement temperatures and (b) in comparison to the superparamagnetic IFX samples with various thicknesses at a fixed measurement temperature $T = 35\,^{\circ}\mathrm{C}$. An extrapolation of the demo samples using the data points from $T = -40\,^{\circ}\mathrm{C}$ to $100\,^{\circ}\mathrm{C}$, shown as dashed blue line, indicates the potential sensitivity at lower linear ranges.

In either case, IFX and demo PMA sensors, linear ranges on the order of kOe are achieved while the sensitivity values are on the order of $10^0\,\%/\mathrm{kOe}$, whereas standard in-plane TMR sensors yield sensitivities on the order of $10^2\,\%/\mathrm{kOe}$ but linear ranges of only a few Oe [7]. Increasing the sensitivity significantly while keeping the linear range high is unrealistic, for the values of the sensitivity are a direct consequence of the linear range. As a result of the low sensitivity, the smallest fields detectable are much larger than for standard TMR sensors. The detectivity D is a function of the measurement frequency f and depends on the sensitivity S and noise power S_V^2 as per

$$D(f) = \frac{\sqrt{S_V^2(f)}}{S \times U}, \tag{5.9}$$

where the measurement voltage is given by U. The total noise of a MR sensor is composed of frequency independent and frequency dependent contributions. It can be modeled as a sum of white and pink noise, yielding the expression for the noise power

$$S_V^2 = \frac{2eUR_0}{N} \coth\left(\frac{eU}{2Nk_bT}\right) + \frac{\alpha}{NMA}\frac{U^2}{f}. \tag{5.10}$$

Here, R_0 denotes the MR element's resistance at zero field, A the area of the MR element, and M or N the number of MR elements connected in parallel or series (see Fig. 3.4.3). The factor α is a fit parameter that indicates the frequency dependent noise level of the sensor. For details on the measurement and calculation of sensor noise and detectivity, the reader may be referred to the work of D. Suess et al. [7] and H. Weitensfelder et al. [10, 155].

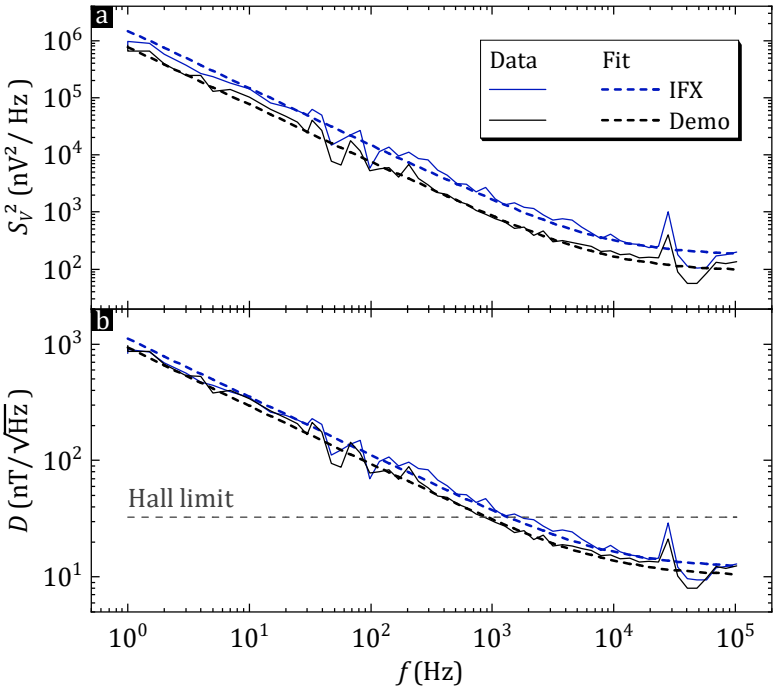

Fig. 5.3.7: (a) Noise power and (b) sensor detectivity as a function of frequency for a demo vendor produced TMR sensor with 40:40:20 (1 nm) free layer and IFX produced TMR sensor with 60:20:20 (1 nm) free layer. Both sensors surpass the detection limit of Hall sensors at frequencies above approx. 1 kHz. The reference curve is given by a standard Infineon TMR sensor with an ellipsoid free layer.

Results of the noise power density and detectivity as a function of frequency for the superparamagnetic 60:20:20 IFX and the ferromagnetic 40:40:20 demo sensor are shown in Fig. 5.3.7. Both sensors have a free layer of $t_{\mathrm{CoFeB}} = 1\,\mathrm{nm}$, and $S = 6\,\%\,\mathrm{kOe}$ and $S = 7\,\%\,\mathrm{kOe}$ at room temperature, respectively. The modules used for these measurements contain $M = 16$, $N = 128$, and $A = 2\,\mu\mathrm{m}^2$. Supply voltages for the superparamagnetic and ferromagnetic sensors are 1.55 V and 1.34 V, respectively. The results show an expected $1/f$ behavior for low frequencies and frequency independent plateau at high frequencies (white noise). Noise and detectivity of the ferromagnetic demo and superparamagnetic IFX sensor are similar, yielding $\alpha_{\mathrm{Demo}} = 6 \times 10^{-9}$ and $\alpha_{\mathrm{IFX}} = 4.5 \times 10^{-9}$. The detectivity limit of a standard Hall sensor[1)] is surpassed at frequencies above 1 kHz.

[1)] data taken from an Infineon Hall sensor with 2.5 V supply voltage, 1 kOhm resistance and S=50 mV/V/T.

5.4 Discussion and outlook

In this chapter, TMR sensors with a reference layer (RL) of in-plane magnetic anisotropy and free layer (FL) of perpendicular magnetic anisotropy (PMA) were investigated.
At first, results for superparamagnetic free layers were discussed, with a focus on the variation of CoFeB free layer thickness t_{CoFeB}. From tunnel magnetoresistance (*TMR*) transfer curves, and the extracted linear ranges (*LR*) and hysteresis values, PMA was found for $t_{\mathrm{CoFeB}} < 1.1\,\mathrm{nm}$. Thicknesses above 1.1 nm show characteristics of effective in-plane magnetic anisotropy. Similar transition thicknesses are found in the literature [61, 212, 216, 222]. A *LR* of up to 1.5 kOe was achieved. However, due to the reciprocal correlation of sensitivity (S) to *LR*, the high *LR* is accompanied by an extremely low S ($< 5\,\%/\mathrm{kOe}$). A similar study by Wisniowski et al. [15] agrees well with these results. The behavior of S as a function of *LR* has two separate components. The first is related to the increase of PMA when t_{CoFeB} is reduced, leading to stronger contributions of the perpendicular interface anisotropy. For lower t_{CoFeB} values, (anti)parallel alignment of RL and FL is achieved at higher fields, which reduces the slope of the *TMR* transfer curves, i.e. the sensitivity. A similar observation was discussed for GMR sensors in chapter 4.5.2. At the same time, a reduction of t_{CoFeB} also reduces the total TMR amplitude itself, since the superparamagnetic nature of the FL increases. Another characteristic of superparamagnetism is found in the change of sensitivity with temperature, expressed by the temperature coefficient T_{k}. For a CoFeB composition of 60:20:20, this coefficient was found to be $T_{\mathrm{k}} = -0.5\,\%/°\mathrm{C}$. By changing the composition to 40:40:20, the superparamagnetic behavior decreases, visible by a higher S against *LR* relation and a smaller $T_{\mathrm{k}} = -0.4\,\%/°\mathrm{C}$.
Furthermore, three different capping layer stacks were compared, which differ in the layers adjacent to the free layer being TaN, Ta/TaN, and MgO/TaN. With the Ta cap, the stack is at a higher risk to feature magnetic dead layers after post annealing as the Ta diffuses into the CoFeB free layer. The additional MgO cap, on the other hand, shields the CoFeB from energetic TaN particles during deposition, which protects against the creation of magnetic dead layers. For none of the capping layers, however, superparamagnetism was suppressed. Further investigation is needed to identify which sputter conditions determine when the CoFeB free layer grows in a continuous layer. Regarding the CoFeB composition, continuous growth is more likely for high Fe ratios, i.e. 40:40:20 and 20:60:20 [14].

The ferromagnetic samples, provided by a demo vendor, display higher sensitivities and linear ranges, simultaneously. Linear ranges of up to 6 kOe appear possible, but require accordingly stable reference systems. However, even though the magnetization of ferromagnetic layers is less sensitive to temperature changes than superparamagnetic layers, the overall magnetoresistance dependence on temperature is significant. In addition to the decrease of TMR amplitude, which is generally the case in TMR sensors, the measurement temperature affects the effective magnetic anisotropy of the FL. At higher temperatures, the PMA decreases, which leads to substantially smaller linear ranges and higher sensitivities. In the case of the 40:40:20 demo sensor, the decrease of PMA dominates over the decrease of TMR amplitude for all temperatures T,

which leads to the sensitivity being an exponential function of T. For application purposes, these characteristics can be challenging. In the automotive industry, sensors are often required to be operable between −40 °C to 150 °C. Usually, temperature drifts can be compensated with simple linear functions of T. For the ferromagnetic sensors of this chapter, however, the temperature strongly affects the linear range. Besides the more complicated sensitivity function with T, the loss of LR on the order of 0.6 %/°C (or −25 Oe/°C) itself is undesirable. Even though the here developed TMR sensors reach a LR up to 6 kOe at −40 °C (disregarding the range of the reference layer), its temperature dependence limits the operable range at 150 °C to only 2 kOe.
In any case, ferromagnetic or superparamagnetic free layer with PMA, the low sensitivity values and consequentially low detectivity remain a challenge for further development.

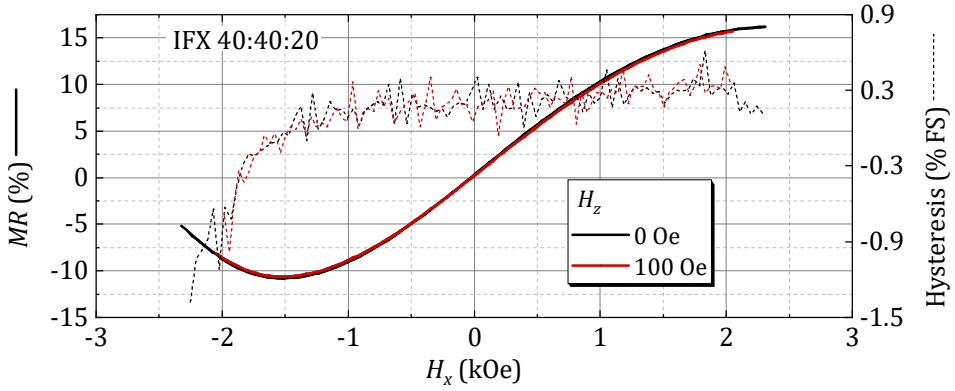

Fig. 5.4.1: Influence of an out-of-plane field H_z applied to a TMR sensor with superparamagnetic free layer.

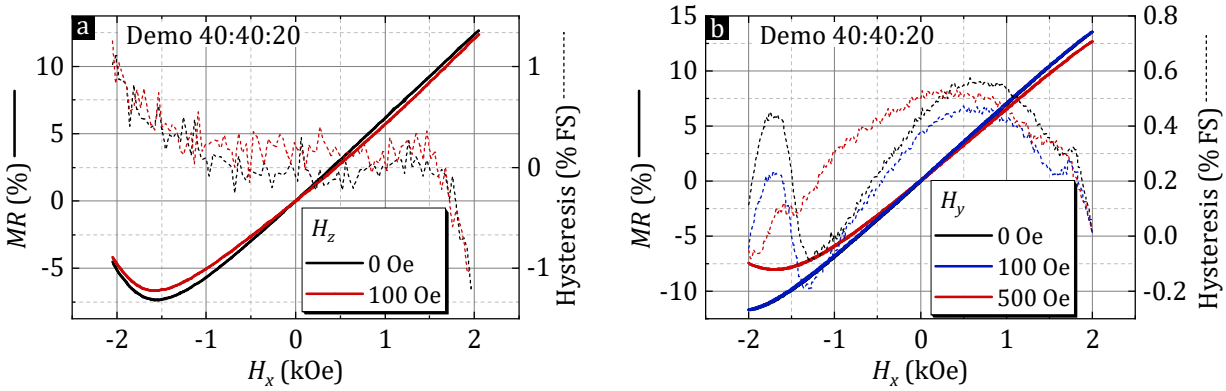

Fig. 5.4.2: Influence of superposed external fields on TMR sensors with a ferromagnetic PMA free layer. (a) Out-of-plane field H_z on PCB level and (b) orthogonal in-plane field H_y on wafer level.

With regard to the use in applications, further influences need to be considered. One of theses influences are parasitic magnetic fields, either originating from other sources within the application or being the H_y and H_z components of the intended magnetic field due to the sensor's positioning. Even though a detailed analysis is yet to be conducted, first results, shown in Figs. 5.4.1 and 5.4.2, paint an optimistic picture. The superparamagnetic IFX 40:40:20 is not influenced by the superposed 100 Oe magnetic field in z direction. The ferromagnetic 40:40:20 demo sample shows a minor change for H_z fields and no significant change when a small static H_y field is applied. However, at a field of $H_y = 500$ Oe, asymmetric changes in the MR transfer curve appear, which

are likely due to the field affecting the reference system, as the most significant differences emerge at the reference layer's unstable field range.

Furthermore, the reliability of a sensor has to be determined before it can be considered for long-lasting applications, particularly in the automotive industry. For this purpose, the sensor is put to extensive stress tests, such as storage in high temperatures, i.e. high temperature stress (HTS). First measurements appear promising once again, as shown in Fig. 5.4.3. After storage at 250 °C for 1 week, no change in sensitivity is detected for the IFX 40:40:20 sensor, despite its superparamagnetic free layer. Only minor differences appear at high fields above the linear range of the sensor.

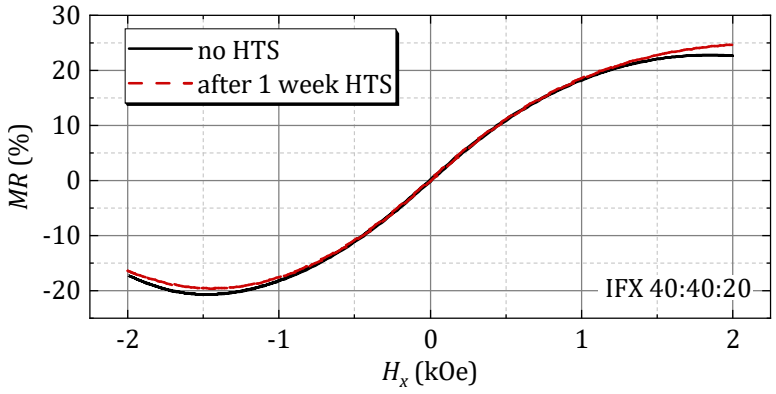

Fig. 5.4.3: Impact of high temperature stress (250 °C annealing for 1 week) on a superparamagnetic IFX 40:40:20 (1.1 nm) TMR sensor on wafer level. The transfer curve shows the magnetoresistance measured against field at 35 °C.

Chapter 6

Application

The physics and characteristics of magnetoresistive (xMR) sensors with a perpendicular magnetic anisotropy (PMA) reference layer (RL) or free layer (FL) were explored in the previous chapters (PMA RL in chapter 4; PMA FL in chapter 5). In this chapter, the applicability of such sensors (in the following called *PMA sensors*) is discussed and compared to existing linear Hall and xMR sensor solutions. First, these existing sensor technologies are briefly introduced. Thereafter, the advantageous and disadvantageous characteristics of PMA sensors are discussed. Finally, the performance of an angle sensor with PMA free layer is reviewed.

6.1 Existing sensor technologies

In this section, established Hall and xMR sensor technologies are introduced. Considered are commonly used technologies, which feature a magnetic field range of linear signal increase (i.e. linear magnetic field sensors). These are the linear Hall effect sensors [236], as well as Giant Magnetoresistance (GMR) and Tunnel Magnetoresistance (TMR) sensors based on shape anisotropy [237] and vortex anisotropy [7, 8, 10, 155].

6.1.1 Hall sensors

In 2016 Hall effect sensors accounted for approx. 75 % of the market for automotive magnetic sensors [2], making it the dominating technology in magnetic sensing. Its development dates back to 1879, when the Hall effect was discovered by Edwin Hall [238]. In its essence, the Hall effect is a consequence of the Lorentz force $\mathbf{F}_\mathrm{L}$ acting on charge carriers in an electric conductor. Its basic working principle is illustrated in Fig. 6.1.1(a). $\mathbf{F}_\mathrm{L}$ is given by

$$\mathbf{F}_\mathrm{L} = q\left(\mathbf{E} + \mathbf{v} \times \mathbf{B}\right), \tag{6.1}$$

with the carrier charge q (i.e. $-e$ for electrons), electric field $\mathbf{E}$, carrier velocity vector $\mathbf{v}$, and magnetic flux density vector $\mathbf{B}$.

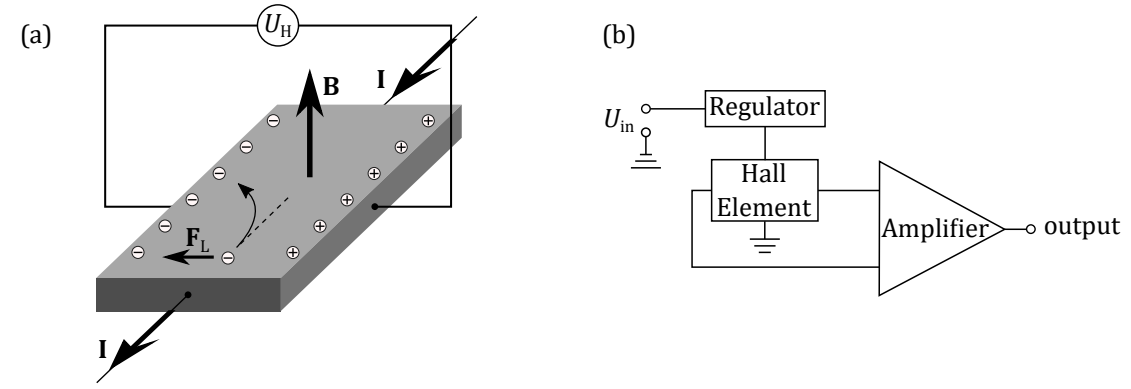

Fig. 6.1.1: (a) Illustration of the working principle in a Hall element. (b) Schematic of a basic Hall effect sensor.

As the Hall effect is a result of $\mathbf{F}_L$, the $\mathbf{B}$ dependence of the Hall voltage U_H yields

$$U_H \propto \mathbf{I} \times \mathbf{B}. \tag{6.2}$$

Thus, U_H scales linearly with the applied magnetic field. In principle, the linear magnetic range for U_H has no limit, since no magnetization saturation is involved. However, the full Hall sensor, containing further electrical elements, does have magnetic field operation constraints. Since the change of the Hall voltage as a function of field is low, i.e. on the order of 6 µV/V/Oe, or 0.6 %/kOe [239][1)], the signal requires a differential amplifier for practical applications. The output of this amplifier is constrained by the limits of the power supply, and thus saturates before these limits are reached. In consequence, the linear range of the Hall sensor is also not without limit. Nevertheless, linear ranges are orders of magnitudes higher than those of shape anisotropy xMR sensors, and are commonly designed to detect fields up to 2 kOe in the automotive industry. The schematic of a basic Hall sensor is shown in Fig. 6.1.1(b). Note the regulator between input supply and Hall element, which stabilizes the current input.
While the introduction above only contained the ordinary Hall effect, several other Hall effects exist, such as the (Inverse) Spin Hall Effect used with spin-currents. For an overview on Hall effects in devices, the reader may be referred to a review paper by A. Karsenty [236].

6.1.2 Magnetoresistive sensors

In this section, two designs for magnetoresistive sensors are presented, used for both GMR and TMR structures: Shape anisotropy and vortex anisotropy xMR sensors. In both concepts, the RL and the FL have an effective magnetic in-plane anisotropy. The reference layer system is analogous to that of the sensors with perpendicularly magnetized free layer, shown in Fig. 5.1.1, chapter 5.1. Meaning, the RL is interlayer exchange coupled to a pinned layer, which in turn is fixed via an exchange bias set by an antiferromagnetic layer below. The easy axis of the RL is set by heating the structure above the Néel temperature of the antiferromagnetic layer, and

[1)] According to Eq. 6.2, the Hall voltage depends on the magnetic field and $I = U_{in}/R$, with U_{in} being the input voltage. Therefore, the sensitivity of a Hall sensor is commonly expressed as a value of U_H/U_{in}/field, which yields the dimensions V/V/Oe or, in case of using the magnetic flux density B, V/V/T.

applying a field along the desired easy axis during the cooling down process[2)]. The two designs of this section differ in their geometrical shape as well as FL magnetization behavior.

6.1.2.1 Shape anisotropy xMR sensor

The working principle and the M-H hysteresis loop of a shape anisotropy xMR sensor are illustrated in Fig. 6.1.2. The concept is to have a RL easy axis in-plane orthogonal to the FL easy axis. While the RL easy axis is set by the antiferromagnet, shape anisotropy (i.e. magnetic dipolar anisotropy) determines the FL easy axis. Common designs are rectangular and elliptic (as in Fig. 6.1.2(a)). At zero field, the FL and RL magnetizations are in a 90° configuration, e.g. RL in x-direction and FL in y-direction. When a field is applied along the RL easy axis, the magnetization of the FL rotates accordingly, resulting in a change in magnetoresistance. Since the x-direction is the intermediate axis of the FL (the hard axis is along the z-axis, i.e. out-of-plane), the rotation is not immediate, but occurs within a linear magnetic range. This linear range depends on the magnetic anisotropy field H_k of the FL, which in turn depends on the shape design of the xMR element.

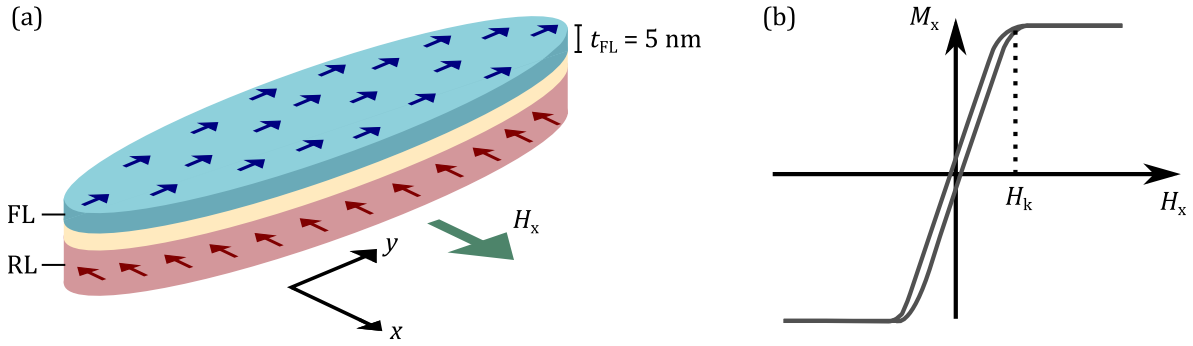

Fig. 6.1.2: Magnetoresistive sensor with shape anisotropy determining the FL easy axis. (a) Illustration of an elliptically shaped TMR layer stack indicating a typical free layer thickness $t_\mathrm{FL} = 5\,\mathrm{nm}$. The RL magnetization direction is locked by an antiferromagnetic layer along the ellipse minor axis. (b) M-H hysteresis loops of the elliptic FL with a field applied along the RL easy axis, i.e. the FL intermediate axis. Typical values for H_k are between 10 an 100 Oe.

Shape anisotropy xMR sensors have very high sensitivities, but at the cost of low linear ranges on the order of 10 to 100 Oe.

[2)] For many systems, it suffices to heat up only to the temperature at which the antiferromagnet loses the ability to pin the adjacent ferromagnetic layer, called the blocking temperature (unrelated to the blocking temperature in superparamagnetism)

6.1.2.2 Vortex anisotropy xMR sensors

A sensor with vortex anisotropy in the FL is designed for low hysteresis and higher linear ranges than shape anisotropy sensors. At zero field, the magnetic moments in the FL of such a sensor arrange themselves in a vortex, as illustrated in Fig. 6.1.3(a). The vortex forms as a result of energy minimization for certain radius-thickness ratios in disk-shaped free layers. Free layer thicknesses are on the order of 40 to 100 nm.

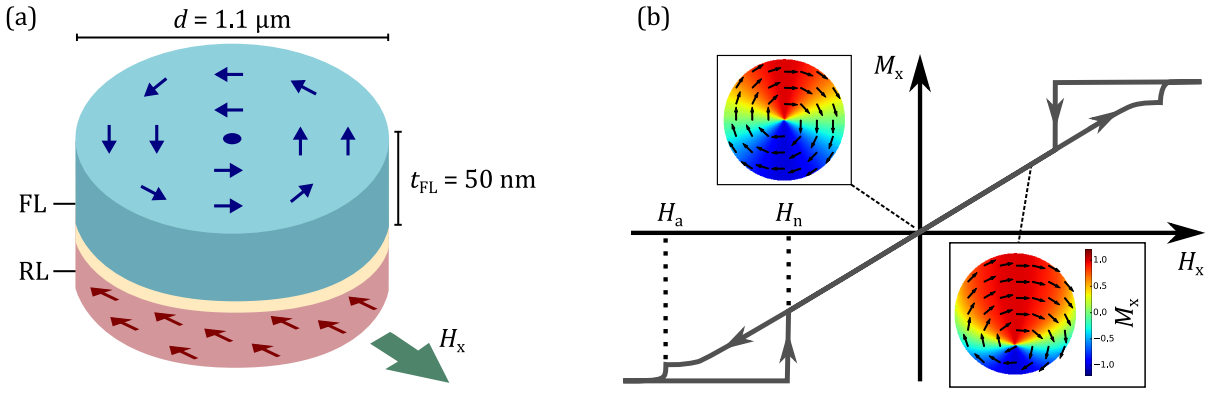

Fig. 6.1.3: Magnetoresistive sensor with a vortex anisotropy in the FL. (a) Illustration of a circular vortex TMR layer stack indicating a typical free layer thickness $t_{FL} = 50$ nm and diameter $d = 1.1$ µm. (b) M-H hysteresis loops of vortex FL with an in-plane applied magnetic field. With increasing fields, the vortex core displacement from the center increases and the magnetization changes linearly, until the vortex is annihilated at H_a. When the field amplitude is decreased again, the magnetization jumps back to the linear regime at the vortex core nucleation field H_n. Nucleation fields up to around 500 Oe can be reached. The insets show simulations results of the FL magnetization, adapted from [8].

When an in-plane field is applied, the vortex core moves across the disk, increasing the ratio of magnetic moments that are aligned with the applied field. The simulated shifted vortex core is shown in the insets of Fig. 6.1.3(b). At strong enough fields, however, the vortex core disappears. This field is called the *annihilation field* H_a. When the field is decreased again, the vortex forms when the *nucleation field* H_n is reached. Between the nucleation and annihilation fields, the movement of the vortex core results in a linear and hysteresis-free change of magnetization, and, accordingly, in an xMR signal of similar properties. Linear ranges are around 500 Oe, but sensitivities are also decreased accordingly.

For a detailed discussion on the FL vortex formation as well as the application of vortex xMR sensors, the reader may be referred to the PhD thesis of T. Wurft [8].

6.2 Application properties of PMA sensors

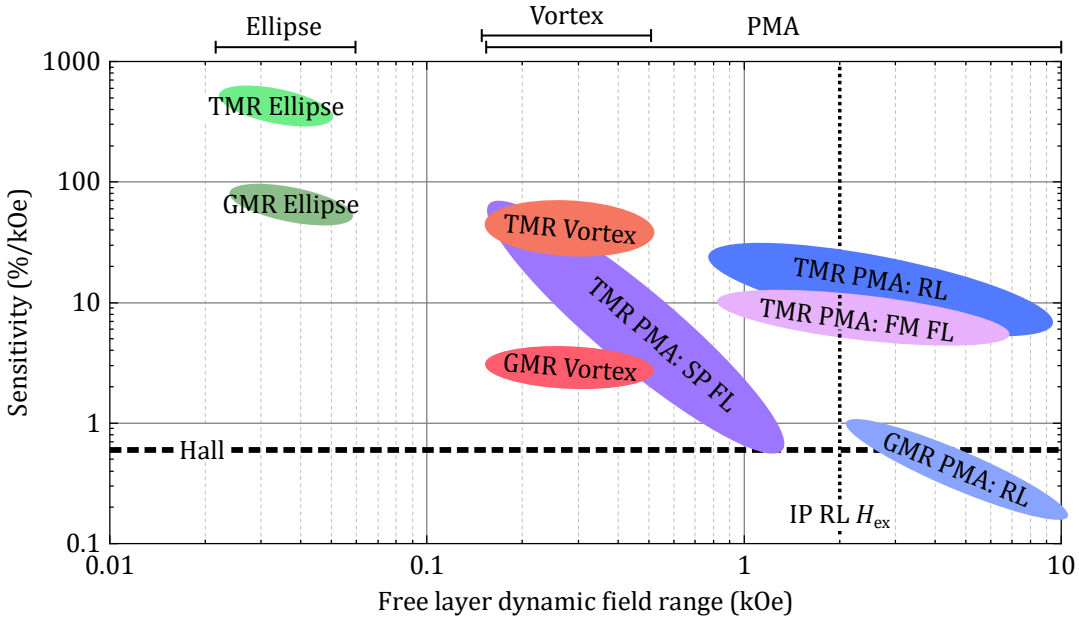

Fig. 6.2.1: Illustration of sensitivity and dynamic field range regime for different xMR sensor technologies. Generally, there is a trade-off between sensitivity and FL dynamic field range. However, TMR sensors have higher sensitivities than GMR sensors at the same field range. PMA sensors achieve the highest field ranges, but IP RL H_{ex} fields have to be considered for PMA FL sensors. The Hall effect itself has no field range limit, but limitations of additional electrical elements, such as dynamic amplifiers, apply. The illustrated areas represent estimates based on measurements in this thesis as well as references [5–8].

In the following, the advantages and disadvantages of PMA sensors for application purposes are discussed. Among the developed sensors of this thesis, one can distinguish between three general designs:
(i) PMA reference layer, ferromagnetic in-plane free layer (PMA RL)
(ii) In-plane reference layer, superparamagnetic PMA free layer (PMA SP FL)
(iii) In-plane reference layer, ferromagnetic PMA free layer (PMA FM FL)
Each design differs in its magnetization and magnetoresistance behavior. The sensitivity and free layer dynamic field range for xMR sensors is summarized in Fig. 6.2.1. The illustrated areas are estimates based on measurements in this thesis as well as taken from the literature [5–8]. Note that the dynamic field range of a PMA FL sensor is limited by the in-plane reference layer exchange field (IP RL H_{ex}) at around 2 kOe.

6.2.1 Advantages of PMA sensors

To discuss the benefits of PMA sensors, comparing it to shape anisotropy based sensors as well as vortex anisotropy based sensors is straightforward, since both designs are used for the same magnetoresistance effects as PMA sensors, namely GMR and TMR. However, due to the comparable dynamic field ranges also Hall effect sensors are taken into consideration. Here,

the basic mechanism differs from xMR sensors, as introduced at the beginning of this chapter. Noteworthy benefits of xMR technology over the Hall effect include a significantly lower power consumption as well as a superior performance at high frequencies.

6.2.1.1 High dynamic field range

The most notable advantage of PMA sensors correlates with the purpose of this thesis: The ability of xMR sensors to reach high dynamic magnetic field ranges. The range is determined by either H_k of the FL or exchange field H_{ex} of the synthetic antiferromagnet (SAF) in the reference system, i.e. the field range at which the SAF structure is antiferromagnetically aligned. In any sensor design of this thesis, either H_k or H_{ex} may be the smaller field and thus the acting range limit. Systems with in-plane reference layer yield up to 2 kOe dynamic range, whereas the highest achieved H_{ex} for PMA reference layers in chapter 4.3 yields $H_{ex} = 10$ kOe, leading to dynamic field ranges up to 9 kOe. These field ranges open up high magnetic field applications for xMR sensor technologies, which thus far could only be addressed by Hall sensors.

6.2.1.2 Adjustability

Even though the H_{ex} represents the maximum possible dynamic range, the FL design can be designed in such a way that $H_k < H_{ex}$, which points to another advantage of PMA sensors: adjustability. Depending on the application requirement, the FL H_k value can be chosen accordingly, ranging from a few Oe to the H_{ex} value of the respective reference system. For that purpose, design techniques were presented in this thesis, involving multilayers (see chapter 4.5.2) and thinning of the FL (see chapter 5.2.1). When the dynamic range limit is set by H_k, the sensor's sensitivity is reciprocally correlated to the dynamic field range by its nature (see chapter 4.5.2). The ability to tune the sensor's linear range therefore allows an optimized sensitivity while meeting the application requirements for the linear range. In comparison to that, other xMR sensor technologies are much more restricted. Shape anisotropy sensors only cover a linear range of a few Oe, vortex anisotropy sensors of up to a few hundred Oe. Furthermore, the linear range of vortex anisotropy sensors is not determined by the FL H_k, but by the nucleation field of the vortex core. Therefore, reducing the linear range of a vortex sensor does not necessarily increase its sensitivity [8]. For Hall based sensors, adjusting the linear range for a higher sensitivity is not possible at the Hall element, as already discussed. Additional elements are necessary, such as dynamic amplifiers and magnetic flux concentrators.

6.2.1.3 Lateral dimension independence

For the performance parameters (e.g. linear range) of shape anisotropy and vortex anisotropy sensors, the lateral dimensions of the sensor elements are essential. As already discussed, shape anisotropy sensors rely on the lateral dimensions to set the FL's easy axis, and the vortex anisotropy in the FL only forms for thicker (> 30 nm) layers and suitable ratios of thickness and diameter. In PMA sensors, on the other hand, performance parameters don't depend on lateral dimensions, since the dominating PMA is an interface effect. Figure 6.2.2 exemplary shows

the sensitivity results for the 40:40:20 CoFeB demo sensor with an in-plane reference layer and ferromagnetic PMA free layer for 35 different modules at 35 °C. Even though the modules differ in the diameter of their TMR elements ranging from 1 µm to 7 µm, the differences in sensitivities are only minor, with no correlation to the respective diameters. Error bars represent the standard deviation for 5 sensors of each module across different wafer positions. The standard deviation is in the same order as the difference of sensitivities between modules.

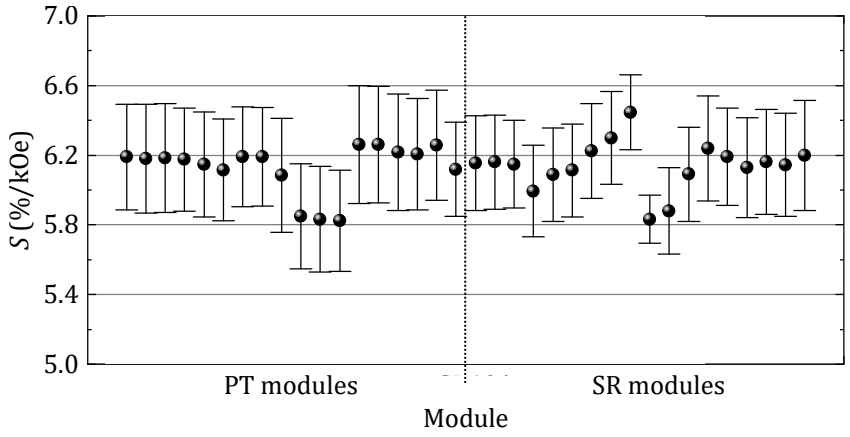

Fig. 6.2.2: Sensitivity results at 35 °C for the ferromagnetic 40:40:20 PMA FL and 35 different modules. The module types PT and SR refer to different circuit designs.

Thus, lateral dimensions are uncorrelated to the performance parameters of PMA sensors. In consequence, PMA sensors offer a higher flexibility regarding the lateral design of their xMR elements.

6.2.1.4 Costs

The two most similar sensor designs in this chapter's comparison are the vortex anisotropy sensor and the PMA FL sensor. Both designs serve the purpose of an xMR sensor with an increased magnetic field range, are sensitive to in-plane fields, and can be fabricated using the same modules and layer stacks, with the only necessary difference being the FL thickness. The vortex anisotropy sensor typically employs FL thicknesses of 50 nm or more, whereas the PMA FL has a thickness of around 1 nm. This significant difference in material and sputter deposition time ultimately leads to a difference in fabrication costs.

6.2.1.5 OOP sensitivity

While shape anisotropy sensors and vortex anisotropy sensors cover only two spatial dimensions, the design of PMA sensors cover all three. Using the design of a PMA reference layer, the sensor operation is, accordingly, suitable for out-of-plane fields. This can be an advantage for application purposes with out-of-plane fields and little spatial flexibility, i.e. where a rotated installation of in-plane sensors is not feasible.

6.2.2 Disadvantages of PMA sensors

6.2.2.1 Process control

All magnetic layers with PMA are highly sensitive to changes in layer thickness, since PMA is an interface effect. Subnanometer thickness variations can significantly change characteristic values such as coercive fields and magnetic anisotropy field in both Co/Pt based multilayers (see chapters 4.2, 4.3, 4.5.2) as well as CoFeB free layers (see chapters 4.6, 5.2). In consequence, precise process control is necessary to ensure the desired performance of PMA sensors.

6.2.2.2 Sensitivity and detectivity

One of the typically stated advantages of xMR sensors compared to Hall effect sensors is their high sensitivity. However, due to the reciprocal correlation of sensitivity and FL magnetic anisotropy field, the high dynamic field ranged PMA sensors have much lower sensitivities. Consequently, GMR sensors with PMA reference layer from chapter 4.5 yield sensitivities on the same order as that of Hall effect sensors. TMR PMA sensors yield higher sensitivities, but are typically lower than those of TMR vortex sensors, as shown in the summarized trade-off between sensitivity and dynamic field range in Fig. 6.2.1.

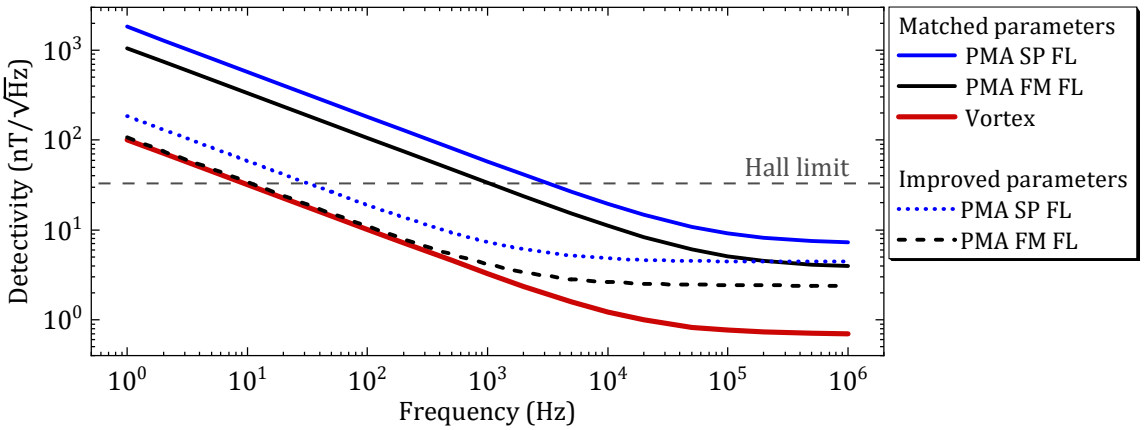

Fig. 6.2.3: Model data for sensor detectivity as a function of frequency. Shown are PMA FL sensors with matching parameters for a measurement of a vortex anisotropy sensor, as well as results with improved parameters. The parameters are summarized in table 6.2.1.

The detectivity, i.e. the minimum field strength the sensor is able to detect, is reciprocal to the sensitivity (see Eq. 5.9) and thus higher for PMA sensors. Both detectivities for the measured PMA SP FL and PMA FM FL sensors surpass the Hall limit only at higher frequencies above 1 kHz (see Fig. 5.3.7). Besides sensitivity, also the noise in a sensor affects detectivity. The noise depends on various factors, such as the number of xMR elements connected in series (N) and parallel (M), their area A, as well as the supply voltage U [19] (see Eq. 5.10). For comparison, Fig. 6.2.3 shows the modeled detectivity of an Infineon TMR vortex sensor and of TMR PMA FL sensors with matched as well as improved parameters. Matched parameters means that the values $N = 48$, $M = 4$, $A = 7\,\mu\text{m}^2$, and $U = 2.5\,\text{V}$ are adopted from the vortex sensor noise measurement, while the noise factor α is taken from the respective fits in Fig. 5.3.7. The vortex

sensor has a typical range and sensitivity with $LR = 0.3\,\mathrm{kOe}$ and $S = 60\,\%/\mathrm{kOe}$. For the modeled PMA sensor with superparamagnetic FL, a LR of $0.5\,\mathrm{kOe}$ and sensitivity $S = 5\,\%/\mathrm{kOe}$ is chosen, whereas for the PMA sensor with ferromagnetic FL the selected parameters are $LR = 2\,\mathrm{kOe}$ and $S = 10\,\%/\mathrm{kOe}$ (compare with Fig. 6.2.1).

Free layer	Parameters	LR (kOe)	S (%/kOe)	α ($\times 10^{-9}$)	N	M	U (V)	A (μm^2)	D @ 10 Hz (nT/$\sqrt{\mathrm{Hz}}$)
Vortex	measured	0.3	60	2	48	4	2.5	7	32
PMA FM	measured	5	7	6	128	16	1.34	2	273
PMA FM	matched	2	10	6	48	4	2.5	7	332
PMA FM	improved	2	10	6	128	32	2.5	32	34
PMA SP	measured	0.5	1	4.5	128	16	1.55	2	331
PMA SP	matched	0.5	1	4.5	48	4	2.5	7	576
PMA SP	improved	0.5	1	4.5	128	32	2.5	32	59

Table 6.2.1: Model parameters for detectivity comparison between TMR vortex and TMR PMA sensors, used for Fig. 6.2.3. The parameter influences on noise and detectivity are given in Eqs. 5.9 and 5.10. All parameters apply for room temperature.

As expected, the plot shows a better performance of the TMR vortex sensor, which is mainly due to its higher sensitivity. However, with improved parameters, the detectivity of PMA FL sensors can be decreased by an order of magnitude, as both frequency dependent and independent components of noise are decreased (see Eq. 5.10). In the exemplary fit of Fig. 6.2.3, the improved parameters are $N = 128$, $M = 32$, and $A = 32\,\mu\mathrm{m}^2$. These parameters are based on existing modules, which are commonly used for structured TMR sensors. As already discussed, the independence of lateral dimensions in PMA sensors allows the simple modification of the element area A. A summary of the parameters and characteristic values is given in table 6.2.1. Note that the measured detectivity of the TMR sensor is already close to that of an optimized vortex sensor design. For a discussion on detectivity optimization in vortex sensors, the reader may be referred to the PhD thesis of H. Weitensfelder [10].

6.2.2.3 Temperature sensitivity

For PMA FL sensors, significant temperature dependencies were presented in this thesis. Superparamagnetic free layers yield higher absolute temperature coefficients for the sensor sensitivity with a T_k of $-0.5\,\%/°\mathrm{C}$ for 60:20:20 CoFeB FLs and $-0.4\,\%/°\mathrm{C}$ for 40:40:20 FLs, compared to the -0.1 to $-0.2\,\%/°\mathrm{C}$ values of existing xMR technologies [233] and $< 0.1\,\%/°\mathrm{C}$ of Hall sensors [239]. Even more challenging for implementation into applications is the non-linear temperature dependence of ferromagnetic PMA free layers. As discussed in chapter 5.3, the linear range of the ferromagnetic FL samples in this thesis decreases with temperature with around $T_{LR} = -0.6\,\%/°\mathrm{C}$ ($\widehat{=} -25\,\mathrm{Oe}/°\mathrm{C}$), which leads to an exponential increase of the sensitivity.

6.3 PMA angle sensors

With their high dynamic field range up to several kOe, the application of PMA sensors for the detection of high field strengths suggests itself, e.g. as magnetic current sensors. Another possible application is that of a magnetic angle sensor [240]. In the following, the concept of magnetic angle sensing is introduced. A standard TMR angle sensor with in-plane reference and free layer is compared to an angle sensor with in-plane reference layer and PMA superparamagnetic free layer (PMA SP FL).

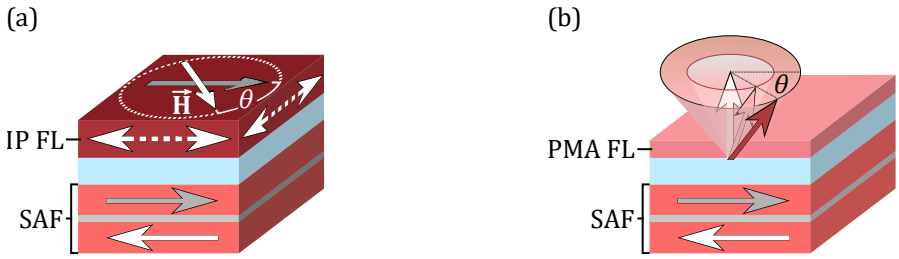

Fig. 6.3.1: Magnetization directions in a TMR angle sensor with an in-plane RL in an in-plane applied field. Shown are an (a) in-plane FL, and (b) PMA FL. The in-plane FL has a magnetic anisotropy field of a few Oe, the sensor is operated at saturated fields. Thus, the magnetization direction rotates with the applied field in the layer plane. The rotation of the PMA FL magnetization forms a cone with the radius depending on the field strength. The projection onto the film plane discloses the field direction.

Figure 6.3.1 illustrates the magnetization directions of a TMR stack in a rotational in-plane magnetic field. In an ideal case, the magnetization of the synthetic antiferromagnet (SAF) in the reference system is not significantly affected by the external field. With FL magnetic anisotropy fields of only a few Oe, a standard TMR angle sensor with in-plane FL (Fig. 6.3.1(a)) is operated at fully saturated magnetization. To minimize the magnetic anisotropy field, a circular shaped MR element and a soft magnetic material in the FL (e.g. NiFe) are used. The magnetization rotation is performed fully in-plane. In case of a sensor with PMA FL, on the other hand, the magnetization vector of the FL forms a cone shape, with the radius depending on the applied field strength. The purpose of an angle sensor is to determine the angle of the applied field, here identified as the angle θ between RL and FL magnetization direction. For PMA sensors, θ is formed through the projection of the FL magnetization onto the film plane, as illustrated in Fig. 6.3.1(b).
In a simple model [241], the conductance G in a TMR element can be expressed by

$$G = \frac{1}{2}\left(G_{\mathrm{P}} + G_{\mathrm{AP}}\right) - \frac{1}{2}\left(G_{\mathrm{P}} - G_{\mathrm{AP}}\right)\cos\theta, \tag{6.3}$$

where the conductance in parallel and antiparallel alignment of RL and FL are denoted as G_{P} and G_{AP}, respectively. The resistance $R = 1/G$ is typically measured using a Wheatstone bridge configuration. The voltage between the resistors connected in parallel is given by

$$U_{\cos} = U_{\mathrm{in}}\left(\frac{R_2}{R_1 + R_2} - \frac{R_4}{R_3 + R_4}\right), \tag{6.4}$$

with the input voltage denoted as U_{in}, and the resistors R_1, R_2 and R_3, R_4 connected in series (see Fig. 6.3.2). Assuming an ideal case with $R_1(\Theta = 0°) = R_2(\Theta = 180°) = R_3(\Theta = 180°) = R_4(\Theta = 0°)$, where Θ denotes the direction of a magnetic field applied in the $x-y$-plane, inserting Eq. 6.3 into Eq. 6.4 yields

$$U_{\cos} = U_{\text{in}} \frac{G_{\text{P}} - G_{\text{AP}}}{G_{\text{P}} + G_{\text{AP}}} \cos\Theta \tag{6.5}$$

However, due to the cosine 180° symmetry, one Wheatstone bridge alone can uniquely identify a field range of only 0° to 180°. In order to achieve a full 360° sensing range, a second Wheatstone bridge with a 90° rotation in the RL magnetization is added, as illustrated in Fig. 6.3.2.

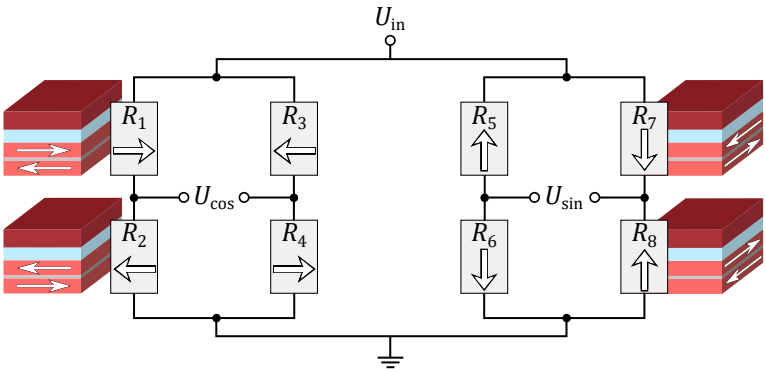

Fig. 6.3.2: Schematic of two Wheatstone bridges for magnetic angle sensing with a 90° rotation of the RL magnetization direction.

The voltage in the second bridge is denoted as $U_{\sin}$. With the ideal case assumption of identical G_{P} and G_{AP}, the calculation for $U_{\sin}$ results in a 90° rotated equation of Eq. 6.5, which thus yields

$$\frac{U_{\sin}}{U_{\cos}} = \frac{\sin\Theta}{\cos\Theta} = \tan\Theta \tag{6.6}$$

In conclusion, the angle of the applied field can be derived by using

$$\Theta = \arctan\frac{U_{\sin}}{U_{\cos}}. \tag{6.7}$$

In practice, there are several deviations from the ideal case, such as the resistors in the Wheatstone bridge configuration not being identical, which introduces different voltage amplitudes. While some effects can be mathematically handled and compensated, fundamental deviations of the assumed cosine dependence, as given in Eq. 6.3, lead to differences between applied and measured angles, quantified as the angle error. A well identified cause of angle errors at high magnetic fields is the destabilization of the SAF in the reference system [241]. The results for angle error against magnetic field strength are shown in Fig. 6.3.3, where standard TMR angle sensors are compared to PMA sensors with superparamagnetic free layer ($t_{\text{CoFeB}} = 1.1\,\text{nm}$). All samples come from the same wafer lot and have the same reference stack to ensure comparability.

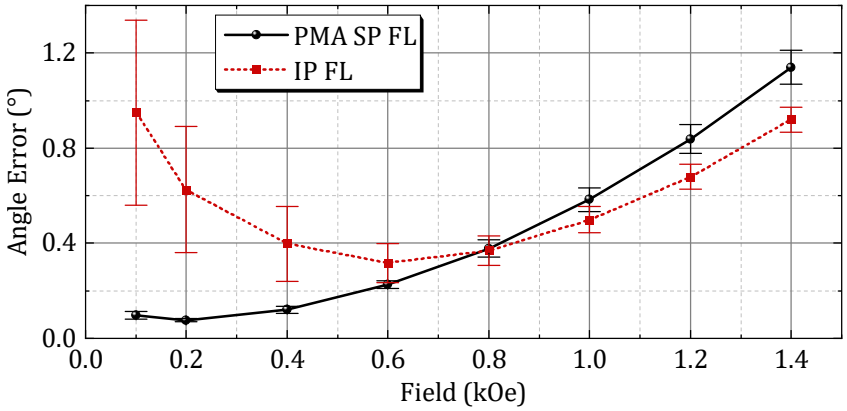

Fig. 6.3.3: Angle error as a function of magnetic field strength for angle sensors with IP FL and angle sensors with PMA SP FL. Shown are averaged values for measurements of multiple devices with the error bars representing the standard deviation.

For both sensor types, the angle error increases for high magnetic fields, as expected. This increase is more pronounced for PMA sensors. A possible reason for this is the smaller stray field of the PMA free layer. The free layer magnetization, oriented along the applied field, accordingly generates a stray field that is parallel to the reference layer, thus stabilizing it. This counteraction to the applied field destabilization is smaller in superparamagnetic PMA free layers, since magnetization and, in consequence, the stray field are much smaller than those of ferromagnetic in-plane free layers.
At low fields, PMA sensors show very small angle errors of below 0.1° for fields under 0.4 kOe. On the other hand, the angle error of in-plane sensors are lowest at 0.6 kOe with a value of ca. 0.3°. At lower fields, the angle error increases again. A behavior that is not observed for the PMA sensors, which might be due to missing in-plane magnetic anisotropy components at low fields. At zero field, ideally the magnetization of the PMA FL is distinctly out-of-plane with negligible in-plane components. Only with an applied field are in-plane components introduced and thus completely dependent on the applied field. The standard sensor, however, has an inherent in-plane magnetic anisotropy, which the applied field has to overcome. Even though the magnetic anisotropy field of the FL is small, unless the applied field is the overwhelmingly dominant contribution, the in-plane magnetic anisotropy introduces a non-negligible component that leads to the observed angle errors.

In conclusion, PMA angle sensors show advantageous behavior in low magnetic field application by yielding smaller angle errors. Simultaneously, PMA angle sensors are able to not only measure the angle, but also the field strength (compare Fig. 6.3.1).

Bibliography

[1] A. Hirohata, K. Yamada, Y. Nakatani, I.-L. Prejbeanu, B. Diény, P. Pirro, and B. Hillebrands, "Review on spintronics: Principles and device applications," *Journal of Magnetism and Magnetic Materials*, vol. 509, no. March, p. 166711, sep 2020. https://doi.org/10.1016/j.jmmm.2020.166711

[2] IHS Markit, "Magnetic Automotive Sensor Market Tracker," 2017.

[3] Infineon Technologies AG, "TLE5046iC Data Sheet," pp. 1–14, 2020.

[4] T. Nakano, M. Oogane, T. Furuichi, and Y. Ando, "Magnetic-sensor performance evaluated from magneto-conductance curve in magnetic tunnel junctions using in-plane or perpendicularly magnetized synthetic antiferromagnetic reference layers," *AIP Advances*, vol. 8, no. 4, p. 045011, apr 2018. https://doi.org/10.1063/1.5027768

[5] T. Nakano, M. Oogane, H. Naganuma, and Y. Ando, "Systematic Investigation on Correlation Between Sensitivity and Nonlinearity in Magnetic Tunnel Junction for Magnetic Sensor," *IEEE Transactions on Magnetics*, vol. 51, no. 11, pp. 1–4, nov 2015. https://doi.org/10.1109/TMAG.2015.2448723

[6] T. Ogasawara, M. Oogane, M. Tsunoda, and Y. Ando, "Effects of annealing temperature on sensing properties of magnetic-tunnel-junction-based sensors with perpendicular synthetic antiferromagnetic Co/Pt pinned layer," *Japanese Journal of Applied Physics*, vol. 57, no. 11, p. 110308, nov 2018. https://doi.org/10.7567/JJAP.57.110308

[7] D. Suess, A. Bachleitner-Hofmann, A. Satz, H. Weitensfelder, C. Vogler, F. Bruckner, C. Abert, K. Prügl, J. Zimmer, C. Huber, S. Luber, W. Raberg, T. Schrefl, and H. Brückl, "Topologically protected vortex structures for low-noise magnetic sensors with high linear range," *Nature Electronics*, vol. 1, no. 6, pp. 362–370, jun 2018. http://dx.doi.org/10.1038/s41928-018-0084-2

[8] T. Wurft, "Investigation of the magnetic vortex state for spin-valve sensors," PhD, University of Bielefeld, 2018.

[9] A. V. Silva, D. C. Leitao, J. Valadeiro, J. Amaral, P. P. Freitas, and S. Cardoso, "Linearization strategies for high sensitivity magnetoresistive sensors,"

The European Physical Journal Applied Physics, vol. 72, no. 1, p. 10601, oct 2015. https://doi.org/10.1051/epjap/2015150214

[10] H. Weitensfelder, "Current Sensing based on x MR Sensors with a Vortex-State Free Layer," PhD thesis, Universitaet Wien, 2020.

[11] L. Néel, "Anisotropie magnétique superficielle et surstructures d'orientation," *Journal de Physique et le Radium*, vol. 15, no. 4, pp. 225–239, 1954. http://dx.doi.org/10.1051/jphysrad:01954001504022500

[12] S. Monso, B. Rodmacq, S. Auffret, G. Casali, F. Fettar, B. Gilles, B. Dieny, and P. Boyer, "Crossover from in-plane to perpendicular anisotropy in Pt/CoFe/AlOx sandwiches as a function of Al oxidation: A very accurate control of the oxidation of tunnel barriers," *Applied Physics Letters*, vol. 80, no. 22, pp. 4157–4159, jun 2002. https://doi.org/10.1063/1.1483122

[13] R. Sbiaa, H. Meng, and S. N. Piramanayagam, "Materials with perpendicular magnetic anisotropy for magnetic random access memory," *physica status solidi (RRL) - Rapid Research Letters*, vol. 5, no. 12, pp. 413–419, dec 2011. https://doi.org/10.1002/pssr.201105420

[14] B. Dieny and M. Chshiev, "Perpendicular magnetic anisotropy at transition metal/oxide interfaces and applications," *Reviews of Modern Physics*, vol. 89, no. 2, p. 025008, jun 2017. https://doi.org/10.1103/RevModPhys.89.025008

[15] P. Wisniowski, J. Wrona, T. Stobiecki, S. Cardoso, and P. P. Freitas, "Magnetic Tunnel Junctions Based on Out-of-Plane Anisotropy Free and In-Plane Pinned Layer Structures for Magnetic Field Sensors," *IEEE Transactions on Magnetics*, vol. 48, no. 11, pp. 3840–3842, nov 2012. https://doi.org/10.1109/TMAG.2012.2198207

[16] P. Wisniowski, M. Dabek, T. Stobiecki, and S. Cardoso, "Magnetic field sensing properties of CoFeB-MgO-CoFeB based tunneling masnetoresistance devices," *Procedia Engineering*, vol. 47, pp. 1414–1417, 2012. https://doi.org/10.1016/j.proeng.2012.09.422

[17] C.-Y. Yang, S.-J. Chang, M.-H. Lee, K.-H. Shen, S.-Y. Yang, H.-J. Lin, and Y.-C. Tseng, "Competing Anisotropy-Tunneling Correlation of the CoFeB/MgO Perpendicular Magnetic Tunnel Junction: An Electronic Approach," *Scientific Reports*, vol. 5, no. 1, p. 17169, dec 2015. https://doi.org/10.1038/srep17169

[18] X. P. Zhao, J. Lu, S. W. Mao, Z. F. Yu, H. L. Wang, X. L. Wang, D. H. Wei, and J. H. Zhao, "L10-MnGa based magnetic tunnel junction for high magnetic field sensor," *Journal of Physics D: Applied Physics*, vol. 50, no. 28, p. 285002, jul 2017. https://doi.org/10.1088/1361-6463/aa750a

[19] Y. C. Lee, C. T. Chao, L. C. Li, Y. W. Suen, L. Horng, T.-H. Wu, C. R. Chang, and J. C. Wu, "Magnetic tunnel junction based out-of-plane field sensor with perpendicular

magnetic anisotropy in reference layer," *Journal of Applied Physics*, vol. 117, no. 17, p. 17A320, may 2015. https://doi.org/10.1063/1.4914121

[20] M. T. Johnson, P. J. H. Bloemen, F. J. A. den Broeder, and J. J. de Vries, "Magnetic anisotropy in metallic multilayers," *Reports on Progress in Physics*, vol. 59, no. 11, pp. 1409–1458, nov 1996. https://doi.org/10.1088/0034-4885/59/11/002

[21] G. Varvaro, S. Laureti, D. Peddis, M. Hassan, G. Barucca, P. Mengucci, A. Gerardino, E. Giovine, O. Lik, D. Nissen, and M. Albrecht, "Co/Pd-Based synthetic antiferromagnetic thin films on Au/resist underlayers: towards biomedical applications," *Nanoscale*, vol. 11, no. 45, pp. 21 891–21 899, 2019. https://doi.org/10.1039/C9NR06866J

[22] F. B. Mancoff, J. H. Dunn, B. M. Clemens, and R. L. White, "A giant magnetoresistance sensor for high magnetic field measurements," *Applied Physics Letters*, vol. 77, no. 12, p. 1879, 2000. https://doi.org10.1063/1.1311316

[23] S. Van Dijken and J. M. D. Coey, "Magnetoresistance sensor with an out-of-plane magnetized sensing layer," *Applied Physics Letters*, 2005. https://doi.org/10.1063/1.1957111

[24] B. Szymański, F. Stobiecki, and M. Urbaniak, "GMR spin valve with alternating in-plane and out-of-plane magnetic anisotropy," *Journal of Alloys and Compounds*, vol. 423, no. 1-2, pp. 236–239, oct 2006. https://doi.org/10.1016/j.jallcom.2005.12.098

[25] P. Matthes, "Magnetic and Magneto-Transport Properties of Hard Magnetic Thin Film Systems," PhD thesis, TU Chemnitz, 2016. https://katalog.bibliothek.tu-chemnitz.de/Record/0017259432

[26] P. Matthes and M. Albrecht, "Pseudo spin valve thin films with crossed magnetic anisotropies," *Sensors and Actuators A: Physical*, vol. 233, pp. 275–278, sep 2015. http://dx.doi.org/10.1016/j.sna.2015.07.021

[27] P. Matthes, S. S. P. K. Arekapudi, F. Timmermann, and M. Albrecht, "Magnetotransport Properties of Perpendicular [Pt/Co]/Cu/[Co/Pt] Pseudo-Spin-Valves," *IEEE Transactions on Magnetics*, vol. 51, no. 1, pp. 1–4, jan 2015. https://doi.org/10.1109/TMAG.2014.2359871

[28] H. X. Wei, Q. H. Qin, Z. C. Wen, X. F. Han, and X.-G. Zhang, "Magnetic tunnel junction sensor with Co/Pt perpendicular anisotropy ferromagnetic layer," *Applied Physics Letters*, vol. 94, no. 17, p. 172902, apr 2009. https://doi.org/10.1063/1.3126064

[29] T. Nakano, M. Oogane, T. Furuichi, K. Ao, H. Naganuma, and Y. Ando, "Magnetic Tunnel Junctions With [Co/Pd]-Based Reference Layer and CoFeB Sensing Layer for Magnetic Sensor," *IEEE Transactions on Magnetics*, vol. 52, no. 7, pp. 1–4, jul 2016. https://doi.org/10.1109/TMAG.2016.2518188

[30] T. Nakano, M. Oogane, T. Furuichi, and Y. Ando, "Magnetic tunnel junctions using perpendicularly magnetized synthetic antiferromagnetic reference layer for wide-dynamic-range magnetic sensors," *Applied Physics Letters*, vol. 110, no. 1, p. 012401, jan 2017. https://doi.org/10.1063/1.4973462

[31] T. Ogasawara, M. Oogane, M. Tsunoda, and Y. Ando, "Large exchange coupling field in perpendicular synthetic antiferromagnetic structures with CoPt alloy," *Japanese Journal of Applied Physics*, vol. 57, no. 8, p. 088004, aug 2018. https://doi.org/10.7567/JJAP.57.088004

[32] T. Ogasawara, M. Oogane, M. Al-Mahdawi, M. Tsunoda, and Y. Ando, "Effect of second-order magnetic anisotropy on nonlinearity of conductance in CoFeB/MgO/CoFeB magnetic tunnel junction for magnetic sensor devices," *Scientific Reports*, vol. 9, no. 1, p. 17018, dec 2019. https://doi.org/10.1038/s41598-019-53439-0

[33] T. Ogasawara, M. Oogane, M. Al-Mahdawi, M. Tsunoda, Y. Ando, "Composition dependence of the second-order interfacial magnetic anisotropy for MgO/CoFeB/Ta films," *AIP Advances*, vol. 9, no. 12, p. 125053, dec 2019. https://doi.org/10.1063/1.5129988

[34] K. Yakushiji, T. Saruya, H. Kubota, A. Fukushima, T. Nagahama, S. Yuasa, and K. Ando, "Ultrathin Co/Pt and Co/Pd superlattice films for MgO-based perpendicular magnetic tunnel junctions," *Applied Physics Letters*, vol. 97, no. 23, p. 232508, dec 2010. https://doi.org/10.1063/1.3524230

[35] K. Yakushiji, H. Kubota, A. Fukushima, and S. Yuasa, "Perpendicular magnetic tunnel junctions with strong antiferromagnetic interlayer exchange coupling at first oscillation peak," *Applied Physics Express*, vol. 8, no. 8, p. 083003, aug 2015. https://doi.org/10.7567/APEX.8.083003

[36] K. Yakushiji, A. Sugihara, A. Fukushima, H. Kubota, and S. Yuasa, "Very strong antiferromagnetic interlayer exchange coupling with iridium spacer layer for perpendicular magnetic tunnel junctions," *Applied Physics Letters*, vol. 110, no. 9, p. 092406, feb 2017. https://doi.org/10.1063/1.4977565

[37] B. E. C. Stoner and E. Wohlfarth, "A mechanism of magnetic hysteresis in heterogeneous alloys," *Philosophical Transactions of the Royal Society of London. Series A, Mathematical and Physical Sciences*, vol. 240, no. 826, pp. 599–642, may 1948. https://doi.org/10.1098/rsta.1948.0007

[38] F. den Broeder, W. Hoving, and P. Bloemen, "Magnetic anisotropy of multilayers," *Journal of Magnetism and Magnetic Materials*, vol. 93, pp. 562–570, feb 1991. https://doi.org/10.1016/0304-8853(91)90404-X

[39] J. Bland and B. Heinrich, "Ultrathin Magnetic Structures I," in *Ultrathin Magnetic Structures I.* Springer, 1994, vol. 1, pp. 1–30.

[40] H. J. G. Draaisma and W. J. M. de Jonge, "Surface and volume anisotropy from dipole-dipole interactions in ultrathin ferromagnetic films," *Journal of Applied Physics*, vol. 64, no. 7, pp. 3610–3613, oct 1988. https://doi.org/10.1063/1.341397

[41] C. Kittel, *Introduction to Solid State Physics*, 8th ed, Wiley, pp. 348–349, 2004.

[42] G. H. O. Daalderop, P. J. Kelly, and M. F. H. Schuurmans, "Magnetocrystalline anisotropy and orbital moments in transition-metal compounds," *Physical Review B*, vol. 44, no. 21, pp. 12 054–12 057, dec 1991. https://doi.org/10.1103/PhysRevB.44.12054

[43] G. H. O. Daalderop, P. J. Kelly, and F. J. A. den Broeder, "Prediction and confirmation of perpendicular magnetic anisotropy in Co/Ni multilayers," *Physical Review Letters*, vol. 68, no. 5, pp. 682–685, feb 1992. https://doi.org/10.1103/PhysRevLett.68.682

[44] P. Bruno, "Magnetic surface anisotropy of cobalt and surface roughness effects within Neel's model," *Journal of Physics F: Metal Physics*, vol. 18, no. 6, pp. 1291–1298, jun 1988. https://doi.org/10.1088/0305-4608/18/6/029

[45] K. Nakamura, S. Tsunashima, M. Hasegawa, and S. Uchiyama, "Perpendicular magnetic anisotropy of PdCo alloy in multilayered structure," *Journal of Magnetism and Magnetic Materials*, vol. 93, no. C, pp. 462–464, feb 1991. https://doi.org/10.1016/0304-8853(91)90384-M

[46] M. Küß, M. Heigl, L. Flacke, A. Hörner, M. Weiler, M. Albrecht, and A. Wixforth, "Nonreciprocal Dzyaloshinskii–Moriya Magnetoacoustic Waves," *Physical Review Letters*, vol. 125, no. 21, p. 217203, nov 2020. https://doi.org/10.1103/PhysRevLett.125.217203

[47] U. Gradmann and J. Müller, "Flat Ferromagnetic, Epitaxial 48Ni/52Fe(111) Films of few Atomic Layers," *Physica Status Solidi (b)*, vol. 27, no. 1, pp. 313–324, 1968. http://doi.wiley.com/10.1002/pssb.19680270133

[48] P. F. Carcia, A. D. Meinhaldt, and A. Suna, "Perpendicular magnetic anisotropy in Pd/Co thin film layered structures," *Applied Physics Letters*, vol. 47, no. 2, pp. 178–180, jul 1985. https://doi.org/10.1063/1.96254

[49] G. Bayreuther, M. Dumm, B. Uhl, R. Meier, and W. Kipferl, "Magnetocrystalline volume and interface anisotropies in epitaxial films: Universal relation and Néel's model (invited)," *Journal of Applied Physics*, vol. 93, no. 10, pp. 8230–8235, may 2003. https://doi.org/10.1063/1.1558638

[50] P. F. Carcia, "Perpendicular magnetic anisotropy in Pd/Co and Pt/Co thin-film layered structures," *Journal of Applied Physics*, vol. 63, no. 10, pp. 5066–5073, may 1988. https://doi.org/10.1063/1.340404

[51] J. Harzer, B. Hillebrands, R. Stamps, G. Güntherodt, D. Weller, C. Lee, R. Farrow, and E. Marinero, "Characterization of large magnetic anisotropies in (100)- and (111)-oriented Co/Pt multilayers by Brillouin light scattering," *Journal of Magnetism*

and Magnetic Materials, vol. 104-107, no. PART 3, pp. 1863–1864, feb 1992. https://doi.org/10.1016/0304-8853(92)91581-D

[52] D. Weiler, R. Farrow, R. Marks, G. Harp, H. Notarys, and G. Gorman, "Interface and Volume Anisotropy of MBE-Grown Co/Pt (111), (110) and (001) and Sputtered CO/Pt Multilayers," *MRS Proceedings*, vol. 313, p. 791, sep 1993. https://doi.org/10.1557/PROC-313-791

[53] M. Bersweiler, K. Dumesnil, D. Lacour, and M. Hehn, "Impact of buffer layer and Pt thickness on the interface structure and magnetic properties in (Co/Pt) multilayers," *Journal of Physics: Condensed Matter*, vol. 28, no. 33, p. 336005, aug 2016. https://doi.org/10.1088/0953-8984/28/33/336005

[54] N. Nakajima, T. Koide, T. Shidara, H. Miyauchi, H. Fukutani, A. Fujimori, K. Iio, T. Katayama, M. Nývlt, and Y. Suzuki, "Perpendicular Magnetic Anisotropy Caused by Interfacial Hybridization via Enhanced Orbital Moment in Co/Pt Multilayers: Magnetic Circular X-Ray Dichroism Study," *Physical Review Letters*, vol. 81, no. 23, pp. 5229–5232, dec 1998. https://doi.org/10.1103/PhysRevLett.81.5229

[55] S. Ikeda, K. Miura, H. Yamamoto, K. Mizunuma, H. D. Gan, M. Endo, S. Kanai, J. Hayakawa, F. Matsukura, and H. Ohno, "A perpendicular-anisotropy CoFeB–MgO magnetic tunnel junction," *Nature Materials*, vol. 9, no. 9, pp. 721–724, sep 2010. https://doi.org/10.1038/nmat2804

[56] X. Kozina, S. Ouardi, B. Balke, G. Stryganyuk, G. H. Fecher, C. Felser, S. Ikeda, H. Ohno, and E. Ikenaga, "A nondestructive analysis of the B diffusion in Ta–CoFeB–MgO–CoFeB–Ta magnetic tunnel junctions by hard x-ray photoemission," *Applied Physics Letters*, vol. 96, no. 7, p. 072105, feb 2010. https://doi.org/10.1063/1.3309702

[57] G. A. Prinz, "Stabilization of bcc Co via Epitaxial Growth on GaAs," *Physical Review Letters*, vol. 54, no. 10, pp. 1051–1054, mar 1985. https://doi.org/10.1103/PhysRevLett.54.1051

[58] K. Tsunekawa, Y.-S. Choi, Y. Nagamine, D. D. Djayaprawira, T. Takeuchi, and Y. Kitamoto, "Influence of Chemical Composition of CoFeB on Tunneling Magnetoresistance and Microstructure in Polycrystalline CoFeB/MgO/CoFeB Magnetic Tunnel Junctions," *Japanese Journal of Applied Physics*, vol. 45, no. No. 43, pp. L1152–L1155, oct 2006. https://doi.org/10.1143/JJAP.45.L1152

[59] T. Miyajima, T. Ibusuki, S. Umehara, M. Sato, S. Eguchi, M. Tsukada, and Y. Kataoka, "Transmission electron microscopy study on the crystallization and boron distribution of CoFeB/MgO/CoFeB magnetic tunnel junctions with various capping layers," *Applied Physics Letters*, vol. 94, no. 12, p. 122501, mar 2009. https://doi.org/10.1063/1.3106624

[60] S. V. Karthik, Y. K. Takahashi, T. Ohkubo, K. Hono, H. D. Gan, S. Ikeda, and H. Ohno, "Transmission electron microscopy study on the effect of various capping layers on CoFeB/MgO/CoFeB pseudo spin valves annealed at different temperatures," *Journal of Applied Physics*, vol. 111, no. 8, p. 083922, apr 2012. https://doi.org/10.1063/1.4707964

[61] D. C. Worledge, G. Hu, D. W. Abraham, J. Z. Sun, P. L. Trouilloud, J. Nowak, S. Brown, M. C. Gaidis, E. J. O'Sullivan, and R. P. Robertazzi, "Spin torque switching of perpendicular Ta/CoFeB/MgO-based magnetic tunnel junctions," *Applied Physics Letters*, vol. 98, no. 2, p. 022501, jan 2011. https://doi.org/10.1063/1.3536482

[62] H. X. Yang, M. Chshiev, B. Dieny, J. H. Lee, A. Manchon, and K. H. Shin, "First-principles investigation of the very large perpendicularmagnetic anisotropy at Fe|MgO and Co|MgO interfaces," *Physical Review B*, vol. 84, no. 5, p. 054401, aug 2011. https://doi.org/10.1103/PhysRevB.84.054401

[63] S. H. Liang, T. T. Zhang, P. Barate, J. Frougier, M. Vidal, P. Renucci, B. Xu, H. Jaffrès, J. M. George, X. Devaux, M. Hehn, X. Marie, S. Mangin, H. X. Yang, A. Hallal, M. Chshiev, T. Amand, H. F. Liu, D. P. Liu, X. F. Han, Z. G. Wang, and Y. Lu, "Large and robust electrical spin injection into GaAs at zero magnetic field using an ultrathin CoFeB/MgO injector," *Physical Review B - Condensed Matter and Materials Physics*, vol. 90, no. 8, pp. 1–9, 2014. https://doi.org/10.1103/PhysRevB.90.085310

[64] A. Kaidatzis, D. Gopman, C. Bran, J. García-Martín, M. Vázquez, and D. Niarchos, "Investigation of split CoFeB/Ta/CoFeB/MgO stacks for magnetic memories applications," *Journal of Magnetism and Magnetic Materials*, vol. 473, pp. 355–359, mar 2019. https://doi.org/10.1016/j.jmmm.2018.10.103

[65] Y. Park, S. Adenwalla, G. P. Felcher, and S. D. Bader, "Superparamagnetic relaxation of Fe deposited on MgO(001)," *Physical Review B*, vol. 52, no. 17, pp. 12 779–12 783, nov 1995. https://doi.org/PhysRevB.52.12779

[66] C. Martínez Boubeta, C. Clavero, J. M. García-Martín, G. Armelles, A. Cebollada, L. Balcells, J. L. Menéndez, F. Peiró, A. Cornet, and M. F. Toney, "Coverage effects on the magnetism of Fe/MgO(001) ultrathin films," *Physical Review B*, vol. 71, no. 1, p. 014407, jan 2005. https://doi.org/10.1103/PhysRevB.71.014407

[67] Y. Jang, C. Nam, J. Y. Kim, B. K. Cho, Y. J. Cho, and T. W. Kim, "Magnetic field sensing scheme using CoFeB/MgO/CoFeB tunneling junction with superparamagnetic CoFeB layer," *Applied Physics Letters*, 2006. https://doi.org/10.1063/1.2370876

[68] C. P. Bean and J. D. Livingston, "Superparamagnetism," *Journal of Applied Physics*, vol. 30, no. 4, pp. S120–S129, apr 1959. https://doi.org/10.1063/1.2185850

[69] W. F. Brown, "Thermal Fluctuations of a Single-Domain Particle," *Physical Review*, vol. 130, no. 5, pp. 1677–1686, jun 1963. https://doi.org/10.1103/PhysRev.130.1677

[70] W. Wernsdorfer, E. B. Orozco, K. Hasselbach, A. Benoit, B. Barbara, N. Demoncy, A. Loiseau, H. Pascard, and D. Mailly, "Experimental Evidence of the Néel-Brown Model of Magnetization Reversal," *Physical Review Letters*, vol. 78, no. 9, pp. 1791–1794, mar 1997. https://doi.org/10.1103/PhysRevLett.78.1791

[71] F. Bødker, M. F. Hansen, C. B. Koch, K. Lefmann, and S. Mørup, "Magnetic properties of hematite nanoparticles," *Physical Review B*, vol. 61, no. 10, pp. 6826–6838, mar 2000. https://doi.org/10.1103/PhysRevB.61.6826

[72] I. J. Bruvera, P. Mendoza Zélis, M. Pilar Calatayud, G. F. Goya, and F. H. Sánchez, "Determination of the blocking temperature of magnetic nanoparticles: The good, the bad, and the ugly," *Journal of Applied Physics*, vol. 118, no. 18, p. 184304, nov 2015. https://doi.org/10.1063/1.4935484

[73] J. M. Almeida and P. P. Freitas, "Field detection in MgO magnetic tunnel junctions with superparamagnetic free layer and magnetic flux concentrators," *Journal of Applied Physics*, vol. 105, no. 7, p. 07E722, apr 2009. https://doi.org/10.1063/1.3077228

[74] J. F. Feng, J. Y. Chen, M. Venkatesan, G. Feng, X. F. Han, and J. M. D. Coey, "Superparamagnetism in MgO-based magnetic tunnel junctions with a thin pinned ferromagnetic electrode," *Physical Review B*, vol. 81, no. 20, p. 205212, may 2010. https://doi.org/10.1103/PhysRevB.81.205212

[75] C. Tsai, C.-W. Cheng, M.-C. Tsai, and G. Chern, "Superparamagnetic States and Perpendicular Magnetic Anisotropy in Ultrathin MgO/CoFeB/Ta Structures," *IEEE Transactions on Magnetics*, vol. 50, no. 1, pp. 1–4, jan 2014. https://doi.org/10.1109/TMAG.2013.2274458

[76] Y. Zhang, G. He, X. Zhang, and G. Xiao, "Magnetotransport and electronic noise in superparamagnetic magnetic tunnel junctions," *Applied Physics Letters*, vol. 115, no. 2, p. 022402, jul 2019. https://doi.org/10.1063/1.5110715

[77] T. Nakano, M. Oogane, T. Furuichi, and Y. Ando, "Wide-dynamic-range magnetic sensor based on magnetic tunnel junctions using perpendicularly magnetized synthetic antiferromagnetic reference layer," *2017 IEEE International Magnetics Conference, INTERMAG 2017*, vol. 012401, p. 12401, 2017.

[78] Y. M. Lee, J. Hayakawa, S. Ikeda, F. Matsukura, and H. Ohno, "Effect of electrode composition on the tunnel magnetoresistance of pseudo-spin-valve magnetic tunnel junction with a MgO tunnel barrier," *Applied Physics Letters*, vol. 90, no. 21, p. 212507, may 2007. https://doi.org/10.1063/1.2742576

[79] W. Heisenberg, "Mehrkörperproblem und Resonanz in der Quantenmechanik," *Zeitschrift für Physik*, vol. 38, no. 6-7, pp. 411–426, jun 1926. https://doi.org/10.1007/BF01397160

[80] P. Dirac, "On the theory of quantum mechanics," *Proceedings of the Royal Society of London. Series A, Containing Papers of a Mathematical and Physical Character*, vol. 112, no. 762, pp. 661–677, oct 1926. . https://doi.org/10.1098/rspa.1926.0133

[81] W. H. Meiklejohn and C. P. Bean, "New Magnetic Anisotropy," *Physical Review*, vol. 102, no. 5, pp. 1413–1414, jun 1956. https://doi.org/10.1103/PhysRev.102.1413

[82] S. S. P. Parkin, N. More, and K. P. Roche, "Oscillations in exchange coupling and magnetoresistance in metallic superlattice structures: Co/Ru, Co/Cr, and Fe/Cr," *Physical Review Letters*, vol. 64, no. 19, pp. 2304–2307, may 1990. https://doi.org/10.1103/PhysRevLett.64.2304

[83] P. Bruno and C. Chappert, "Oscillatory coupling between ferromagnetic layers separated by a nonmagnetic metal spacer," *Physical Review Letters*, vol. 67, no. 12, pp. 1602–1605, sep 1991. https://doi.org/10.1103/PhysRevLett.67.1602

[84] D. M. Edwards, J. Mathon, R. B. Muniz, and M. S. Phan, "Oscillations of the Exchange in Magnetic Multilayers as an Analog of de Haas-van Alphen Effect," *Physical Review Letters*, vol. 67, no. 11, pp. 1476–1476, sep 1991. https://doi.org/10.1103/PhysRevLett.67.1476

[85] D. M. Edwards, J. Mathon, R. B. Muniz, M. S. Phan, "Oscillations in the exchange coupling of ferromagnetic layers separated by a nonmagnetic metallic layer," *Journal of Physics: Condensed Matter*, vol. 3, no. 26, pp. 4941–4958, jul 1991. https://doi.org/10.1088/0953-8984/3/26/015

[86] P. Bruno, "Theory of interlayer magnetic coupling," *Physical Review B*, vol. 52, no. 1, pp. 411–439, jul 1995. https://doi.org/10.1103/PhysRevB.52.411

[87] P. Grünberg, R. Schreiber, Y. Pang, U. Walz, M. B. Brodsky, and H. Sowers, "Layered magnetic structures: Evidence for antiferromagnetic coupling of Fe layers across Cr interlayers," *Journal of Applied Physics*, vol. 61, no. 8, pp. 3750–3752, apr 1987. https://doi.org/10.1063/1.338656

[88] A. Fert, P. Grünberg, A. Barthélémy, F. Petroff, and W. Zinn, "Layered magnetic structures: interlayer exchange coupling and giant magnetoresistance," *Journal of Magnetism and Magnetic Materials*, vol. 140-144, no. PART 1, pp. 1–8, 1995. https://doi.org/10.1016/0304-8853(94)00880-9

[89] M. A. Ruderman and C. Kittel, "Indirect Exchange Coupling of Nuclear Magnetic Moments by Conduction Electrons," *Physical Review*, vol. 96, no. 1, pp. 99–102, oct 1954. https://doi.org/10.1103/PhysRev.96.99

[90] T. Kasuya, "A Theory of Metallic Ferro- and Antiferromagnetism on Zener's Model," *Progress of Theoretical Physics*, vol. 16, no. 1, pp. 45–57, jul 1956. https://doi.org/10.1143/PTP.16.45

[91] K. Yosida, "Magnetic Properties of Cu-Mn Alloys," *Physical Review*, vol. 106, no. 5, pp. 893–898, jun 1957. https://doi.org/10.1103/PhysRev.106.893

[92] J. Mathon, D. Edwards, R. Muniz, and M. Phan, "Theory of oscillatory exchange coupling in magnetic multilayers," *Journal of Magnetism and Magnetic Materials*, vol. 104-107, no. 3, pp. 1721–1724, feb 1992. https://doi.org/10.1016/0304-8853(92)91523-V

[93] R. Gross, A. Marx, "*Festkörperphysik*, 2012, München, Oldenbourg, p. 698, isbn = "978-3-486-71294-0".

[94] P. Bruno, "Theory of interlayer exchange interactions in magnetic multilayers," *Journal of Physics: Condensed Matter*, vol. 11, no. 48, pp. 9403–9419, dec 1999. https://iopscience.iop.org/article/10.1088/0953-8984/11/48/305

[95] P. Grünberg and D. E. Bürgler, "Metallic Multilayers: Discovery of Interlayer Exchange Coupling and GMR," in *Handbook of Spintronics*, Y. Xu, D. D. Awschalom, and J. Nitta, Dordrecht: Springer Netherlands, 2015, pp. 1–16. http://link.springer.com/10.1007/978-94-007-7604-3http://link.springer.com/10.1007/978-94-007-7604-3{_}6-1

[96] P. Bruno, "Interlayer exchange coupling: a unified physical picture," *Journal of Magnetism and Magnetic Materials*, vol. 121, no. 1-3, pp. 248–252, mar 1993. https://doi.org/10.1016/0304-8853(93)91197-F

[97] W. Thomson, "XIX. On the electro-dynamic qualities of metals: Effects of magnetization on the electric conductivity of nickel and of iron," *Proceedings of the Royal Society of London*, vol. 8, pp. 546–550, dec 1857. https://doi.org/10.1098/rspl.1856.0144

[98] A. P. Ramirez, "Colossal magnetoresistance," *Journal of Physics: Condensed Matter*, vol. 9, no. 39, pp. 8171–8199, sep 1997. https://doi.org/10.1088/0953-8984/9/39/005

[99] P. J. Chen, Y. L. Iunin, S. F. Cheng, and R. D. Shull, "Underlayer Effect on Perpendicular Magnetic Anisotropy in Co 20 Fe 60 B 20 /MgO Films," *IEEE Transactions on Magnetics*, vol. 52, no. 7, pp. 1–4, jul 2016. https://doi.org/10.1109/TMAG.2015.2511662

[100] J. Sun and J. Kosel, "Extraordinary Magnetoresistance in Semiconductor/Metal Hybrids: A Review," *Materials*, vol. 6, no. 2, pp. 500–516, feb 2013. https://doi.org/10.3390/ma6020500

[101] M. N. Baibich, J. M. Broto, A. Fert, F. N. Van Dau, F. Petroff, P. Etienne, G. Creuzet, A. Friederich, and J. Chazelas, "Giant Magnetoresistance of (001)Fe/(001)Cr Magnetic Superlattices," *Physical Review Letters*, vol. 61, no. 21, pp. 2472–2475, nov 1988. https://doi.org/10.1103/PhysRevLett.61.2472

[102] G. Binasch, P. Grünberg, F. Saurenbach, and W. Zinn, "Enhanced magnetoresistance in layered magnetic structures with antiferromagnetic interlayer exchange," *Physical Review B*, vol. 39, no. 7, pp. 4828–4830, mar 1989. https://doi.org/10.1103/PhysRevB.39.4828

[103] S. S. P. Parkin, Z. G. Li, and D. J. Smith, "Giant magnetoresistance in antiferromagnetic Co/Cu multilayers," *Applied Physics Letters*, vol. 58, no. 23, pp. 2710–2712, jun 1991. https://doi.org/10.1063/1.104765

[104] R. Schad, C. Potter, P. Beliën, G. Verbanck, J. Dekoster, G. Langouche, V. Moshchalkov, and Y. Bruynseraede, "Interplay between interface properties and giant magnetoresistance in epitaxial Fe/Cr superlattices," *Journal of Magnetism and Magnetic Materials*, vol. 148, no. 1-2, pp. 331–332, jul 1995. https://doi.org/10.1016/0304-8853(95)00259-6

[105] B. Dieny, V. S. Speriosu, S. S. P. Parkin, B. A. Gurney, D. R. Wilhoit, and D. Mauri, "Giant magnetoresistive in soft ferromagnetic multilayers," *Physical Review B*, vol. 43, no. 1, pp. 1297–1300, jan 1991. https://doi.org/10.1103/PhysRevB.43.1297

[106] R. Coehoorn, *Magnetic Multilayers and Giant Magnetoresistance*, ser. Springer Series in Surface Sciences, U. Hartmann, Ed. Berlin, Heidelberg: Springer Berlin Heidelberg, pp. 65–127, 2000, vol. 37. https://doi.org/10.1007/978-3-662-04121-5

[107] K. B. Fathoni, Y. Sakuraba, T. Sasaki, Y. Miura, J. W. Jung, T. Nakatani, and K. Hono, "Band match enhanced current-in-plane giant magnetoresistance in epitaxial Co 50 Fe 50 /Cu multilayers with metastable bcc-Cu spacer," *APL Materials*, vol. 7, no. 11, p. 111106, nov 2019. https://doi.org/10.1063/1.5119370

[108] X. Zhang and W. Butler, "Theory of Giant Magnetoresistance and Tunneling Magnetoresistance," in *Handbook of Spintronics*, Y. Xu, D. D. Awschalom, and J. Nitta, Dordrecht: Springer Netherlands, 2015, pp. 1–56. https://doi.org/10.1007/978-94-007-7604-3

[109] E. Tsymbal and D. Pettifor, "Perspectives of giant magnetoresistance," in *Solid State Physics - Advances in Research and Applications*, 2001, vol. 56, no. C, pp. 113–237. https://linkinghub.elsevier.com/retrieve/pii/S0081194701800199

[110] N. Mott, "The electrical conductivity of transition metals," *Proceedings of the Royal Society of London. Series A - Mathematical and Physical Sciences*, vol. 153, no. 880, pp. 699–717, feb 1936. Available: https://royalsocietypublishing.org/doi/10.1098/rspa.1936.0031

[111] N. Mott, "Electrons in transition metals," *Advances in Physics*, vol. 13, no. 51, pp. 325–422, jul 1964. https://doi.org/10.1080/00018736400101041

[112] R. Meservey, P. M. Tedrow, and P. Fulde, "Magnetic Field Splitting of the Quasiparticle States in Superconducting Aluminum Films," *Physical Review Letters*, vol. 25, no. 18, pp. 1270–1272, nov 1970. https://doi.org/10.1103/PhysRevLett.25.1270

[113] P. M. Tedrow and R. Meservey, "Spin-Dependent Tunneling into Ferromagnetic Nickel," *Physical Review Letters*, vol. 26, no. 4, pp. 192–195, jan 1971. https://doi.org/10.1103/PhysRevLett.26.192

[114] P. M. Tedrow, R. Meservey, "Spin Polarization of Electrons Tunneling from Films of Fe, Co, Ni, and Gd," *Physical Review B*, vol. 7, no. 1, pp. 318–326, jan 1973. https://doi.org/10.1103/PhysRevB.7.318

[115] M. Julliere, "Tunneling between ferromagnetic films," *Physics Letters A*, vol. 54, no. 3, pp. 225–226, sep 1975. https://doi.org/10.1016/0375-9601(75)90174-7

[116] R. Meservey and P. M. Tedrow, "Spin-polarized electron tunneling," vol. 4, no. 4, 1994. https://doi.org/10.1016/0370-1573(94)90105-8

[117] S. V. Karthik, T. M. Nakatani, A. Rajanikanth, Y. K. Takahashi, and K. Hono, "Spin polarization of Co–Fe alloys estimated by point contact Andreev reflection and tunneling magnetoresistance," *Journal of Applied Physics*, vol. 105, no. 7, p. 07C916, apr 2009. https://doi.org/10.1063/1.3058699

[118] S. X. Huang, T. Y. Chen, and C. L. Chien, "Spin polarization of amorphous CoFeB determined by point-contact Andreev reflection," *Applied Physics Letters*, vol. 92, no. 24, p. 242509, jun 2008. https://doi.org/10.1063/1.2949740

[119] S. Ikeda, J. Hayakawa, Y. Ashizawa, Y. M. Lee, K. Miura, H. Hasegawa, M. Tsunoda, F. Matsukura, and H. Ohno, "Tunnel magnetoresistance of 604% at 300K by suppression of Ta diffusion in CoFeB/MgO/CoFeB pseudo-spin-valves annealed at high temperature," *Applied Physics Letters*, vol. 93, no. 8, p. 082508, aug 2008. https://doi.org/10.1063/1.2976435

[120] S. Yuasa and D. D. Djayaprawira, "Giant tunnel magnetoresistance in magnetic tunnel junctions with a crystalline MgO(001) barrier," *Journal of Physics D: Applied Physics*, vol. 40, no. 21, pp. R337–R354, nov 2007. https://doi.org/10.1088/0022-3727/40/21/R01

[121] W. H. Butler, X.-G. Zhang, T. C. Schulthess, and J. M. MacLaren, "Spin-dependent tunneling conductance of Fe|MgO|Fe sandwiches," *Physical Review B*, vol. 63, no. 5, p. 054416, jan 2001. https://doi.org/10.1103/PhysRevB.63.054416

[122] X.-G. Zhang and W. H. Butler, "Large magnetoresistance in bcc Co/MgO/Co and FeCo/MgO/FeCo tunnel junctions," *Physical Review B*, vol. 70, no. 17, p. 172407, nov 2004. https://doi.org/10.1103/PhysRevB.70.172407

[123] W. Butler, X.-G. Zhang, S. Vutukuri, M. Chshiev, and T. Schulthess, "Theory of tunneling magnetoresistance for epitaxial systems," *IEEE Transactions on Magnetics*, vol. 41, no. 10, pp. 2645–2648, oct 2005. https://doi.org/10.1109/TMAG.2005.854763

[124] W. H. Butler, "Tunneling magnetoresistance from a symmetry filtering effect," *Science and Technology of Advanced Materials*, vol. 9, no. 1, p. 014106, jan 2008. https://doi.org/10.1088/1468-6996/9/1/014106

[125] J. Mathon and A. Umerski, "Theory of tunneling magnetoresistance of an epitaxial Fe/MgO/Fe(001) junction," *Physical Review B*, vol. 63, no. 22, p. 220403, may 2001. https://doi.org/10.1103/PhysRevB.63.220403

[126] L. Berger, "Influence of Spin-Orbit Interaction on the Transport Processes in Ferromagnetic Nickel Alloys, in the Presence of a Degeneracy of the 3d Band," *Journal of Applied Physics*, vol. 34, no. 4, pp. 1360–1361, apr 1963. https://doi.org/10.1063/1.1729509

[127] J. Smit, "Magnetoresistance of ferromagnetic metals and alloys at low temperatures," *Physica*, vol. 17, no. 6, pp. 612–627, jun 1951. https://doi.org/10.1016/0031-8914(51)90117-6

[128] R. I. Potter, "Magnetoresistance anisotropy in ferromagnetic NiCu alloys," *Physical Review B*, vol. 10, no. 11, pp. 4626–4636, dec 1974. https://doi.org/doi/10.1103/PhysRevB.10.4626

[129] T. McGuire and R. Potter, "Anisotropic magnetoresistance in ferromagnetic 3d alloys," *IEEE Transactions on Magnetics*, vol. 11, no. 4, pp. 1018–1038, jul 1975. https://doi.org/10.1109/TMAG.1975.1058782

[130] R. Gross and A. Marx, "Magnetoresistive Effekte, Der anisotrope Magnetwiderstand," *Script: Spinelektronic*, pp. 83–94, 2004. https://www.wmi.badw.de/teaching/Lecturenotes/ME/ME_Kapitel3.pdf

[131] A. Kobs, S. Heße, W. Kreuzpaintner, G. Winkler, D. Lott, P. Weinberger, A. Schreyer, and H. P. Oepen, "Anisotropic Interface Magnetoresistance in Pt/Co/Pt Sandwiches," *Physical Review Letters*, vol. 106, no. 21, p. 217207, may 2011. https://doi.org/10.1103/PhysRevLett.106.217207

[132] A. Kobs, S. Heße, H. Oepen, and P. Weinberger, "Anisotropic interface magnetoresistances in Pt(111)/Co/Pt(111)," *Philosophical Magazine*, vol. 92, no. 22, pp. 2835–2847, aug 2012. https://doi.org/10.1080/14786435.2012.676213

[133] A. Kobs and H. P. Oepen, "Disentangling interface and bulk contributions to the anisotropic magnetoresistance in Pt/Co/Pt sandwiches," *Physical Review B*, vol. 93, no. 1, p. 014426, jan 2016. https://doi.org/10.1103/PhysRevB.93.014426

[134] A. Philippi-Kobs, A. Farhadi, L. Matheis, D. Lott, A. Chuvilin, and H. P. Oepen, "Impact of Symmetry on Anisotropic Magnetoresistance in Textured Ferromagnetic Thin Films," *Physical Review Letters*, vol. 123, no. 13, p. 137201, sep 2019. https://doi.org/10.1103/PhysRevLett.123.137201

[135] P. Kelly and R. Arnell, "Magnetron sputtering: a review of recent developments and applications," *Vacuum*, vol. 56, no. 3, pp. 159–172, mar 2000. https://doi.org/10.1016/S0042-207X(99)00189-X

[136] J. T. Gudmundsson, "Physics and technology of magnetron sputtering discharges," *Plasma Sources Science and Technology*, vol. 29, no. 11, p. 113001, nov 2020. https://doi.org/10.1088/1361-6595/abb7bd

[137] F. Shi, "Introductory Chapter: Basic Theory of Magnetron Sputtering," in *Magnetron Sputtering [Working Title]*. IntechOpen, nov 2018. https://doi.org/10.5772/intechopen.80550

[138] D. Maurya, A. Sardarinejad, and K. Alameh, "Recent Developments in R.F. Magnetron Sputtered Thin Films for pH Sensing Applications – An Overview," *Coatings*, vol. 4, no. 4, pp. 756–771, dec 2014. http://www.mdpi.com/2079-6412/4/4/756

[139] J. C. Gallop, *SQUIDs, the Josephson Effects and Superconducting Electronics*. CRC Press, oct 2017. https://doi.org/10.1201/9780203738887

[140] W. Buckel, "Supraleitung," *Die Naturwissenschaften*, vol. 58, no. 4, pp. 177–183, apr 1971. https://doi.org/10.1007/BF00591842

[141] I. Quantum Design, "Magnetic Property Measurement System ® MPMS 3 User's Manual," no. 1500. https://www.mrl.ucsb.edu/sites/default/files/mrl_docs/instruments/1500-100Rev.F1MPMS3UsersManual.pdf

[142] B. Josephson, "Possible new effects in superconductive tunnelling," *Physics Letters*, vol. 1, no. 7, pp. 251–253, jul 1962. https://doi.org/10.1016/0031-9163(62)91369-0

[143] R. L. Fagaly, "Superconducting quantum interference device instruments and applications," *Review of Scientific Instruments*, vol. 77, no. 10, p. 101101, oct 2006. https://doi.org/10.1063/1.2354545

[144] N. Schmidt, "FePt-based thin films : doping with 3d and 4f elements," PhD thesis, University of Augsburg, 2020.

[145] R. Gross and A. Marx, "Applied Superconductivity: Josephson Effect and Superconducting Electronics," *Manuscript to the lectures*, pp. 194–196, 2005. https://www.wmi.badw.de/teaching/Lecturenotes/AS/AS_Chapter3.pdf

[146] A.-O. Mandru, O. Yıldırım, M. A. Marioni, H. Rohrmann, M. Heigl, O.-T. Ciubotariu, M. Penedo, X. Zhao, M. Albrecht, and H. J. Hug, "Pervasive artifacts revealed from magnetometry measurements of rare earth-transition metal thin films," *Journal of Vacuum Science & Technology A*, vol. 38, no. 2, p. 023409, mar 2020. https://doi.org/10.1116/1.5135504

[147] J. Kerr, "XLIII. On rotation of the plane of polarization by reflection from the pole of a magnet," *The London, Edinburgh, and Dublin Philosophical Magazine and Journal of Science*, vol. 3, no. 19, pp. 321–343, may 1877. https://doi.org/10.1080/14786447708639245

[148] J. Kerr, "XXIV. On reflection of polarized light from the equatorial surface of a magnet," *The London, Edinburgh, and Dublin Philosophical Magazine and Journal of Science*, vol. 5, no. 30, pp. 161–177, mar 1878. https://doi.org/10.1080/14786447808639407

[149] M. Faraday, "I. Experimental researches in electricity. Nineteenth series," *Philosophical Transactions of the Royal Society of London*, vol. 136, pp. 1–20, dec 1846. https://doi.org/10.1098/rstl.1846.0001

[150] Z. Q. Qiu and S. D. Bader, "Surface magneto-optic Kerr effect," *Review of Scientific Instruments*, vol. 71, no. 3, pp. 1243–1255, mar 2000. https://doi.org/10.1063/1.1150496

[151] A. Hubert and R. Schäfer, *Magnetic Domains*, 3rd ed. Berlin, Heidelberg: Springer Berlin Heidelberg, pp. 24–27, 1998. http://link.springer.com/10.1007/978-3-540-85054-0

[152] J. C. Maxwell, "Magnetic action on light," in *A Treatise on Electricity and Magnetism*. Cambridge: Cambridge University Press, 1873, ch. XXI, pp. 399–417. https://www.cambridge.org/core/product/identifier/CBO9780511709340A035/type/book_part

[153] L. J. van der Pauw, "A method of measuring a specific resistivity and Hall effect of discs of arbitrary shape," in *Semiconductor Devices: Pioneering Papers*. World Scientific, 1991, vol. 20, no. 8, pp. 174–182. https://doi.org/10.1142/9789814503464_0017

[154] D. W. Koon, A. A. Bahl, and E. O. Duncan, "Measurement of contact placement errors in the van der Pauw technique," *Review of Scientific Instruments*, vol. 60, no. 2, pp. 275–276, feb 1989. https://doi.org/10.1063/1.1140423

[155] H. Weitensfelder, H. Brueckl, A. Satz, K. Pruegl, J. Zimmer, S. Luber, W. Raberg, C. Abert, F. Bruckner, A. Bachleitner-Hofmann, R. Windl, and D. Suess, "Comparison of Sensitivity and Low-Frequency Noise Contributions in Giant-Magnetoresistive and Tunneling-Magnetoresistive Spin-Valve Sensors with a Vortex-State Free Layer," *Physical Review Applied*, vol. 10, no. 5, p. 054056, nov 2018. https://doi.org/10.1103/PhysRevApplied.10.054056

[156] D. C. Worledge and P. L. Trouilloud, "Magnetoresistance measurement of unpatterned magnetic tunnel junction wafers by current-in-plane tunneling," *Applied Physics Letters*, vol. 83, no. 1, pp. 84–86, jul 2003. https://doi.org/10.1063/1.1590740

[157] D. W. Abraham, P. L. Trouilloud, and D. C. Worledge, "Rapid-turnaround characterization methods for MRAM development," *IBM Journal of Research and Development*, vol. 50, no. 1, pp. 55–67, jan 2006. https://doi.org/10.1147/rd.501.0055

[158] T. Wurft, W. Raberg, K. Prügl, A. Satz, G. Reiss, and H. Brückl, "Evolution of magnetic vortex formation in micron-sized disks," *Applied Physics Letters*, vol. 115, no. 13, p. 132407, sep 2019. https://doi.org/10.1063/1.5116299

[159] R. Law, R. Sbiaa, T. Liew, and T. C. Chong, "Effects of Ta seed layer and annealing on magnetoresistance in CoFe/Pd-based pseudo-spin-valves with perpendicular

anisotropy," *Applied Physics Letters*, vol. 91, no. 24, p. 242504, dec 2007. https://doi.org/10.1063/1.2824832

[160] J. Cao, J. Kanak, T. Stobiecki, P. Wisniowski, and P. Freitas, "Effect of Buffer Layer Texture on the Crystallization of CoFeB and on the Tunnel Magnetoresistance in MgO Based Magnetic Tunnel Junctions," *IEEE Transactions on Magnetics*, vol. 45, no. 10, pp. 3464–3466, oct 2009. https://doi.org/10.1109/TMAG.2009.2025382

[161] C.-J. Lin, G. Gorman, C. Lee, R. Farrow, E. Marinero, H. Do, H. Notarys, and C. Chien, "Magnetic and structural properties of Co/Pt multilayers," *Journal of Magnetism and Magnetic Materials*, vol. 93, no. 7, pp. 194–206, feb 1991. https://doi.org/10.1016/0304-8853(91)90329-9

[162] J. Moritz, F. Garcia, J. C. Toussaint, B. Dieny, and J. P. Nozières, "Orange peel coupling in multilayers with perpendicular magnetic anisotropy: Application to (Co/Pt)-based exchange-biased spin-valves," *Europhysics Letters (EPL)*, vol. 65, no. 1, pp. 123–129, jan 2004. https://doi.org/10.1209/epl/i2003-10063-9

[163] J. W. Knepper and F. Y. Yang, "Oscillatory interlayer coupling in Co/Pt multilayers with perpendicular anisotropy," *Physical Review B*, vol. 71, no. 22, p. 224403, jun 2005. https://doi.org/10.1103/PhysRevB.71.224403

[164] M. Czapkiewicz, J. Kanak, T. Stobiecki, M. Kachel, M. ZoŁ\k{a}dź, I. Sveklo, A. Maziewski, and S. Van Dijken, "Micromagnetic properties of Co/Pt multilayers deposited on various buffer layers," *Materials Science-Poland*, vol. 26, no. 4, pp. 839–849, 2008. https://cris.vtt.fi/en/publications/micromagnetic-properties-of-copt-multilayers-deposited-on-various

[165] J. Kanak, M. Czapkiewicz, T. Stobiecki, M. Kachel, I. Sveklo, A. Maziewski, and S. van Dijken, "Influence of buffer layers on the texture and magnetic properties of Co/Pt multilayers with perpendicular anisotropy," *physica status solidi (a)*, vol. 204, no. 12, pp. 3950–3953, dec 2007. https://doi.org/10.1002/pssa.200777104

[166] S. Bandiera, R. R. Sousa, B. B. Rodmacq, and B. Dieny, "Asymmetric Interfacial Perpendicular Magnetic Anisotropy in Pt/Co/Pt Trilayers," *IEEE Magnetics Letters*, vol. 2, pp. 3 000 504–3 000 504, 2011. https://doi.org/10.1109/LMAG.2011.2174032

[167] Y. An, L. Duan, T. Liu, Z. Wu, and J. Liu, "Applied Surface Science Structural and magnetic properties of Pt in Co / Pt multilayers," *Applied Surface Science*, vol. 257, no. 17, pp. 7427–7431, 2011. http://dx.doi.org/10.1016/j.apsusc.2011.02.109

[168] S. Emori and G. S. D. Beach, "Optimization of out-of-plane magnetized Co/Pt multilayers with resistive buffer layers," *Journal of Applied Physics*, vol. 110, no. 3, p. 033919, aug 2011. https://doi.org/10.1063/1.3622613

[169] J. Chatterjee, T. Tahmasebi, S. Mertens, G. S. Kar, T. Min, and J. D. Boeck, "Seed Layer Effect on the Magnetic Properties of Ultrathin Co/Pt Multilayers With Perpendicular Magnetic Anisotropy," *IEEE Transactions on Magnetics*, vol. 50, no. 11, pp. 1–4, nov 2014. http://ieeexplore.ieee.org/document/6971467/

[170] S. T. Lim, M. Tran, J. W. Chenchen, J. F. Ying, and G. Han, "Effect of different seed layers with varying Co and Pt thicknesses on the magnetic properties of Co/Pt multilayers," *Journal of Applied Physics*, vol. 117, no. 17, p. 17A731, may 2015. https://doi.org/10.1063/1.4916295

[171] J. Chatterjee, T. Tahmasebi, J. Swerts, G. S. Kar, and J. De Boeck, "Impact of seed layer on post-annealing behavior of transport and magnetic properties of Co/Pt multilayer-based bottom-pinned perpendicular magnetic tunnel junctions," *Applied Physics Express*, vol. 8, no. 6, p. 063002, jun 2015. https://doi.org/10.7567/APEX.8.063002

[172] Y. Li, X. Jin, P. Pan, F. N. Tan, W. S. Lew, and F. Ma, "Temperature-dependent interlayer exchange coupling strength in synthetic antiferromagnetic [Pt/Co] 2 /Ru/[Co/Pt] 4 multilayers," *Chinese Physics B*, vol. 27, no. 12, p. 127502, dec 2018. https://doi.org/10.1088/1674-1056/27/12/127502

[173] P. Chowdhury, P. D. Kulkarni, M. Krishnan, H. C. Barshilia, A. Sagdeo, S. K. Rai, G. S. Lodha, and D. V. Sridhara Rao, "Effect of coherent to incoherent structural transition on magnetic anisotropy in Co/Pt multilayers," *Journal of Applied Physics*, vol. 112, no. 2, p. 023912, jul 2012. https://doi.org/10.1063/1.4739284

[174] K. Yakushiji, H. Takagi, N. Watanabe, A. Fukushima, K. Kikuchi, Y. Kurashima, A. Sugihara, H. Kubota, and S. Yuasa, "Three-dimensional integration technology of magnetic tunnel junctions for magnetoresistive random access memory application," *Applied Physics Express*, vol. 10, no. 6, p. 063002, jun 2017. https://doi.org/10.7567/APEX.10.063002

[175] O. Hellwig, A. Berger, J. B. Kortright, and E. E. Fullerton, "Domain structure and magnetization reversal of antiferromagnetically coupled perpendicular anisotropy films," *Journal of Magnetism and Magnetic Materials*, vol. 319, no. 1-2, pp. 13–55, dec 2007. https://doi.org/10.1016/j.jmmm.2007.04.035

[176] S.-L. Jiang, G. Yang, J. Teng, Q.-X. Guo, L.-L. Li, and G.-H. Yu, "Interface-engineered spin-dependent transport in perpendicular Co/Pt multilayers," *Applied Surface Science*, vol. 387, pp. 375–378, nov 2016. http://dx.doi.org/10.1016/j.apsusc.2016.06.089

[177] J. S. Tsay and C. S. Shern, "Diffusion and alloy formation of Co ultrathin films on Pt(111)," *Journal of Applied Physics*, vol. 80, no. 7, pp. 3777–3781, oct 1996. https://doi.org/10.1063/1.363329

[178] S. J. Yun, S. H. Lim, and S.-R. Lee, "Strong interlayer exchange coupling and high post-annealing stability in perpendicularly magnetized [Pt/Co]/Ru/[Co/Pt] structures," *AIP Advances*, vol. 6, no. 2, p. 025112, feb 2016. https://doi.org/10.1063/1.4942206

[179] Y. Liu, J. Yu, and H. Zhong, "Strong antiferromagnetic interlayer exchange coupling in [Co/Pt]6/Ru/[Co/Pt]4 structures with perpendicular magnetic anisotropy," *Journal of Magnetism and Magnetic Materials*, vol. 473, pp. 381–386, mar 2019. https://doi.org/10.1016/j.jmmm.2018.10.090

[180] K. Yakushiji, H. Kubota, A. Fukushima, and S. Yuasa, "Perpendicular magnetic tunnel junction with enhanced anisotropy obtained by utilizing an Ir/Co interface," *Applied Physics Express*, 2016. https://doi.org/10.7567/APEX.9.013003

[181] Z. H. Yuan, L. Huang, J. F. Feng, Z. C. Wen, D. L. Li, X. F. Han, T. Nakano, T. Yu, and H. Naganuma, "Double-pinned magnetic tunnel junction sensors with spin-valve-like sensing layers," *Journal of Applied Physics*, vol. 118, no. 5, p. 053904, aug 2015. http://aip.scitation.org/doi/10.1063/1.4927840

[182] L. Huang, Z. H. Yuan, B. S. Tao, C. H. Wan, P. Guo, Q. T. Zhang, L. Yin, J. F. Feng, T. Nakano, H. Naganuma, H. F. Liu, Y. Yan, and X. F. Han, "Noise suppression and sensitivity manipulation of magnetic tunnel junction sensors with soft magnetic Co 70.5 Fe 4.5 Si 15 B 10 layer," *Journal of Applied Physics*, vol. 122, no. 11, p. 113903, sep 2017. https://doi.org/10.1063/1.4990478

[183] M. Shinozaki, J. Igarashi, H. Sato, and H. Ohno, "Free-layer size dependence of anisotropy field in nanoscale CoFeB/MgO magnetic tunnel junctions," *Applied Physics Express*, vol. 11, no. 4, p. 043001, apr 2018. https://doi.org/10.7567/APEX.11.043001

[184] H. Sato, T. Yamamoto, M. Yamanouchi, S. Ikeda, S. Fukami, K. Kinoshita, F. Matsukura, N. Kasai, and H. Ohno, "Comprehensive study of CoFeB-MgO magnetic tunnel junction characteristics with single- and double-interface scaling down to 1X nm," *Technical Digest - International Electron Devices Meeting, IEDM*, pp. 60–63, 2013. https://doi.org/10.1109/IEDM.2013.6724550

[185] J. Chatterjee, S. Auffret, R. Sousa, P. Coelho, I.-l. Prejbeanu, and B. Dieny, "Novel multifunctional RKKY coupling layer for ultrathin perpendicular synthetic antiferromagnet," *Scientific Reports*, vol. 8, no. 1, p. 11724, dec 2018. http://www.nature.com/articles/s41598-018-29913-6

[186] D.-K. Lee and S.-C. Hong, "Correlation between Structures and Magnetism in Iron: Ferromagnetism and Antiferromagnetism," *Journal of Magnetics*, vol. 12, no. 2, pp. 68–71, jun 2007. https://doi.org/10.4283/JMAG.2007.12.2.068

[187] X. Kou, J. Schmalhorst, A. Thomas, and G. Reiss, "Temperature dependence of the resistance of magnetic tunnel junctions with MgO barrier," *Applied Physics Letters*, vol. 88, no. 21, p. 212115, may 2006. https://doi.org/10.1063/1.2206680

[188] S. G. Wang, R. C. C. Ward, G. X. Du, X. F. Han, C. Wang, and A. Kohn, "Temperature dependence of giant tunnel magnetoresistance in epitaxial Fe/MgO/Fe magnetic tunnel junctions," *Physical Review B*, vol. 78, no. 18, p. 180411, nov 2008. https://doi.org/10.1103/PhysRevB.78.180411

[189] S. S. P. Parkin, C. Kaiser, A. Panchula, P. M. Rice, B. Hughes, M. Samant, and S.-H. Yang, "Giant tunnelling magnetoresistance at room temperature with MgO (100) tunnel barriers," *Nature Materials*, vol. 3, no. 12, pp. 862–867, dec 2004. https://doi.org/10.1038/nmat1256

[190] Y.-Y. Chen, Z. Shi, S. Zhou, W.-B. Rui, and J. Du, "Tunable interface anisotropy in a Pt/CoFe/Pt multilayer," *Chinese Physics B*, vol. 22, no. 6, p. 067504, jun 2013. https://doi.org/10.1088/1674-1056/22/6/067504

[191] K. Eid, R. Fonck, M. A. Darwish, W. P. Pratt, and J. Bass, "Current-perpendicular-to-plane-magnetoresistance properties of Ru and Co/Ru interfaces," *Journal of Applied Physics*, vol. 91, no. 10, p. 8102, 2002. https://doi.org/10.1063/1.1447294

[192] J. Bass and W. P. Pratt, "Spin-diffusion lengths in metals and alloys, and spin-flipping at metal/metal interfaces: an experimentalist's critical review," *Journal of Physics: Condensed Matter*, vol. 19, no. 18, p. 183201, may 2007. https://doi.org/10.1088/0953-8984/19/18/183201

[193] D. Houssameddine, U. Ebels, B. Delaët, B. Rodmacq, I. Firastrau, F. Ponthenier, M. Brunet, C. Thirion, J.-P. Michel, L. Prejbeanu-Buda, M.-C. Cyrille, O. Redon, and B. Dieny, "Spin-torque oscillator using a perpendicular polarizer and a planar free layer," *Nature Materials*, vol. 6, no. 6, pp. 447–453, jun 2007. http://www.nature.com/articles/nmat1905

[194] C. Muehlenhoff, C. Vogler, W. Raberg, D. Suess, and M. Albrecht, "Spin-Canting Effects in GMR Sensors With Wide Dynamic Field Range," *IEEE Sensors Journal*, vol. 21, no. 12, pp. 13 176–13 183, jun 2021. https://ieeexplore.ieee.org/document/9382283/

[195] C. Abert, L. Exl, F. Bruckner, A. Drews, and D. Suess, "Journal of Magnetism and Magnetic Materials magnum.fe: A micromagnetic finite-element simulation code based on FEniCS," *Journal of Magnetism and Magnetic Materials*, vol. 345, pp. 29–35, 2013. http://dx.doi.org/10.1016/j.jmmm.2013.05.051

[196] A. D. Kent, J. Yu, U. Rüdiger, and S. S. P. Parkin, "Domain wall resistivity in epitaxial thin film microstructures," *Journal of Physics: Condensed Matter*, vol. 13, no. 25, pp. R461–R488, jun 2001. https://doi.org/10.1088/0953-8984/13/25/202

[197] A. Kent, U. Ruediger, J. Yu, S. Zhang, P. Levy, Y. Zhong, and S. Parkin, "Magnetoresistance due to domain walls in micron scale Fe wires with stripe domains," *IEEE Transactions on Magnetics*, vol. 34, no. 4, pp. 900–902, jul 1998. https://doi.org/10.1109/20.706305

[198] Y. Wu, Y. Suzuki, U. Rüdiger, J. Yu, A. D. Kent, T. K. Nath, and C. B. Eom, "Magnetotransport and magnetic domain structure in compressively strained colossal magnetoresistance films," *Applied Physics Letters*, vol. 75, no. 15, pp. 2295–2297, oct 1999. https://doi.org/10.1063/1.124995

[199] D. Mitin, M. Grobis, and M. Albrecht, "Scanning magnetoresistive microscopy: An advanced characterization tool for magnetic nanosystems," *Review of Scientific Instruments*, vol. 87, no. 2, p. 023703, feb 2016. http://dx.doi.org/10.1063/1.4941292

[200] S. Yamamoto, S. Schultz, Yun Zhang, and H. Bertram, "Scanning magnetoresistance microscopy (SMRM) as a diagnostic for high density recording," *IEEE Transactions on Magnetics*, vol. 33, no. 1, pp. 891–896, 1997. https://doi.org/10.1109/20.560127

[201] O. Kazakova, R. Puttock, C. Barton, H. Corte-León, M. Jaafar, V. Neu, and A. Asenjo, "Frontiers of magnetic force microscopy," *Journal of Applied Physics*, vol. 125, no. 6, p. 060901, feb 2019. http://dx.doi.org/10.1063/1.5050712

[202] R. A. Hajjar, M. Mansuripur, and H. D. Shieh, "Measurements of the anomalous magnetoresistance effect in Co/Pt and Co/Pd multilayer films for magneto-optical data storage applications," *Journal of Applied Physics*, vol. 69, no. 8, pp. 4686–4688, apr 1991. https://doi.org/10.1063/1.348297

[203] W. Butler, X.-G. Zhang, D. Nicholson, and J. MacLaren, "Spin-dependent scattering and giant magnetoresistance," *Journal of Magnetism and Magnetic Materials*, vol. 151, no. 3, pp. 354–362, dec 1995. https://doi.org/10.1016/0304-8853(95)00507-2

[204] S. S. P. Parkin, R. Bhadra, and K. P. Roche, "Oscillatory magnetic exchange coupling through thin copper layers," *Physical Review Letters*, vol. 66, no. 16, pp. 2152–2155, apr 1991. https://doi.org/10.1103/PhysRevLett.66.2152

[205] B. Dieny, P. Humbert, V. S. Speriosu, S. Metin, B. A. Gurney, P. Baumgart, and H. Lefakis, "Giant magnetoresistance of magnetically soft sandwiches: Dependence on temperature and on layer thicknesses," *Physical Review B*, vol. 45, no. 2, pp. 806–813, jan 1992. https://doi.org/10.1103/physrevb.45.806

[206] J. Mathon, A. Umerski, and M. Villeret, "Oscillations with Co and Cu thickness of the current-perpendicular-to-plane giant magnetoresistance of a Co/Cu/Co(001) trilayer," *Physical Review B*, vol. 55, no. 21, pp. 14 378–14 386, jun 1997. https://doi.org/10.1103/PhysRevB.55.14378

[207] L. A. Michez, B. J. Hickey, S. Shatz, and N. Wiser, "New results for the dependence of the magnetoresistance of magnetic multilayers on the layer thickness," *EPL (Europhysics Letters)*, vol. 83, no. 5, p. 57007, sep 2008. https://doi.org/10.1209/0295-5075/83/57007

[208] W. F. Egelhoff, P. J. Chen, Powell, Stiles, McMichael, Lin, Sivertsen, Judy, Takano, Berkotz, Anthony, and Brug, "Optimizing the giant magnetoresistance of symmetric

and bottom spin valves," *Journal of Applied Physics*, vol. 79, no. May, p. 5277, 1996. http://dx.doi.org/10.1063/1.361352

[209] T. Nakano, M. Oogane, and Y. Ando, "Annealing effect on interlayer exchange coupling in perpendicularly magnetized synthetic antiferromagnetic structure based on Co/Pd multilayers with ultrathin Ru spacer," *Japanese Journal of Applied Physics*, vol. 57, no. 7, p. 073001, jul 2018. https://doi.org/10.7567/JJAP.57.073001

[210] J. C. Slonczewski, "Conductance and exchange coupling of two ferromagnets separated by a tunneling barrier," *Physical Review B*, vol. 39, no. 10, pp. 6995–7002, apr 1989. https://doi.org/10.1103/PhysRevB.39.6995

[211] S. Ishikawa, H. Sato, M. Yamanouchi, S. Ikeda, S. Fumaki, F. Matsukura, and H. Ohno, "Co/Pt multilayer-based magnetic tunnel junctions with a CoFeB/Ta insertion layer," vol. 719, no. September 2013, pp. 3–6, 2014. https://doi.org/10.1063/1.4862724

[212] J. Sinha, M. Gruber, M. Kodzuka, T. Ohkubo, S. Mitani, K. Hono, and M. Hayashi, "Influence of boron diffusion on the perpendicular magnetic anisotropy in Ta|CoFeB|MgO ultrathin films," *Journal of Applied Physics*, vol. 117, no. 4, p. 043913, jan 2015. https://doi.org/10.1063/1.4906096

[213] Z. Wang, M. Saito, K. P. McKenna, S. Fukami, H. Sato, S. Ikeda, H. Ohno, and Y. Ikuhara, "Atomic-Scale Structure and Local Chemistry of CoFeB–MgO Magnetic Tunnel Junctions," *Nano Letters*, vol. 16, no. 3, pp. 1530–1536, mar 2016. https://doi.org/10.1021/acs.nanolett.5b03627

[214] C. Y. You, T. Ohkubo, Y. K. Takahashi, and K. Hono, "Boron segregation in crystallized MgO/amorphous-Co40Fe40B20 thin films," *Journal of Applied Physics*, vol. 104, no. 3, p. 033517, aug 2008. https://doi.org/10.1063/1.2963709

[215] Chando Park, L. Miloslavsky, I. Lim, Sangmun Oh, C. Kaiser, Qunwen Leng, and M. Pakala, "Influence of Boron Diffusion on Transport and Magnetic Properties in CoFeB/MgO/CoFeB Magnetic Tunnel Junction," *IEEE Transactions on Magnetics*, vol. 45, no. 10, pp. 3457–3459, oct 2009. https://doi.org/10.1109/TMAG.2009.2022495

[216] Z. R. Tadisina, A. Natarajarathinam, B. D. Clark, A. L. Highsmith, T. Mewes, S. Gupta, E. Chen, and S. Wang, "Perpendicular magnetic tunnel junctions using Co-based multilayers," *Journal of Applied Physics*, vol. 107, no. 9, p. 09C703, may 2010. https://doi.org/10.1063/1.3358242

[217] K. M. Lee, J. W. Choi, J. Sok, and B. C. Min, "Temperature dependence of the interfacial magnetic anisotropy in W/CoFeB/MgO," *AIP Advances*, vol. 7, no. 6, pp. 1–8, 2017. http://dx.doi.org/10.1063/1.4985720

[218] G.-G. An, J.-B. Lee, S.-M. Yang, J.-H. Kim, W.-S. Chung, and J.-P. Hong, "Highly stable perpendicular magnetic anisotropies of CoFeB/MgO frames employing

W buffer and capping layers," *Acta Materialia*, vol. 87, pp. 259–265, apr 2015. https://doi.org/10.1016/j.actamat.2015.01.022

[219] J.-y. Choi, D.-g. Lee, J.-u. Baek, and J.-g. Park, "Double MgO-based Perpendicular Magnetic-Tunnel-Junction Spin-valve Structure with a Top Co2Fe6B2 Free Layer using a Single SyAF [Co/Pt]n Layer," *Scientific Reports*, vol. 8, no. 1, p. 2139, dec 2018. http://www.nature.com/articles/s41598-018-20626-4

[220] S. Kim, S. C. Baek, M. Ishibashi, K. Yamada, T. Taniguchi, T. Okuno, Y. Kotani, T. Nakamura, K. J. Kim, T. Moriyama, B. G. Park, and T. Ono, "Contributions of Co and Fe orbitals to perpendicular magnetic anisotropy of MgO/CoFeB bilayers with Ta, W, IrMn, and Ti underlayers," *Applied Physics Express*, 2017. https://doi.org/10.7567/APEX.10.073006

[221] L. E. Nistor, B. Rodmacq, C. Ducruet, C. Portemont, I. L. Prejbeanu, and B. Dieny, "Correlation Between Perpendicular Anisotropy and Magnetoresistance in Magnetic Tunnel Junctions," *IEEE Transactions on Magnetics*, vol. 46, no. 6, pp. 1412–1415, jun 2010. https://doi.org/10.1109/TMAG.2010.2045641

[222] Y. W. Oh, K. D. Lee, J. R. Jeong, and B. G. Park, "Interfacial perpendicular magnetic anisotropy in CoFeB/MgO structure with various underlayers," *Journal of Applied Physics*, vol. 115, no. 17, pp. 2012–2015, 2014. https://doi.org/10.1063/1.4864047

[223] S. Yuasa, A. Fukushima, H. Kubota, Y. Suzuki, and K. Ando, "Giant tunneling magnetoresistance up to 410% at room temperature in fully epitaxial Co/MgO/Co magnetic tunnel junctions with bcc Co(001) electrodes," *Applied Physics Letters*, vol. 89, no. 4, pp. 1–4, 2006. http://aip.scitation.org/doi/10.1063/1.2236268

[224] L. Yuan, S. H. Liou, and D. Wang, "Temperature dependence of magnetoresistance in magnetic tunnel junctions with different free layer structures," *Physical Review B - Condensed Matter and Materials Physics*, vol. 73, no. 13, pp. 1–8, 2006. https://link.aps.org/doi/10.1103/PhysRevB.73.134403

[225] S. Hashimoto, Y. Ochiai, and K. Aso, "Perpendicular magnetic anisotropy and magnetostriction of sputtered Co/Pd and Co/Pt multilayered films," *Journal of Applied Physics*, vol. 66, no. 10, pp. 4909–4916, nov 1989. https://doi.org/10.1063/1.343760

[226] A. Fukushima, T. Taniguchi, A. Sugihara, K. Yakushiji, H. Kubota, and S. Yuasa, "Giant magnetoresistance in perpendicularly magnetized synthetic antiferromagnetic coupling with Ir spacer," *AIP Advances*, vol. 8, no. 5, p. 055925, may 2018. https://doi.org/10.1063/1.5007304

[227] A. Dinia and K. Ounadjela, "Temperature dependence of the magnetoresistance in Co/Ru sandwich and superlattice structures," *Journal of Magnetism and Magnetic Materials*, vol. 146, no. 1-2, pp. 66–76, apr 1995. https://doi.org/10.1016/0304-8853(94)01657-7

[228] G. Feng, H. C. Wu, J. F. Feng, and J. M. D. Coey, "Temperature dependent coercivity crossover in pseudo-spin-valve magnetic tunnel junctions with perpendicular anisotropy," *Applied Physics Letters*, vol. 99, no. 4, p. 042502, jul 2011. https://doi.org/10.1063/1.3614000

[229] P. W. T. Pong and W. F. Egelhoff, "Enhancement of tunneling magnetoresistance by optimization of capping layer thicknesses in CoFeB/MgO/CoFeB magnetic tunnel junctions," *Journal of Applied Physics*, vol. 105, no. 7, p. 07C915, apr 2009. https://doi.org/10.1063/1.3063664

[230] Z.-P. Li, S. Li, Y. Zheng, J. Fang, L. Chen, L. Hong, and H. Wang, "The study of origin of interfacial perpendicular magnetic anisotropy in ultra-thin CoFeB layer on the top of MgO based magnetic tunnel junction," *Applied Physics Letters*, vol. 109, no. 18, p. 182403, oct 2016. https://doi.org/10.1063/1.4966891

[231] J. Sinha, M. Hayashi, A. J. Kellock, S. Fukami, M. Yamanouchi, H. Sato, S. Ikeda, S. Mitani, S.-h. Yang, S. S. P. Parkin, and H. Ohno, "Enhanced interface perpendicular magnetic anisotropy in Ta|CoFeB|MgO using nitrogen doped Ta underlayers," *Applied Physics Letters*, vol. 102, no. 24, p. 242405, jun 2013. https://doi.org/10.1063/1.4811269

[232] S. M. Rossnagel and H. Kim, "Diffusion barrier properties of very thin TaN with high nitrogen concentration," *Journal of Vacuum Science & Technology B: Microelectronics and Nanometer Structures*, vol. 21, no. 6, p. 2550, 2003. https://doi.org/10.1116/1.1625953

[233] Infineon, "TLE 5501 Data sheet," p. 19, 2018.

[234] M. Bersweiler, H. Sato, and H. Ohno, "Magnetic and Free-layer Properties of MgO/(Co)FeB/MgO Structures: Dependence on CoFeB Composition," *IEEE Magnetics Letters*, vol. 8, 2017. http://ieeexplore.ieee.org/document/8025339/

[235] Y. Fu, I. Barsukov, J. Li, A. M. Gonçalves, C. C. Kuo, M. Farle, and I. N. Krivorotov, "Temperature dependence of perpendicular magnetic anisotropy in CoFeB thin films," *Applied Physics Letters*, vol. 108, no. 14, p. 142403, apr 2016. http://aip.scitation.org/doi/10.1063/1.4945682

[236] A. Karsenty, "A Comprehensive Review of Integrated Hall Effects in Macro-, Micro-, Nanoscales, and Quantum Devices," *Sensors*, vol. 20, no. 15, p. 4163, jul 2020. https://www.mdpi.com/1424-8220/20/15/4163

[237] F. Bruckner, B. Bergmair, H. Brueckl, P. Palmesi, A. Buder, A. Satz, and D. Suess, "A device model framework for magnetoresistive sensors based on the Stoner–Wohlfarth model," *Journal of Magnetism and Magnetic Materials*, vol. 381, pp. 344–349, may 2015. http://dx.doi.org/10.1016/j.jmmm.2015.01.009

[238] E. H. Hall, "On a New Action of the Magnet on Electric Currents," *American Journal of Mathematics*, vol. 2, no. 3, p. 287, sep 1879. https://doi.org/10.2307/2369245

[239] Honeywell, "Hall Effect Sensing and Application," *Manual - MICRO SWITCH Sensing and Control*, pp. 2–76. https://sensing.honeywell.com/hallbook.pdf

[240] W. Raberg, C. Muehlenhoff, and J. Zimmer, "Stray field robust xMR sensor using perpendicular anisotropy," *US patent* US10852369, p. 14, 2020. https://web.ip7.tech/app/detailview/index/US10852369

[241] H. Jaffrès, D. Lacour, F. Nguyen Van Dau, J. Briatico, F. Petroff, and A. Vaurès, "Angular dependence of the tunnel magnetoresistance in transition-metal-based junctions," *Physical Review B*, vol. 64, no. 6, p. 064427, jul 2001. https://doi.org/10.1103/PhysRevB.64.064427